BOTTOMONIUM STUDIES AT LHC ENERGY USING ALICE MUON SPECTROMETER

By

Wadut Shaikh

PHYS05201504011

Saha Institute of Nuclear Physics, Kolkata

A thesis submitted to the

Board of Studies in Physical Sciences

In partial fulfillment of requirements

for the Degree of

DOCTOR OF PHILOSOPHY

of

HOMI BHABHA NATIONAL INSTITUTE

November, 2020

Homi Bhabha National Institute

Recommendations of the Viva Voce Committee

As members of the Viva Voce Board, we certify that we have read the dissertation prepared by **Wadut Shaikh** entitled **"Bottomonium studies at LHC energy using ALICE muon spectrometer"** and recommend that it maybe accepted as fulfilling the dissertation requirement for the Degree of Doctor of Philosophy.

.....**Date:**

Chairman : **Prof. Pradip Kr. Roy**, SINP

.....**Date:04/02/2020**

Guide : **Prof. Sukalyan Chattopadhyay**, SINP

.....Date:

Member 1 : **Prof. Debasish Das**, SINP

.....**Date:**

Member 2 : **Prof. Supratik Mukhopadhyay**, SINP

.....**Date:**

Member 3 : **Prof. Subhasis Chattopadhyay**, VECC

Final approval and acceptance of this dissertation is contingent upon the candidate's submission of the final copies of the dissertation to HBNI.

I hereby certify that I have read this dissertation prepared under my direction and recommend that it may be accepted as fulfilling the dissertation requirement.

Date:04/02/2021

Place: Kolkata

Guide: Prof. Sukalyan Chattopadhyay

STATEMENT BY AUTHOR

This dissertation has been submitted in partial fulfillment of requirements for an advanced degree at Homi Bhabha National Institute (HBNI) and is deposited in the Library to be made available to borrowers under rules of the HBNI.

Brief quotations from this dissertation are allowable without special permisiion, provided that accurate acknowledgement of source is made. Requests for permisiion for extended quotation from or reproduction of this manuscriptin whole or in part may be granted by the Competent Authority of HBNI when in his or her judgement the proposed use of the material is in the interests of scholarship. In all other instances, however, permission must be obtained from the author.

.....

Wadut Shaikh

DECLARATION

I, hereby declare that the investigation presented in the thesis has been carried out by me. The work is original and has not been submitted earlier as a whole or in part for a degree / diploma at this or any other Institution / University.

.....

Wadut Shaikh

List of Publications arising from the thesis

Journal:

a. Published

1. **"Inclusive Υ production in p-Pb collisions at $\sqrt{s_{\rm NN}}$ = 8.16 TeV"**
   S. Acharya *et* al. [ALICE Collaboration], Phys. Lett. B 806 (2020) 135486 [arXiv:1708.02385 [hep-ph]].

b. Submitted

1. **"Nuclear modification factor of average D mesons in an anisotropic quark-gluon plasma at energies available at the CERN Large Hadron Collider"**
   Wadut Shaikh, Mahatsab Mandal, Pradip Roy, Sukalyan Chattopadhyay, Phys. Rev. C.

2. **"Υ production and nuclear modification at forward rapidity in Pb-Pb collisions at $\sqrt{s_{\rm NN}}$ = 5.02 TeV"**
   S. Acharya *et* al. [ALICE Collaboration], Phys. Lett. B, [arXiv:2011.05758 [nucl-ex]].

Conference/Symposium

1. **"Nuclear modification factor of average D meson in an anisotropic quark-gluon plasma at the LHC energies"**
   Wadut Shaikh, Mahatsab Mandal, Pradip Roy, Sukalyan Chattopadhyay.
   DAE Symp. Nucl. Phys. **64**, 820, (2019).

2. **"Scanning for fault detection of the Cathode Pad Chambers of ALICE second muon tracking station using an Amptek Mini X-ray source"**
   Wadut Shaikh,Tinku Sinha, Indranil Das, Sukalyan Chattopadhyay.
   DAE Symp. Nucl. Phys. **64**, 898, (2019).

3. **"Quarkonium Measurements at Forward Rapidity with ALICE at the LHC"**
   Wadut Shaikh [ALICE Collaboration].
   The XVIII International Conference on Strangeness in Quark Matter (SQM 2019), Springer Proceedings in Physics, 141–145 (2020) [arXiv:1910.06695 [hep-ex]].

Other Publications:

a. Preliminary Physics Summary

1. **"Inclusive Υ production in p-Pb collisions at $\sqrt{s_{\rm NN}}$ = 8.16 TeV"**
   Roberta Arnaldi, Biswarup Paul, **Wadut Shaikh**
   ALICE-PUBLIC-2018-008 [https://alice-notes.web.cern.ch/node/820].

b. Analysis note:

1. **"Inclusive Upsilon production in p-Pb collisions at center of mass energy = 8.16 TeV"**
   Wadut Shaikh, Biswarup Paul, Indranil Das, Sukalyan Chattopadhyay
   ANA-714 [https://alice-notes.web.cern.ch/node/714].

2. **"Centrality dependence of inclusive Upsilon(1S) production in p-Pb collisions at 8.16 TeV"**
   Biswarup Paul, **Wadut Shaikh**, Indranil Das, Sukalyan Chattopadhyay
   ANA-753 [https://alice-notes.web.cern.ch/node/753].

3. **"Inclusive Upsilon(1S), Upsilon(2S) and Upsilon(3S) production at forward rapidity in pp collisions at $\sqrt{s}$ = 5 TeV with the ALICE experiment"**
   Wadut Shaikh, Florian Damas, Indranil Das, Sukalyan Chattopadhyay, Mohamad Tarhin
   ANA-879 [https://alice-notes.web.cern.ch/node/879].

4. **"Measurement of Υ production in Pb-Pb collisions at $\sqrt{s_{\rm NN}}$ = 5.02 TeV"**
   Florian Damas, **Wadut Shaikh**
   ANA-951 [https://alice-notes.web.cern.ch/node/951].

Dedicated to My Abba, Maa

ACKNOWLEDGEMENTS

This thesis would never have been possible without the support and guidance of various people at Saha Institute of Nuclear Physics and colleagues from CERN.

Firstly, I would like to thank Prof. Sukalyan Chattopadhyay for giving me the opportunity to complete my Ph.D. work under his supervision. It is truly an honor for me to have a supervisor who gave me advice, ideas, motivation, and moral support throughout my Ph.D. period. His guidance helped me in all the time of research and writing of this thesis. I appreciate his immense knowledge in detector physics, the power of managing administrative responsibilities and the friendly conversations. His two best lines, "jibone ki sukh" and "chepe diacho" that I like too much.

I would like to thank Dr. Indranil Das who familiarize me with the ALICE software and helped me a lot at each step during my Ph.D. work. I am grateful to Roberta Arnaldi, Biswarup da, Laure Marie Massacrier and Cynthia Hadjidakis for giving me the opportunity to work with them. My heartfelt thanks to Roberta for the help in the analysis and fixing the strategies to complete the work within a given period.

I am thankful to Philippe Pillot and Tahir bhai for the help and in-depth discussion on my ALICE service work. I also wish to thank Javier Castillo, Mohamad Tarhini, Florian for helping me doing MC simulation.

My thanks also go out to the comments, suggestions, discussions and support I received from the collaborative work of ALICE PWG-DQ QQ2MuMu group. I am especially grateful to all present and past conveners for their help.

I would like to extend my heartfelt thanks to Prof. Pradip Kumar Roy and Mahatsab da for valuable discussion on theoretical work. I would also like to thank Tinku mam, Dabasish Sir, Aridndam da for their help in detector activities. I gratefully acknowledge the assistance of my Ph.D. committee members.

My special thanks go to 249-mates: Argha da, Arnab da, Ashim da, Biswarup da (nuclear), Debabrata, Gourav, Kalyanmoy da, Pritam, Prasant, Rajarshi, Samsul, Shamik da, Sourav da, Souvik da, Anindita, Sweta for their availability to help and providing useful (sometimes meaningless) tips and tricks on everything. Big thanks go to Jhuma, Anisa di, Hushnud apa for their help in analysis and discussion on various topics. To all of you, I am most grateful for your friendship and support during these five years.

I am thankful to Fantastic-3-mates Sajad, Shuvankar and Snehal with whom I shared many unforgettable moments during my Ph.D. period.

I would like to extend my sincere thanks to the Principal and other staff of Mugberia Gangadhar Mahavidyalaya.

I would like to express my gratitude to my beloved Maa, Abba, Setara, Aktara, didi, dula bhai for their inspiration, constant encouragement, support and endless patience. Lots of love for my nephew Kasif, Atif. I am also thankful to my parents-in-law, Sneha, Suhana for their supports.

Finally, I wish to thank my wife Nisha for her love, constant support, keeping things going smoothly and for always showing how proud she is of me.

Lastly, I sincerely apologize to all the people whom I have missed mentioning on this page.

Contents

List of Figures

List of Tables

CHAPTER 1

Introduction

In this chapter, we shall address the basic concepts of Standard Model (SM), Quantum Chromodynamics (QCD) and Quark–Gluon Plasma (QGP). The quarkonia as a probe of the QGP, will also be discussed. In this context, the quarkonia production mechanism, the Cold Nuclear Matter (CNM) effects and the Hot Matter effects (QGP effects) will be described in detail. In the end, a discussion on Upsilon (Υ) production in relativistic hadron collisions will be presented.

1.1 Standard Model of particle physics

The Standard Model (SM) [1] is the most successful theory of particle physics that describes the strong, the electromagnetic and the weak interactions among the fundamental particles. The elementary particles listed in SM are shown in Fig 1.1 which can be classified into two main groups according to their spins: fermions (half-integer spin) and bosons (integer spin).

Fermions can be further divided into leptons and quarks. There are three generations of leptons which include electron (e^-), muon (μ^-), tau (τ^-) having one unit of negative charge and its corresponding leptonic left-handed neutrinos (ν_e, ν_μ, ν_τ). Their counter-

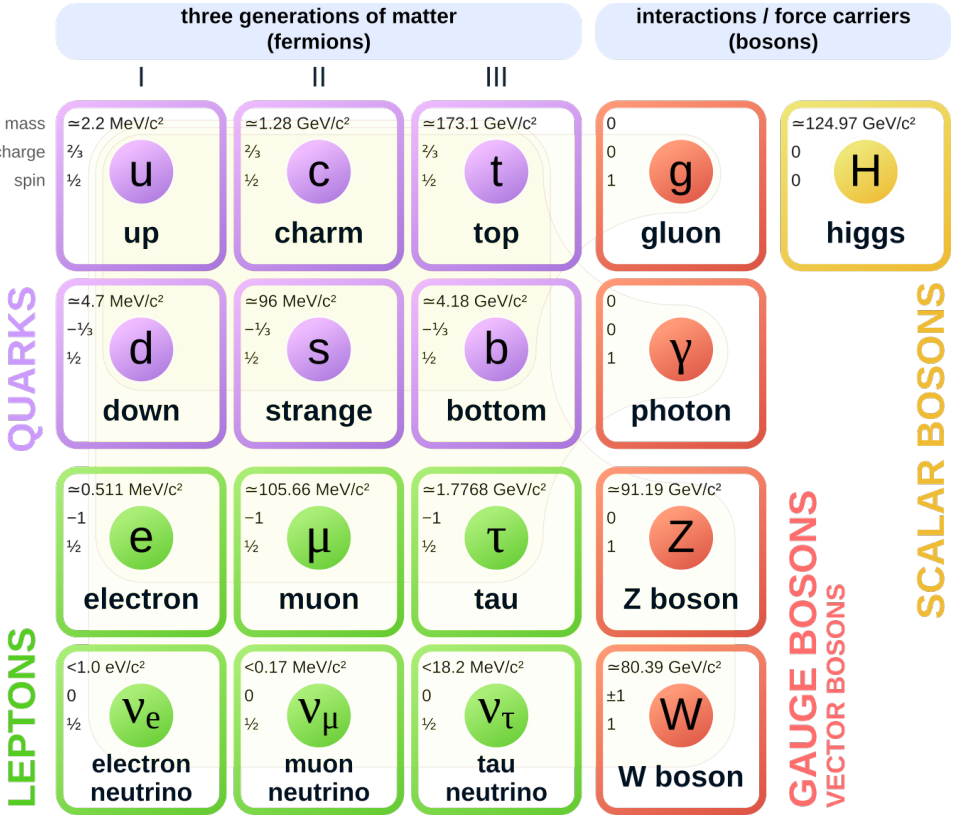

Figure 1.1: The elementary particles of the Standard Model.

part anti-particles have one unit of positive charge anti-leptons (e^+, μ^+, τ^+) associated to right-handed anti-neutrino with corresponding flavour ($\bar{\nu_e}$, $\bar{\nu_\mu}$, $\bar{\nu_\tau}$). On the other side, there are six flavours of quarks (up u, down d, charm c, strange s, top t, bottom b) and their anti-quarks ($\bar{u}$, $\bar{d}$, $\bar{c}$, $\bar{s}$, $\bar{t}$, $\bar{b}$) that are grouped into three generations. The u, c and t quarks have positive electric charge +2/3 while d, s and b quarks have negative electric charge -1/3. In addition of electric charge, the quarks have also the color charges namely red, green and blue. In general, the quarks are confined inside the hadrons. The baryons (e.g neutron, proton) are made of three quarks (qqq) while mesons (e.g pions, kaons) are made of a quark and an anti-quark ($q\bar{q}$).

The SM includes three of the four fundamental forces:– the strong force, the electromagnetic force and the weak force. (Gravity is not included in the SM).

- **The electromagnetic force** governs the interaction between the charged particles by exchanging photons. The photon, massless (rest mass zero) neutral boson, is the mediator for the electromagnetic force. The branch of physics that describes this force is known as Quantum Electrodynamics (QED).

- **The weak force** is the weakest force among the three forces in the SM. The fermions and quarks can interact weakly by the exchange of massive vector gauge bosons $W^{\pm}$ or Z. Due to the higher mass of mediator of the weak force, the range of this force is limited to $\approx 10^{-18}$ fm. The weak and the electromagnetic force are combined in the electroweak theory.

- **Strong force** is the strongest force in the SM. The particle which has a color charge (quarks and gluon) can participate in strong interaction by exchanging gluons. Quantum Chromodynamics (QCD) is the theory that describes the strong interaction.

The basic feature of fundamental forces in SM are listed in Table 1.1.

Table 1.1: The fundamental forces in Standard Model [1] and their basic properties.

Force	Range(m)	Mediators	Mass of the mediators (GeV/c^2)
electromagnetic	∞	photon	0
weak	10^{-18}	$W^{\pm}$,Z^0	80.2,91
strong	10^{-15}	gluon	0

In SM the formalism, the particle mass is generated through the interaction with the Higgs field. The quanta of this field is known as the Higgs boson which has been discovered in 2012 by the two experiments ATLAS [2] and CMS [3] at CERN.

1.2 QCD and asymptotic freedom

The Quantum Chromodynamics (QCD) is a non-Abelian gauge theory that describes the interaction of particles via the strong interaction. Unlike the QED where the photon is neutral, in QCD the gluons are color charged and can couple to each other. Hence, the virtual gluon can exist in the QCD vacuum. The screening caused by virtual gluons increases the effective color charge of the screened particle and therefore the coupling decreases with increasing momentum transfer as shown in Fig. 1.2. In the other words, the intensity of the strong interaction grows stronger with increasing distance (smaller Q) and weaker with decreasing the distance (larger Q). When the momentum transfer is high enough (Q$\rightarrow \infty$), the strong coupling vanishes and therefore the bound quarks behave as free particles. This regime is known as asymptotic freedom. In this region, the perturbative QCD is valid for describing the strong interaction. When Q reaches the QCD scale ($\Lambda_{\mathrm{QCD}} \sim 200$ MeV [4]), the coupling constant becomes large and the perturbative QCD no longer work. This happens inside the hadrons where the coupling becomes extremely strong and it is impossible to isolate the quarks. Therefore, the quarks are confined inside the hadrons. This mechanism is known as confinement and in this regime Lattice QCD (lQCD)[5], a non-perturbative technique used to describe the QCD equations.

1.3 Quark Gluon Plasma (QGP) Phase transition

As per the above discussion, it can be suggested that the behavior of high energy density strongly-interacting matter is different from that of the low-energy state of ordinary hadronic matter. The high energy density in QCD can be created by increasing the temperature of the system and/or by increasing the baryo-chemical potential μ_{b}. If the temperature of the system is extremely high and/or the baryon density is high enough,

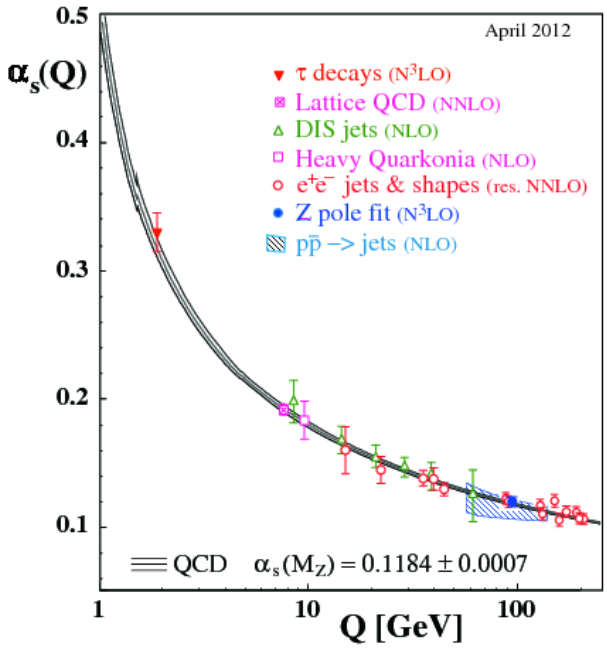

Figure 1.2: Summary of the measurements of the strong interaction coupling constant (α_s) as a function of the energy scale Q [6]

the ordinary hadronic matter undergoes a phase where the constituent quarks and gluons (partons) are no longer confined. Analogous to the QED plasma, the presence of color charge generates a Debye screening effect that limits the interaction length of the strong force and allows the deconfinement of constituent partons. This deconfined state of quarks and gluons is known as Quark-Gluon Plasma (GQP) [7]. It is believed that the microsecond universe has gone through this state of deconfined quarks and gluons. As the QGP expand and cool, it undergoes the phase transition to the hadronic matter. The QGP state may also exist in the neutron stars core where the net baryonic density is very high but the temperature is low.

These conditions can be created at a small scale in the laboratory by colliding the ultra-relativistic heavy-ion beams. The energy released in these collisions leads to high energy density. Under this condition, the hardons start to overlap and the strong interaction among its constituents becomes weak. Thus, the matter undergoes a phase transition to a deconfined state of the QGP.

1.3.1 QCD Phase Diagram

The QCD phase diagram is usually described by the T–μ_b phase space plot where T is the temperature and μ_b denote baryon chemical potential. Fig.1.3 shows a schematic diagram of such a phase-space. The μ_b is the measure of the excess of baryons over anti-baryons and is related to the net baryon density. In the early universe, an equal amount of matter and anti-matter were produced so μ_b was zero but in our current world, the abundance of matter over anti-matter leads to $\mu_b > 0$. At a particular μ_b, the state of hadronic matter changes when the temperature reaches a critical value T_c. The recent calculations from the lQCD [8] predict $T_c = 156.5 \pm 1.5$ MeV at $\mu_b = 0$.

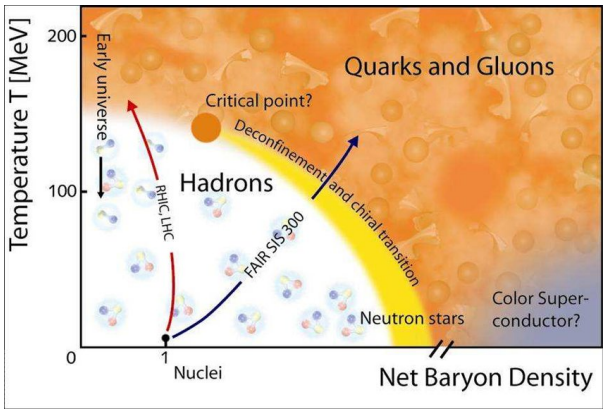

Figure 1.3: A representative QCD phase diagram of nuclear matter in temperature (T) and baryon chemical potential (μ_b) plane.

The nature of the phase transition between the partonic deconfined state and the hadronic matter is still an open question. At $\mu_b = 0$, the lQCD models predict [9] that the transition is a smooth cross-over. But these predictions are not reliable at $\mu_b \neq 0$. The experimental, as well as the theoretical investigations, are ongoing in order to understand the nature of the phase transition over the entire phase-space diagram.

1.4 Experimental study of the QGP

The region with low chemical potential and high temperature in QCD phase diagram can be accessed by colliding heavy-ion nuclei in the particle accelerators at Brookhaven National Laboratory (BNL) in USA and the Large Hadron Collider (LHC) at CERN in Switzerland.

1.4.1 Evolution of heavy-ion collision

A schematic view of heavy-ion collisions and it's space-time evolution are depicted in Fig.1.4. We shall briefly explain the dynamics of each stages of evolution:

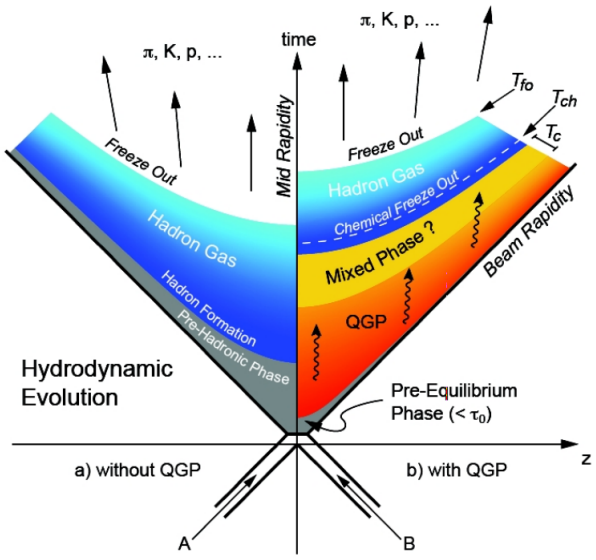

Figure 1.4: The space-time evolution of the matter produced in ultra-relativistic heavy-ion collisions.

- **Pre-equilibrium:** The collision takes place a $\tau = 0$. At this stage, the large momentum transfers between the partons of the nuclei take place by the multiple hard scatterings, which lead to the creation of electroweak bosons and heavy flavor quarks.

- **Thermalisation:** The strong interaction between the partons, created in these collisions of the two nuclei, leads to the thermalization of the system in a time scale $1 < \tau < 10$ fm/c. If the system has high energy density and it is in thermal equilibrium, then the QGP may be formed.

- **Chemical freeze-out:** As the system expands and cools, the quarks and gluons start to form the hadrons once the temperature reaches below the T_{C}. The chemical freeze-out can happen when there is no more inelastic scattering between the hadrons and therefore the number of different hadrons become constant.

- **Kinetic freeze-out:** At $\tau > 20$ fm/c, the hadrons gas continue to expansion. When the density of the medium becomes too low that the elastic scatterings among the hadrons stop and the kinetic freeze-out takes place.

1.4.2 Observables of the QGP

Since the QGP fireball produced in the heavy-ion collisions is extremely short-lived ($\sim 10^{-24}$ sec.), it is experimentally impossible to directly detect and measure the properties of the QGP. Thus, indirect observables are used to probe the QGP. Based on the momentum transfer associated with the probes, they can be classified into two main groups.

• **Soft probes** involves low momentum transfer process and therefore it is likely to be created at different stages of the evolutions. The modification of particle yields and ratios, anisotropic flow, electromagnetic probes, strangeness enhancement are listed in this group.

• **Hard probes** are created in the hard scattering during the early stage of the collisions through the process of high momentum transform. Examples of hard probes are jets quenching, heavy flavour, quarkonia and weak boson productions.

This thesis focuses on the Upsilon ($b\bar{b}$, a quarkonia) production in hadron collisions. The description of all above mention probes are beyond the scope of this thesis and only the quarkonia production will be discussed in the following section.

1.5 Quarkonium and the Nuclear matter effects

Quarkonia are the bound state of heavy quark q and its anti-quark $\bar{q}$, namely, charmonia ($c\bar{c}$) and bottomonia ($b\bar{b}$). In the high energy collisions, the quarkonia are produced in the initial hard scattering of partons where a large amount of momentum is transferred. At the LHC energy, the gluon-gluon fusion process is the dominant source of heavy quarks pair production [10]. Especially in bottomonium sector, the production is dominated by the initial hard scattering process [11] in hadron collisions. Due to their long lifetime, the quarkonia are able to experience all the stages of the medium evolution of the p–Pb or Pb–Pb collisions. However, the presence of a dense and deconfined medium can affect the hadronization of the $q\bar{q}$ pair. Hence the modification in the quarkonium production cross-section is an important probe to study the matter produced in Pb–Pb and p–Pb collisions. The evaluation of a bottomonium state produced in heavy-ion collisions is pictorially shown in Fig. 1.5. A $b\bar{b}$ quark pair is produced during the initial hard scattering and hadronizes into an Upsilon(Υ, bottomonium state) at the beginning of the collision. The Υ afterward passage through the QGP which develops around it. Unless the Υ is explicitly broken up by the QGP, it remains intact in the medium as the system evolves and eventually hadronizes into particle species. At the LHC energy, the regeneration of Υ from free q and $\bar{q}$ is expected to be negligible.

Hence, by measuring the production of quarkonium states in the hadron collisions one can explore how they have been affected by the medium and learn about the medium itself.

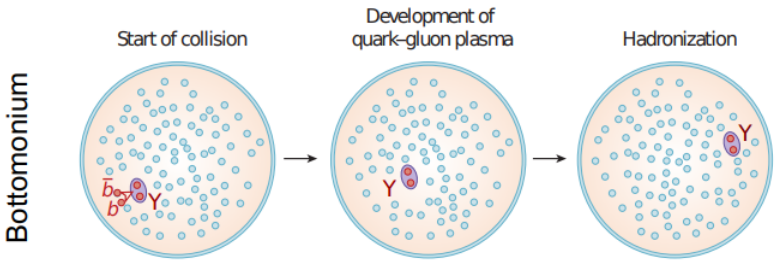

Figure 1.5: A pictorial representation of a bottomonium and it's passage through the QGP [12].

1.5.1 Hot Nuclear Matter or QGP induced effects on the Quarkonia

In the following section, the various effects of QGP on quarkonia production in nucleus-nucleus collisions will be discussed.

Color screening mechanism and sequential suppression

T. Matsui and H. Satz predicted that the production of the quarkonium can be suppressed in the deconfined QGP medium due the presence of color screening effect [13]. The debye screening of color charge is analogous to the well-known electric charge screening process in quantum electrodynamics. In the presence of color charge in the deconfined medium , the effective potential [14] of a quarkonia can be expressed as:

$$V_{q\bar{q}}(r,T) \approx -\frac{4}{3}\frac{\alpha_s}{r}e^{-r/r_D(T)} \tag{1.1}$$

where

α_s = strong interaction coupling constant

r_D = Debye screening radius, depend on the medium temperature

when the r_D is larger than the binding radius ($r_{q\bar{q}}$) of quarkonium state, it survives in the QGP while the state break up when $r_D < r_{q\bar{q}}$. The temperature at which the $r_D = r_{q\bar{q}}$, is known as the dissociation temperature (T_D).

The r_D is inversely proportional to the temperature of the medium. Hence, the effective interaction range of a heavy quark decreases with increasing temperature and higher radius quarkonium state (less bound) melt first. A state can survive in the QGP above the critical temperature (T_c) but dissociate once the temperature exceeds the T_D. The survival probability of quarkonium state in the QGP depends on its radius and binding energy. In Table 1.2 the binding energy, radius and T_D/T_c of different quarkonium state are listed.

Table 1.2: The binding energy(E_b), radius (r) and T_D/T_c of different quarkonium states.

State	E_b (GeV)	r (fm)	T_D/T_c
J/ψ	0.64	0.25	2.10
ψ(2S)	0.05	0.45	1.12
Υ(1S)	1.10	0.14	>4
Υ(2S)	0.53	0.28	1.60
Υ(3S)	0.20	0.39	1.17

If the temperature of the QGP is gradually increased above the T_c, the quarkonia states will dissociate one by one and a hierarchy in the suppression of different quarkonia states will be observed according to their binding energy and radius. This is known as sequential suppression.

(Re)generation

At the high energy nucleus-nucleus collisions, the large number of produced heavy quark and anti-quarks in the medium may recombine together to form quarkonium states [15, 16]. This phenomenon is known as regeneration or recombination. Apart from the density of heavy quarks, the rate of regeneration also depends on the expansion

of QGP and the kinematic distribution of these heavy quarks. The regeneration mechanism for J/ψ at the LHC energy is illustrated in Fig. 1.6.

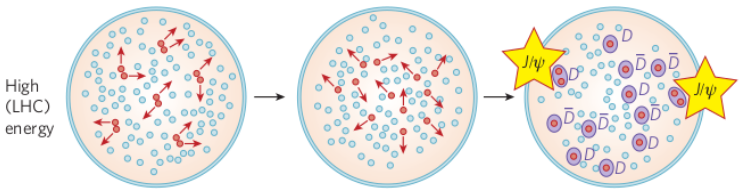

Figure 1.6: A sketch of the re(generation) mechanism for J/ψ in heavy-ion collisions at the LHC energy [12].

In the ultra relativistic heavy-ion collisions at LHC, a large number of $c\bar{c}$ pairs ($\sim$116) are produced in one collision and get defused to free c and $\bar{c}$ in the deconfined medium. This uncorrelated c and $\bar{c}$ may form a bound state at the hadronization stage (some model suggests this process continues throughout the medium evolution).

Interaction with constituents of the medium

Besides the color screening and (re)generation effects in the heavy-ion collisions, the quarkonium yields may get modified compared to pp collisions due to the interaction with the constituents (comovers) of the QGP [17, 18]. The comovers can scatter with the $q\bar{q}$ and as a consequence, the quarkonium state may dissociate. This dissociation of $q\bar{q}$ increases with increasing energy density.

1.5.2 Cold Nuclear Matter effects on the Quarkonia

The cold nuclear matter (CNM) effects that are not related to the QGP formation may also modify the quarkonium production. In order to disentangle the CNM effects from the hot nuclear matter effects, the quarkonium production is studied in p–Pb collisions in which the QGP is not expected to be formed. The CNM effects can be classified into

two groups i.e initial state effects and final state effects.

1.5.3 Initial-state effects

The initial state effects are linked to the early stages of the collisions (before the hadronization of the $q\bar{q}$). The degree of modification due to these effects are same for all the charmonium states. Similarly, all the bottomonium states will be affected identically but the extent is different from charmonium family because of the mass difference between the two quark flavors (c and b). These effects are discussed below.

Modification of nuclear parton distribution functions

Parton Distribution Functions (PDFs) represent the density of partons with a particular flavor carrying a fraction of momentum x of the total nucleon's momentum. The PDFs are global and obtained through fitting the experimental data taken from deep inelastic scattering (DIS) experiments as well as Drell-Yan (DY) production. An example of PDF for an energy transfer of $Q^2 = 10$ GeV^2 with H1 experiment at HERA is shown in Fig. 1.7.

The deep inelastic scattering off nucleons has revealed that the inelastic cross section of the nucleons are modified in the nuclear environment compared to the nucleons in isolation. The modified PDFs can be expressed as [20]:

$$R_i^A(x, Q^2) = \frac{f_i^A(x, Q^2)}{f_i(x, Q^2)} \tag{1.2}$$

where

$f_i^A(x, Q^2)$ is the PDF for a parton of flavor i in nucleus A

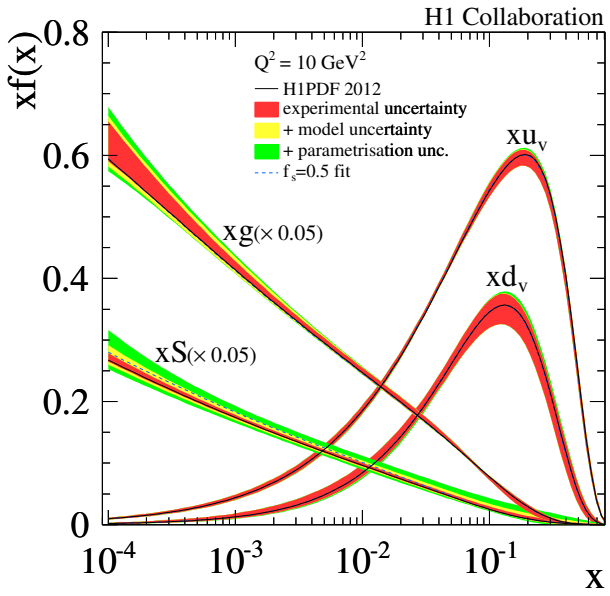

Figure 1.7: The parton distribution functions of H1PDF 2012 at the energy transfer scale of $Q^2 = 10$ GeV^2 [19].

$f_i(x, Q^2)$ is the isolated proton PDF of parton flavor i

In absence of any nuclear effects, the $R_i^A(x, Q^2)$ should be equal to 1. The schematic distribution of the nuclear modification $R_i^A(x, Q^2)$ is shown in Fig. 1.8. In this figure, three different regions can be identified corresponding to three different effects [21]:

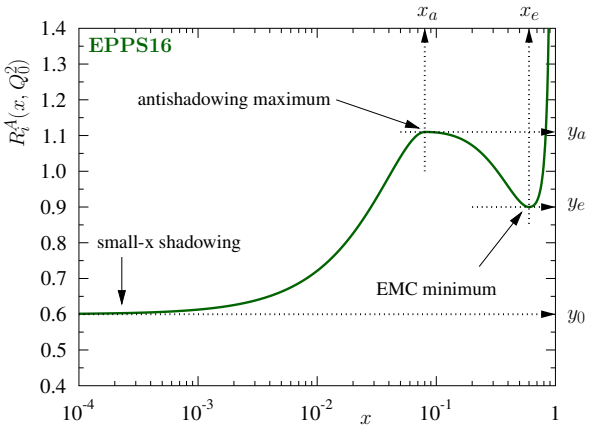

Figure 1.8: An example of nuclear modification function as a function of x in the EPPS16 parametrisation [22].

- **Shadowing** corresponds to the low-x ($x < 0.03$) where $R_i^A(x, Q^2) < 1$. In this

region the number of partons in bound state decrease compared to the number of free protons. These effect arise due to the recombination of gluons because the large phase-space density.

- **Anti-Shadowing** corresponds to the intermediate x ($0.03 < x < 0.1$) where $R_i^A(x, Q^2) > 1$. This is opposite to the shadowing effect which leads to excess in this region.

- **EMC effects** correspond to the high-x ($0.3 \leq x \geq 0.7$) where $R_i^A(x, Q^2) < 1$ and was first proposed by the European Muon Collaboration (EMC). This effect is not fully understood and may be interpreted as the modification in parton distribution in bound nucleons by the nuclear environment [23].

Apart from these three effects, the Fermi-motion region corresponds to the large value of x where $R_i^A(x, Q^2) > 1$. This effect is explained by the Fermi motion of the nucleons [21].

Different parameterization of $R_i^A(x, Q^2)$ has been performed. Fig. 1.9 shows such a parameterization (EPSO9), which is applicable for Pb nucleus at $Q^2 = 1.69$ GeV^2 and 100 GeV^2 [24].

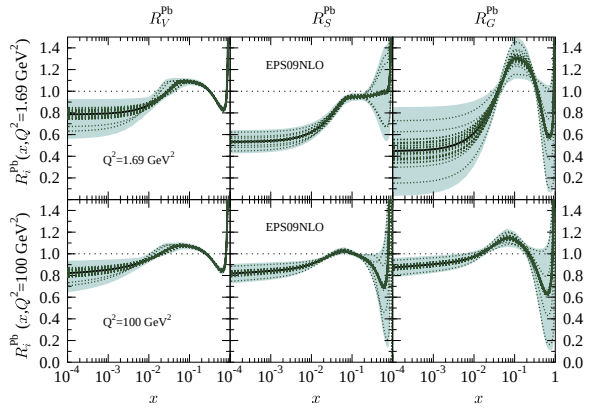

Figure 1.9: The nuclear modifications for the lead ions at energy scale $Q^2 = 1.69$ GeV^2 (top) and 100 GeV^2 (bottom). The left, middle and right column represent $R^A(x, Q^2)$ for the valence quarks, sea quarks and gluons, respectively.

At the LHC energies, the dominant source for the creation of heavy quark pairs is the gluon fusion gg$\rightarrow$ Q$\bar{\text{Q}}$. Hence the quarkonium production is sensitive to the gluon nuclear modification function. The small-x region is accessible at the LHC energies and therefore one can expect the dominance of the shadowing effects.

Gluon saturation

At low-x region the gluon PDFs indicate an increase of gluon density with the energy. As the density of gluon increases, the distance between the gluon decreases. The individual gluons begin to overlap and they can no longer be resolved. Once the maximum occupancy is achieved, no further increase of gluon density is possible. This is known as gluon saturation and it is characterized by a saturation scale Q_s. When $Q_s >> \Lambda_{\text{QCD}}$, the saturation can be studied within the framework of effective field theory known as the Color Glass Condensate (CGC) [25].

At LHC energies, the J/ψ production in mid and forward rapidity can be fairly reproduced by employing the CGC+NRQCD formalism for $p_{\text{T}} < 5$ GeV/c [26]. However, for the Υ production the gluon saturation is not relevant as $Q^2 >> Q_s^2$ [27].

Coherent Parton Energy Loss

A high energy parton traveling through the nuclear environment is expected to experience multiple scattering with the constituents of matter and lose energy by emitting the soft gluons.

The quarkonium production in a p–A collision at LHC is schematically shown in Fig. 1.10 wherein the target rest frame (nucleus), the energy available for the hard scattering is sizeably greater than the mass of the $Q\bar{Q}$ pair. The $Q\bar{Q}$ pair is produced through the splitting of a gluon from proton followed by the scattering of a gluon in the nucleus. The long-lived $Q\bar{Q}$ allows the two gluons to interfere and resulting in coherent

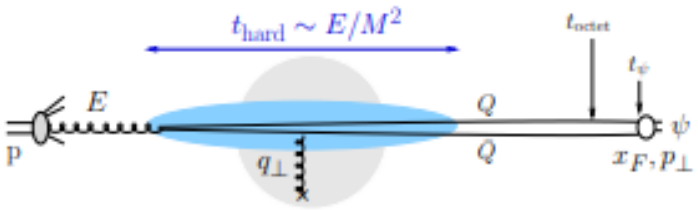

Figure 1.10: The J/ψ production in a p–A collision at different time scales [28].

energy loss of the parton [28].

Cronin effect

In high energy p–A collisions, an incoming parton can undergo multiple scattering in the nucleus before the hard process. Thus, a parton can acquire an extra transverse momentum which may be inherited by the quarkonium formed from this parton. This lead to the broadening of transverse momentum distributions of the quarkonia in p–A collision with respect to that for the pp collisions. This effect is known as the Cronin effect [29].

1.5.4 Final-state effects

The final state effects are those which affect the heavy quark pair ($Q\bar{Q}$) during the formation of the bound state or after the bound state has been formed [30] and may modify each state by a different extent. These effects are discussed in the following section.

Nuclear Absorption

While traversing through the nuclear medium, the quarkonium may be absorbed. This is called nuclear absorption. The probability of a quarkonium state to survive in the p–A collision, can be express as $P^s \sim exp(-\rho_A \sigma_{\rm abs} L)$, where ρ_A is the density of normal nuclear matter, $\sigma_{\rm abs}$ is the absorption cross section that represents for the probability of inelastic scattering with a nucleon and L is the mean path length of the $Q\bar{Q}$ in the nuclear matter. This absorption effect is expected to be negligible at LHC energies as the collision time $\tau_{\rm coll}$ is much smaller than the formation time of the quarkonium state. Fig. 1.11 shows the J/ψ absorption cross section as function of center of mass energy ($\sqrt{s_{\rm NN}}$) and it can be observed that the cross section decreases with increasing the collision energy [31].

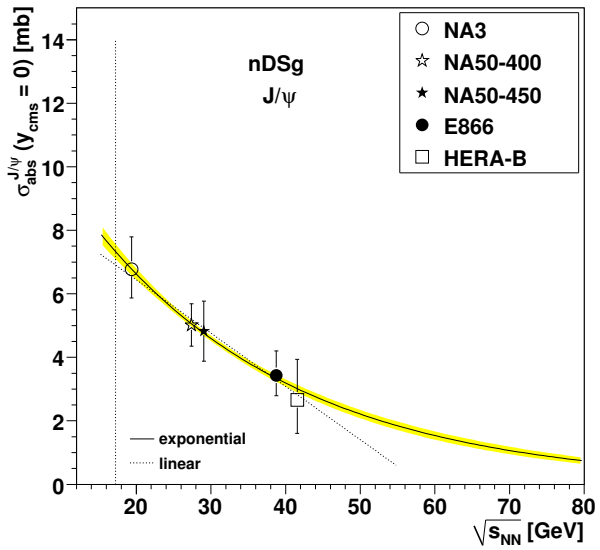

Figure 1.11: The collision energy dependence of the J/ψ absorption cross section for nDSg PDF [31].

Comover Interactions

The quarkonium states produced in p–A collisions may interact with other comoving particles available in the collision to produce the secondary particles. The decrease in the quarkonium production cross-section depends on the interaction cross section of the quarkonium state with surrounding comover particles and the density of the comover particles. The higher excited states experience stronger comover suppression due to their larger size, which increases their interaction cross section with comovers.

1.6 Quarkonium Production

We have already mentioned that the measurements of quarkonium production yields in pp collisions are used as a baseline for understanding QGP (Pb–Pb) and CNM (p–Pb) effects. Apart from this, the measurements of the production cross section are also an important tool to investigate the perturbative and non-perturbative aspects of the Quantum Chromodynamics (QCD) [7, 32] at the LHC energies. The production is treated as the result of an initial hard scattering of partons which produces the heavy-quark pair ($Q\bar{Q}$) followed by the formation of a $Q\bar{Q}$ colorless bound state. The former stage can be described by means of perturbative quantum chromodynamics (pQCD). The latter step is a non-perturbative process as it involves long distances and soft momentum scales. The steps involved in the production of a J/ψ meson in pp collisions is shown in Fig. 1.12.

There are several models available to describe quarkonium production in pp collisions, namely, the Color Evaporation Model [33, 34], the Color Singlet Model [35] and Non-Relativistic QCD [36]. The most recent theoretical development is to combine the NRQCD with the Color Glass Condensate(GCG + NRQCD) [37] which leads to a better description of the experimental results. Hence, the measurements of quarkonium in pp

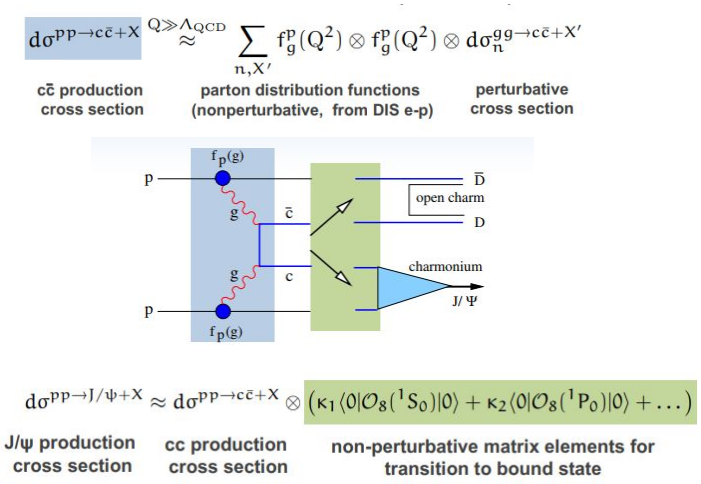

Figure 1.12: The factorization scheme for the J/ψ production in a pp collisions [12].

collisions help to constrain the various theoretical models.

1.7 Advantages of bottomonium study

We have already discussed the advantages of using the quarkonia as a tool to study the matter produced in high-energy collisions, due to their heavy mass, short formation time and long lifetime. The quarkonium state electromagnetically decay to two lepton pairs. The $Q\bar{Q}$ bound state annihilate to a massive photon that produced a leptons pair, l^+l^-. As the leptons do not interact with matter via the strong interaction, they are well-suited for studying the dense medium created in Pb–Pb collisions as well as the medium produced in p–Pb and pp collisions [38].

Apart from this, the study of bottomonium has some advantages over the charmonium in heavy ion collisions. The large difference of binding energies in the bottomonium excited states and their higher dissociation temperatures make them for better suited for an effective field theory approach. The constituent b quark is more massive, hence the

CNM effects such as shadowing effect, are expected to be small in bottomonium than for chamonium [11, 32]. At the LHC energies, the (re)generation effects are expected to be negligible as smaller number (by an order of magnitude) of b quarks are produced compared to c quarks.

The feed down is a key factor for the study of the sequential melting of quarkonia. Fig. 1.13 shows the bottomonium family and their decay patterns. The decay paths are shown with arrows. The recent theoretical developments and experimental evidence suggest that the Υ(3S) state is almost directly produced and provide a clean probe for studying the medium produced at high temperatures [7, 39].

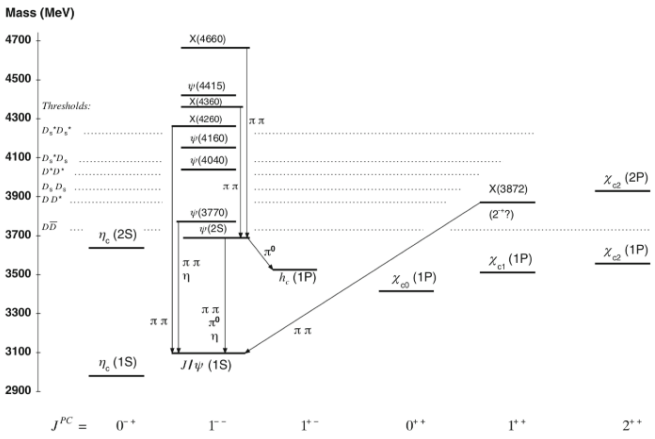

Figure 1.13: The mass order and feed-down pattern [4] of the bottomonium family.

1.8 Goal of the thesis

In this thesis, the Υ production cross section measurements in pp, p–Pb and Pb–Pb collisions in Run 2 with ALICE-MS at LHC energies will be reported. The main goal of this thesis is to explore the properties of the deconfined medium created at the LHC via measuring the modification of Upsilon yields in Pb–Pb collisions with respect to binary scaled pp collisions. In order to describe the observed yields, new phenomenological

models are being developed. The implementation of the rate equations and transport model [17, 40–43] using a wide range of approaches for the creation of a thermodynamic system and its interaction with the $b\bar{b}$ quark pair, has been undertaken. The numerical results have been compared with the experimental observation. The statistical hadronization model, commonly applied to the charm sector, has been also proposed as a scenario for the production of bottomonia [44].

The modification to the bottomonium production might also be induced by CNM mechanisms, which are not related to the formation of the deconfined matter. For a better understanding of the Υ suppression in Pb–Pb collisions, one needs to separate the CNM effects from the hot matter effects. The magnitude of the CNM effects is usually estimated from the p–Pb collision. This also allows for the investigation of any additional final state mechanisms, which may modify the production of the more loosely bound resonances [17, 18, 45].

The bottomonium production in pp collisions leads to a stringent test for models and in particular, for the investigation of the non-perturbative aspects. These measurements also provide a reference for the study of the properties of the deconfined matter produced in the Pb–Pb collisions and CNM effects in p–Pb collisions at LHC energies.

Selective previous measurements

The production of Υ states have been measured by the CMS [46, 47] and ALICE [48] experiment at the LHC in Run 1 Pb–Pb collisions at center of mass energy $\sqrt{s_{\rm NN}} = 2.76$ TeV in the mid-rapidity range $|y| < 2.4$ and forward rapidity range $2.5 < y < 4.0$, respectively. The suppression relative to the pp collisions scaled by the number of binary nucleon-nucleon (NN) collisions increase for more central collisions in both the rapid-

ity interval. A large suppression of Υ(2S) and Υ(3S) was observed by the CMS [49], hence indicating the sequential suppression of quarkonium states in the QGP. Moreover, the suppression of Υ(1S) at the forward rapidity, measured by ALICE was found to be larger than the mid-rapidity CMS measurements. This provides new constraints for theoretical calculation [40, 41, 48]. The Run 2 measurements of Υ in Pb–Pb collisions by both ALICE [50] and CMS [51] experiments confirm the results of Run 1 and provide more precision measurements. The zero elliptic flow coefficient (v_2) for Υ(1S), recently measured by both ALICE [52] and CMS [53] experiments, clearly indicates different in-medium effects for the charmonia and the bottomonia in the heavy-ions collisions.

At Relativistic Heavy Ion Collider (RHIC) the inclusive Υ(1S+2S+3S) production has been also measured at central rapidity by the STAR [54] and PHENIX [55] Collaborations in Au–Au collisions at $\sqrt{s_{\rm NN}}$ 200 GeV. The extent of suppression was found to be consistent with the melting of the Υ(2S) and Υ(3S) states.

To study the CNM effects, Υ production were measured in p–Pb at the LHC. The measurements by ALICE [56], ATLAS [57], CMS [58], LHCb [59] suggest a suppression of Υ(nS) production in p–Pb relative to scaled pp collisions, which seems to be more pronounced for the higher Υ states. These effects have been explored with higher precision measurements using Run 2 data sample during the course of this thesis work.

In Fig. 1.14, the differential cross section times branching ratio for Υ(nS) states together with the theoretical model predictions based on [60, 61] are shown. The measurements from CMS [62] and LHCb [63] are in fair agreement with the NRQCD predictions. The new results on Υ(nS) cross-section in the pp collisions during Run 2 will be presented in this thesis.

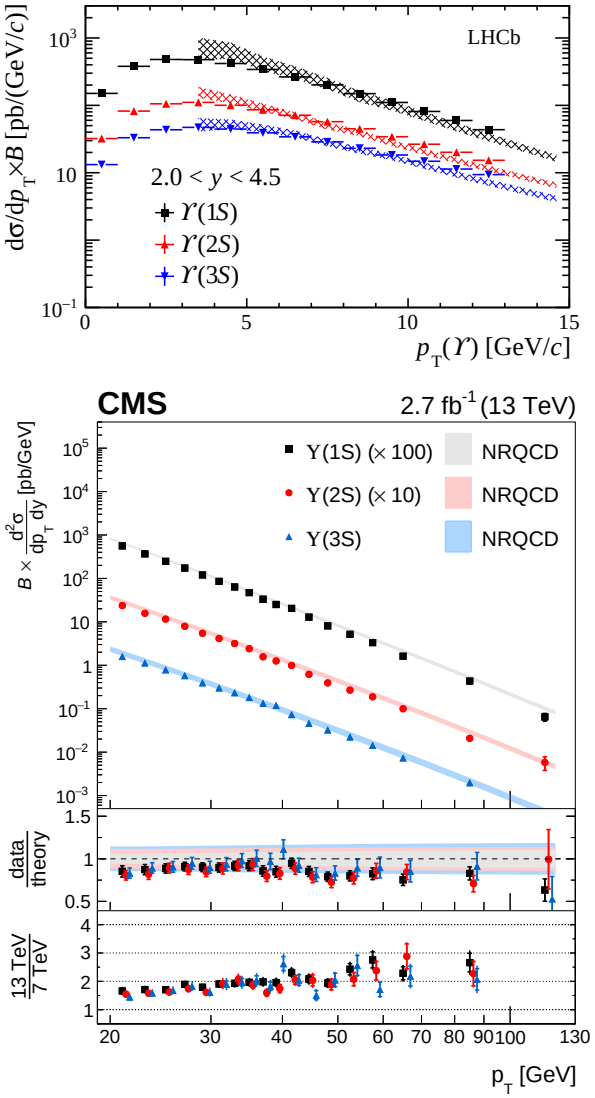

Figure 1.14: The differential cross section times branching ratio for the Υ(nS) states measured by the LHCb [63] (top) and CMS [62] (bottom). The experimental results have been compared with NRQCD predictions [60, 61].

Bibliography

[1] D. Griffiths, *Introduction to Elementary Particles*. 2008.

[2] ATLAS collaboration, G. Aad et al., *Observation of a new particle in the search for the Standard Model Higgs boson with the ATLAS detector at the LHC*, *Phys. Lett. B* **716** (2012) 1–29, [1207.7214].

[3] CMS collaboration, S. Chatrchyan et al., *Observation of a New Boson at a Mass of 125 GeV with the CMS Experiment at the LHC*, *Phys. Lett. B* **716** (2012) 30–61, [1207.7235].

[4] Particle Data Group collaboration, J. Beringer, J. F. Arguin, R. M. Barnett, K. Copic, O. Dahl, D. E. Groom et al., *Review of particle physics*, *Phys. Rev. D* **86** (Jul, 2012) 010001.

[5] T. Hatsuda and T. Kunihiro, *QCD phenomenology based on a chiral effective Lagrangian*, *Phys. Rept.* **247** (1994) 221–367, [hep-ph/9401310].

[6] S. Bethke, *World Summary of α_s (2012)*, *Nucl. Phys. B Proc. Suppl.* **234** (2013) 229–234, [1210.0325].

[7] N. Brambilla et al., *Heavy Quarkonium: Progress, Puzzles, and Opportunities*, *Eur. Phys. J. C* **71** (2011) 1534, [1010.5827].

[8] HotQCD collaboration, A. Bazavov et al., *Chiral crossover in QCD at zero and non-zero chemical potentials*, *Phys. Lett. B* **795** (2019) 15–21, [1812.08235].

[9] B. Muller, *Physics and signatures of the quark-gluon plasma*, *Reports on Progress in Physics* **58** (jun, 1995) 611–636.

[10] M. L. Mangano, *Two lectures on heavy quark production in hadronic collisions*, *Proc. Int. Sch. Phys. Fermi* **137** (1998) 95–137, [hep-ph/9711337].

[11] M. Strickland, *Thermal Bottomonium Suppression*, *AIP Conf. Proc.* **1520** (2013) 179–184, [1207.5327].

[12] Alexander Rothkopf, "Quarkonium."
URL: https://indico.cern.ch/event/656452/contributions/2953749/attachments/1648288/2635177/QM2018_QUARKONIUM_FINAL.pdf, 05, 2018.

[13] T. Matsui and H. Satz, *J/ψ Suppression by Quark-Gluon Plasma Formation*, *Phys. Lett. B* **178** (1986) 416–422.

[14] K. Yagi, T. Hatsuda and Y. Miake, *Quark-gluon plasma: From big bang to little bang*, vol. 23. 2005.

[15] R. L. Thews, M. Schroedter and J. Rafelski, *Enhanced J/ψ production in deconfined quark matter*, *Phys. Rev. C* **63** (2001) 054905, [hep-ph/0007323].

[16] A. Andronic, P. Braun-Munzinger, K. Redlich and J. Stachel, *Statistical hadronization of heavy quarks in ultra-relativistic nucleus-nucleus collisions*, *Nucl. Phys. A* **789** (2007) 334–356, [nucl-th/0611023].

[17] E. G. Ferreiro and J.-P. Lansberg, *Is bottomonium suppression in proton-nucleus and nucleus-nucleus collisions at LHC energies due to the same effects?*, *JHEP* **10** (2018) 094, [1804.04474].

[18] E. Ferreiro, *Charmonium dissociation and recombination at LHC: Revisiting comovers*, *Phys. Lett. B* **731** (2014) 57–63, [1210.3209].

[19] H1 collaboration, F. Aaron et al., *Inclusive Deep Inelastic Scattering at High Q^2 with Longitudinally Polarised Lepton Beams at HERA*, *JHEP* **09** (2012) 061, [1206.7007].

[20] K. Eskola, H. Paukkunen and C. Salgado, *EPS09: A New Generation of NLO and LO Nuclear Parton Distribution Functions*, *JHEP* **04** (2009) 065, [0902.4154].

[21] N. Armesto, *Nuclear shadowing*, *J. Phys. G* **32** (2006) R367–R394, [hep-ph/0604108].

[22] K. J. Eskola, P. Paakkinen, H. Paukkunen and C. A. Salgado, *EPPS16: Nuclear parton distributions with LHC data*, *Eur. Phys. J. C* **77** (2017) 163, [1612.05741].

[23] K. Rith, *Present Status of the EMC effect*, *Subnucl. Ser.* **51** (2015) 431–449, [1402.5000].

[24] K. Eskola, H. Paukkunen and C. Salgado, *Nuclear PDFs at NLO - status report and review of the EPS09 results*, *Nucl. Phys. A* **855** (2011) 150–157, [1011.6534].

[25] E. Iancu and R. Venugopalan, *The Color glass condensate and high-energy scattering in QCD*, pp. 249–3363. 3, 2003. hep-ph/0303204. 10.1142/9789812795533_0005.

[26] Y.-Q. Ma and R. Venugopalan, *Comprehensive Description of J/ψ Production in Proton-Proton Collisions at Collider Energies*, *Phys. Rev. Lett.* **113** (2014) 192301, [1408.4075].

[27] E. Ferreiro, F. Fleuret, J. Lansberg, N. Matagne and A. Rakotozafindrabe, *Upsilon production in p(d)A collisions at RHIC and the LHC*, *Eur. Phys. J. C* **73** (2013) 2427, [1110.5047].

[28] F. Arleo and S. Peigne, *Heavy-quarkonium suppression in p-A collisions from parton energy loss in cold QCD matter*, *JHEP* **03** (2013) 122, [1212.0434].

[29] B. Kopeliovich, I. Potashnikova and I. Schmidt, *Nuclear suppression of J/Psi: from RHIC to the LHC*, *Nucl. Phys. A* **864** (2011) 203–212, [1012.5648].

[30] R. Vogt, *Cold Nuclear Matter Effects on J/ψ and Υ Production at the LHC*, *Phys. Rev. C* **81** (2010) 044903, [1003.3497].

[31] C. Lourenco, R. Vogt and H. K. Woehri, *Energy dependence of J/psi absorption in proton-nucleus collisions*, *JHEP* **02** (2009) 014, [0901.3054].

[32] A. Andronic et al., *Heavy-flavour and quarkonium production in the LHC era: from proton–proton to heavy-ion collisions*, *Eur. Phys. J. C* **76** (2016) 107, [1506.03981].

[33] H. Fritzsch, *Producing heavy quark flavors in hadronic collisions—' a test of quantum chromodynamics*, *Physics Letters B* **67** (1977) 217 – 221.

[34] J. Amundson, O. J. Eboli, E. Gregores and F. Halzen, *Quantitative tests of color evaporation: Charmonium production*, *Phys. Lett. B* **390** (1997) 323–328, [hep-ph/9605295].

[35] R. Baier and R. Ruckl, *Hadronic Production of J/psi and Upsilon: Transverse Momentum Distributions*, *Phys. Lett. B* **102** (1981) 364–370.

[36] G. T. Bodwin, E. Braaten and G. Lepage, *Rigorous QCD analysis of inclusive annihilation and production of heavy quarkonium*, *Phys. Rev. D* **51** (1995) 1125–1171, [hep-ph/9407339].

[37] Y.-Q. Ma and R. Venugopalan, *Comprehensive description of j/ψ production in proton-proton collisions at collider energies*, *Phys. Rev. Lett.* **113** (Nov, 2014) 192301.

[38] J. W. Harris and B. Muller, *The Search for the quark - gluon plasma*, *Ann. Rev. Nucl. Part. Sci.* **46** (1996) 71–107, [hep-ph/9602235].

[39] CMS Collaboration collaboration, *Suppression of excited* Υ *states relative to the ground state in pb-pb collisions at* $\sqrt{s_{\rm nn}} = 5.02$ TeV, *Phys. Rev. Lett.* **120** (Apr, 2018) 142301.

[40] B. Krouppa and M. Strickland, *Predictions for bottomonia suppression in 5.023 TeV Pb-Pb collisions*, *Universe* **2** (2016) 16, [1605.03561].

[41] X. Du, R. Rapp and M. He, *Color Screening and Regeneration of Bottomonia in High-Energy Heavy-Ion Collisions*, *Phys. Rev. C* **96** (2017) 054901, [1706.08670].

[42] X. Yao, W. Ke, Y. Xu, S. A. Bass and B. Müller, *Coupled Boltzmann Transport Equations of Heavy Quarks and Quarkonia in Quark-Gluon Plasma*, *JHEP* **01** (2021) 046, [2004.06746].

[43] A. Islam and M. Strickland, *Bottomonium suppression and elliptic flow from real-time quantum evolution*, *Phys. Lett. B* **811** (2020) 135949, [2007.10211].

[44] A. Andronic, P. Braun-Munzinger, K. Redlich and J. Stachel, *Decoding the phase structure of QCD via particle production at high energy*, *Nature* **561** (2018) 321–330, [1710.09425].

[45] X. Du and R. Rapp, *In-Medium Charmonium Production in Proton-Nucleus Collisions*, *JHEP* **03** (2019) 015, [1808.10014].

[46] CMS collaboration, S. Chatrchyan et al., *Indications of suppression of excited* Υ *states in PbPb collisions at* $\sqrt{S_{NN}} = 2.76$ *TeV*, *Phys. Rev. Lett.* **107** (2011) 052302, [1105.4894].

[47] CMS collaboration, S. Chatrchyan et al., *Observation of Sequential Upsilon Suppression in PbPb Collisions*, *Phys. Rev. Lett.* **109** (2012) 222301, [1208.2826].

[48] ALICE collaboration, B. B. Abelev et al., *Suppression of* $\Upsilon(1S)$ *at forward rapidity in Pb-Pb collisions at* $\sqrt{s_{\rm NN}} = 2.76$ *TeV*, *Phys. Lett. B* **738** (2014) 361–372, [1405.4493].

[49] CMS collaboration, V. Khachatryan et al., *Suppression of* $\Upsilon(1S), \Upsilon(2S)$ *and* $\Upsilon(3S)$ *production in PbPb collisions at* $\sqrt{s_{\mathrm{NN}}} = 2.76$ *TeV*, Phys. Lett. B **770** (2017) 357–379, [1611.01510].

[50] ALICE collaboration, S. Acharya et al., Υ *suppression at forward rapidity in Pb-Pb collisions at* $\sqrt{s_{\mathrm{NN}}} = 5.02$ *TeV*, Phys. Lett. B **790** (2019) 89–101, [1805.04387].

[51] CMS collaboration, A. M. Sirunyan et al., *Measurement of nuclear modification factors of* Υ*(1S),* Υ*(2S), and* Υ*(3S) mesons in PbPb collisions at* $\sqrt{s_{\mathrm{NN}}} = 5.02$ *TeV*, Phys. Lett. B **790** (2019) 270–293, [1805.09215].

[52] ALICE collaboration, S. Acharya et al., *Measurement of* Υ(1S) *elliptic flow at forward rapidity in Pb-Pb collisions at* $\sqrt{s_{\mathrm{NN}}} = 5.02$ *TeV*, Phys. Rev. Lett. **123** (2019) 192301, [1907.03169].

[53] CMS collaboration, *Measurement of the elliptic flow of* Υ*(1S) and* Υ*(2S) mesons in PbPb collisions at* $\sqrt{s_{\mathrm{NN}}} = 5.02$, .

[54] STAR collaboration, L. Adamczyk et al., *Suppression of* Υ *production in d+Au and Au+Au collisions at* $\sqrt{s_{NN}}$*=200 GeV*, Phys. Lett. B **735** (2014) 127–137, [1312.3675].

[55] PHENIX collaboration, A. Adare et al., *Measurement of* $\Upsilon(1S + 2S + 3S)$ *production in* $p + p$ *and Au+Au collisions at* $\sqrt{s_{_{NN}}} = 200$ *GeV*, Phys. Rev. C **91** (2015) 024913, [1404.2246].

[56] ALICE collaboration, B. B. Abelev et al., *Production of inclusive* Υ*(1S) and* Υ*(2S) in p-Pb collisions at* $\sqrt{\mathbf{s}_{\mathrm{NN}}} = \mathbf{5.02}$ *TeV*, Phys. Lett. B **740** (2015) 105–117, [1410.2234].

[57] ATLAS collaboration, M. Aaboud et al., *Measurement of quarkonium production*

in proton–lead and proton–proton collisions at 5.02 TeV *with the ATLAS detector*, *Eur. Phys. J. C* **78** (2018) 171, [1709.03089].

[58] CMS collaboration, S. Chatrchyan et al., *Event Activity Dependence of Y(nS) Production in* $\sqrt{s_{NN}}$*=5.02 TeV pPb and* $\sqrt{s}$*=2.76 TeV pp Collisions*, *JHEP* **04** (2014) 103, [1312.6300].

[59] LHCb collaboration, R. Aaij et al., *Study of* Υ *production in pPb collisions at* $\sqrt{s_{NN}} = 8.16$ *TeV*, *JHEP* **11** (2018) 194, [1810.07655].

[60] H. Han, Y.-Q. Ma, C. Meng, H.-S. Shao, Y.-J. Zhang and K.-T. Chao, $\Upsilon(nS)$ *and* $\chi_b(nP)$ *production at hadron colliders in nonrelativistic QCD*, *Phys. Rev. D* **94** (2016) 014028, [1410.8537].

[61] Y. Feng, B. Gong, L.-P. Wan and J.-X. Wang, *An updated study of* Υ *production and polarization at the Tevatron and LHC*, *Chin. Phys. C* **39** (2015) 123102, [1503.08439].

[62] CMS collaboration, A. Sirunyan et al., *Measurement of quarkonium production cross sections in pp collisions at* $\sqrt{s} = 13$ *TeV*, *Phys. Lett. B* **780** (2018) 251–272, [1710.11002].

[63] LHCb collaboration, R. Aaij et al., *Measurement of* Υ *production in pp collisions at* $\sqrt{s}$*= 13 TeV*, *JHEP* **07** (2018) 134, [1804.09214].

CHAPTER 2

The LHC and the ALICE detector

The experimental results reported in this thesis have been obtained from the data taken by 'A Large Ion Collider Experiment' (ALICE) detector at the Large Hadron Collider (LHC) in ultra-relativistic collisions. In this chapter, the LHC and ALICE detector will be discussed in brief. The sub-detectors of ALICE related to the analysis will be discussed in more detail. A short discussion on the particle trajectory and the reconstruction of the track will also be presented.

2.1 CERN and the Large Hadron Collider

The European Organization for Nuclear Research also known as CERN [1], is an international research laboratory for particle and nuclear physics. It was established in 1954 at the Franco–Swiss border. Currently, it is supported by 23 member states and over 600 institutes and universities around the globe use, CERN's experimental facilitates.

The Large Hadron Collider (LHC) is the world's largest and most powerful particle accelerator build by the CERN. It is a two-ring superconducting hadron collider placed in the pre-existing 27 km tunnel of the Large Electron Positron (LEP) collider. The superconducting magnets with several accelerating structures boost the energy of the

beam of particles. The beams coming from two opposite directions are allowed to collide at four interaction points. The four main experiments located at each interaction point are A Large Ion Collider Experiment (ALICE) [2], A Toroidal LHC Apparatus (ATLAS)) [3], Compact Muon Solenoid (CMS) [4] and Large Hadron Collider beauty (LHCb) [5]. The LHC collides the proton as well as the heavy-ion (Pb, Xe) beams. The maximum possible energy to which a proton beam may be accelerated is $E_{\mathrm{p}} = 7$ TeV. In case of Pb, the maximum possible energy per nucleon is E_{A} =(Z/A).E_{p}=2.75 TeV.

The CERN accelerator complex is schematically shown in Fig. 2.1. The proton beam is produced by knocking off the electrons from the hydrogen atoms. The beam is then injected into the PS Booster (PSB) from LINAC2 at an energy of 50 MeV. The PSB accelerates the protons up to 1.4 GeV and injects them into the Proton Synchrotron (PS) where they are accelerated to 25 GeV. After that, the protons are injected to Super Proton Synchrotron (SPS) and accelerated to 450 GeV. Finally, at LHC the protons have been accelerated to 6.5 TeV. In addition of the proton beam, the LHC also collides the heavy-ions. In Pb–Pb collisions, the Pb ions are produced by ionizing the highly purified vaporized lead. The lead beam is injected to the Low Energy Ion Ring (LEIR) through the LINAC3 and accelerated to 72 MeV/u (per nucleon). The beam then follows the successive acceleration chain as for protons. Finally, in the LHC, the Pb beam has been accelerated up to 2.56 TeV/u.

The LHC has delivered pp, p–Pb, Pb–Pb and Xe–Xe collisions at various center of mass energies during Run 1 (2009-2013) and Run 2 (2015-2018) operations. The different collision systems with approximate luminosity recorded in ALICE are reported in Table 2.1. The next proton beams will be injected in the summer of 2022 after the rigorous upgrade activities during the Long Shutdown 2. The Covid-19 pandemic has induced an one year delay in the schedule.

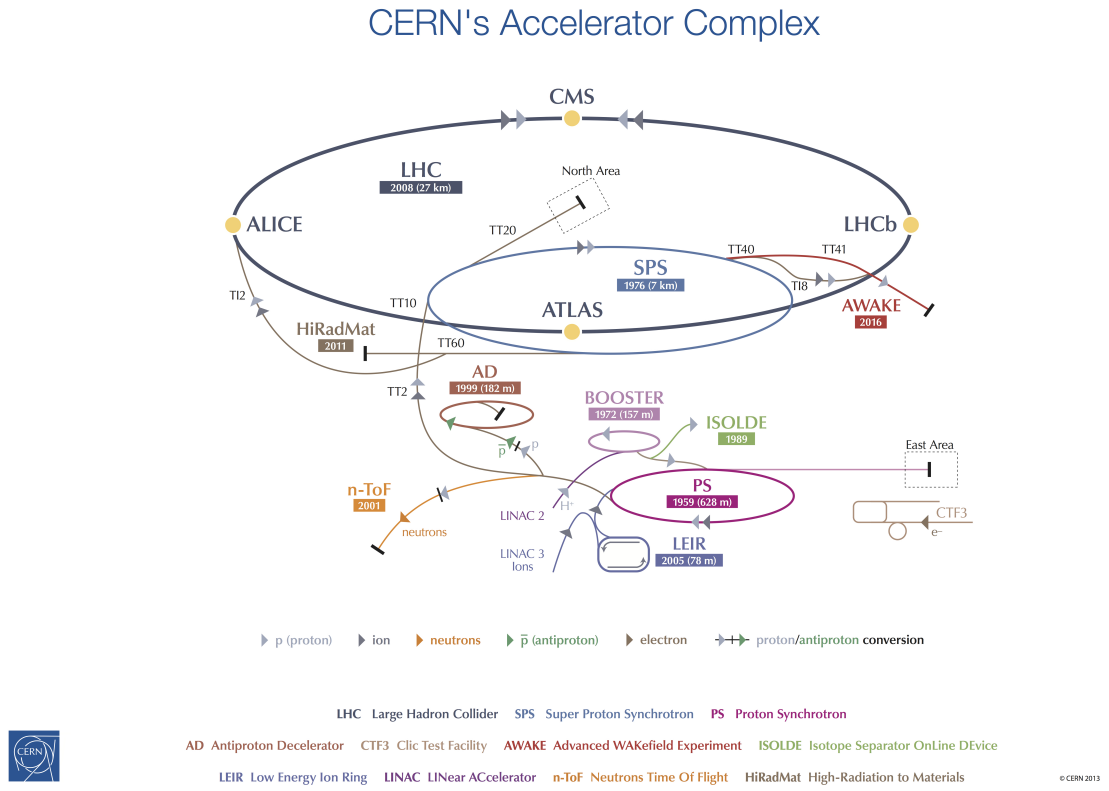

Figure 2.1: The schematic view of the CERN accelerator complex system.

2.2 A Large Ion Collider Experiment (ALICE)

ALICE [2], one of the major experiment at LHC, aims to study the properties of QCD matter at the high temperature and energy densities. ALICE has the capability to measure the particle tracks in a wide range of momentum and charge particle multiplicity up to $dN/d\eta \sim 8000$. The schematic view of the ALICE experiment is shown Fig. 2.2. ALICE is made of 18 subsystems which can be classified into two broad groups: (a) the **Central detectors** which include Inner Tracking System (ITS) [6], the Time Projection Chamber (TPC) [7], the Time Of Flight (TOF) [8], the Transition Radiation Detector (TRD) [9], the High Momentum Particle Identification detector (HMPID) [10], the Electromagnetic Calorimeter (EMCal) [11], the Di-jet Calorimeter (DCal), the Photon Spectrometer (PHOS) [12] and the Photon Multiplicity Detector (PMD) [13] and (b)

Table 2.1: ALICE data taking in Run 1 nd Run 2 (2009-2018).

System	Year	Energy (TeV)	≈ Recorded Luminosity
pp	2009-13	0.9, 2.76, 7, 8	200 μb^{-1}, 100 nb^{-1}, 1.5 pb^{-1}, 2.5 pb^{-1}
	2015,17	5.02	1.3 pb^{-1}
	2015,18	13	35 pb^{-1}
p–Pb	2013	5.02	15 pb^{-1}
	2016	5.02, 8.16	3 pb^{-1}, 25 pb^{-1}
Xe–Xe	2017	5.44	0.3 $^{-}b^{-1}$
Pb–Pb	2010,11	2.76	75 $^{-}b^{-1}$
	2015	5.02	250 $^{-}b^{-1}$
	2018	5.02	536 $^{-}b^{-1}$

the **Forward detectors** which consists of T0 [14], V0 [14], the Zero Degree Calorimeters (ZDC) [15], the ALICE Diffractive (AD) and the Muon Spectrometer [16].

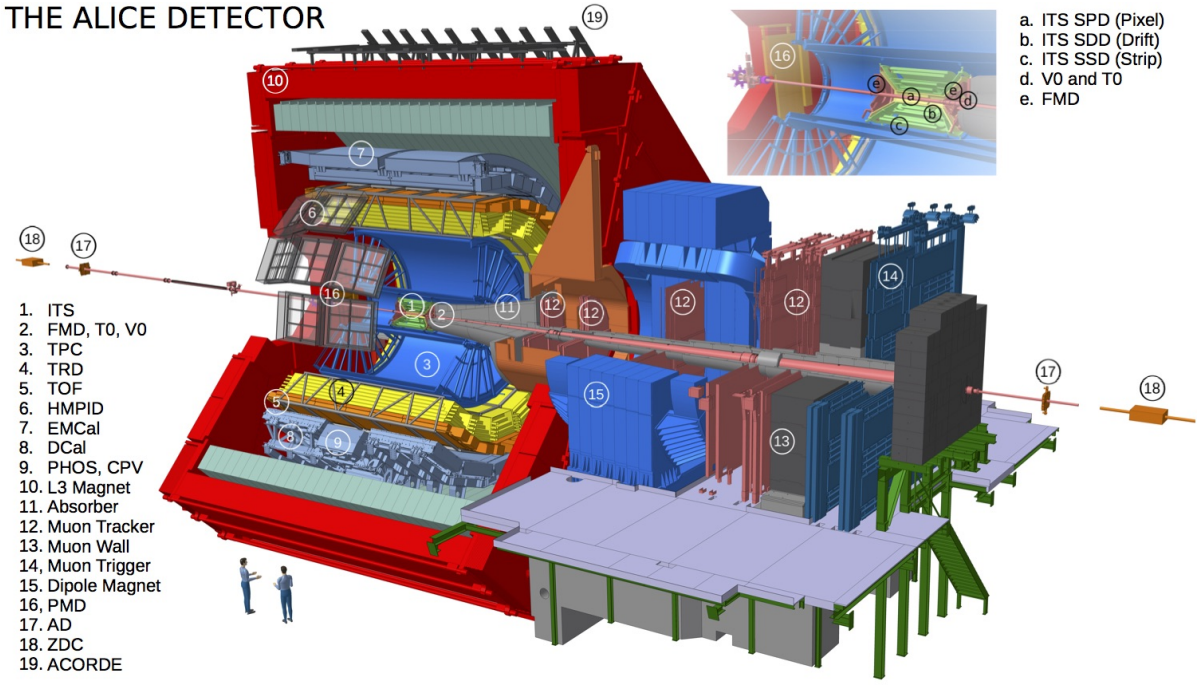

Figure 2.2: The layout of the ALICE detector.

The analysis results reported in this thesis have been carried using the data collected by the Muon Spectrometer. The other detectors used in the analysis are Silicon Pixel Detector (SPD) of ITS, T0, VO, ZDC. In the following section, these detectors will be discussed in more detail.

The ALICE coordinate system [17] is a right-handed orthogonal Cartesian system with the origin at the interaction point (IP). The x axis is perpendicular to the beam direction and pointing from the IP to the accelerator center as the positive direction. The y axis is perpendicular to the x axis and the beam direction. Positive y point upwards from the IP. The z axis is parallel to the beam direction with a negative value of z towards the muon spectrometer.

2.3 Central Barrel Detectors

The ALICE central barrel part measures hadrons, electrons, and photons. It covers polar angle from 45° to 135° (rapidity, $-0.9 \leq \eta \leq 0.9$) and placed inside the L3 magnet of ALICE. The detector arrangement in central barrel is shown in Fig. 2.3.

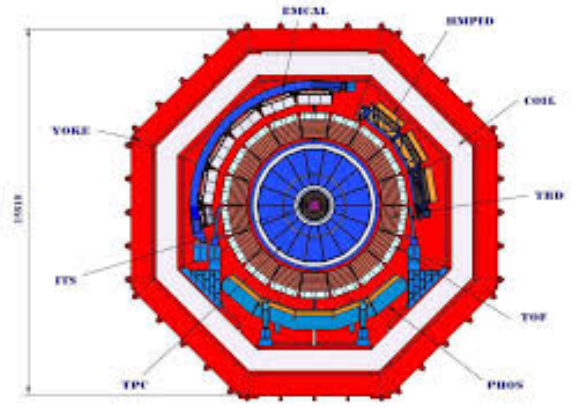

Figure 2.3: The layout of different central barrel detectors inside the L3 magnet of ALICE

The acceptance, distance from the interaction point and the main purpose of different central barrel detectors are reported in Table 2.2.

Table 2.2: ALICE central barrel detectors and its features [18].

Detector	Acceptance		Position (cm)	main purpose
	Polar	Azimuthal		
ITS layer 1,2 (SPD)	$\|\eta\|< 2.0$	full	r = 3.9	tracking, vertex
	$\|\eta\|< 1.4$	full	r = 7.6	tracking, vertex
ITS layer 3,4 (SDD)	$\|\eta\|< 0.9$	full	r = 15.0	tracking,PID
	$\|\eta\|< 0.9$	full	r = 23.9	tracking,PID
ITS layer 5,6 (SSD)	$\|\eta\|< 1.0$	full	r = 38.0	tracking,PID
	$\|\eta\|< 1.0$	full	r = 43.0	tracking,PID
TPC	$\|\eta\|< 0.9$	full	$85 < r < 247$	tracking,PID
TRD	$\|\eta\|< 0.8$	full	$290 < r < 386$	tracking,$e^{\pm}$
TOF	$\|\eta\|< 0.9$	full	$370 < r < 399$	PID
PHOS	$\|\eta\|< 0.12$	$220^{\circ} < \phi < 320^{\circ}$	$460 < r < 478$	photons
EMCal	$\|\eta\|< 0.7$	$80^{\circ} < \phi < 187^{\circ}$	$430 < r < 455$	photons and jets
HMPID	$\|\eta\|< 0.6$	$1^{\circ} < \phi < 59^{\circ}$	r = 490	PID
ACORDE	$\|\eta\|< 1.3$	$30^{\circ} < \phi < 150^{\circ}$	r = 850	cosmic

2.3.1 Silicon Pixel Detector (SPD) of ITS

The ITS is the innermost detector surrounding the beam-pipe and provides the primary vertex resolution, and reconstructs the secondary vertex for hyperons, D, and B meson decays. It consists of six layers of silicon detector grouped in three subsystems: the Silicon Pixel Detector (SPD), the Silicon Drift Detector (SDD), and the Silicon Strip Detector (SSD). A schema of ITS is shown in Fig. 2.4.

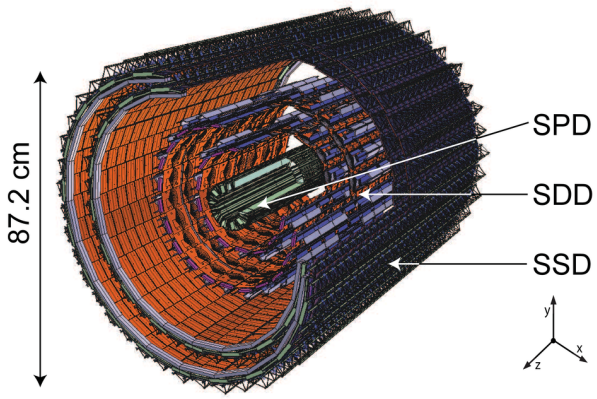

Figure 2.4: The layout of ALICE ITS detector.

The SPD is made of two layers of pixel detectors closest to the interaction point. Each module consists of a 2D-sensor matrix of silicon detector, which are in reverse biased. It can sustain up to 80 particle/cm^2 and provide the vertex information at about 1MHz rate for the events trigger by Forward Muon Spectrometer.

2.4 ALICE forward detectors

The ALICE forward detectors are essentially used for centrality determination in A–A and p–A collisions. These detectors are also used for particle multiplicity evaluation in pp, p–A and A–A collisions. A brief description of V0, ZDC together with a detail description of the Muon spectrometer are given below:

2.4.1 V0

The V0 detector [14, 19] consists of two arrays of scintillator counters called V0A and V0C placed asymmetrically on either side from IP. The V0A is located at z = +330 cm and covers the pseudorapidity range $2.8 < \eta < 5.1$ while VOC is placed at z = -90 cm and cover $-3.7 < \eta < -1.7$. The position of V0 detector in ALICE layout is shown in Fig. 2.5

The V0 provides the lowest level triggers (L0) for the ALICE experiment and rejects beam-induced backgrounds. It is also used as a luminosity estimator. Furthermore, the V0 detector is used to measure the multiplicity, centrality and event plane direction.

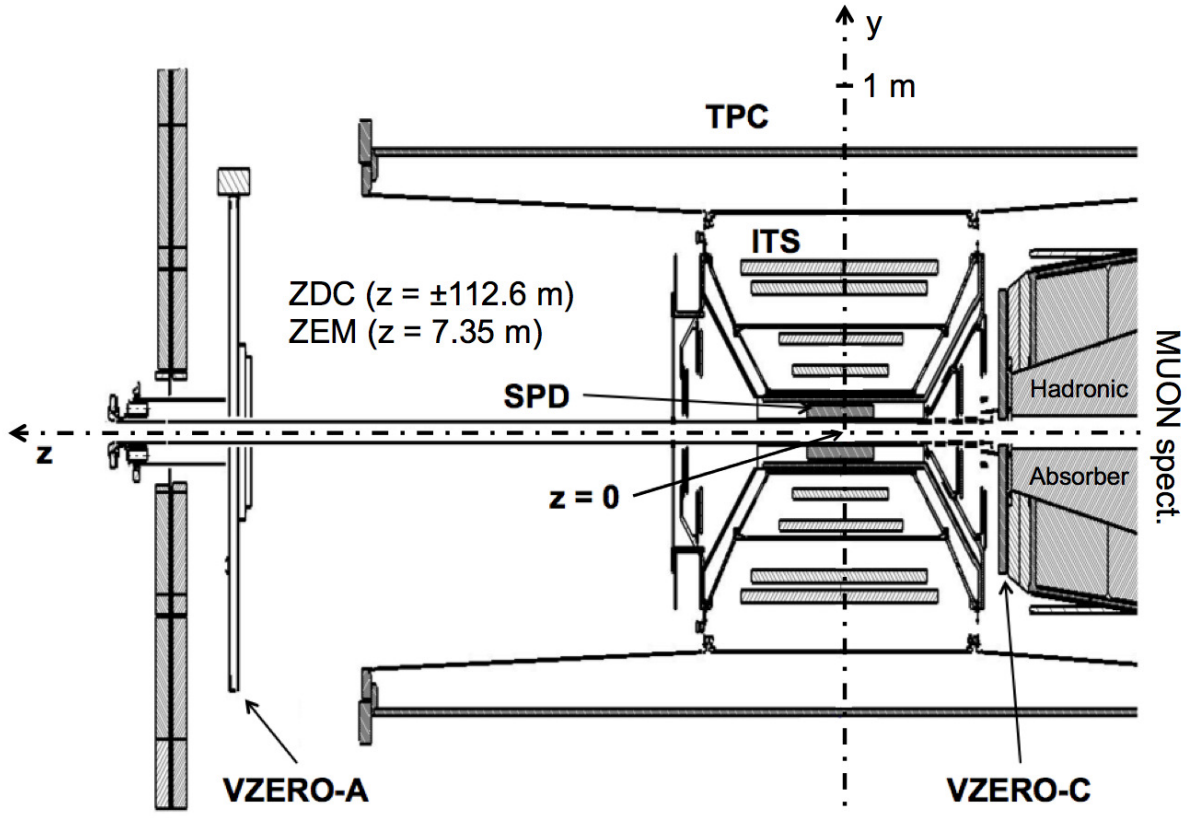

Figure 2.5: The schematic layout of the V0 detector [19] of ALICE.

2.4.2 Zero Degree Calorimeter (ZDC)

The Zero Degree Calorimeter [15] made up of two pairs of hadronic calorimeters to detect spectator protons (ZP) and spectator neutrons (ZN). They are placed at z = ±112.5 on both sides of IP [18] and are readout by quartz fibers. The ZDC system also includes a set of electromagnetic calorimeters (ZEM) on the opposite side of the Muon Spectrometer located at z = 7.35 m from IP. It detects the emitting particle energy in the pseudo-rapidity range $4.8 < \eta < 5.7$. The placement of different components of ZDC is depicted in Fig. 2.6.

The ZDC measures the energy of the spectator nucleons to evaluate the number of participants and thus help to estimate the collision centrality. It also provides Level-1 trigger in Pb–Pb collisions.

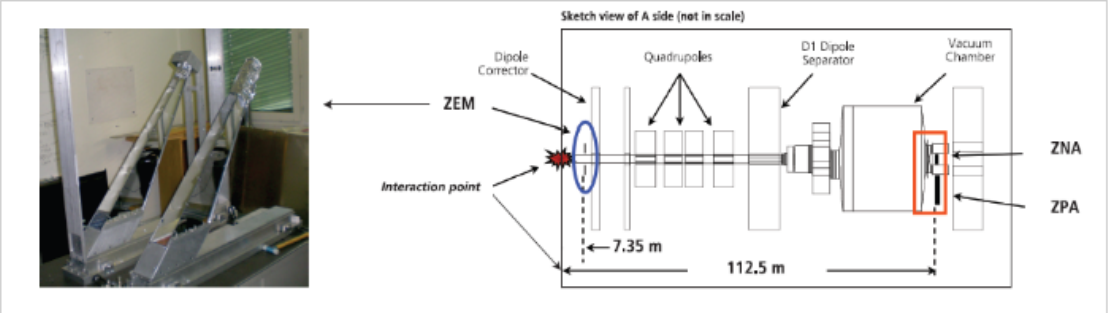

Figure 2.6: The components of ZDC [20] of ALICE.

2.4.3 Muon Spectrometer

The Muon Spectrometer (MS) [16] of ALICE was built to measure the muon decays from the heavy quarkonia (J/ψ, ψ(2S), Υ(1S), Υ(2S), Υ(3S)), low mass vector bosons (ϕ, ω, ρ), weak bosons ($W^{\pm}$, Z^{0}) and open heavy-flavors (B and D mesons families) in pp, p–A and A–A collisions at LHC energies. The MS is located at the backward region and covers the pseudorapidity range $-4.0 < y < -2.5$. It can measure muons with a wide range of transverse momentum down to $p_{\mathrm{T}} = 0$.

The muon spectrometer consists of a front absorber, five tracking stations together with a warm dipole magnet, two stations of trigger chambers shielded by a thick iron wall. The layout of the spectrometer is shown in Fig.2.7. Detail description of each component will be given below.

Front Absorber

The front absorber of muon spectrometer has a conical structure of length 4 m located inside the L3 magnet at a distance 90 cm from the IP. The layout is shown in Fig. 2.8.

The absorber is made up of light materials (i.e carbon, concrete) in order to reduce

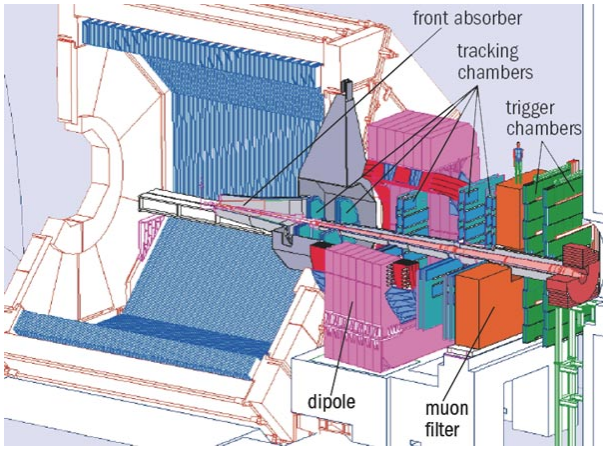

Figure 2.7: The layout of the ALICE Muon Spectrometer [21].

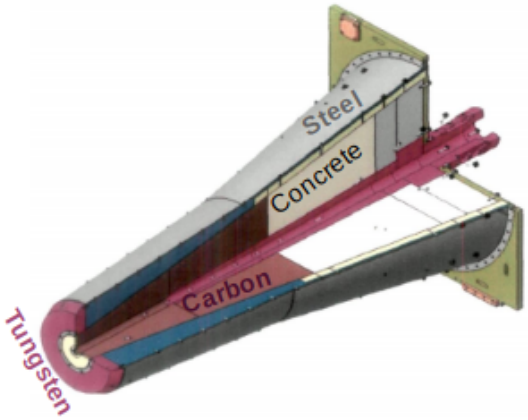

Figure 2.8: The composition of the Front absorber of the Muon Spectrometer.

multiple small angle scattering and energy loss by traversing muons. But the back end of the absorber is made up of dense materials (Steel, Pb) to filter the secondary particles produced within the absorber [22]. It reduces the forward flux of primary hadrons from A–A collisions and decreases the background of secondary muons from π, K meson decay. The front end cone close to ITS is covered with 10 mm layer of tungsten in the sector between 10.5° and 12.5° where it faces the TPC. At the end of the absorber, a 100 mm thick tungsten absorbs most of the low energy electrons produced in absorbers. An additional 100 mm ring of tungsten is added to the 2° cone to improve the shielding against particles produced from the beam pipe due to the beam hallow. In order to

stop the slow neutrons, three layers of polyethylene have been added at the end of the absorber.

Dipole Magnet

The Dipole magnet is located about 7 m away from the IP next to the L3 magnet as shown in Fig 2.9. It provides the bending power to measure the momenta of the muons. The basic concept of the dipole magnet is based on a window-frame return yoke, constructed from low carbon steel sheets. The dimension of this largest warm dipole magnet in the world is 5 m in length, 6.6 m wide, and 8.6 m high and it weighs 850 tons [23].

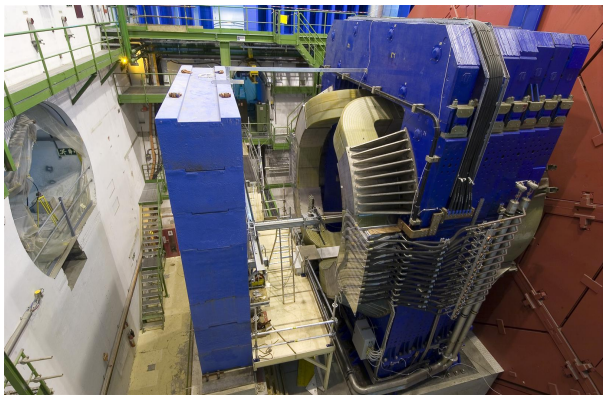

Figure 2.9: A photograph of the Dipole Magnet of the Muon Spectrometer, which is world's largest warm dipole magnet.

The magnet is also used as a support for the absorbers and beam the shielding. An additional radial space (10 cm to 15 cm) is provided to hold the support frames of the tracking chambers inside the magnet. The central field strength is about 0.7 T and the field integral is 3.0 Tm along the beam axis.

Tracking Chambers

The Muon Spectrometer tracking system is located at 5 m from the IP and it is nearly 10 m long. The tracking system is equipped with five stations and each station is composed

of two tracking chambers. The first two stations are placed downstream from the IP and the absorber. The third station is located inside the dipole magnet. The fourth and fifth stations are placed in between the dipole magnet and the muon filter. The first two stations have quadrant structures and the rest of them are in the shape of slats. The positions of tracking stations in the spectrometer layout are shown in Fig. 2.10.

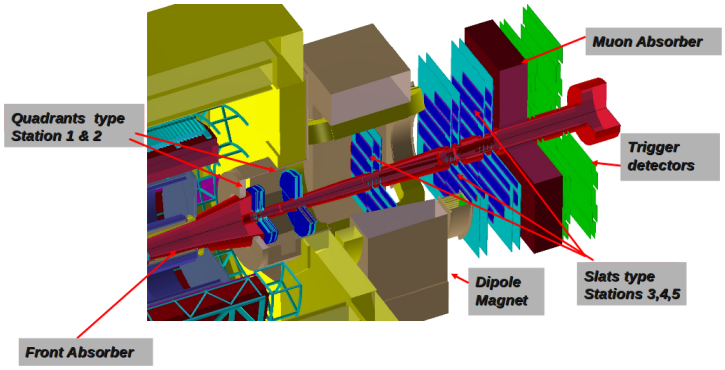

Figure 2.10: The layout of the muon tracking stations of the Muon Spectrometer.

The muon tracking chambers were designed to achieve a spatial resolution of about 100 μm to separate different Υ states with an invariant mass resolution of the order of 100 MeV/c^2. The tracking system is expected to cover also a total area of about 100 m^2. The above mention requirements are satisfied by the use of Cathode Pad Chambers (CPC). These tracking detectors are equipped with a central plane of anode wires sandwiched between two segmented cathode planes and are operated following the principle of Multiwire Proportional Counters (MWPC) with a gas mixture of Ar+CO_2 (80% + 20%).

The basic working principle of CPC is shown in Fig. 2.11. The cathode planes are divided into pads, which are used to locate the position of a particle traversing the detector. When a charged particle passes through the active gas volume of the detector, the ionization (create e^+e^-) takes place along its trajectory. These primary electrons travel towards the nearest anode wire, where the avalanche takes place due to the high electric field. The electrons are captured by the anode wire while the ions travel towards the cathode. The pads having a specific geometry are used to sample the space charges

induced on the cathode planes. The relative value of the induced charges on the pads and the pad coordinates are used to determine the position (x,y) of the charged particle crossing through the detector.

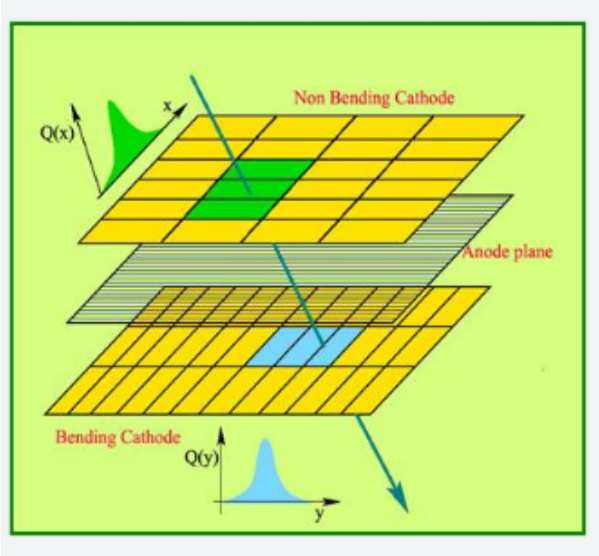

Figure 2.11: The working principle of a Cathode Pad Chamber [24].

In order to maintain the number of overlapping clusters to be less than 1%, the pad occupancy needs to be kept below 5% [25]. Thus, a fine granularity segmentation of the readout pads is needed. The smallest size (4.2×6.3 mm^2) pads are used in the first station near the beam pipe, where the charged particle multiplicity is the highest. As the hit density decreases with the distance from the beam, larger pads are used at larger radii. This leads to a total number of channels to about one million. To minimize the multiple scattering of the muons in the chambers, the material budget is kept less than 3% of the radiation length. Two different geometries are used for the chambers. First two stations have a quadrant geometry while the rest of them have a slat (rectangular) geometry as shown in the photograph at stations 2 and 4 in Fig. 2.12.

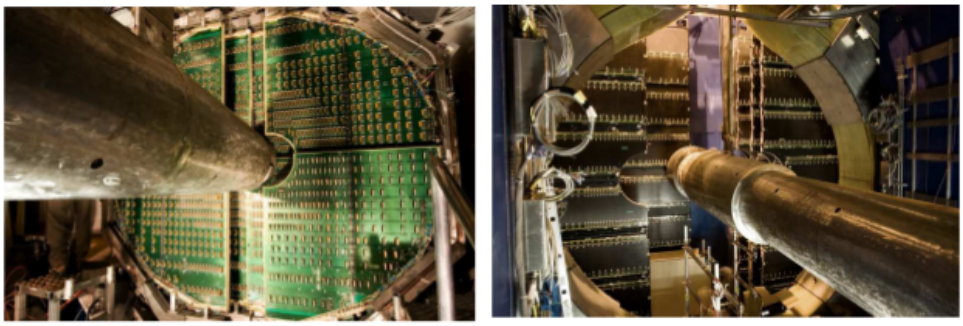

Figure 2.12: The quadrant type geometry of station 2 built by SINP and AMU (left) and slat type geometry of station 4 and 5.

Muon Filter

The Muon Filter is the iron wall placed at 15 m from the IP, between the 5^{th} tracking station and the first trigger station. The dimension of the wall is 5.6× 5.6×1.2 m^3. It reduces the background of the trigger stations by absorbing the residual secondary hadrons and low momentum muons emerging from the hadron absorber. The combined effect of the front absorber and the muon filter introduces a muon momentum threshold of 4 GeV/c, which leads to a good rejection of soft muons and enhances the trigger chamber performance.

Muon Trigger Chambers

The Muon Trigger (MTR) is made of two stations (MT1 and MT2), placed behind the muon filter at about 16 m and 17 m from IP. Each trigger station is consists of two parallel detection planes of 18 single-gap Resistive Plate Chambers (RPC) separated by 15 cm so that the total number of RPCs is 72. The trigger system has a programmable predefined cut - low p_{T} cut (p_{T}^{μ}≥0.5 GeV/c) to reduce the combinatorial background in quarkonium analysis.

The design of an RPC is shown in Fig. 2.13. Each RPC consists of two parallel plates made out of high resistivity Bakelite, an anode and a cathode.

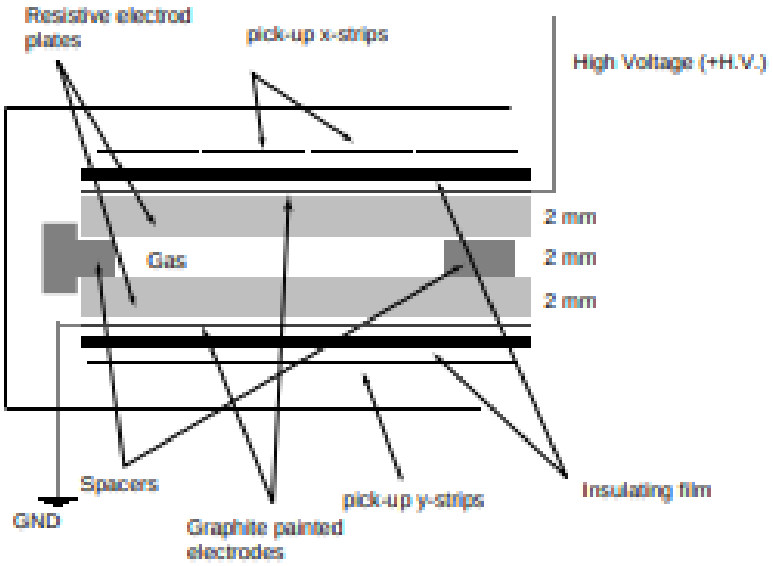

Figure 2.13: The schematic layout of the RPC in Trigger chamber [26].

A High voltage is applied across the resistive electrode plates by means of a conductor layer coated on their outer surfaces. The plastic spacers is placed inside the gas gap to keep them separated by a constant distance of 2 mm. At the atmospheric pressure, the detector is filled with a a gas mixture $Ar + C_2H_2F_4 + i - butane + SF_6$ (50.5:41.3:7.2:1) and kept in flow mode. When an ionizing particle passes through the gas gap, the electrons give rise to a discharge on the anode, which is absorbed by the gas. As the discharge time (≈10 ns) is much shorter than the relaxation time of the electrodes, they behave as an insulator throughout the whole discharge process. The signal is then picked up by induction method using insulated conductive strips placed on the electrodes.

Beam Shield

The beam pipe is surrounded by a beam shield along the length of the Muon Spectrometer. The shield comes in a form of conical tube made out of high Z tungsten-lead mixture embedded in a 4 cm thick stainless steel envelope.

Detector readout

The muon tracking station has Front-End Electronics (FEE), based on a 16-channel MANAS chip which ensures the following functionalities: charge amplifier, filter, shaper, and track & hold. The channels of four such chips are fed into two 12-bit ADCs, which are readout by the Muon Arm Readout Chip (MARC). This chain is embedded on front-end boards (MANUs). To read the 1,076,224 channels of the tracking system total 16,816 MANU cards are necessary. The data from the MANU card is transferred to the Concentrator ReadOut Cluster Unit System (CROCUS) via the bus PATCHs (Protocol for ALICE Tracking Chambers). Each chamber is readout by two CROCUS, which concentrate and format the data from the chamber, transfer them to the DAQ and dispatch the trigger signals coming from the Central Trigger Processor (CTP). The CROCUS also allows the control of the FEE and the calibration processes. The readout architecture is shown in Fig. 2.14.

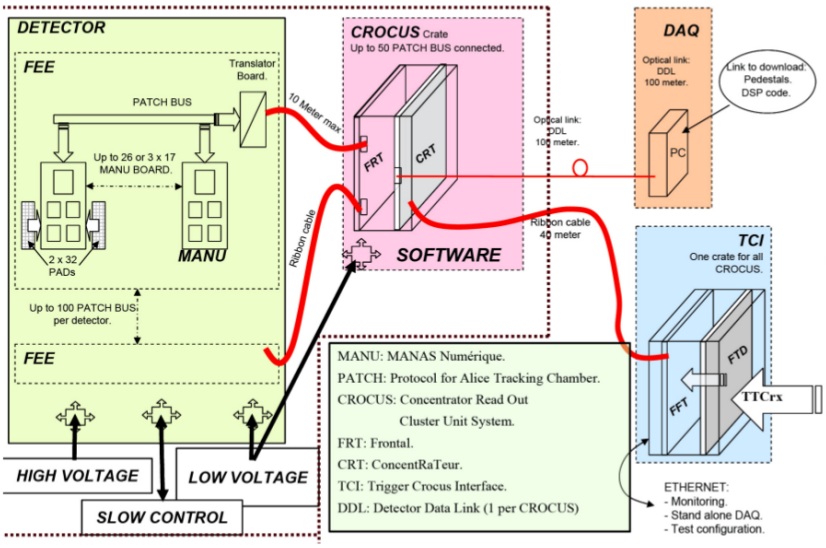

Figure 2.14: The schematic of the detector readout [27] for ALICE.

2.5 ALICE trigger system

ALICE has a 3-layer trigger structure and is controlled by the Central Trigger Processor (CTP) and complemented by a software-based High Level Trigger (HLT). The CTP [28] is a hardware trigger system that generates the trigger decision based on the trigger signals from the different detectors.

Due to the different response time of different sub-detectors, a three-level trigger system has been implemented in ALICE [18]:

1. **Level 0 (L0)** is the fastest trigger level. L0 is issued to the CTP and delivered to the corresponding sub-detectors after 1.2 μs. A L0 trigger can be sent by V0, T0, SPD, EMCAL, PHOS and MTR.

2. **Level 1 (L1)** The second level trigger, called L1, is received by the sub-detector after 6.5 μs. L1 is generated from the inputs from TRD and ZDC in the events accepted by L0.

3. **Level 2 (L2)** The final trigger level, L2 which is delivered after 88 μs after the interaction and is used to readout the TPC. The event is finally stored after L2 trigger.

2.6 Data Reconstruction

The recorded events usually undergo several cycles of reconstruction in order to be ready for physics analyses. Each reconstruction cycle is known as 'pass' which is performed offline using the Alice offline framework [29]. The results of a reconstruction 'pass' are saved in Event Summary Data (ESD) files. These include necessary information from the different detectors and which are used for analysis. In the next step, the Quality Assurance (QA) is carried out of the ESD files. The QA checked ESD files can be filtered

into Analysis Object Data (AOD) files, which contained less information and is useful for specific analysis.

Bibliography

[1] https://home.cern/about/who-we-are/our-governance/member-states.

[2] *The ALICE experiment at the CERN LHC*, *Journal of Instrumentation* **3** (aug, 2008) S08002–S08002.

[3] *The ATLAS experiment at the CERN large hadron collider*, *Journal of Instrumentation* **3** (aug, 2008) S08003–S08003.

[4] *The CMS experiment at the CERN LHC*, *Journal of Instrumentation* **3** (aug, 2008) S08004–S08004.

[5] *The LHCb detector at the LHC*, *Journal of Instrumentation* **3** (aug, 2008) S08005–S08005.

[6] ALICE collaboration, G. Dellacasa et al., *ALICE technical design report of the inner tracking system (ITS)*, .

[7] ALICE collaboration, G. Dellacasa et al., *ALICE: Technical design report of the time projection chamber*, .

[8] ALICE collaboration, G. Dellacasa et al., *ALICE technical design report of the time-of-flight system (TOF)*, .

[9] ALICE collaboration, P. Cortese, *ALICE transition-radiation detector: Technical Design Report*, .

[10] ALICE collaboration, S. Beole et al., *ALICE technical design report: Detector for high momentum PID*, .

[11] ALICE collaboration, P. Cortese et al., *ALICE electromagnetic calorimeter technical design report*, .

[12] ALICE collaboration, G. Dellacasa et al., *ALICE technical design report of the photon spectrometer (PHOS)*, .

[13] ALICE collaboration, G. Dellacasa et al., *ALICE technical design report: Photon multiplicity detector (PMD)*, .

[14] ALICE collaboration, P. Cortese et al., *ALICE technical design report on forward detectors: FMD, T0 and V0*, .

[15] ALICE collaboration, G. Dellacasa et al., *ALICE technical design report of the zero degree calorimeter (ZDC)*, .

[16] ALICE collaboration, S. Beole et al., *The forward muon spectrometer of ALICE*, .

[17] L. B. et al., *Definition of the ALICE coordinate system and basic rules for sub-detector components numbering*, *ALICE-INT* (2003) 038.

[18] ALICE collaboration, B. B. Abelev et al., *Performance of the ALICE Experiment at the CERN LHC*, *Int. J. Mod. Phys. A* **29** (2014) 1430044, [1402.4476].

[19] ALICE collaboration, E. Abbas et al., *Performance of the ALICE VZERO system*, *JINST* **8** (2013) P10016, [1306.3130].

[20] http://alice.web.cern.ch/detectors/more-details-alice-zdc.

[21] https://cerncourier.com/a/alice-gets-ready-to-pinpoint-muon-pairs/.

[22] ALICE collaboration, S.Grigoryan, *Contribution of Secondary Pi/K Mesons, produced in the Absorber, into the Dimuon Background in Pb-Pb collisions, ALICE-INT-2002-06*, .

[23] ALICE collaboration, D. Swoboda, *ALICE Muon Arm Dipole Magnet. ALICE Internal Note, 1999– 06, 1999*, .

[24] http://www.saha.ac.in/web/henppd-introduction-detector-working.

[25] I. Das, *Development, Implementation and Performance Report of Dimuon High Level Trigger of ALICE*, 2010.

[26] ALICE collaboration, K. Aamodt et al., *The ALICE experiment at the CERN LHC*, *JINST* **3** (2008) S08002.

[27] V. Chambert, L. Bimbot, M. Comets, S. Drouet, B. Espagnon, C. Hadjidakis et al., *The electronics of ALICE Dimuon tracking chambers*, in *Topical Workshop on Electronics for Particle Physics (TWEPP-08)*, (Naxos, Greece), pp. 242–246, Sept., 2008.

[28] ALICE Collaboration collaboration, C. W. Fabjan, L. Jirdén, V. Lindestruth, L. Riccati, D. Rorich, P. Van de Vyvre et al., *ALICE trigger data-acquisition high-level trigger and control system: Technical Design Report*. Technical Design Report ALICE. CERN, Geneva, 2004.

[29] J. F. Grosse-Oetringhaus, C. Zampolli, A. Colla, F. Carminati and the Alice Collaboration, *The ALICE online-offline framework for the extraction of conditions data*, *Journal of Physics: Conference Series* **219** (apr, 2010) 022010.

CHAPTER 3

The readout upgrade of the Second Tracking Station of the Muon Spectrometer of ALICE

In the previous chapter, we have discussed the ALICE experiment and the Muon Spectrometer in detail. The Muon Spectrometer has delivered a good quality of data in pp, p–Pb, Pb–Pb and Xe–Xe collisions at various LHC energies. However, there are some limitations in order to fully exploit the data generated by the LHC. For this purpose, readout upgrade of the tracking station of the Muon Spectrometer has been undertaken, which is a part of the ALICE upgrade program.

3.1 ALICE Upgrade Program during Long shutdown 2

The LHC has ended the four-year long Run 2 program in December 2018 and entered the two-year upgrade period, known as Long Shutdown 2 (LS2). The implementation of improvements to the accelerated complex and upgrade of electronics during LS2 will

certainly boost the ALICE physics goal in Run 3 and Run 4. For example, during Run 3 the instantaneous luminosity in Pb–Pb collisions will increase by a factor of ~ 6 and the minimum-bias interaction rate will reach about 50 kHz, which is 50 times higher than the rate recorded by ALICE during Run 2 heavy-ions collisions. The statistical significance of pp and p–Pb data will also subsequently increase which will provide a more accurate reference for comparison with results from Pb–Pb collisions. In order to utilize these large interaction rates and enhance the Physics scope, ALICE is implementing the following upgradations [1, 2]:

- New high-resolution, low-material Inner Tracking System (ITS).
- Upgrade of Time Projection Chamber. The existing wire plane replaced by GEM foils.
- New silicon sensor-based Muon Forward Tracker (MFT) to be placed in front of hadron absorber of the Muon Spectrometer for accurate vertex determination.
- Upgrade of the readout electronics of Muon Spectrometer, PHOS, TOF, and TRD for high rate operation.
- Upgrade of the forward trigger detectors and ZDC.
- Upgrade on the online systems, offline reconstruction and analysis framework.

3.2 Physics goals for the upgrade

The general physics motivations for the upgrade of the ALICE experiment can be found in the Letter of Intent [1]. The main goal of the upgrade is to carry out high precision measurements of rare probes in very low and intermediate transverse momentum. This will be a unique facility at LHC. To study the quark-medium interaction, heavy-flavor mesons and baryons should be measured down to very low p_T ranges. Furthermore,

the high-precision measurements in the quarkonium sector as a probe of study of the deconfinement medium and its temperature will be extended the physics understanding of the high-density QCD at the LHC [3].

3.3 Muon Spectrometer upgrade

The primary limitation of the existing Muon Spectrometer of ALICE comes from the multiple scattering of muon tracks by the hadron absorber. As a result, it does not determine the vertex position of the decay muons accurately. This prevents the spectrometer from separating the prompt and the non-prompt J/ψ, which does not allow the study of the important source of beauty production at forward rapidity. Furthermore, the statistical significance of low mass, low p_{T} muon analysis is compromised due to the high background emerging from semi-muonic decays of π and K mesons. In order to remove these limitations, a new silicon pixel tracker called Muon Forward Tracker (MFT), will be installed in front of the absorber. The MFT will improve the vertexing capabilities of the spectrometer.

3.4 Working principle of tracking station readout upgrade

The present readout system for the muon trackers can support a physics trigger rate of $\sim$ 2kHz. Thus, this scheme needs to be changed in order to utilize the high interaction rates.

The muon tracking chamber is upgraded with new front-end electronics (FEE) and a new readout system to handle the higher rate interaction in upcoming Run 3 and Run 4.

For safety purposes, the FEE was designed to operate at 100kHz, while the interaction rate will be at 50kHz [4]. A common ASIC chip, called SAMPA has been developed for this rate of interaction. The existing MANAS chip of the tracking station is replaced by the Dual SAMPA (DS) chips providing a total of 64 readout channels. The data from the dual SAMPA boards will be shipped out through FE links implemented on printed circuit boards (PCB). The data from the DS will send to the new concentrator boards (SOLAR) and finally reached to the new Common Readout Units (CRU) of the ALICE central Data Acquisition System. The data flow configuration is shown in Fig. 3.1.

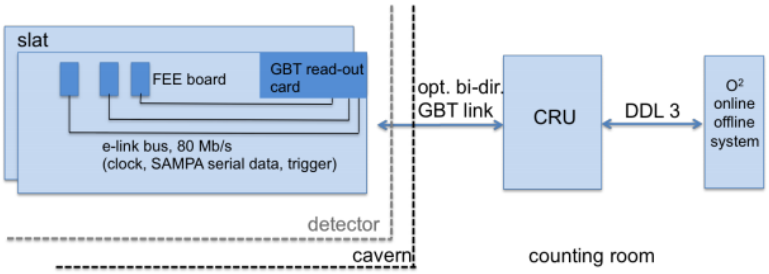

Figure 3.1: The schematic diagram of the Muon Tracker readout configuration in Run 3 [4].

The FEE parameters are designed with the following specifications [4]:

- The detector implementation is not modified. Hence, the geometrical layout, location and connections to the chambers of the 64 channel FEE boards remain unchanged.
- The chambers are operated with the existing gas and high voltage parameters.
- The maximum input signal will be kept at 500 fC and the gain is around 4 mV/fC.
- The colling system remains the same as the existing one. No significant variance in power consumption.

The dual SAMPA cards having the following features [4]:

- 10-bit ADC
- 10 MHz sampling rate
- 330 ns shaping time
- noise level below 2000 e^- for large pads and 1000 e^- for small pads

The Dual SAMPA card for stations 1 and 2 is shown in Fig. 3.2.

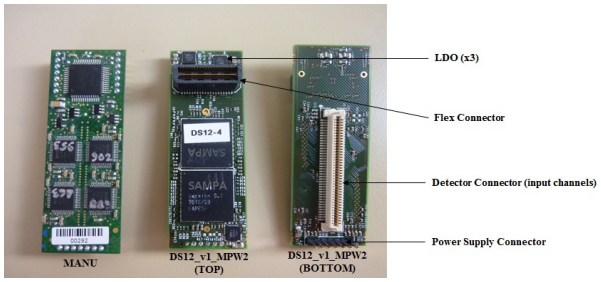

Figure 3.2: Photograph of MANU and Dual SAMPA cards for stations 1 and 2 [5].

3.5 Existing and proposed readout of the second station

The existing readout has been discussed in chapter 2. The main features are:

1. FEE based on 16-channel MANAS chip, which utilizes the muon trigger. The MANU card reads 64 pads.
2. Total of 225 MANU cards/detection plane for 2nd tracking station.
3. Serial readout of MANU cards arranged in 12 parallel bus-lines in a quadrant.

For readout upgrade, the following features have been considered:

1. Replace the MANU card with Dual-Sampa12 (DS12), which reads 64 pads. The Sampa is a self-trigger ASIC.

2. Each DS12 has to be readout in parallel to ensure the high output.

3. Each DS12 will has the following signals:

Table 3.1: The signal specifications of DS12

Type	No. of tracks	Signals	Comment
I2C	2	ASDA, ASCLK	Shared by 5 DS
E-Link	2×2	CLK, DATA	4 signals for DS
Trigger	4×2×2	Physics_trigger, Heart_beat, Hard_reset, Sync	Chained among 5 DS
Address	3	Address	Hard-wired on PCB
LV	2×2	Low voltage supply	2 for Analog 1.75 V 2 for Digital 1.75 V

Apart from these 29 signal lines, each DS will have 6 GND connections. Therefore, the total number of tracks to be laid out is ∼35×225∼8000 on a PCB board which is full of holes for the Kapton readout cables from the pad plane. Thus, the only solution is to design a multilayer 1.15 m × 1.2 m motherboard for parallel readout of DS12 for Station 2. But the fabrication of such PCB is not possible in India as well as in the rest part of the world.

Hence the indigenously proposed scheme for Station 2 is : signal tracks on the rigid PCB + signal transmission by ribbon cable as shown in Fig 3.3. Each ribbon cable will control a group of 5 DS-12 cards.

The 40-pin connector which has been used in the design is shown in Fig 3.4.

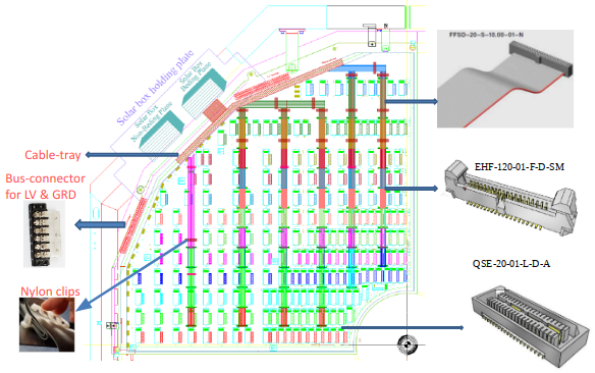

Figure 3.3: The schematic layout of the readout PCB for Station 2.

HeartBit_P	1	2	HeartBit_N
Sync_P	3	4	Sync_N
GND	5	6	HardReset_N
HardReset_P	7	8	GND
Physics_P	9	10	Physics_N
GND	11	12	CLK0_N
CLK0_P	13	14	CLK1_N
CLK1_P	15	16	CLK2_N
CLK2_P	17	18	CLK3_N
CLK3_P	19	20	CLK4_N
CLK4_P	21	22	GND
DIN0_P	23	24	DIN0_N
GND	25	26	DIN1_N
DIN1_P	27	28	GND
DIN2_P	29	30	DIN2_N
GND	31	32	DIN3_N
DIN3_P	33	34	GND
DIN4_P	35	36	DIN4_N
GND	37	38	ASDA
GND	39	40	ASCLK

HeartBit_OUT_N	1	2	Sync_OUT_N
HeartBit_OUT_P	3	4	Sync_OUT_P
GND	5	6	GND
HardReset_OUT_N	7	8	Physics_OUT_N
HardReset_OUT_P	9	10	Physics_OUT_P
GND	11	12	GND
GND	13	14	ADR0
GND	15	16	ADR1
GND	17	18	GND
ADR2	19	20	ASDA
GND	21	22	ASCLK
GND	23	24	GND
CLK_P	25	26	DATA_P
CLK_N	27	28	DATA_N
GND	29	30	GND
Physics_P	31	32	HardReset_P
Physics_N	33	34	HardReset_N
GND	35	36	GND
Sync_P	37	38	HeartBit_P
Sync_N	39	40	HeartBit_N

Figure 3.4: The 40-pin connectors for readout: EHF-120-01-F-D-SM (left) (on the ribbon) and QSE-20-01-L-D-A (right) (on DS-12 card)

Advantages of the proposed scheme:

1. Modular design – the readout PCB can be broken in desirable pieces containing multiplies of 5 DS-12 cards.

2. Rigid PCB – support the LV + GRD + signal tracks from EHF-120-01-F-D-SM-40 pin to QSE-20-01-L-D-A-40 pin.

3. Ribbon cables – Solar box to EHF-120-01-F-D-SM-40 pin (same as on existing translator card).

4. The EHF-120-01-F-D-SM connector is close to DS12 –short signal tracks ensuring smaller capacitative coupling.

5. Scheme for grouping and anchoring the ribbon cables.

6. Validation will be easier and future maintenance will be convenient.

3.6 Upgrade readout plane of second tracking station

The second tracking station of Muon Spectrometer has been designed and fabricated by the Saha Institute of Nuclear Physics and Aligarh Muslim University. Hence, the readout upgrade (R/O) has been planned and executed by these two centers. I have participated at every stage of this upgrade work.

3.6.1 Designed of Printed Circuit Board (PCB) for R/O upgrade

The second station is based on a quadrant structure and the readout electronics are distributed on its surface. Each CPC quadrant has two readout planes i.e. the bending plane (BP) and the non-bending plane (NBP). In each plane (BP/NBP), the readout PCB has been segmented into seven pieces. The segment arrangements for a NBP PCB is shown in Fig. 3.5.

In the present design, each PCB segment has a maximum of six rows of readout lines and each row comprises of maximum three blocks of five Dual Sampa (DS12) cards (some blocks have four DS). The density of the DS cards is maximum near the beam pipe i.e. in PCB1. The distribution of DS cards near the beam tube on the bending PCB1 is shown in Fig. 3.6.

The number of DS cards on each PCB are listed in Table 3.2. This numbers are same on both planes. Hence, the total no. of DS cards and DS blocks (ribbon cables) are

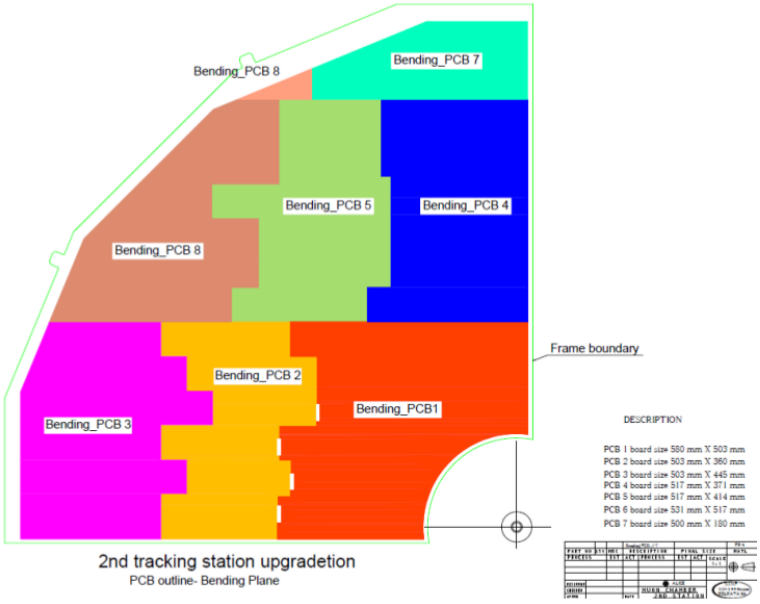

Figure 3.5: The arrangement of PCB segments in one CPC quadrant.

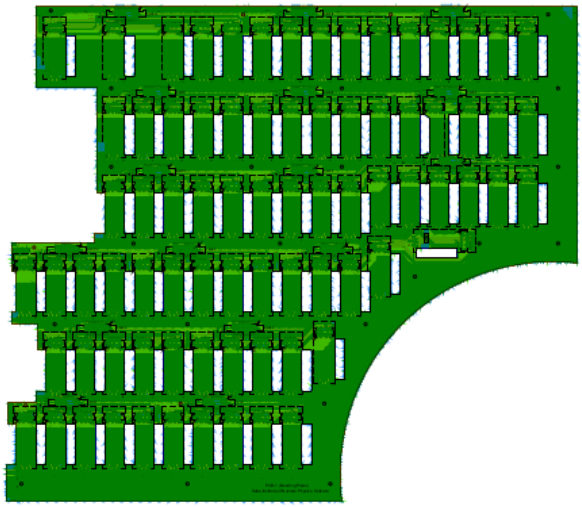

Figure 3.6: The distribution of DS blocks on bending PCB1

(2×221 = 442) and (2×45 = 90), respectively.

The PCBs have four layers and the approximate total thickness is 0.564 mm. The layers and their individual thickness are:

- 1_Top Layer COPPER, 18 μm base + 18 μm plated = 0.036 mm

Table 3.2: The no. of DS boards for each PCB of BP/NBP plane

PCB	No. of DS	No. of blocks of 5/4 DS
1	79	16
2	30	6
3	23	5
4	35	7
5	25	5
6	20	4
7	9	2
8	0	0
Total	221	45

- 2_Middle Layer Digital Bus + GND COPPER, 18 μm base + 18 μm plated = 0.036 mm
- 3_Middle Layer GND COPPER, 18 μm base + 18 μm plated = 0.036 mm
- 4_Bottom Layer Analog Bus +GND COPPER, 18 μm base + 18 μm plated = 0.036 mm

The dielectric constant (DK) of FR4 is 5.7. An additional prepreg layer of thickness 0.12 mm is placed between 2_Middle Layer and 3_Middle Layer. The electrical connection of different layers is made with the Plated Through-Hole (PTH). The diameters of PTH and positions are as follows:

- PTH 1_Top to 2_Middle 0.3 mm drill diameter
- PTH 4_Bottom to 3_Middle 0.3 mm drill diameter
- PTH 1_Top to 4_Bottom 0.4 mm drill diameter with Plated Annular ring
- PTH 1_Top to 4_Bottom 0.3 mm drill diameter

The schematic diagram of the 4-layer PCB is illustrated in Fig. 3.7.

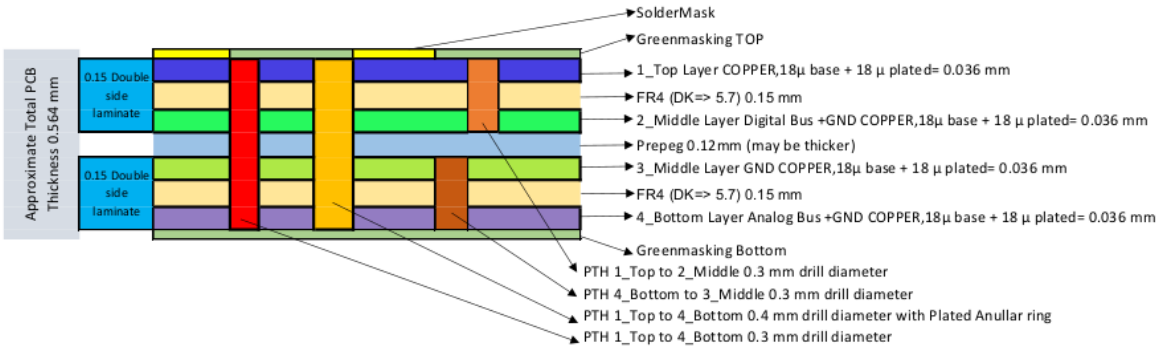

Figure 3.7: The stack up design for the 4-Layer PCB.

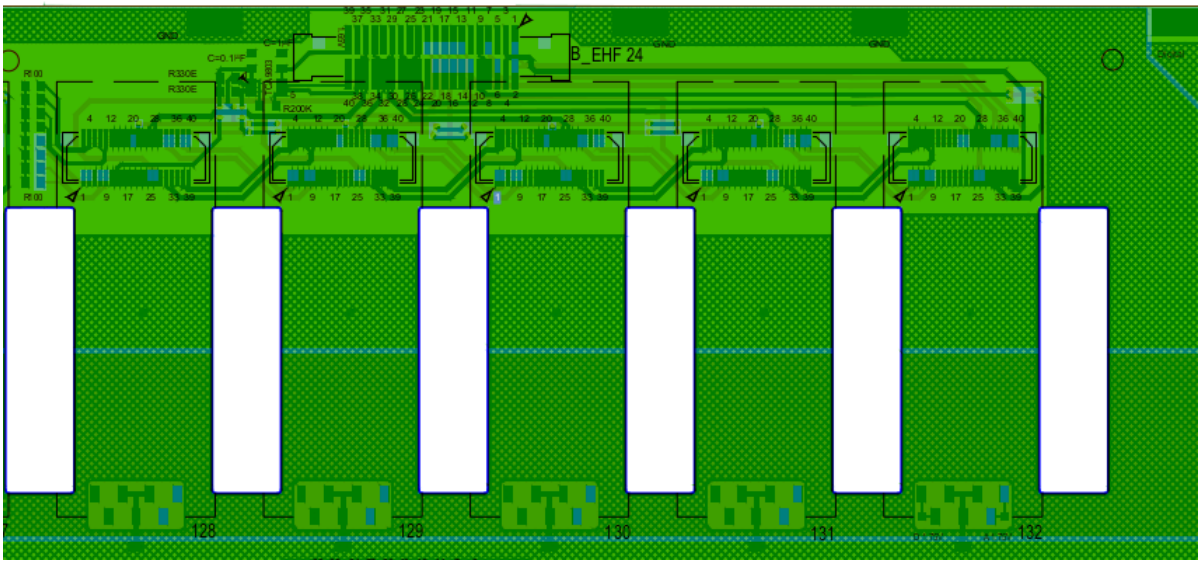

Figure 3.8: DS and EHF card boards in one readout block consisting of 5 DS12.

The connection of the five DS cards to the EHF connector is shown in Fig. 3.8. Here, the left-most DS is always labeled as DS0 and the right most DS (terminating DS) is labeled as DS4 (DS3 for four DS block). The DS card as well as the EHF connector have 40 pin connections. The seven-pin connector at the bottom side of each DS card is utilized to provide the LV and ground connections. The connection between EHF to DS, DS to DS, DS to GND, EHF to GND, IC to DS and EHF are listed in the following tables.

Table 3.3: Pin Connections of Solar Card (EHF) To Dual Sampa (DS-0) (QSE) Card.

Solar Card (EHF) To Dual Sampa (DS-0)				
Solar Card(EHF Connector)	Pin No.		Pin No.	DS_0 Card(QSE Connector)
Heart Beat_P	1	$\longleftrightarrow$	38	Heart Beat_P
Heart Beat_N	2	$\longleftrightarrow$	40	Heart Beat_N
Sync_P	3	$\longleftrightarrow$	37	Sync_P
Sync_N	4	$\longleftrightarrow$	39	Sync_N
Hard Reset_P	7	$\longleftrightarrow$	32	Hard Reset_P
Hard Reset_N	6	$\longleftrightarrow$	34	Hard Reset_N
Physics_P	9	$\longleftrightarrow$	31	Physics_P
Physics_N	10	$\longleftrightarrow$	33	Physics_N
Clk_0_P	13	$\longleftrightarrow$	25	Clk_0_P
Clk_0_N	12	$\longleftrightarrow$	27	Clk_0_N
DIN_0_P	23	$\longleftrightarrow$	26	DIN_0_P
DIN_0_N	24	$\longleftrightarrow$	28	DIN_0_N

Table 3.4: GND pin connection of Solar and all DS (common ground).

GND pin connection	
GND Pin no. for Solar (EHF Connector)	GND Pin no. for all DS (QSE Connector)
5,8,11,22,25,28,31,34,37	5,6,11,12,15,17,18,21,23,24,29,30,35,36

Table 3.5: Pin Connections of Dual Sampa (DS) (QSE Connector).

DS Inter Connection				
DS0(DS1, DS2, DS3)	Pin No.		Pin No.	DS1(DS2, DS3, DS4)
Heart Beat_Out_N	1	$\longleftrightarrow$	40	Heart Beat_N
Heart Beat_Out_P	3	$\longleftrightarrow$	38	Heart Beat_P
Sync_Out_N	2	$\longleftrightarrow$	39	Sync_N
Sync_Out_P	4	$\longleftrightarrow$	37	Sync_P
Hard Reset_Out_N	7	$\longleftrightarrow$	34	Hard Reset_N
Hard Reset_Out_P	9	$\longleftrightarrow$	32	Hard Reset_P
Physics_Out_N	8	$\longleftrightarrow$	33	Physics_N
Physics_Out_P	10	$\longleftrightarrow$	31	Physics_P

Table 3.6: Pin connection of Solar (EHF Connector) to DS1(QSE Connector).

Solar to DS1				
Solar Card (EHF Connector)	Pin No.		Pin No.	DS1(QSE Connector)
CLK_1_N	14	$\longleftrightarrow$	27	CLK_N
CLK_1_P	15	$\longleftrightarrow$	25	CLK_P
DIN_1_N	26	$\longleftrightarrow$	28	DIN_N
DIN_1_P	27	$\longleftrightarrow$	26	DIN_P

Table 3.7: Pin connection of Solar (EHF Connector) to DS2(QSE Connector).

Solar to DS2				
Solar Card (EHF Connector)	Pin No.		Pin No.	DS2(QSE Connector)
CLK_2_N	16	$\longleftrightarrow$	27	CLK_N
CLK_2_P	17	$\longleftrightarrow$	25	CLK_P
DIN_2_N	30	$\longleftrightarrow$	28	DIN_N
DIN_2_P	29	$\longleftrightarrow$	26	DIN_P

Table 3.8: Pin connection of Solar (EHF Connector) to DS3(QSE Connector).

Solar to DS3				
Solar Card (EHF Connector)	Pin No.		Pin No.	DS3(QSE Connector)
CLK_3_N	18	$\longleftrightarrow$	27	CLK_N
CLK_3_P	19	$\longleftrightarrow$	25	CLK_P
DIN_3_N	32	$\longleftrightarrow$	28	DIN_N
DIN_3_P	33	$\longleftrightarrow$	26	DIN_P

Table 3.9: Pin connection of Solar (EHF Connector) to DS4(QSE Connector).

Solar to DS4				
Solar Card (EHF Connector)	Pin No.		Pin No.	DS4(QSE Connector)
CLK_4_N	20	$\longleftrightarrow$	27	CLK_N
CLK_4_P	21	$\longleftrightarrow$	25	CLK_P
DIN_4_N	36	$\longleftrightarrow$	28	DIN_N
DIN_4_P	35	$\longleftrightarrow$	26	DIN_P

Table 3.10: GND pins for all DS

GND pin connection for DS	
Dual Sampa (QSE Connector)	GND Pin no.
DS0	14,16,19
DS1	16,19
DS2	14,19
DS3	19
DS4	14,16

A buffer IC has been placed between the last DS and the Solar card. The IC pin connection is shown in Fig. 3.9.

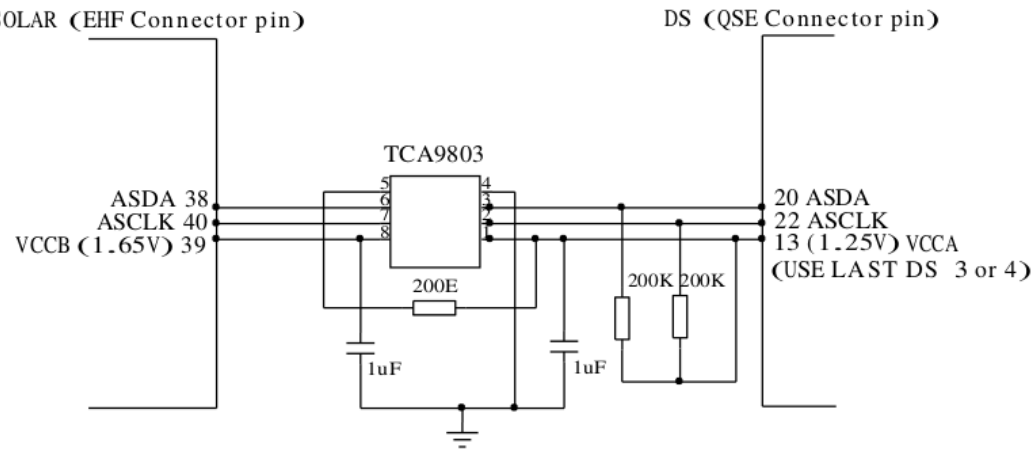

Figure 3.9: IC connection to SOLAR (EHF Connector pin) and DS (QSE Connector pin)

The parallel connection of 20 and 22 pins of all DS is connected with 3 and 2 pins of IC, respectively. The terminating resistance of 100 Ω is connected between the last DS and GND of the PCB as shown in Fig. 3.10. This is because the impedance of the signal tracks is calculated to be ∼ 100 Ω for the present layout.

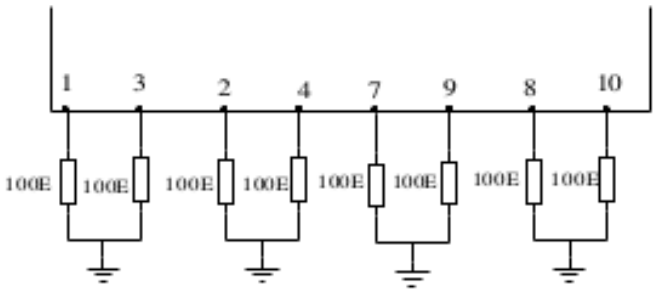

Figure 3.10: The termination scheme for the differential pulses.

3.6.2 In house testing of PCB

Each PCB board has been tested and validated at the Saha Institute of Nuclear Physics. Before the testing, the first task was the proper cleaning of the board and continuity check of the LV power supply connection. In few cases, an external jumper is needed for the continuation of the power connections across the segment boundaries. A photograph of the test setup is shown in Fig. 3.11.

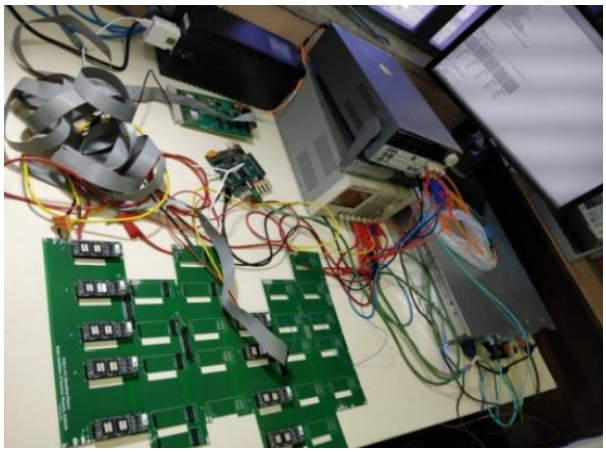

Figure 3.11: The photograph of the in house testing set up at Saha Institute of Nuclear Physics.

For the testing of a PCB segment, the EHF connector is connected to the SOLAR card via a 5 m long ribbon cable. The SOLAR card is connected to the DAQ system through an optical cable. The PCB bus lines have been provided with both digital and analog voltages of 1.75V using a common ground. The SOLAR card has been supplied 5V analog voltage.

The PCBs were tested with pedestal runs where the average signal threshold with no input of each pad was measured. There were minimal errors in the design and fabrication of the PCB. The most common errors were due to improper soldering, inadequate cleaning and synchronization of timing between clock and data. Thus, proper cleaning and removing the short between the pin connections have resolved the issues. The pulses

corresponding to the clock and the data is shown in Fig. 3.12.

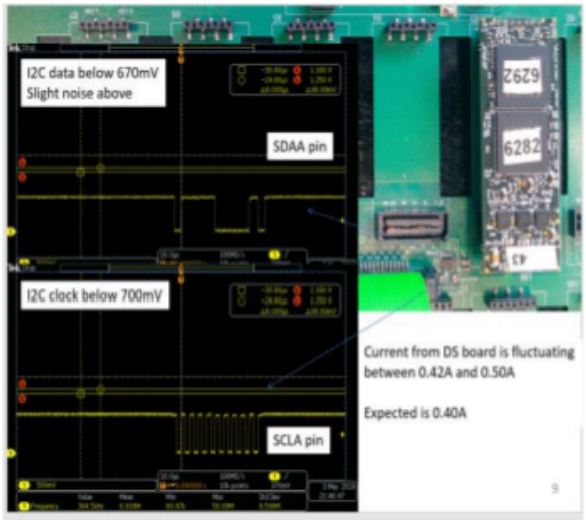

Figure 3.12: The data and clock pulses as observed on a storage oscilloscope [6]

3.6.3 PCB testing at CERN

All the bending and non-bending PCB boards have been mounted on the quadrants and validated at CERN with CRU-based DAQ. The test setup is shown in Fig. 3.13 where a quadrant of the second station (non-bending) is connected to the SOLAR crate via 45 flex cables. The data from the SOLAR crate have been transmitted to the CRU via an optical connection (GBT).

With this setup, the pedestal value and noise level for each pad of each quadrant have been measured (a total of ∼2,60,000 pads). The Fig. 3.14 shows the pedestal value and the noise level for the BP of all the quadrants of the second tracking station.

The pedestal value and noise level in each quadrant have been found to be uniform and a better visualization can be found in Fig 3.15. So it can be concluded that the production of the PCB and proper mounting on the detector has been successfully validated. The quadrants are ready to be installed at the experimental site of ALICE, which is 60 m below the ground.

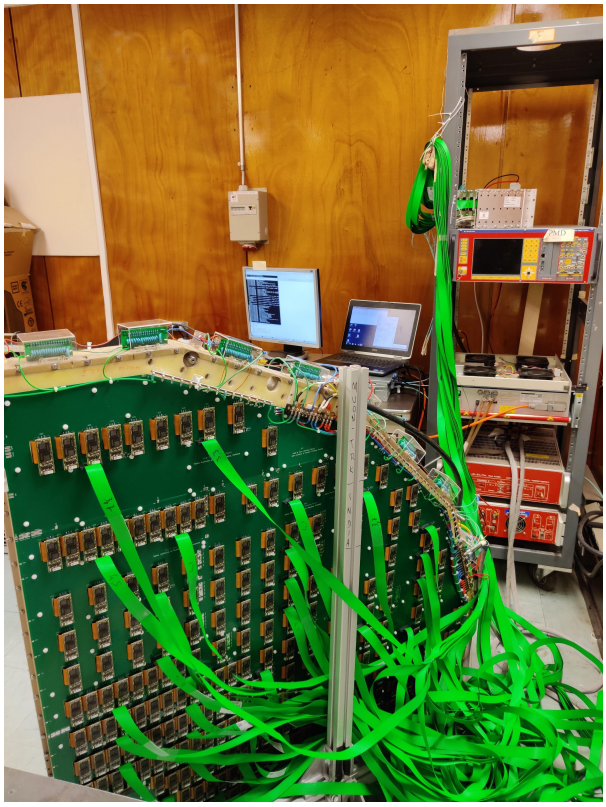

Figure 3.13: The set-up for PCB testing at CERN.

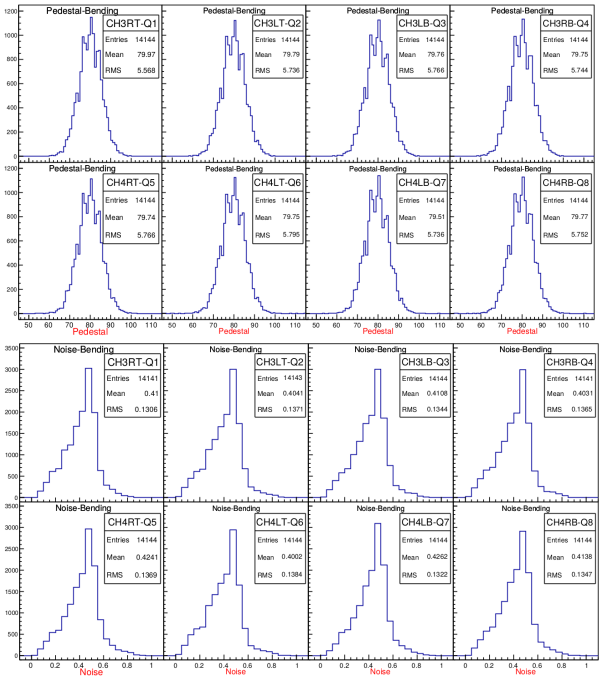

Figure 3.14: The pedestal value (top) and noise level (bottom) for BP of each quadrant of second station.

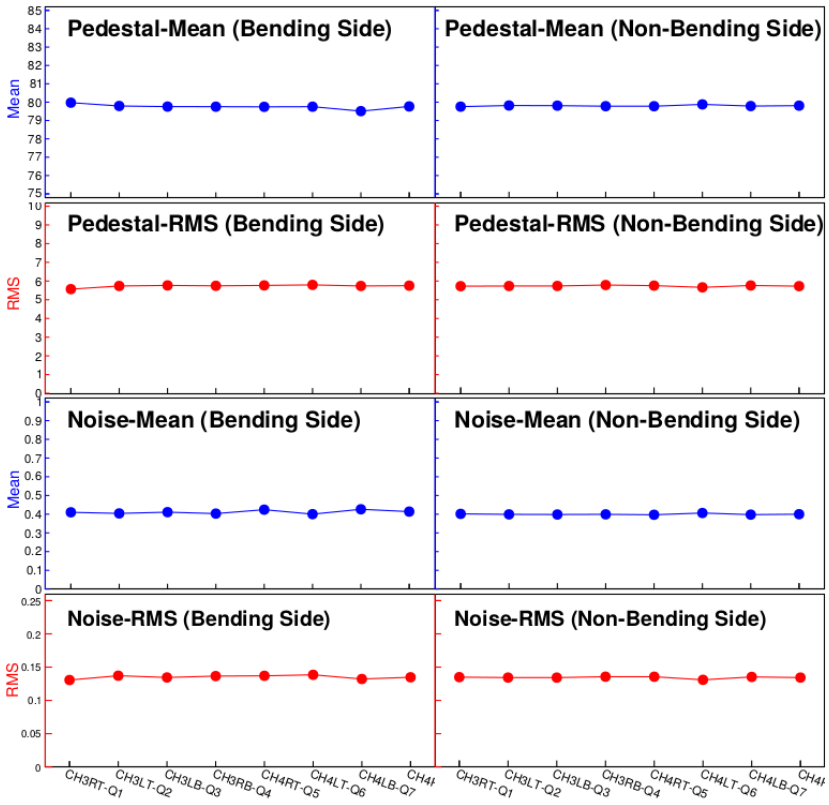

Figure 3.15: RMS and mean value of the pedestal and the noise for all the readout PCBs.

Bibliography

[1] B. A. et al and, *Upgrade of the ALICE experiment: Letter of intent*, *Journal of Physics G: Nuclear and Particle Physics* **41** (jul, 2014) 087001.

[2] ALICE Collaboration collaboration, *Addendum of the Letter of Intent for the upgrade of the ALICE experiment : The Muon Forward Tracker*, Tech. Rep. CERN-LHCC-2013-014. LHCC-I-022-ADD-1, CERN, Geneva, Aug, 2013.

[3] Z. Citron et al., *Report from Working Group 5: Future physics opportunities for high-density QCD at the LHC with heavy-ion and proton beams*, vol. 7, pp. 1159–1410. 12, 2019. 1812.06772. 10.23731/CYRM-2019-007.1159.

[4] ALICE Collaboration collaboration, *Upgrade of the ALICE Readout & Trigger System*, Tech. Rep. CERN-LHCC-2013-019, ALICE-TDR-015, CERN, Geneva, Aug, 2013.

[5] "Dual sampa twiki page." https://twiki.cern.ch/twiki/bin/view/ALICE/DS12_MPW2.

[6] S. Chattopadhyay, A. Das, D. Das, L. Das, D. Das, W. Shaikh et al., *The In-house design validation of new version of electronic Read-Out (Bending Plane) of the Second Tracking Station of ALICE-MS*, *DAE Symp. Nucl. Phys.* **64** (2020) 948–949.

CHAPTER 4

Service task on tracking chamber status maps and Data analysis

During the thesis period, I have been carried out a service task for ALICE on "Monitoring the data/MC agreement of tracking chamber status maps". This work addressed the unexpected chamber efficiency issues of pp 13 TeV data, collected during 2017, which will be discussed in the first half of this chapter. In the second part of this chapter, the common framework for Υ analysis in pp, p–Pb and Pb–Pb collisions with ALICE Muon Spectrometer will be discussed.

4.1 Monitoring the MC/data agreement of Muon tracking chamber status maps

To find out the unexpected issues related to the tracking chamber efficiency, a single muon simulation has been performed. The comparison of cluster maps, generated from the real data and the simulation, helps to identify the discrepancies that are responsible for "unexpected" efficiency issues.

4.1.1 Motivations

The primary goal is to track the unexpected detector related issues that are not reproduced by detector simulation. Hence, it biases the detector acceptance × efficiency (A×ϵ) and the tracking systematic uncertainties become large.

During the reconstruction of data and MC events, the actual detector status has been considered. This information is summarized in the status maps. The status maps are constructed from the information on detector configuration, pedestal value, occupancy and High Voltage (HV) stored in the Offline Conditions Data Base (OCDB) on which some predefined selection cuts are applied. This function is used to remove the faulty pads. Nevertheless, a few detector issues i.e. improper HV connection of chamber readout, cable swapping can not be spotted online and hence not accurately reproduced in the status map.

The purpose of this monitoring is to find out these issues which are not included in the status map and identify their origin. If an issue can be identified, either we find a possible solution (resolving the detector or an automatic way to include it in the status map) or add the problematic elements to the RejectList.

4.2 Method

The detail of the method to produce the status maps and comparisons in data and MC are discussed in the following sections.

4.2.1 Overview

An easy way to find out the issues is to compare, run-by-run and chamber-by-chamber (10 chambers for each run), the cluster distribution devoted to the reconstructed tracks

between the data and simulations. For this purpose, the single muon simulation has been done with roughly tuned input shape to reproduce the muon distributions in actual data. The advantage of this tuned input shape is that this MC set can also be used to evaluate tracking efficiency systematics [1]. If some difference between the cluster maps of data and MC is found, it means that there are some "unexpected" faults that are not removed and/or not properly removed by the cluster maps or not in the present RejectList.

4.2.2 Cluster map storage

In real data, the cluster maps are produced during the Quality Assurance (QA) task and saved in QAresults.root files. The QA task runs right after the reconstruction. In general, this is done in the same job as of reconstruction and the final results are merged run-by-run subsequently.

The cluster maps in MC can be produced from the reconstruction QA, which is stored in Merged.QA.Data.root files. One needs to active the MUON QA macro to merge the Merged.QA.Data.root files if the simulation is divided into several jobs.

4.2.3 Simulation of single muon and merging the QA results

The single muon simulation has been carried out over the Worldwide LHC Computing Grid (WLCG) utilizing the AliMuonAccEffSubmitter facility, devoted in $ALICE_PHYSICS/PWG/muondep (directory of ALIPhysics software). This is based on template files (placed in $ALICE_PHYSICS/PWG/ muondep/AccEffTemplates) having several variables that can be tuned to the requirement of submitter. So one can switch between the different generators, OCDB settings, output files storage positions, etc.

The macro SubmitSingleMu.C [2] has been used to configure AliMuonAccEffSub-

mitter for single muon simulation. One can modify the following variables as per the requirement:

- The value of parameter of the p_{T}/y generation input function (GenParamCustomSingleBen.C, available in $ALICE_PHYSICS/PWG/muondep/AccEffTemplates)
- The alignment settings stored in OCDB
- The p_{T} minimum cut for the efficiency task
- The AliPhysics version as per LHC period
- The statistics of the MC sample i.e the no. of generated event per run number and the proportionality factor.

One can run the macro for simulation in different modes:

▶ **LOCALTEST:** This mode is to test that the simulation works properly. It generates the output files in the local directory and run the full simulation locally

▶ **FULL:** This is the actual mode for simulation. In this mode, the files are generated and copied in the specified AliEn directory. It launches the jobs on the CERN grid for a set of runlist.

▶ **TEST:** This mode is the same as the "FULL" mode except for submitting the jobs.

▶ **MERGE:** Once jobs are complete, this mode merges the output file as per run number.

4.2.4 Comparison plots of cluster maps

The cluster maps are produced using the macro SaveQA.C, available on the twiki page [3]. Depending upon the reconstruction parameter of a given period, one has to choose either it is a LowMultiplicity or HighMultiplicity period (pp). Two QA files (provide the full data/MC path) are needed for the input parameter of the macro and one can choose the

directory where to find the final maps in the root file. In the following line, one example of an input path is given.

DATA alien:///alice/data/2017/LHC17c/000270667/muon_calo_pass1/QAresults.root

MC alien:///alice/cern.ch/user/w/wshaikh/Service_Work/LHC17c/270667/AnalysisResults.root

4.2.5 Results

The status maps of the LHC17x (x= c,e,f,h,i,j,k,l,m,o,r) period in data and MC have been produced. The difference in the status map between data and MC is spotted and illustrated in the following figures. This study contributes to the systematic evaluation of tracking efficiency and $A \times \epsilon$.

LHC17c

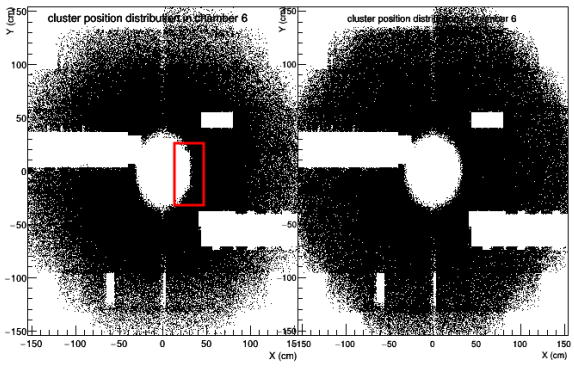

Figure 4.1: The cluster map of chamber 6. This difference found in all runs of the LHC17c period.

For the problem spotted on chamber 7 (4.2), it has been found that chambers 8, 9 and 10 were working fine in this region for those runs. So the impact of this effect is negligible.

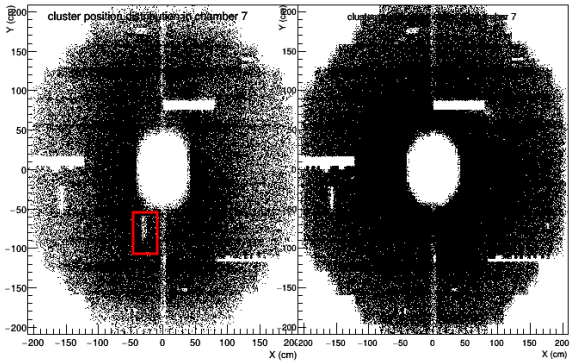

Figure 4.2: The cluster map of chamber 7. This difference found in 270543, 270544, 270565, 270598, 270601 run number of the LHC17c period

LHC17k

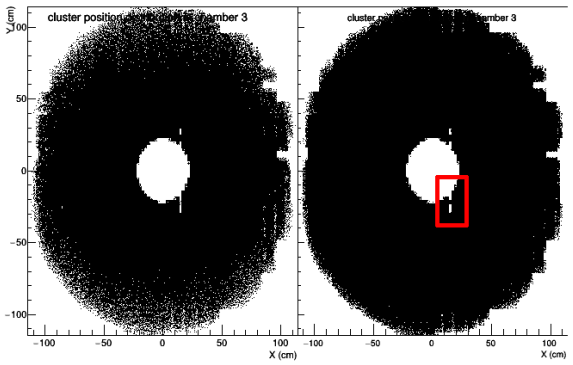

Figure 4.3: The cluster map of chamber 3. This difference found in run number 275073 of the LHC17k period

The discrepancy in chamber 7 as shown in Fig. 4.8, produces a hole in the acceptance that is not reproduced in MC as chamber 8 is also not working in this region. Hence, these 2 runs have been removed from the physics analysis.

The rest of the period's status map can be found in the dedicated Twiki page for "Monitoring the data/MC agreement of tracking chamber status maps" [4].

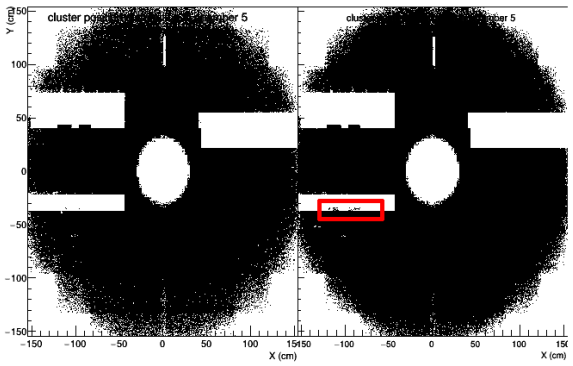

Figure 4.4: The cluster map of chamber 5. This difference found in almost all run of the LHC17k period

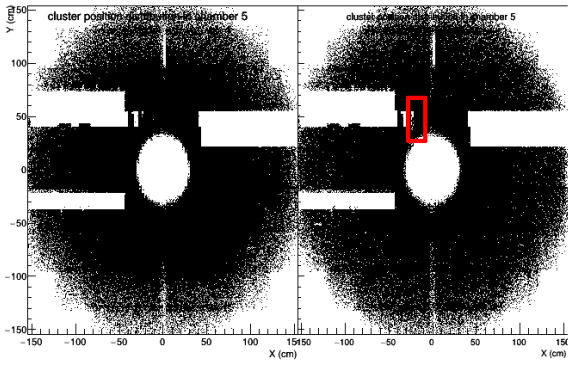

Figure 4.5: The cluster map of chamber 5. This difference found in run number 275979 of the LHC17k period

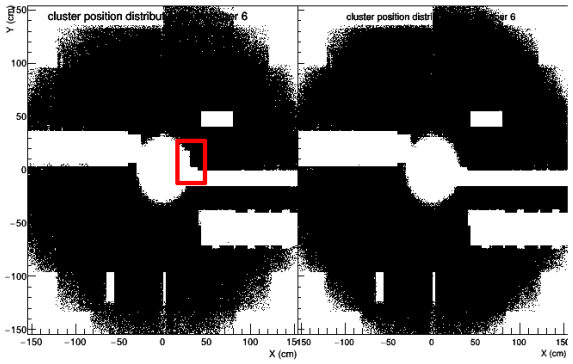

Figure 4.6: The cluster map of chamber 6. This difference found in all run of the LHC17k period

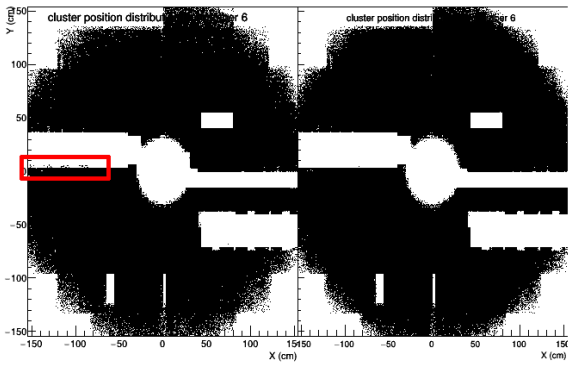

Figure 4.7: The cluster map of chamber 6. This difference found in most of the runs of LHC17k period

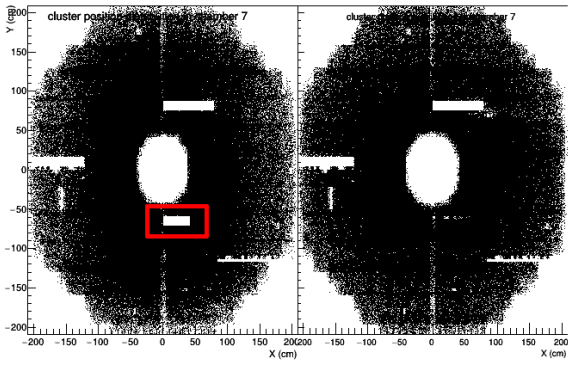

Figure 4.8: The cluster map of chamber 7. This difference found in run number 276307, 276312 of LHC17k period

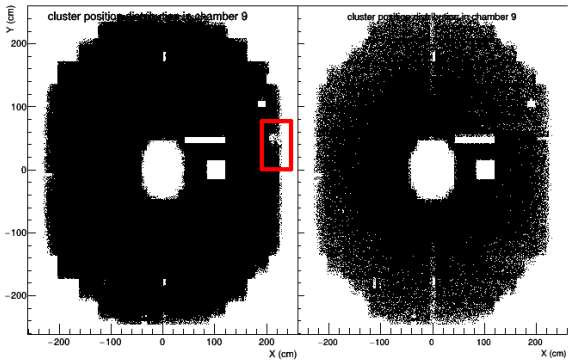

Figure 4.9: The cluster map of chamber 9. This difference found in all run of LHC17k period.

4.3 Data analysis framework

In high energy experiments, the kinematic variables such as transverse momentum (p_{T}), transverse mass (m_{T}), rapidity (y), pseudo-rapidity (η) are frequently used in literature. Under the Lorentz transformation these variables follow the simple transformation rules. In 4-momentum $p^{\mu} = p^{\mu}(E, p_x, p_y, p_z)$ representation, the kinematic variable for a particle of mass m (for that $E^2 = p^2 + m^2$) are defined as follows:

Transverse Momentum

The 3-momentum can be split into the longitudinal (p_z) and the transverse (p_{T}) components where

$$p_{\mathrm{T}} = \sqrt{p_x^2 + p_y^2}$$

Transverse Mass

$$m_{\mathrm{T}} = \sqrt{p_{\mathrm{T}}^2 + m^2}$$

where m is rest mass

Rapidity

For a particle of mass m, total energy E and longitudinal momentum component p_z, the rapidity is defined by,

$$y = \frac{1}{2} ln\left(\frac{E + p_z}{E - p_z}\right) = \frac{1}{2} ln\left(\frac{E + p_z}{m_T}\right) \tag{4.1}$$

Rapidity is a dimensionless quantity and its magnitude can be either positive or

negative. The advantage of using this variable is that the rapidity distribution remain unchanged under a longitudinal Lorentz transformation. Suppose, y_P and y_Q are the rapidity of a particle in two frame of reference P and Q, respectively. Under the Lorentz boost along the z-direction y_P and y_Q are related in the following way:

$$y_P = y_Q + \frac{1}{2} ln\left(\frac{1+\beta}{1-\beta}\right) \tag{4.2}$$

where β = v/c. In the non-relativistic limit, the rapidity is equal to longitudinal velocity β.

Pseudorapidity

To measure the rapidity of a particle one need the information of total energy E and its longitudinal momentum p_z. However, in a many-particle physics experiment, the only measurable quantity is the angle of the detected particle with respect to the beam axis. Let us assume, θ be the emitted angle of a particle relative to the beam axis. Then rapidity can be rewritten as

$$y = \frac{1}{2} ln\left(\frac{E+p_z}{E-p_z}\right) = \frac{1}{2} ln\left(\frac{\sqrt{m^2+p^2}+p\cos\theta}{\sqrt{m^2+p^2}-p\cos\theta}\right)$$

,

At relativistic high energy limit $p >> m$

$$y = \frac{1}{2} ln\left(\frac{p+p\cos\theta}{p-p\cos\theta}\right) = -ln(\tan\theta/2) \equiv \eta$$

where η is called Pseudorapidity. So at high energy,

$$\eta = -ln(\tan\theta/2) \tag{4.3}$$

4.4 Data analysis

During the Run-2 periods, ALICE collected data in various colliding system i.e. pp, p–Pb, Pb–Pb and Xe-Xe at nominal magnetic B = 0.5 T except for the Xe–Xe collision (B = 0.2 T). In this dissertation, we have analysed the data for pp collisions at $\sqrt{s}$ = 5.02 TeV, p–Pb collisions at $\sqrt{s_{\rm NN}}$ = 8.16 TeV and Pb–Pb collisions at $\sqrt{s_{\rm NN}}$ = 5.02 TeV. In the following section the data sample, trigger class, physics selection criteria, track cuts are discussed.

4.4.1 pp collisions at $\sqrt{s}$ = 5.02 TeV

The analysis is based on the data collected in pp collisions of periods LHC17p and LHC17q at the center of mass energy of $\sqrt{s}$ = 5.02 TeV during November 2017. This study is performed on the MUON AOD files produced in `muon_calo_pass1` reconstruction pass for both LHC17p and LHC17q periods. The analyzed dataset is based on the dimuon events recorded in the Muon Spectrometer of ALICE. The CMUL7-B-NOPF-MUFAST (CMUL7) is used as the main trigger class of the dimuon data sample. A physics selection (PS) is applied to remove background events (AliVEvent::kMuonUnlikeLowPt7). The total number of analyzed runs with QA selection and the number of dimuon triggered events used in this analysis are listed in the following Table. 4.1. The Run Condition Table (RCT) based run list is reported in Table. 4.2 [5]

Table 4.1: The statistics of the analyzed pp data.

Period	total no. runs	CMUL7	after PS
LHC17p	38	6845960	6746753
LHC17q	13	12171623	11752119

Table 4.2: The RCT based QA check run list of LHC17p and LHC17q periods.

282008	282016	282021	282025	282031	282050	282051	282078	282098	282099
282118	282119	282120	282122	282123	282126	282127	282146	282147	282206
282224	282227	282229	282230	282247	282302	282304	282305	282306	282307
282309	282312	282313	282314	282340	282341	282342	282343		
282365	282366	282367	282391	282392	282398	282402	282411	282415	282437
282439	282440	282441							

4.4.2 p–Pb collisions at $\sqrt{s_{\rm NN}} = 8.16$ TeV

The data were collected for p–Pb (LHC16r) and Pb–p (LHC16s) beam configurations at the center of mass energy of $\sqrt{s_{\rm NN}} = 8.16$ TeV during November–December of 2016. The present study has been performed on the MUON AOD files produced in `muon_calo_pass2` and `muon_calo_pass3` reconstruction passes of the LHC16r and LHC16s period, respectively. The total number of analyzed runs with QA selection, number of dimuon triggers and luminosity used in this analysis are listed in the following (with physics selection and without pile-up cut) Table. 4.3.

Table 4.3: The statistics of the analyzed p–Pb data.

Beam configuration	Period	pass	total no. runs	CMUL7	Luminosity (μb^{-1})
p–Pb	LHC16r	`muon_calo_pass2`	57	25822700	≈8.4
Pb–p	LHC16s	`muon_calo_pass3`	80	72114339	≈12.8

The detail study on the QA selection can be found at [6]. The QA selected run numbers are reported in Table 4.4

Table 4.4: The QA check selected run list of LHC16r(p–Pb) and LHC16s (Pb–p) periods.

p–Pb									
266318	266316	266312	266305	266304	266300	266299	266296	266235	266234
266208	266197	266196	266193	266190	266189	266187	266117	266086	266085
266084	266081	266076	266074	266034	266025	266023	266022	265841	265840
265797	265795	265792	265789	265788	265787	265785	265756	265754	265746
265744	265742	265741	265740	265714	265713	265709	265701	265700	265698
265697	265696	265694	265691	265607	265596	265594			
Pb–p									
267131	267130	267110	267109	267077	267072	267070	267067	267063	267062
267022	267020	266998	266997	266994	266993	266988	266944	266943	266942
266940	266915	266912	266886	266885	266883	266882	266880	266878	266857
266807	266805	266800	266776	266775	266708	266706	266703	266702	266676
266674	266669	266668	266665	266659	266658	266657	266630	266621	266618
266615	266614	266613	266595	266593	266591	266588	266587	266584	266549
266543	266539	266534	266533	266525	266523	266522	266520	266518	266516
266514	266487	266480	266479	266472	266470	266441	266439	266438	266437

4.4.3 Pb–Pb collisions at $\sqrt{s_{\mathrm{NN}}} = 5.02$ TeV

The analysis is based on the full Run2 Pb–Pb collisions data set, recorded during the 2015 and 2018 campaigns at $\sqrt{s_{\mathrm{NN}}} = 5.02$ TeV. The relevant informations are reported in Table 4.5. The QA reports for MUON can be found in the references [7, 8]. To get the combined data set, we merge the data sets at the tree level.

Table 4.5: The parameters of the analyzed data sets of Pb–Pb runs.

Year	Period	Number of QA runs	pass	AOD	Official MC production
2015	15o	137	muon_calo_pass1	229	16e2(_plus)
2018	18q	130	muon_calo_pass3	225	19a2
	18r	98			

In order to detect the $\Upsilon \to \mu^+\mu^-$ candidates, the unlike-sign dimuon trigger (CMUL7-B-NOPF-MUFAST) has been selected. A physics selection (*AliVEvent::kMuonUnlikeLowPt7*) has been applied to reject the background events such as beam-gas collisions. Finally, we only consider events within the $0-90\%$ centrality class in order to avoid the pileup. The QA selected run numbers are listed in Table 4.6.

Table 4.6: The QA check selected run list of LHC15o, LHC18q and LHC18r periods for the Pb–Pb run.

LHC15o									
246994	246991	246989	246984	246982	246980	246949	246948	246945	246942
246937	246930	246871	246867	246865	246864	246859	246855	246851	246847
246846	246845	246844	246809	246808	246807	246806	246805	246804	246765
246763	246760	246759	246758	246757	246755	246751	246750	246676	246675
246495	246493	246488	246487	246434	246433	246431	246428	246424	246392
246391	246390	246276	246275	246272	246225	246222	246220	246217	246182
246181	246178	246153	246152	246151	246148	246115	246113	246089	246087
246053	246049	246048	246042	246037	246036	246012	246003	246001	245996
245963	245954	245952	245949	245833	245831	245829	245793	245785	245775
245766	245759	245752	245738	245731	245729	245705	245700	245692	245683
245554	245543	245542	245540	245535	245507	245505	245504	245501	245496
245450	245446	245410	245409	245407	245401	245353	245347	245346	245345
245343	245259	245253	245233	245232	245231	245152	245151	245146	245145
245068	245066	245064	244983	244982	244980	244918			
LHC18q									
296623	296622	296619	296618	296616	296615	296553	296552	296551	296550
296549	296548	296547	296516	296514	296511	296510	296509	296472	296433
296424	296423	296420	296419	296414	296383	296381	296380	296379	296378
296377	296376	296312	296309	296307	296304	296303	296280	296279	296273
296270	296269	296247	296246	296244	296243	296242	296241	296198	296197
296196	296195	296194	296192	296191	296143	296142	296135	296134	296133
296132	296128	296123	296068	296066	296065	296063	296062	296061	295947
295945	295943	295942	295941	295937	295936	295913	295910	295909	295908
295881	295863	295861	295860	295859	295856	295855	295854	295831	295829
295826	295825	295822	295819	295818	295816	295791	295788	295786	295763
295762	295759	295758	295755	295754	295753	295725	295723	295719	295718
295717	295716	295714	295677	295676	295675	295673	295671	295668	295667
295666	295665	295615	295612	295589	295588	295587	295586	295585	295584
LHC18r									
297595	297590	297588	297558	297544	297542	297541	297540	297537	297512
297483	297481	297479	297452	297451	297450	297446	297442	297441	297415
297414	297413	297408	297405	297380	297379	297372	297367	297366	297363
297317	297315	297312	297310	297278	297222	297221	297219	297218	297196
297194	297193	297133	297132	297129	297128	297124	297123	297119	297118
297117	297085	297035	297031	297029	296979	296976	296975	296971	296969
296968	296967	296966	296941	296938	296935	296934	296932	296931	296930
296903	296900	296899	296894	296890	296852	296851	296850	296849	296848
296839	296838	296836	296799	296794	296793	296791	296787	296786	296785
296784	296781	296752	296750	296749	296694	296691	296690		

4.4.4 Track selection criteria

In order to improve the purity of data samples, the following offline selection criteria on the single muon and the opposite-sing dimuon tracks have been applied:
single muon selection

- The single muon tracks in the tracking chamber are considered only when they were matched with a track reconstructed in the trigger system above a low p_{T}^{μ} threshold. These cuts remove the light hadrons escaping from the front absorber and also reject a part of low-p_{T} muons coming from mesons (π, K) decay.

- The geometrical acceptance of the ALICE muon spectrometer is $-4.0 < \eta < -2.5$. This selection rejects the tracks that are reconstructed outside this acceptance.

- The transverse position of the muon track at the end of the front absorber (R_{abs}) lies in the range of $17.6 < R_{\mathrm{abs}} < 89.5$ cm. This cut rejects the tracks where multiple scattering is large in the Front Absorber.

- The muon tracks pass through a p$\times$DCA within 6σ selection cut, where p is the total track momentum and the Distance of Closest Approach (DCA) is the transverse distance of the track to the primary vertex. This selection reduces the background coming from beam-gas interaction and the secondary particles produced in the front absorber.

di-muon selection

- The two muons together must have zero charge.

- The transverse momentum of the dimuons is constrained according to $p_{\mathrm{T}} < 15$ GeV/c.

- The dimuon must be in the rapidity range $2.5 < y < 4.0$.

4.4.5 Di-muon invariant mass spectrum

Upsilon, a resonance particle is characterized by a peak in the invariant mass spectrum at given energy that represents the mass of the particle. After applying the aforementioned offline analysis cuts on the AOD file, the invariant mass M_{inv} of the muon pair is computed as:

$$M_{\mathrm{inv}} = \sqrt{2m_{\mu}^2 + 2E_{\mu_A}E_{\mu_B}(1 - cos\theta_{AB})} \tag{4.4}$$

where m_{μ} is the mass of muon, E_{μ_A} and E_{μ_B} represent the energy of the decay muons and θ_{AB} is the angle between the momentum of muons.

An opposite-singe di-muon invariant mass distribution in pp collisions at $\sqrt{s} = 5.02$ TeV in the Upsilon mass region range is shown in Fig. 4.10

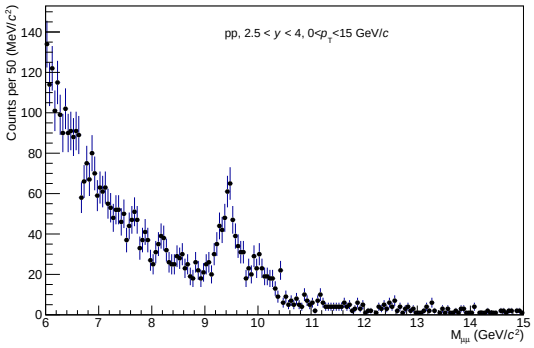

Figure 4.10: The dimuon invariant mass spectrum in pp collisions at $\sqrt{s} = 5.02$ TeV in mass range $6 < M_{\mathrm{inv}} < 15$ GeV/c^2.

4.4.6 Steps of data analysis

The general structure of the data analysis is shown in Fig. 4.11. The analysis task runs over the AOD files to extract the kinematic distribution on a event-by-event basis. The invariant mass spectrum has been generated from the decay muon kinematic distributions. In order to get the yields, the invariant mass spectrum has been fitted with different empirical signal and background functions to extract the Υ counts and corrected with the acceptance and efficiency. The cross section has been evaluated by scaling the yields with luminosity and branching ratio.

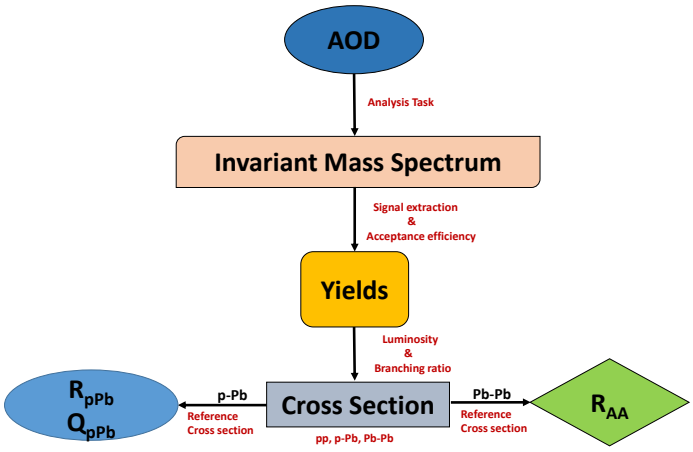

Figure 4.11: The global analysis scheme for the data sets.

Finally the nuclear modification factor in p–Pb and Pb–Pb collisions were evaluated by taking the ratio of the measured cross section to the reference cross section value extract from pp collisions at the same center of mass energy.

Bibliography

[1] M. Tarhini, *Measurement of Z-boson and J/ψ Production in p-Pb and Pb-Pb Collisions at $\sqrt{s_{\mathrm{NN}}}$ = 5.02 TeV with ALICE at the LHC*. Theses, Université Paris-Saclay, June, 2017.

[2] "Submitsinglemu.c."
https://twiki.cern.ch/twiki/pub/ALICE/MuonRejectList/SubmitSingleMu.C.

[3] "Saveqa.c."
https://twiki.cern.ch/twiki/pub/ALICE/MuonRejectList/SaveQA.C.

[4] "Monitoring the data/mc agreement of tracking chamber status maps."
https://twiki.cern.ch/twiki/bin/viewauth/ALICE/MuonRejectList.

[5] "Qa selection pp."
https://twiki.cern.ch/twiki/bin/viewauth/ALICE/MuonppQA2017.

[6] "Qa selection p–pb."
https://twiki.cern.ch/twiki/bin/view/ALICE/MuonpPbQA2016.

[7] "Qa selection pb–pb, 2015."
https://twiki.cern.ch/twiki/bin/view/ALICE/MuonPbPbQA2015.

[8] "Qa selection pb–pb, 2018."
https://twiki.cern.ch/twiki/bin/view/ALICE/MuonPbPbQA2018.

CHAPTER 5

Υ production in pp collisions at $\sqrt{s} = 5.02$ TeV

In this chapter, the analysis of inclusive Υ production at forward rapidity in pp collision at $\sqrt{s} = 5.02$ TeV has been presented. The main motivation of this analysis is to use these results as the input of the interpolation procedure for pp reference and normalization of Υ(nS) $R_{\rm AA}$ analysis at $\sqrt{s_{\rm NN}} = 5.02$ TeV.

5.1 Data sample, event and track selection

The data sample, trigger class, event and track selection criteria have been described in detail in chapter 4.

5.2 Luminosity

To compute the cross section of a process, the integrated luminosity of the data sample must be known. The luminosity is estimated using the following expression, with T0

trigger as the reference.

$$\mathcal{L}_{int} = \sum_{run} N^{\mathrm{L2a}}_{CMUL} \times \frac{N^{\mathrm{L0b}}_{CTVX} \times purity_{CTVX} \times pile-up_{CTVX}}{N^{\mathrm{L0b}}_{CMUL}} \times \frac{1}{\sigma_{\mathrm{T0}}} \tag{5.1}$$

The data periods are the same as the one used for J/ψ analysis. Therefore the integrated luminosity has been adopted from J/ψ analysis which is 1230 $\pm$ 22 nb^{-1} [1]. Although the analyses are based on the same runs, the luminosity has to be normalized by the number of CMUL events after the physics selection:

$$\mathcal{L}^{\Upsilon}_{int} = \mathcal{L}^{\mathrm{J}/\psi}_{int} \times \frac{N^{\Upsilon}_{CMUL,PS}}{N^{\mathrm{J}/\psi}_{CMUL,PS}} = 1229 \pm 22 \text{ nb}^{-1} \tag{5.2}$$

5.3 Signal extraction

The data collected during the two periods, LHC17p and LHC17q have sufficient statistics that allow a detailed study of Υ production cross-section as a function of rapidity and traverse momentum. The data sample have been analyzed in two rapidity windows ($2.5 < y < 3.25$ and $3.25 < y < 4.0$) and 4 bins of p_{T} in range $0 < p_{\mathrm{T}} < 15$ GeV/c for Υ(1S). For the higher states of Υ, we have analyzed the data sample integrated over p_{T} and rapidity.

5.3.1 Invariant mass fit procedure

The number of Υ(nS) reconstructed by the muon spectrometer is calculated by fitting the invariant mass spectrum of the unlike-sign muon pairs. For the three Υ states, three Extended Crystal Ball (CB2) functions and a sum of two exponential (DE) functions for continuum background have been used. The details for CB2 and DE can be found in Appendix A.

Due to the low signal-over-background ratio, some signal parameters are constrained or fixed in the fit procedure. The details of the fit procedure are described below:

- Υ(nS) signal shapes are parametrized by CB2 functions.
- the tails in CB2 functions are fixed and are the same for all 3 resonances (see 5.3.2 for details);
- Υ(1S) mass ($m_{\Upsilon(1S)}$) and width ($\sigma_{\Upsilon(1S)}$) are let free;
- the fit has been performed in mass ranges [6-14] GeV/c^2);
- Υ(nS) (n=2,3) mass and width are constrained by Υ(1S) parameters as following

$$m_{\Upsilon(nS)} = m_{\Upsilon(1S)} + (m^{\rm PDG}_{\Upsilon(nS)} - m^{\rm PDG}_{\Upsilon(1S)}), \quad \sigma_{\Upsilon(nS)} = \sigma_{\Upsilon(1S)} \times \frac{\sigma^{\rm MC}_{\Upsilon(nS)}}{\sigma^{\rm MC}_{\Upsilon(1S)}} \tag{5.3}$$

  with the PDG mass values from reference [2];
- the background parameters are kept free;
- maximum log-likelihood fit method has been used.

Fig. 5.1 shows a typical fit to the invariant mass spectrum, with VWG for the background shape and CB2 as signal function. The red solid line represents the combined fit shape and the consecutive three peaks stand for Υ(1S), Υ(2S) and Υ(3S), respectively.

5.3.2 The study of signal extraction systematic

The different tests have been performed to extract the Υ(nS) counts and its associated systematic uncertainty:

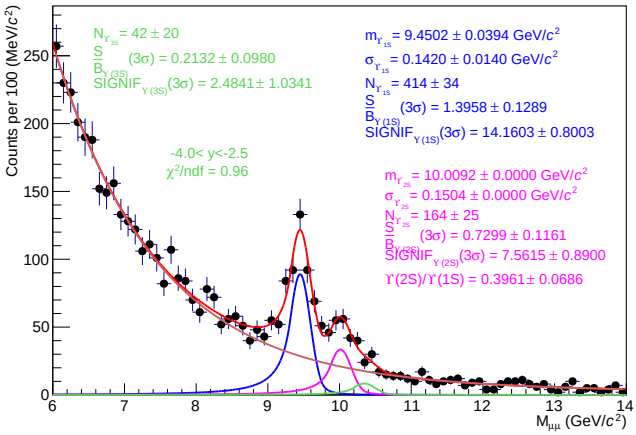

Figure 5.1: A typical fit to the dimuon invariant mass distribution in pp collisions at $\sqrt{s} = 5.02$ TeV. The distribution is fitted with the sum of VWG to characterize the background and three CB2 functions to characterize there Υ states.

Signal shape

The Υ peaks have was fitted with NA60 function also. The associated systematic due to these two signal functions are negligible. Hence, we have not considered the NA60 function for signal extraction systematic.

Fitting mass range

Two fitting mass ranges around the Υ mass have been considered for the systematic estimation,

- $6 < M < 14$ GeV/c^2
- $7 < M < 13$ GeV/c

Width scaling

The Υ(nS) peaks overlap each other due to the mass resolution of the muon spectrometer. Therefore, the higher state i.e Υ(2S) and Υ(3S) widths have to be scaled to the Υ(1S)

one as mentioned 5.3.1. For this constrain, we have assigned a systematic by varying the scaled ratio.

- "simple" width scaling: $\sigma_{\Upsilon(nS)} = \sigma_{\Upsilon(1S)} \times \frac{\sigma^{\rm MC}_{\Upsilon(nS)}}{\sigma^{\rm MC}_{\Upsilon(1S)}}$ (*reference* fit model)
- "no" width scaling: $\sigma_{\Upsilon(nS)} = \sigma_{\Upsilon(1S)}$
- "double" width scaling: $\sigma_{\Upsilon(nS)} = \sigma_{\Upsilon(1S)} \times (2\ \frac{\sigma^{\rm MC}_{\Upsilon(nS)}}{\sigma^{\rm MC}_{\Upsilon(1S)}} - 1)$

with n = 2, 3 and $\sigma_{\Upsilon(1S)}$ is free in the fit.

We have also checked by varying 6% of the default width for 2S and 3S states and no significant change has been found with the aforementioned process.

Background functions

3 functions have been used to fit the background continuum:

- the sum of two exponentials (DE)
- a single exponential (Expo)
- a power law (Pow)

This variation leads to a contribution of 6 to 11% to the systematic uncertainty. Thus, the choice of the background function is the most important source of signal extraction systematic.

Tail parameter

As already mentioned in 5.3.1, the tails of signal functions can not be let free in the fit due to its low signal over background ratio. By default, these parameters are fixed to

the ones extracted from 5.02 TeV MC signal shapes, represented in Fig. 5.2. The values for the different states are found to be similar. So the Υ(nS) signal tails are fixed to the Υ(1S) tails.

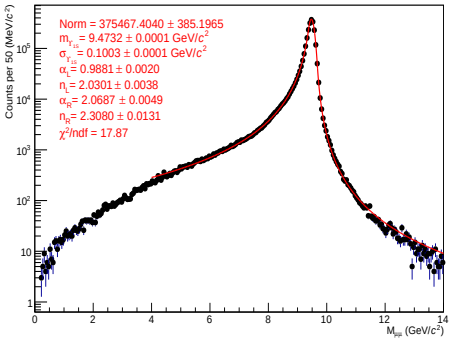

(a) Υ(1S) signal shape

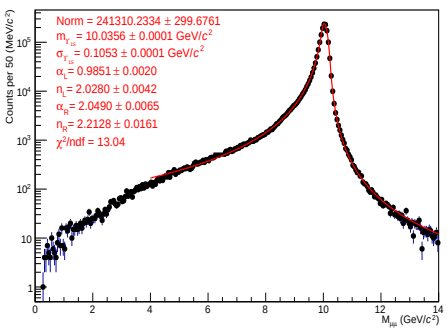

(b) Υ(2S) signal shape

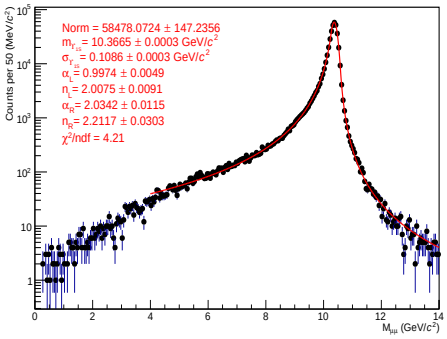

(c) Υ(3S) signal shape

Figure 5.2: The Υ(nS) signal shapes from pure MC simulation fitted with CB2 distribution.

For an alternative tail set, the data-driven tails have been considered. Due to the low statistics, the tails can not be extracted from pp 5.02 TeV data. Thus, it has been decided to use the higher statistics of the 13 TeV pp data [3].

The extracted data-driven tails and the corresponding covariance matrix have been used to generate several sets of parameters, as shown in Fig. 5.3. Then the signal extraction is performed on these sets with the reference fit model described above. The corresponding results are shown in Fig. 5.4. The associated systematic, estimated as one RMS of the signal extraction distributions due to the tail parameters variation are: 4.7%, 6.1% and 14.5% for Υ(1S), Υ(2S) and Υ(3S), respectively.

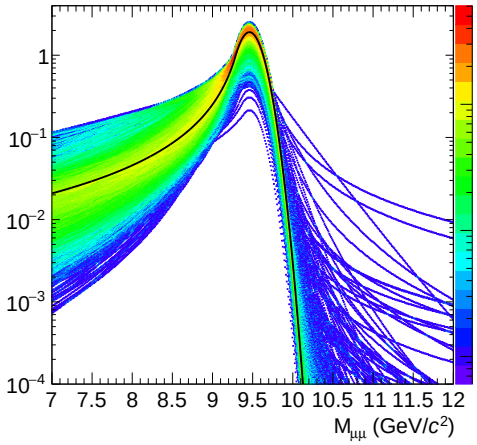

Figure 5.3: The distribution of tails generated from 13 TeV analysis [3].

The statistical and systematic uncertainties in signal extraction are evaluated as follow:

$$\sigma_{stat} = \frac{\sum_i^n \sigma_i}{n}, \quad \sigma_{syst} = \sqrt{\frac{\sum_i^n (x_i - \mu)^2}{n-1}} \tag{5.4}$$

where x_i is a test result, σ_i is the corresponding statistical uncertainty determined by the fit, n the number of tests and μ the average of the test results. In addition, the percentage of signal extraction systematic due to tail parameter variation (see 5.3.2) are added in quadrature to get the final systematic uncertainty.

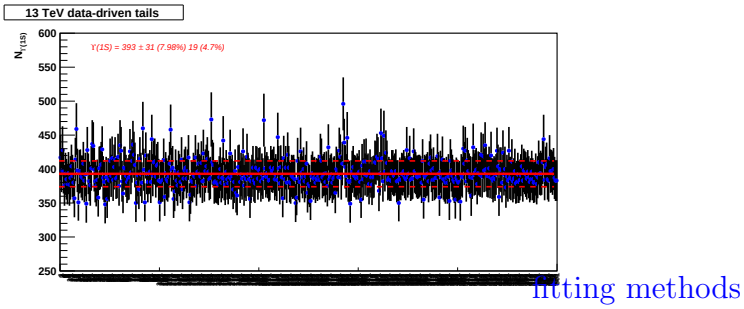

(a) Υ(1S)

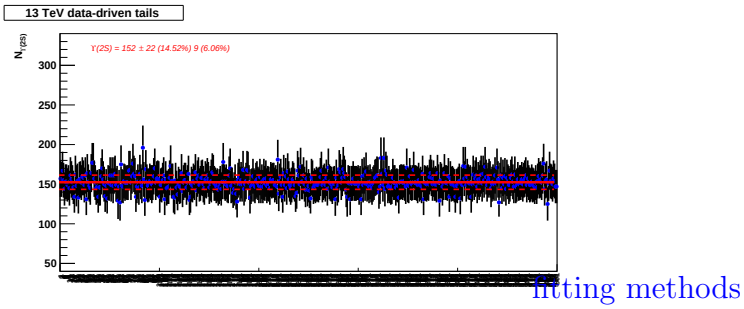

(b) Υ(2S)

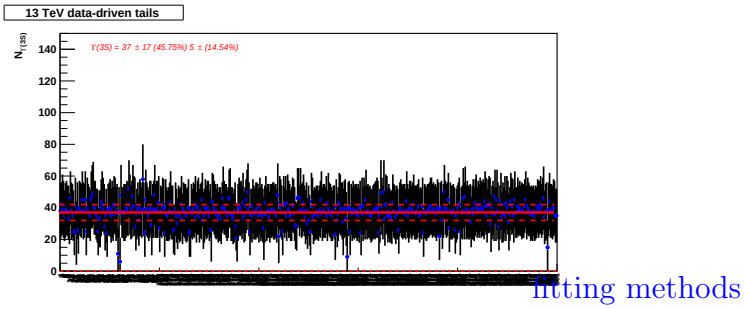

(c) Υ(3S)

Figure 5.4: The signal extraction systematic (Signal function: CB2, Background function: DE, range: [6,14]) for data driven tail, generated from pp 13 TeV. In all above figures, X-axis represents the fitting method with different sets of tail and Y-axis represents the Υ(nS) count. The solid red line shows the mean value averaged over all trials. The dashed lines show the standard deviation.

5.3.3 Signal extraction results

The systematic uncertainty is evaluated by combining all the sources reported in 5.3.2 for a total of 18 tests. The covariance matrix of each test must have converged with a good χ^2/NDF (< 2). The systematic from the tail parameters have been included separately.

Integrated

The signal extraction systematics integrated over p_{T} and y are shown in Fig. 5.5 and the results are reported in the Table 5.1.

Table 5.1: The number of Υ(nS) from data (integrated over p_{T} and y).

particle	$N_{\Upsilon} \pm$ stat $\pm$ sys
Υ(1S)	401$\pm$ 34 $\pm$ 26
Υ(2S)	153$\pm$ 22 $\pm$ 11
Υ(3S)	38 $\pm$ 17 $\pm$ 7

Differential

For differential study, we have divided the data sample in 4 p_{T} ($0 < p_{\mathrm{T}} < 2$, $2 < p_{\mathrm{T}} < 4$, $4 < p_{\mathrm{T}} < 6$, $6 < p_{\mathrm{T}} < 15$ GeV/c) and 5 rapidity ($-4 < y < -3.5$, $-3.5 < y < -3$, $-3 < y < -2.5$,$-4.0 < y < -3.25$, $-3.25 < y < -2.5$) bins.

In the differential bins, Υ(1S) width fluctuation is observed. It has been checked that fixing the width of Υ(1S) or keeping it free in the fit procedure gives the same $N_{\Upsilon(1S)}$ within uncertainties. To avoid the extra systematic contribution, it has been decided to keep the Υ(1S) width free in the fit procedure.

The tail parameters are extracted from the MC signal shape in the differential bins under study. The fit procedure is identical to the integrated case.

The invariant mass fit and signal systematics in 4 p_{T} differential bins are shown in Fig. 5.6 and in Fig. 5.7 respectively. The corresponding number of Υ(1S) are reported in Table 5.2.

Table 5.2: The number of Υ(1S) in p_{T} bins

p_{T} (in GeV/c)	$N_{\Upsilon} \pm stat \pm syst$
$[0-2]$	$56 \pm 13 \pm 4$
$[2-4]$	$141 \pm 20 \pm 9$
$[4-6]$	$119 \pm 17 \pm 7$
$[6-15]$	$86 \pm 14 \pm 5$
sum	$402 \pm 32 \pm 13$

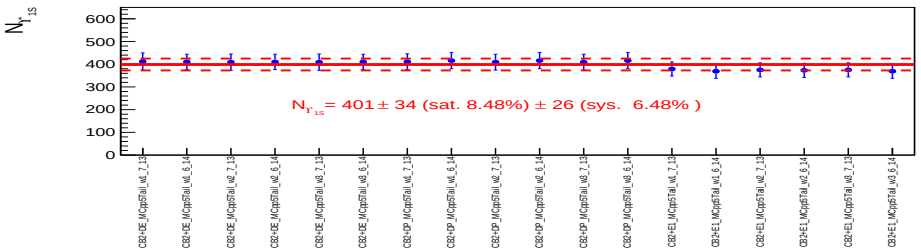

(a) Signal systematic of Υ(1S)

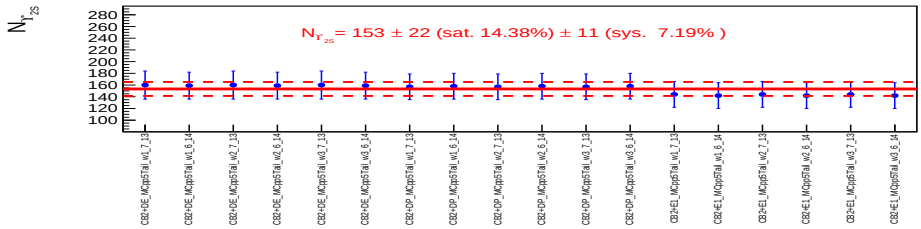

(b) Signal systematic of Υ(2S)

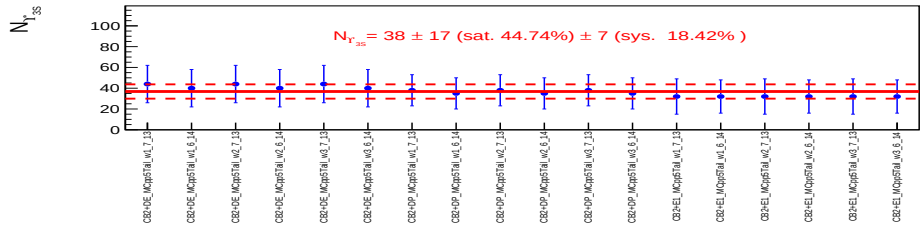

(c) Signal systematic of Υ(3S)

Figure 5.5: The distribution of the extracted number of Υ(nS) integrated over p_{T} and y as a function of the fitting methods.

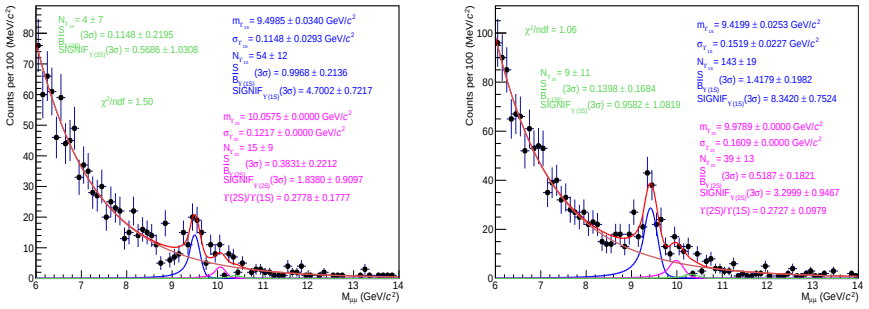

(a) $0 < p_{\mathrm{T}} < 2$ GeV/c (b) $2 < p_{\mathrm{T}} < 4$ GeV/c

(c) $4 < p_{\mathrm{T}} < 6$ GeV/c (d) $6 < p_{\mathrm{T}} < 15$ GeV/c

Figure 5.6: The fit to the dimuon invariant mass spectrum of Υ in different p_{T} bins.

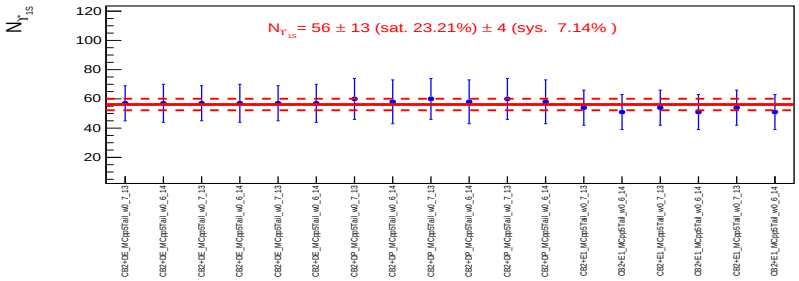

(a) $0 < p_{\mathrm{T}} < 2$ GeV/c

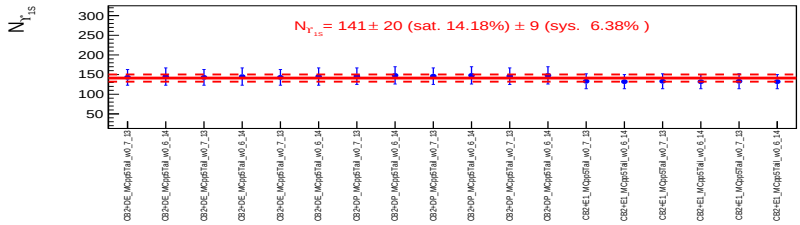

(b) $2 < p_{\mathrm{T}} < 4$ GeV/c

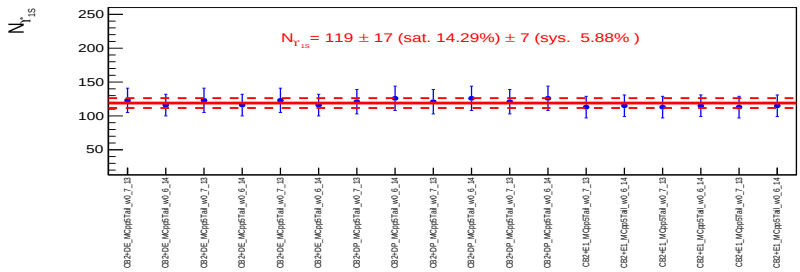

(c) $4 < p_{\mathrm{T}} < 6$ GeV/c

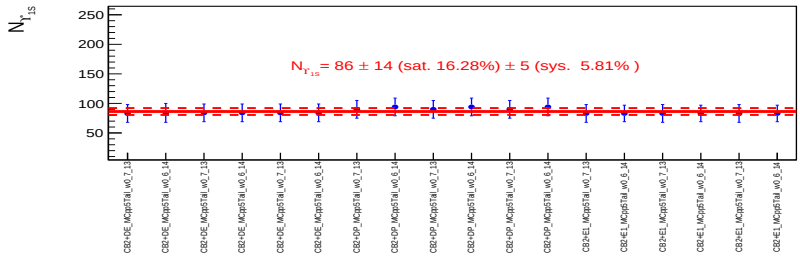

(d) $6 < p_{\mathrm{T}} < 15$ GeV/c

Figure 5.7: The distribution of extracted number of Υ(1S) in p_{T} bins as function of fitting methods.

The invariant mass fit and signal systematics in 3 rapidity bins are shown in Fig. 5.8 and in Fig. 5.9, respectively. The corresponding number of $\Upsilon(1S)$ are reported in Table 5.3.

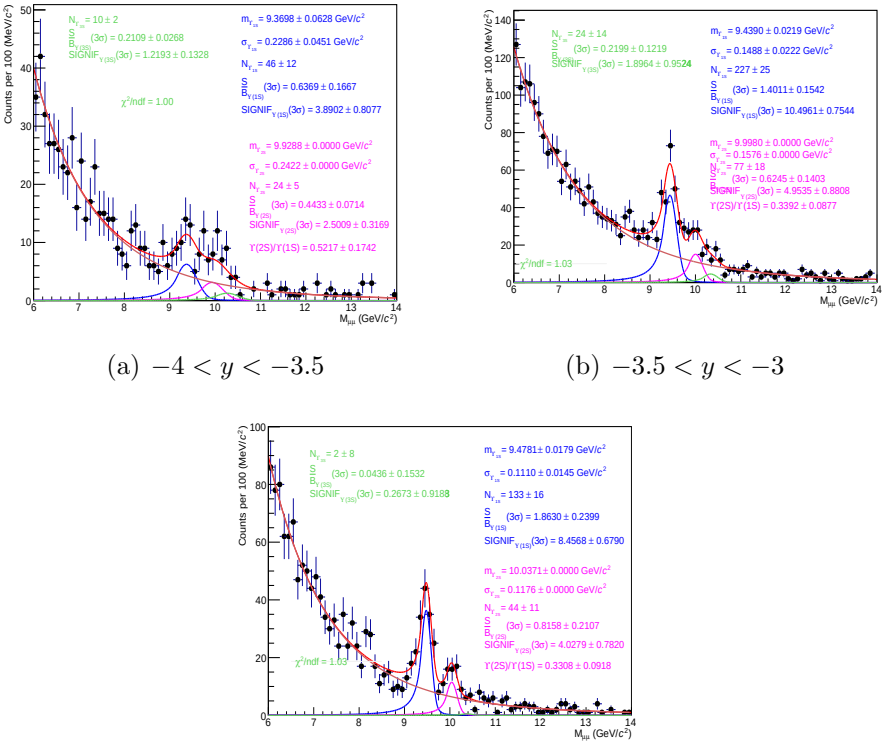

(a) $-4 < y < -3.5$ (b) $-3.5 < y < -3$

(c) $-3 < y < -2.5$

Figure 5.8: The fit to the dimuon invariant mass spectrum of Υ in different y bins.

Table 5.3: The number of $\Upsilon(1S)$ in y bins.

y	$N_\Upsilon \pm stat \pm syst$
$[-4, -3.5]$	$48 \pm 13 \pm 4$
$[-3.5, -3]$	$226 \pm 29 \pm 16$
$[-3, -2.5]$	$133 \pm 18 \pm 8$
sum	$407 \pm 37 \pm 18$

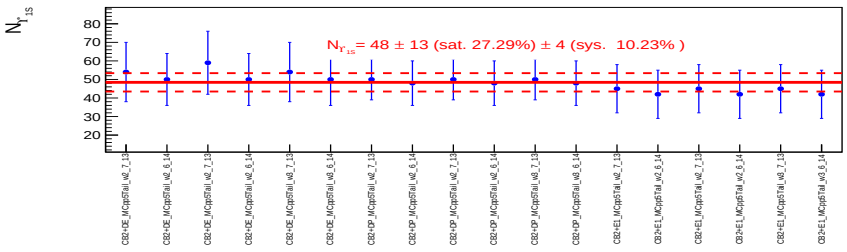

(a) $-4 < y < -3.5$

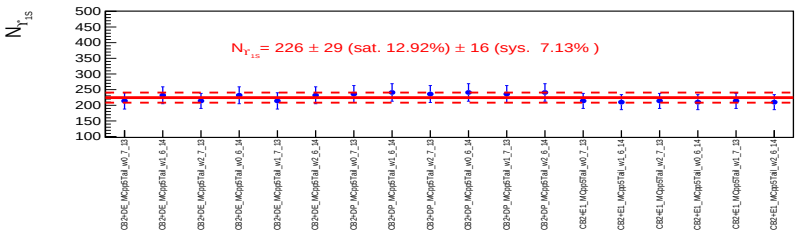

(b) $-3.5 < y < -3$

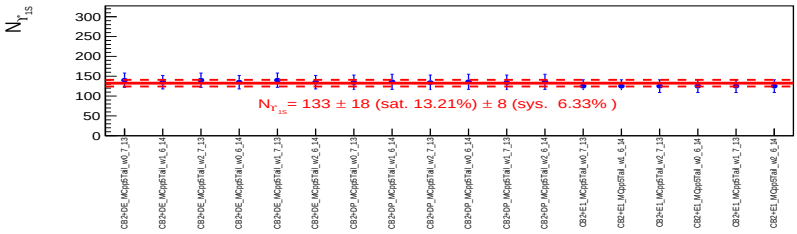

(c) $-3 < y < -2.5$

Figure 5.9: The distribution of extracted number of Υ(1S) in three y bins as function of fitting methods.

It may be noted that for the rapidity interval of $-4 < y < -3.5$, the $\Upsilon(1S)$ significance is small and has a large fluctuation in the extracted numbers among the different fitting configurations. It suggests that this particular bin does not contain enough statistics to be considered.

So a different rapidity binning ($4.0 < y < 3.25$ and $3.25 < y < 2.50$) has been considered. The invariant mass fits are shown in Fig. 5.10. In this case, the statistics is adequate leading to satisfactory statistical significance.

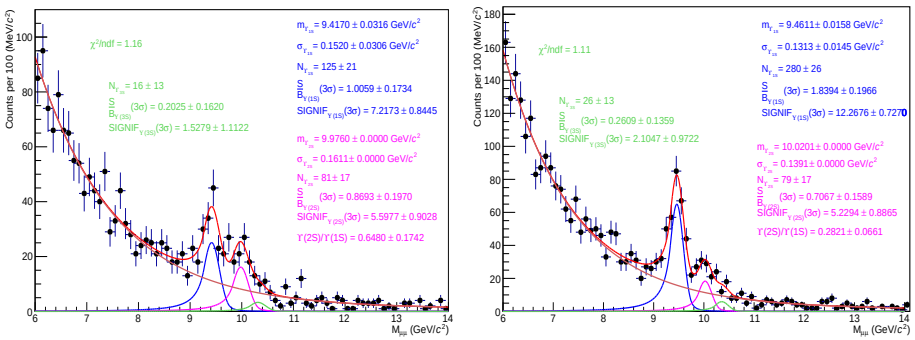

(a) $-4.0 < y < -3.25$ (b) $-3.25 < y < -2.5$

Figure 5.10: The fit to the dimuon invariant mass spectrum of Υ in different y bins (second splitting).

The $\Upsilon(1S)$ signal systematics are shown in Fig. 5.11 and the corresponding number of $\Upsilon(1S)$ are reported in Table 5.4.

Table 5.4: The number of $\Upsilon(1S)$ in y bins (second splitting).

y	$N_\Upsilon \pm stat \pm syst$
$[-4, -3.25]$	$121 \pm 20 \pm 9$
$[-3.25, -2.5]$	$273 \pm 27 \pm 17$
sum	$394 \pm 34 \pm 19$

5.4 Detector acceptance and efficiency correction

The extracted Υ signal need to be corrected by the acceptance times efficiency ($A \times \epsilon$) of the Muon Spectrometer in order to get the corrected yields for the individual states. To

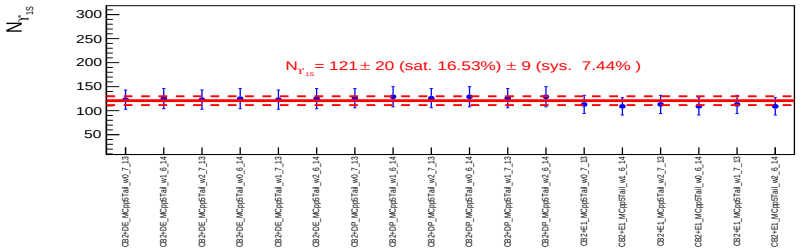

(a) $-4.0 < y < -3.25$

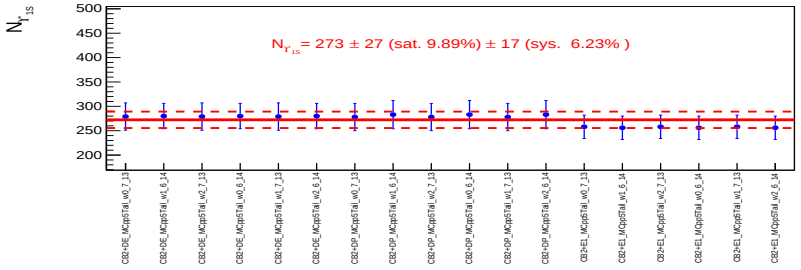

(b) $-3.25 < y < -2.5$

Figure 5.11: The distribution of extracted number of Υ(1S) in two y bins (second splitting) as function of fitting methods.

evaluate the $A \times \epsilon$ of muon spectrometer, the Monte Carlo (MC) simulation method has been used. The MC simulations have been performed by mimicking the ideal detector conditions during the data taking on run-by-run basis.

5.4.1 MC simulation

In the first step of the simulation procedure, rapidity and traverse momentum distributions of Υ based on LHC, CDF and RICH data [4] have been used, assuming no polarization, as suggested by ALICE and LHCb measurements at LHC on quarkonium polarization [5–7]. The Υ decays to $\mu^+\mu^-$ is implemented using EVTGEN [8] and PHOTOS [9] to allow for the radiative photons emission. The particle transport and the detector response are handled via GEANT3 [10]. Using the GEANT4 [11] configuration, an independent test of the detector simulation has also been performed. The results

from both GEANT3 and GEANT4 are compatible with a maximum deviation of 2%.

The $A \times \epsilon$ corrections have been applied to the analyzed data set to obtain the Υ(1S) p_{T} and y realistic distributions in pp collisions at $\sqrt{s} = 5.02$ TeV. An iterative procedure has been performed to tune the Υ input p_{T} and y MC distributions using the corrected distributions. The 1$^{\mathrm{st}}$ MC production can be found in LHC18c5a period (/alice/sim/2018/LHC18c5a). We have followed the following steps to get final set. The final MC set can be found /alice/cern.ch/user/j/jcastill/pp17wrk/UpsiMC_LHC17pq/ResultsUpsiAlipp5DataDriven.

- step1: 1$^{\mathrm{st}}$ set of MC simulation for Υ(nS) are generated using parameterized p_{T} and y input distributions.
- step2: Next the number of Υ(1S) extracted as a function of p_{T}, y and corrected by the $A \times \epsilon$ calculated in step 1. These yields ($N_{\Upsilon(1\mathrm{S})}/A \times \epsilon$) are fitted with the following functions:

$$f(p_{\mathrm{T}}) = a \times \frac{p_{\mathrm{T}}}{(b + {p_{\mathrm{T}}}^{c})^{d}}$$

$$f(y) = a + b \times y * y$$

- step3: Next, $f(p_{\mathrm{T}})$ and $f(y)$ are used as input shape of new Υ(1S) MC simulation.
- step4: iteration process has been repeated from step 2 onwards until the input shapes are very close to the Υ(1S) yields distributions shown in Fig. 5.12.

Due to the limited statistics of Υ(2S) and Υ(3S) in pp data at $\sqrt{s_{\mathrm{NN}}} = 5.02$ TeV, the MC input shapes are assumed to be the same as Υ(1S).

Acceptance times efficiency correction is defined as :

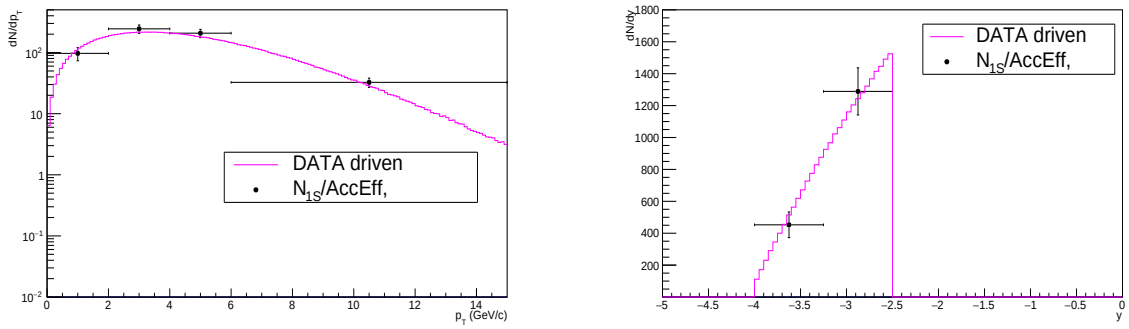

(a) p_{T} (b) y

Figure 5.12: The data points plotted on the MC input shape.

$$A \times \epsilon = \frac{N_{\mathrm{reconstructed}}}{N_{\mathrm{generated}}}$$

where $N_{\mathrm{reconstructed}}$ is the number of reconstructed Υ and $N_{\mathrm{generated}}$ is the generated Υ in same kinematic domain.

For the evaluation of $A \times \epsilon$, we have used the same run numbers and analysis cuts as used to analyze the data. The integrated $A \times \epsilon$ of the different Υ resonances are shown in Fig. 5.13 and the values are reported in Tab. 5.5. The acceptance times efficiency decreases at the end of the LHC17q period due to inefficiency in the tracking chambers caused by HV trips in this high-rate period.

Table 5.5: The value of integrated $A \times \epsilon$ of Υ(nS).

particle	$A \times \epsilon \pm stat.$ (%)
Υ(1S)	28.93 $\pm$ 0.05
Υ(2S)	28.79 $\pm$ 0.06
Υ(3S)	28.95 $\pm$ 0.11

The $A \times \epsilon$ of Υ(1S) as function of p_{T} and y are shown in Fig. 5.14 and the values are reported in Tab. 5.6.

Table 5.6: The value of $A \times \epsilon$ as a function of p_{T} (left) and rapidity (right) for Υ(1S).

p_{T} (GeV/c)	$A \times \epsilon \pm stat.$ (%)
$[0-2]$	28.93 ± 0.05
$[2-4]$	28.82 ± 0.03
$[4-6]$	28.64 ± 0.04
$[6-15]$	29.34 ± 0.06

y	$A \times \epsilon \pm stat.$ (%)
$[4-3.25]$	34.16 ± 0.04
$[3.25-2.5]$	26.79 ± 0.04

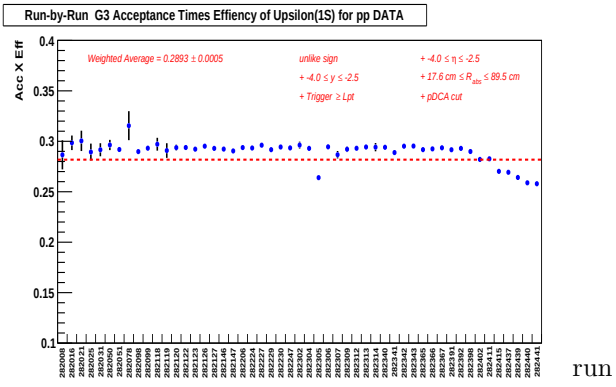

(a) $A \times \epsilon$ of Υ(1S)

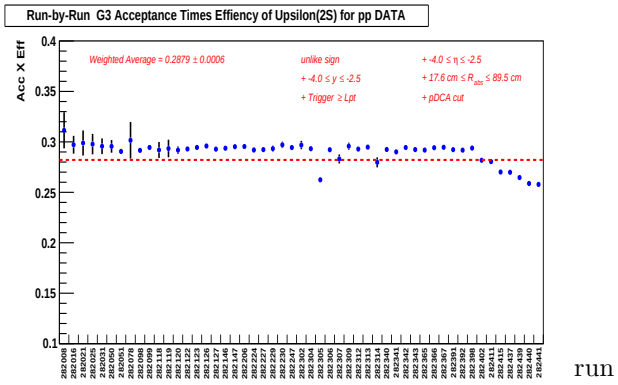

(b) $A \times \epsilon$ of Υ(2S)

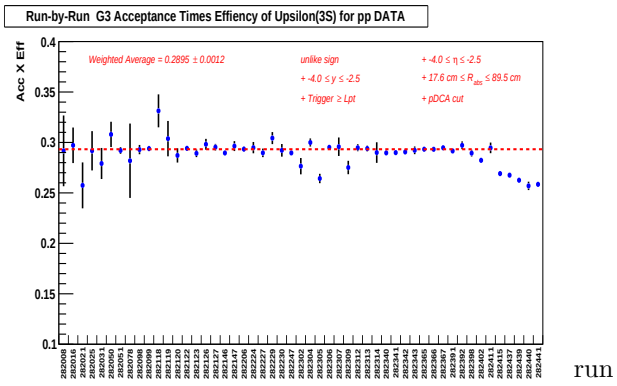

(c) $A \times \epsilon$ of Υ(3S)

Figure 5.13: The $A \times \epsilon$ for Υ as function of run numbers in pp collision at $\sqrt{s}$= 5.02 TeV.

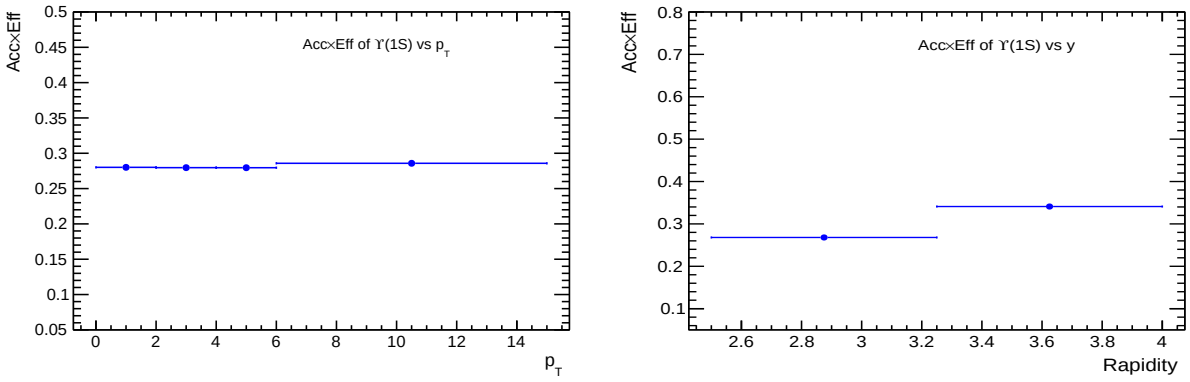

(a) $A \times \epsilon$ of Υ(1S) vs p_{T}

(b) $A \times \epsilon$ of Υ(1S) vs y

Figure 5.14: The $A \times \epsilon$ for Υ(1S) as function p_{T} and y.

5.5 Systematic uncertainties

Several sources contribute to the systematic uncertainty on the Υ production cross section, which have been discussed in the following sections.

5.5.1 Signal extraction

The estimation of the signal extraction systematic has been discussed in 5.3.2 and the corresponding results can be found in 5.3.3.

5.5.2 Luminosity

The main two sources of systematic uncertainty on the luminosity are the visible cross-section uncertainty calculated with the T0 detector via the Van der Meer scan technique [12] and the uncertainty on the normalization factor between the number of minimum bias events and the number of triggered events. The latter was evaluated by using minimum bias triggers issued either the TO or V0 detector. For both cases (To or V0), the results are in agreement. The dominant part of uncertainty on the luminosity determination comes from the uncertainty on the visible cross section, which is 1.8%. This uncertainty is correlated as a function of p_{T} and y and also correlated among all the higher states.

5.5.3 MC input

The systematic uncertainty on the Υ MC p_{T} and y input distributions have two sources:

• The p_{T} – rapidity correlations on input MC shape, which are not considered in MC simulations.

• The statistical uncertainties on the data points used to tune these input distributions.

The multi-differential study in not possible due to the lower statistic in pp 5.02 TeV Upsilon measurements. To estimate the systematic uncertainty on the $p_{\mathrm{T}} - y$ correlation, the double-differential p_{T} and y shapes are used from the LHCb Upsilon measurements at $\sqrt{s}$= 13 TeV [13]. For each p_{T}/y shape, the MC calculations are reweighed by the ratio of differential shape over the integrated. The input shape in different p_{T} (y) interval as function of y (p_{T}) are shown in Fig. 5.15.

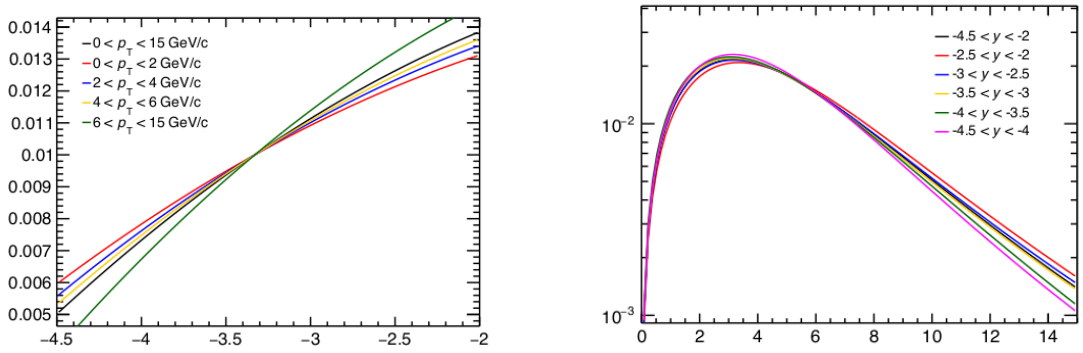

(a) y shape in different p_{T} interval

(b) p_{T} shape in different y interval

Figure 5.15: The input MC shapes used for the evaluation of the $A \times \epsilon$ systematics due to the p_{T}–y correlations.

For each combination of p_{T} and y weights (20 combinations), the $A \times \epsilon$ has been evaluated and the RMS of the value has been considered as systematic. The systematic uncertainties, integrated or differential in rapidity and p_{T} due to correlation have been found to be less than 1%. The corresponding values are reported in Table 5.7.

The MC input systematic uncertainties related to the statistical uncertainty on the yields have been evaluated by randomly moving them with gaussian smearing within their uncertainties. The procedure was repeated 50 times and each time the distributions have been fitted. These shapes together with the existing input shape are shown in Fig. 5.16.

Each new input shape has been used to re-weight the MC and calculate a new $A \times \epsilon$. The RMS of these corrections is taken as the systematic uncertainty.

Table 5.7: The systematic uncertainties (in %) on MC p_{T} and y correlations.

Υ(1S)		
Integrated		0.76
p_{T} (GeV/c)	[0,2]	0.53
	[2,4]	0.84
	[4,6]	0.51
	[6,15]	0.93
rapidity	[-3.25,-2.5]	0.97
	[-4.0,-3.25]	0.84
Υ(2S)		
Integrated		0.76
Υ(3S)		
Integrated		0.76

5.5.4 Tracking efficiency

The tracking systematic is $\sim$ 1% at single muon level, thus $\sim$ 2% for dimuons. This contribution is assumed to be uncorrelated in p_{T} and y and also for all Υ state [1].

5.5.5 Trigger efficiency

The two sources of systematic uncertainties are:

(a) the trigger response function systematic due to the difference in the shape of this function between data and MC

(b) uncertainties on the efficiency maps of the trigger chamber.

Systematic due to Trigger Response function

The response function is defined as:

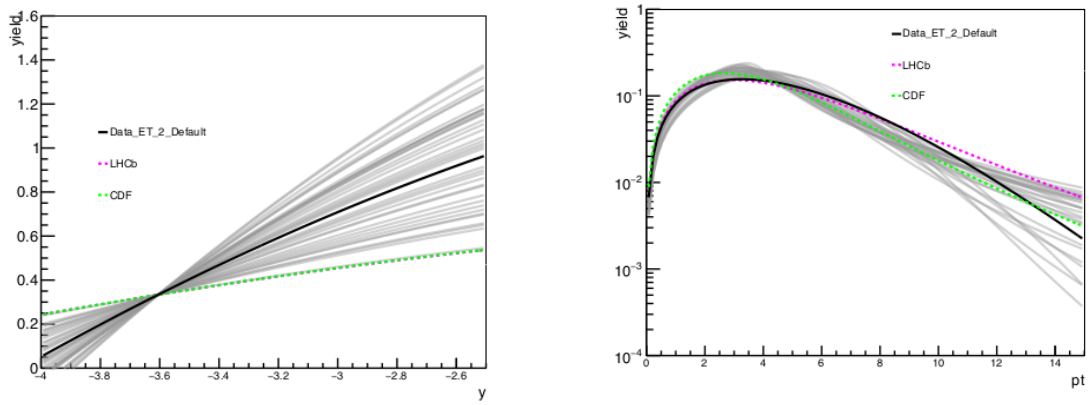

(a) y (b) p_{T}

Figure 5.16: The input MC shapes used for the evaluation of the $A \times \epsilon$ systematic due to the statistical uncertainties on data points.

$$RF = \frac{L_{pT}}{A_{pT}}$$

where:

L_{pT} : $GetMatchTrigger() >= 2$ (1.0 GeV/c single muon p_T cut)

A_{pT} : $GetMatchTrigger() >= 1$ (0.5 GeV/c single muon p_T cut)

The usual procedure used to extract the systematic is as follows:

- Evalute RF in DATA and MC. Then fit it with the following function:

$$F(p_{\mathrm{T}}) = a + b \times \left(1 + erf(\frac{p_{\mathrm{T}} - p_{\mathrm{T}}^{\mathrm{mean}}}{2\sigma})\right) \tag{5.5}$$

- Select muons matching the A_{pT} trigger in Υ MC simulations and weight by the RF_{MC} or RF_{DATA}

- Extract the number of Upsilon in two cases and take the relative difference as systematic.

Table 5.8: The MC input systematic uncertainties (in %) due to statistical errors on data points.

Υ(1S)		
Integrated		1.50
p_{T} (GeV/c)	[0,2]	1.57
	[2,4]	1.47
	[4,6]	1.38
	[6,15]	1.35
rapidity	[-3.25,-2.5]	2.00
	[-4.0,-3.25]	3.42
Υ(2S)		
Integrated		1.50
Υ(3S)		
Integrated		1.50

But for the present data set (pp 5.02 TeV) $L_{pT} = A_{pT} = 0.5$ GeV/c. So one can not use the method described above for trigger systematic evaluation due to RF. Therefore, a new strategy has been adopted which is as follows:

- Evaluate the RF for Upsilon in MC pp 5.02 TeV. where

  $RF_{MC_{pp}} = \frac{L_{pT}}{T_{pT}}$, where L_{pT} : $GetMatchTrigger() >= 1$ (0.5 GeV/c single muon p_T cut) and T_{pT} : without any trigger matching cut and fitted with $F(p_{\mathrm{T}})$ (Fig. 5.17)

- One can not compute $RF_{DATA_{\mathrm{pp}}}$ in pp 5.02 TeV data in same way as in MC, because of hadronic contamination to the trigger matching condition. So for RF calculation, a data sample (Pb-Pb 5.02 TeV) has been chosen in which $L_{pT} = 1$ GeV/c and $A_{pT} = 0.5$ GeV/c.

- Compute the RF in data/MC considering $L_{pT} = 1$ GeV/c and $A_{pT} = 0.5$ GeV/c and fit the RF with $F(p_{\mathrm{T}})$ (Fig. 5.18)

- Then evaluate the relative difference of fit parameters ($p_{\mathrm{T}}^{\mathrm{mean}}$, σ) between MC and

data of Pb–Pb.

- Modify the parameters (pcut, σ) of the fit function obtained from step 1 by the same relative difference estimated from step 4. This acts as $RF_{DATA_{pp}}$ for data in pp at 5.02 TeV (Fig. 5.19)

- Select muons matching the A_{pT} trigger in Υ MC pp 5.02 TeV simulation. Fill the histogram with a weight of $RF_{MC_{pp}}/RF_{DATA_{pp}}$ and without the weight.

- Extract the number of Upsilon in the two cases and take the relative difference as systematic.

The different RF distributions are represented in Fig. 5.17, 5.18 and 5.19. This procedure leads to an integrated systematic uncertainty is 0.6%. The numerical value of this uncertainty for differential bins are reported in Table 5.9.

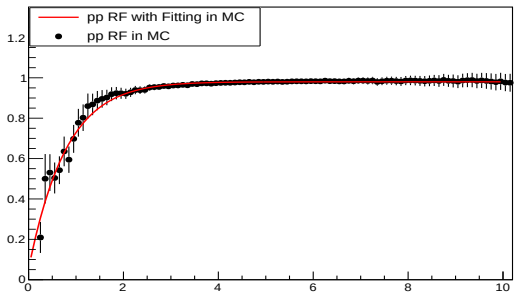

Figure 5.17: The RF function from MC simulation for pp 5.02 TeV.

Systematic on the efficiency maps of trigger chamber

The procedure is the same as followed for J/ψ pp 5.02 TeV analysis[1]. The relative difference of Υ number in the following simulations is taken as the systematic uncertainty on the efficiency map chamber.

- realistic MC

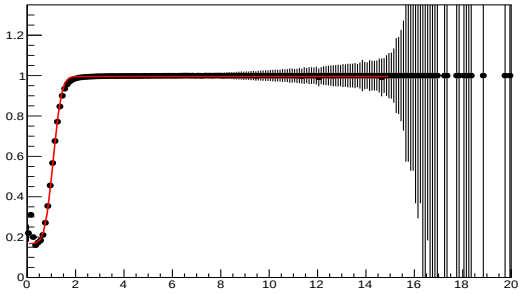

(a) DATA

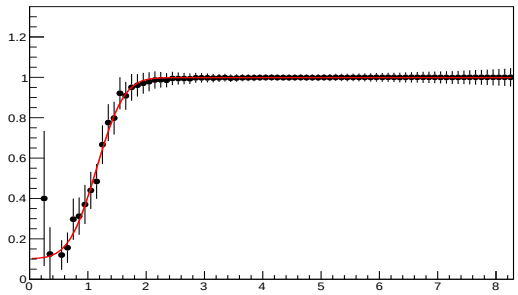

(b) MC

Figure 5.18: The RF function for Pb–Pb 5.02 TeV

- modified simulations with a blurred trigger response at the local boards level

The trigger intrinsic systematic is 1% for integrated (Υ(1S), Υ(2S), Υ(3S)) as well as p_{T} and rapidity bins (minor variation in differential bin). The uncertainty distributions are shown in Fig. 5.20.

5.5.6 Matching

The systematic on the trigger-tracker matching has been estimated as 1% [14].

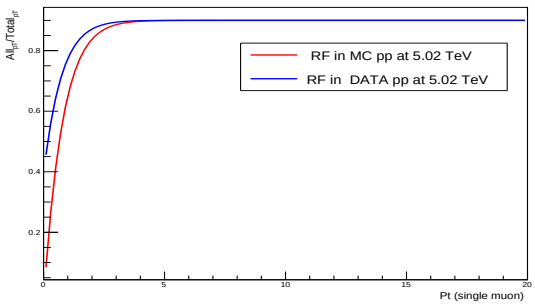

Figure 5.19: The RF function for pp 5.02 TeV using DATA and MC.

Table 5.9: The percentages values of the systematic uncertainties on the trigger response function.

p_{T} (in GeV/c)	$\frac{Weg_{\Upsilon}(1S)-NoWeg_{\Upsilon}(1S)}{Weg_{\Upsilon}(1S)}$ (%)
$[0, 2]$	1.1
$[2, 4]$	0.5
$[4, 6]$	0.6
$[6, 15]$	0.4
y	$\frac{Weg_{\Upsilon}(1S)-NoWeg_{\Upsilon}(1S)}{Weg_{\Upsilon}(1S)}$ (%)
$[-4.0, -3.5]$	0.5
$[-3.5, -3.0]$	0.6
$[-3.0, -2.5]$	0.1
$[-4.0, -3.25]$	0.6
$[-3.25, -2.5]$	0.3

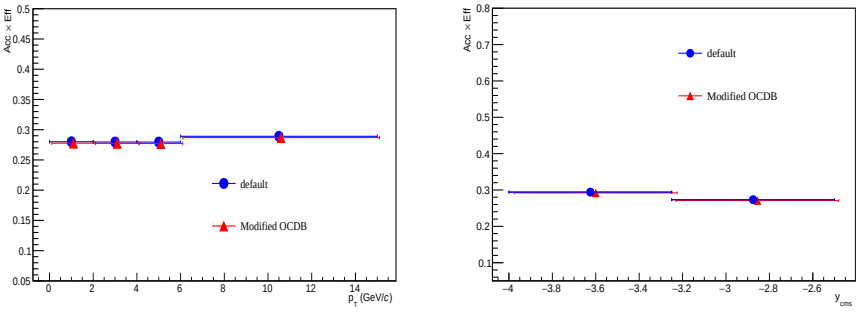

(a) p_{T} (b) rapidity

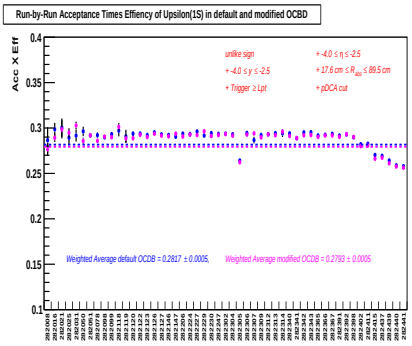

(c) Integrated Υ(1S) as function of run number

Figure 5.20: The uncertainty on the efficiency maps of the trigger chambers.

5.5.7 Summary

The summary of different systematic contributions have been tabulated in Table 5.10. The largest contribution comes from signal extraction.

Table 5.10: The summary of the systematic uncertainties (in %) for Υ analysis in pp collisions at $\sqrt{s} = 5.02$ TeV.

sources	Υ(1S)			Υ(2S)	Υ(3S)
	Integrated	p_{T}	y	Integrated	Integrated
Signal extraction	6.5	$5.8 - 7.1$	$6.2 - 7.4$	7.4	18.4
Luminosity	1.8	1.8	1.8	1.8	1.8
MC input	1.7	$1.5 - 1.7$	$2.2 - 3.5$	1.7	1.7
Tracker	2	2	2	2	2
Trigger response	0.6	$0.4 - 1.1$	$0.1 - 0.6$	0.6	0.6
Trigger efficiency	1	1	1	1	1
Matching	1	1	1	1	1

5.6 Results

The inclusive production cross-section of Υ has been evaluated for pp collisions at $\sqrt{s} = 5.02$ TeV. The integrated, y-differential and p_{T}-differential cross-section are defined as :

$$\sigma_{\Upsilon(\mathrm{nS})} = \frac{N_{\Upsilon(\mathrm{nS})}}{A \times \epsilon} \frac{1}{BR_{\Upsilon(\mathrm{nS})\to\mu^+\mu^-}} \frac{1}{\mathcal{L}_{\mathrm{int}}}$$

$$\frac{d\sigma_{\Upsilon(\mathrm{nS})}}{dy} = \frac{N_{\Upsilon(\mathrm{nS})}}{A \times \epsilon} \frac{1}{BR_{\Upsilon(\mathrm{nS})\to\mu^+\mu^-}} \frac{1}{\mathcal{L}_{\mathrm{int}}} \frac{1}{\Delta y}$$

$$\frac{d^2\sigma_{\Upsilon(\mathrm{nS})}}{dy dp_{\mathrm{T}}} = \frac{N_{\Upsilon(\mathrm{nS})}}{A \times \epsilon} \frac{1}{BR_{\Upsilon(\mathrm{nS})\to\mu^+\mu^-}} \frac{1}{\mathcal{L}_{\mathrm{int}}} \frac{1}{\Delta y \Delta p_{\mathrm{T}}}$$

where :

- $N_{\Upsilon(\mathrm{nS})}$ is the number of Υ obtained from signal extraction in 5.3.

- $\mathcal{L}_{\rm int}$ is the integrated luminosity.
- $A \times \epsilon$ is the acceptance time efficiency correction evaluated in 5.4.
- $BR_{\Upsilon(\rm nS)\to\mu^+\mu^-}$ is the $\Upsilon \to \mu^+\mu^-$ branching ratio (2.48 $\pm$ 0.05% for Υ(1S), 1.93 $\pm$ 0.17% for Υ(2S), 2.18 $\pm$ 0.21% for Υ(3S), from [2]).
- Δy, $\Delta p_{\rm T}$ represent rapidity and $p_{\rm T}$ bin width.

5.6.1 Cross-section

Integrated over $p_{\rm T}$ and rapidity

The Υ(nS) integrated production cross-section ($2.5 < y < 4.0$, $0 < p_{\rm T} < 15$ GeV/c) results are presented in Tab. 5.11. Where, the first uncertainty represent statistical and second uncertainty is systematic.

Table 5.11: The value of Υ(nS) production cross-section (integrated over $p_{\rm T}$ and y) in pp collisions at $\sqrt{s} = 5.02$ TeV.

particle	$\sigma \pm$ (stat.) $\pm$ (syst.) (nb)
Υ(1S)	45.47 $\pm$ 3.86 $\pm$ 3.48
Υ(2S)	22.40 $\pm$ 3.22 $\pm$ 2.67
Υ(3S)	4.90 $\pm$ 2.19 $\pm$ 1.03

The Υ(nS) production cross-sections have been compared with other LHC measurements at different energies and illustrated in Fig. 5.21 and the corresponding numerical values are listed in Table 5.12. In Fig. 5.21, the vertical error bar represents the quadratic sum of statistical and systematic error. Υ(1S) and Υ(3S) results at 5.02 TeV with ALICE are consistent with other LHC measurements while the Υ(2S) results overestimate the other LHC Υ(2S) measurements. For the LHCb data point, we have also included the branching ratio error in cross section. The rapidity and $p_{\rm T}$ coverage of LHCb data

are $-4.0 < y < -2.5$ and $0 < p_{\mathrm{T}} < 15$, respectively.

Table 5.12: The values of the Υ(nS) production cross-sections (integrated over p_{T} and y) at LHC.

collaboration	$\sqrt{s}$	$\sigma_{1\mathrm{S}}$ (nb)	$\sigma_{2\mathrm{S}}$ (nb)	$\sigma_{3\mathrm{S}}$ (nb)
ALICE	5	45.47 ± 5.20	22.40 ± 4.18	4.90 ± 2.42
ALICE	7	54.2 ± 8.4	18.4 ± 4.7	not available
ALICE	8	71 ± 9.2	26 ± 6.4	9 ± 4.1
ALICE	13	105.9 ± 8.5	40.5 ± 5.12	18.4 ± 3.62
LHCb	2.76	27.09 ± 1.29	6.49 ± 0.57	4.08 ± 0.69
LHCb	7	65.95 ± 2.28	20.92 ± 1.93	9.06 ± 0.91
LHCb	8	82.21 ± 2.84	26.35 ± 2.43	10.98 ± 1.10
LHCb	13	118.40 ± 2.82	36.66 ± 3.26	16.07 ± 1.56

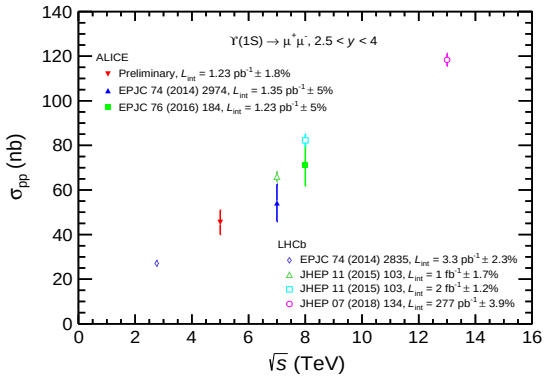

(a) Υ(1S)

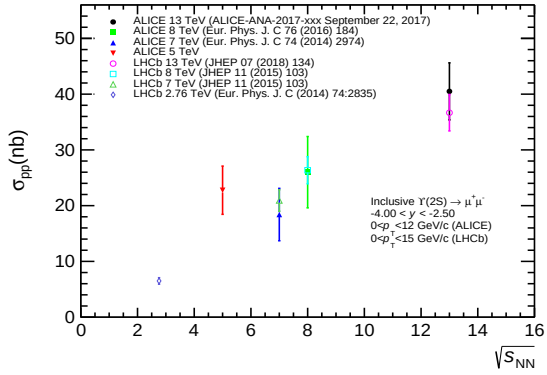

(b) Υ(2S)

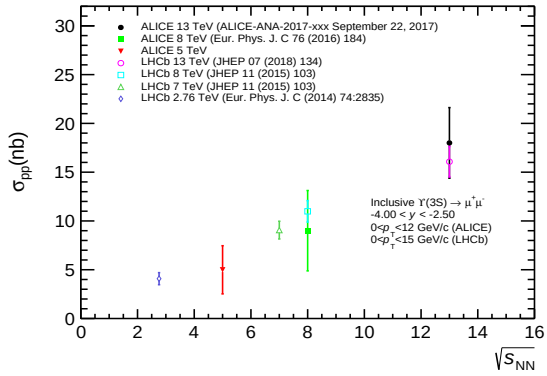

(c) Υ(3S)

Figure 5.21: The integrated Υ(nS) production cross-sections at different center-of-mass energies. The reference of each measurements can be found at figure legend.

Rapidity and y differential cross-section

The rapidity and p_{T} dependence of Υ(1S) cross-section are shown in Fig. 5.22 where the horizontal line (x axis) represent the bin width, vertical line represent statistical error and box around the point represent the systematic error. The numerical values are reported in Table 5.13 and 5.14.

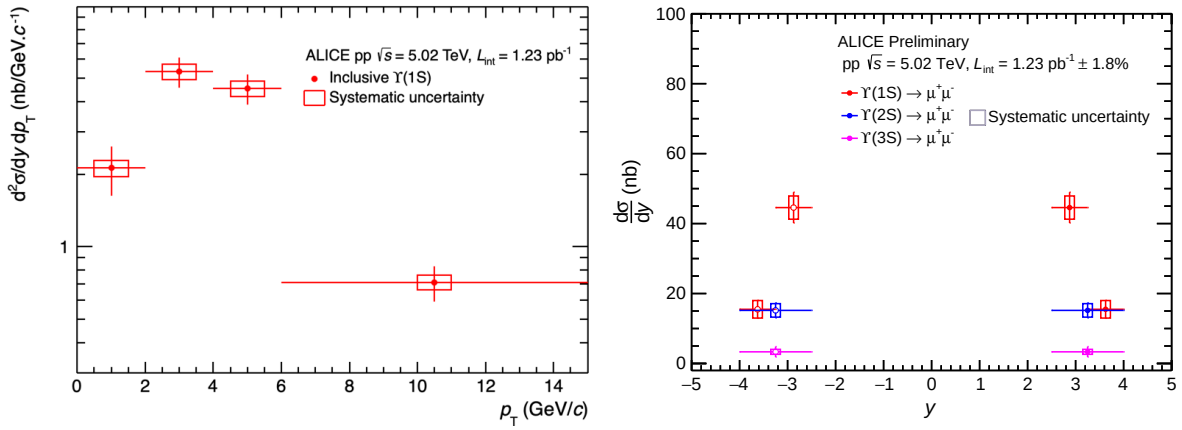

Figure 5.22: The differential cross-section of Υ(nS) as function of p_{T} (left) and rapidity (right).

Table 5.13: The values of the differential production cross-sections of Υ(1S) in p_{T} bins at $\sqrt{s} = 5.02$ TeV.

p_{T} (in GeV/c)	$\frac{d^2\sigma}{dydp_{\mathrm{T}}}$ (nb GeV^{-1}c)
$[0, 2]$	$2.12 \pm 0.49 \pm 0.17$
$[2, 4]$	$5.35 \pm 0.76 \pm 0.40$
$[4, 6]$	$4.54 \pm 0.65 \pm 0.32$
$[6, 15]$	$0.71 \pm 0.12 \pm 0.05$

Table 5.14: The values of the differential production cross-sections of Υ(1S) in rapidity bins at $\sqrt{s} = 5.02$ TeV

y	$\frac{d\sigma}{dy}$ (nb GeV^{-1}c)
$[-4, -3.25]$	$15.49 \pm 2.56 \pm 1.40$
$[-3.25, -2.5]$	$44.58 \pm 4.41 \pm 3.37$

5.6.2 Υ(nS)-to-Υ(1S) production cross-section ratio

The integrated production cross-section ratio of Υ(2S) to Υ(1S) and Υ(3S) to Υ(1S) at 5.02 TeV are 0.497 $\pm$ 0.084 $\pm$ 0.060 and 0.104 $\pm$ 0.047 $\pm$ 0.021 respectively. The distributions of this ratio in different fitting methods are shown in Fig. 5.23. In this ratio, the detector and luminosity related systematic and some part of signal systematic get cancel out. The remaining systematic is due to the branching ratio and acceptance times efficiency.

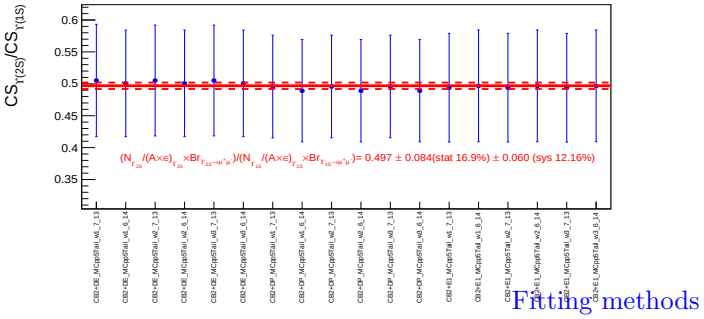

(a) $\sigma_{\Upsilon(2S)}/\sigma_{\Upsilon(1S)}$

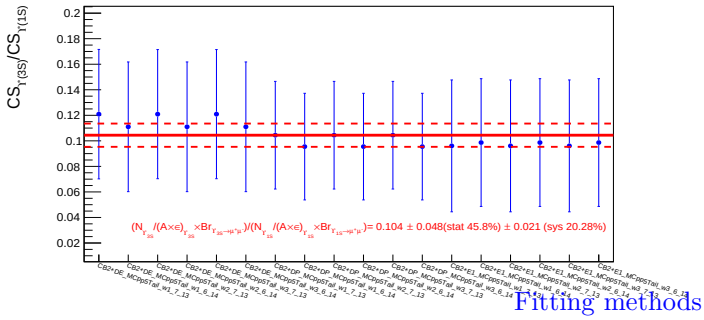

(b) $\sigma_{\Upsilon(3S)}/\sigma_{\Upsilon(1S)}$

Figure 5.23: The cross section ratios obtained as a function of the fitting methods.

5.6.3 Comparison with theory and CMS measurement

The Υ(1S) cross-sections have been compared with theoretical calculations based an improved CEM (ICEM) model from Cheung *et al.* [15] using k_{T} factorization approach

as well as a NLO CEM model calculations from Lansberg *et al.* [16] for hadroproduction up to α_s^4. Both approaches account for the feed-down contributions from heavier bottomonium decays.

The differential cross sections are plotted in Fig. 5.24 as a function of p_{T} for the $\Upsilon(1S)$ on the left panel and as a function of y for the three Υ states, together with the CMS measurements performed at midrapidity [17].

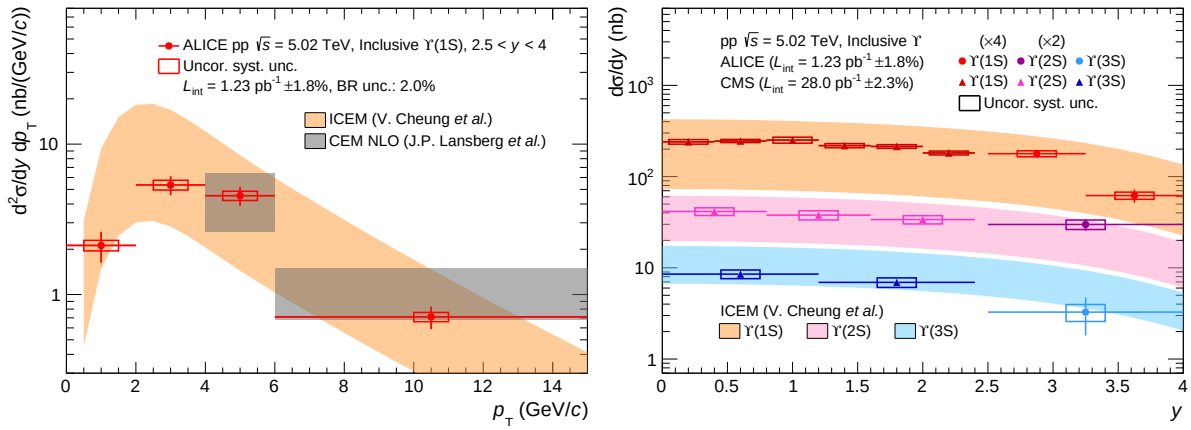

Figure 5.24: p_{T} dependence of the $\Upsilon(1S)$ cross section (left) and y dependence of the $\Upsilon(1S)$, $\Upsilon(2S)$ and $\Upsilon(3S)$ (right) measured by ALICE and CMS. The two panels also show calculations from the improved color evaporation model [15] with bands representing the uncertainties on the renormalization scales and on the mass of the beauty quark. Results from CEM with NLO corrections [16] are shown in the left panel.

The two calculations based on CEM give a fair description of the measured p_{T} spectrum within uncertainties. The rapidity dependence (left panel of Fig. 5.24) shows that the ALICE forward acceptance covers the region where the production cross-section drops from the midrapidity plateau. This observation is in agreement with the ICEM calculations. The measured $\Upsilon(2S)$ production cross sections lie in the upper limit of the model calculation while the $\Upsilon(3S)$ values are on the lower limit of the calculation uncertainties.

5.6.4 Energy dependence of Υ integrated cross-section of ALICE

The rapidity and p_{T} integrated (y, $0 < p_{\mathrm{T}} < 15$ GeV/c) cross-section of Υ states are shown as a function of the collision energy in Fig. 5.25. A steady rise of the cross section is observed with increasing $\sqrt{s}$ for all Υ. These ALICE results have been compared with the theoretical calculations from ICEM [18] which reproduce the energy dependence trend. However, the Υ(3S) results lie on the lower limit of the theoretical calculation uncertainties.

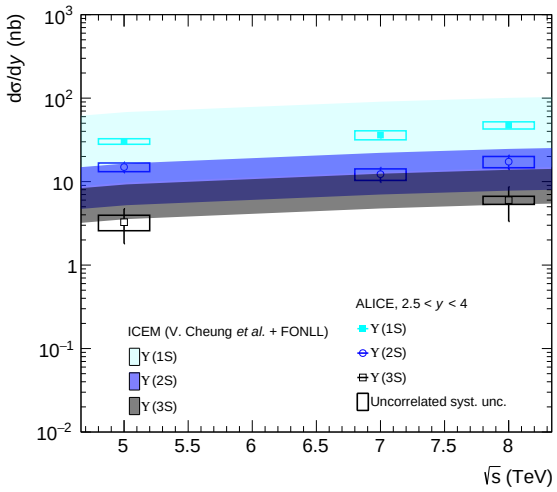

Figure 5.25: The p_{T} and rapidity integrated cross-section of Υ(1S), Υ(2S), Υ(3S) as a function of the energy, in pp collisions measured by the ALICE. The branching ratio and luminosity uncertainties are added in the systematic boxes. The ALICE results are also compared to the theoretical calculation from ICEM + FONLL [18, 19].

5.7 Summary

The inclusive Υ(nS) production cross sections have been measured at forward rapidity ($2.5 < y < 4$) in pp collisions at $\sqrt{s} = 5.02$ TeV. Due to the larger beam luminosity, the double differential cross section studies have been carried out for the first time as a function of p_{T} and y along with the integrated Υ(1S), Υ(2S) and Υ(3S) cross section

measurements. The inclusive cross sections, integrated over y and p_{T} ($p_{\mathrm{T}} < 15$ GeV/c) are: $\sigma_{\Upsilon(1S)} = 45.5 \pm 3.9(\mathrm{stat.}) \pm 3.5(\mathrm{syst.})$ nb, $\sigma_{\Upsilon(2S)} = 22.4 \pm 3.2(\mathrm{stat.}) \pm 2.7(\mathrm{syst.})$ nb and $\sigma_{\Upsilon(3S)} = 4.9 \pm 2.2(\mathrm{stat.}) \pm 1.0(\mathrm{syst.})$ nb. The corresponding excited-to-ground state cross section ratios amount to: $\sigma_{\Upsilon(2S)}/\sigma_{\Upsilon(1S)} = 0.50 \pm 0.08(\mathrm{stat.}) \pm 0.06(\mathrm{syst.})$ and $\sigma_{\Upsilon(3S)}/\sigma_{\Upsilon(1S)} = 0.10 \pm 0.05(\mathrm{stat.}) \pm 0.02(\mathrm{syst.})$.

The energy dependence of Υ(nS) states exhibits a steady increase of the cross-section is observed with increasing center-of-mass energy for all the Υ states. The differential cross-section are compared to ICEM calculations [15] and CEM calculations with NLO corrections [16]. A good agreement within the uncertainties is observed between the experimental results and the model calculations. The Υ(nS) measurements at $\sqrt{s} = 5.02$ TeV provides additional experimental constraints on quarkonium production models. The rapidity dependence of Υ(1S) cross-sections have been also compared with CMS measurements at mid-rapidity [17] and it can be concluded that the ALICE forward acceptance covers the region where the production cross section drops from the mid-rapidity plateau region.

Bibliography

[1] ALICE Collaboration collaboration, *J/ψ production in pp collisions at $\sqrt{s}$ = 5.02 TeV, ANA-909, 2019*, .

[2] Particle Data Group collaboration, M. Tanabashi, K. Hagiwara, K. Hikasa, K. Nakamura, Y. Sumino, F. Takahashi et al., *Review of particle physics*, *Phys. Rev. D* **98** (Aug, 2018) 030001.

[3] ALICE Collaboration collaboration, *Measurement of the Υ production cross-section at forward rapidity in pp collisions at $\sqrt{s}$ = 5.02 TeV TeV with the ALICE experiment , ANA-931, 2019*, .

[4] F. Bossu, Z. del Valle, A. de Falco, M. Gagliardi, S. Grigoryan and G. Martinez Garcia, *Phenomenological interpolation of the inclusive J/psi cross section to proton-proton collisions at 2.76 TeV and 5.5 TeV*, 1103.2394.

[5] ALICE collaboration, S. Acharya et al., *Measurement of the inclusive J/ψ polarization at forward rapidity in pp collisions at $\sqrt{\mathbf{s}} = \mathbf{8}$ TeV*, *Eur. Phys. J.* **C78** (2018) 562, [1805.04374].

[6] ALICE collaboration, B. Abelev et al., *J/ψ polarization in pp collisions at $\sqrt{s} = 7$ TeV*, *Phys. Rev. Lett.* **108** (2012) 082001, [1111.1630].

[7] LHCb collaboration, R. Aaij et al., *Measurement of the Υ polarizations in pp collisions at $\sqrt{s} = 7$ and 8 TeV*, *JHEP* **12** (2017) 110, [1709.01301].

[8] D. Lange, *The EvtGen particle decay simulation package*, *Nucl. Instrum. Meth. A* **462** (2001) 152–155.

[9] E. Barberio, B. van Eijk and Z. Was, *PHOTOS: A Universal Monte Carlo for QED radiative corrections in decays*, *Comput. Phys. Commun.* **66** (1991) 115–128.

[10] R. Brun, F. Bruyant, F. Carminati, S. Giani, M. Maire, A. McPherson et al., *GEANT: Detector Description and Simulation Tool; Oct 1994*. CERN Program Library. CERN, Geneva, 1993, 10.17181/CERN.MUHF.DMJ1.

[11] GEANT4 collaboration, S. Agostinelli et al., *GEANT4: A Simulation toolkit*, *Nucl. Instrum. Meth.* **A506** (2003) 250–303.

[12] A. Collaboration, *ALICE 2017 luminosity determination for pp collisions at* $\sqrt{s}$ *= 5 TeV*, 2018.

[13] LHCb collaboration, R. Aaij et al., *Measurement of* Υ *production in pp collisions at* $\sqrt{s}$*= 13 TeV*, *JHEP* **07** (2018) 134, [1804.09214].

[14] ALICE collaboration, S. Acharya et al., *Energy dependence of forward-rapidity* J/ψ *and* ψ(2S) *production in pp collisions at the LHC*, *Eur. Phys. J. C* **77** (2017) 392, [1702.00557].

[15] V. Cheung and R. Vogt, *Production and polarization of prompt* $\Upsilon(nS)$ *in the improved color evaporation model using the* k_T*-factorization approach*, *Phys. Rev. D* **99** (2019) 034007, [1811.11570].

[16] J.-P. Lansberg, H.-S. Shao, N. Yamanaka, Y.-J. Zhang and C. Noûs, *Complete NLO QCD study of single- and double-quarkonium hadroproduction in the colour-evaporation model at the Tevatron and the LHC*, 2004.14345.

[17] CMS collaboration, A. M. Sirunyan et al., *Measurement of nuclear modification factors of* $\Upsilon(1S)$*,* $\Upsilon(2S)$*, and* $\Upsilon(3S)$ *mesons in PbPb collisions at* $\sqrt{s_{\mathrm{NN}}}$ *= 5.02 TeV*, *Phys. Lett. B* **790** (2019) 270–293, [1805.09215].

[18] V. Cheung and R. Vogt, *Production and polarization of prompt J/ψ in the improved color evaporation model using the k_T-factorization approach*, *Phys. Rev. D* **98** (2018) 114029, [1808.02909].

[19] M. Cacciari, S. Frixione, N. Houdeau, M. L. Mangano, P. Nason and G. Ridolfi, *Theoretical predictions for charm and bottom production at the LHC*, *JHEP* **10** (2012) 137, [1205.6344].

CHAPTER 6

Υ production in p–Pb collisions at $\sqrt{s_{\mathrm{NN}}}$ = 8.16 TeV

This chapter focuses on the analysis of inclusive Υ production in p–Pb collision at $\sqrt{s_{\mathrm{NN}}}$ = 8.16. I shall report the Upsilon production as a function of traverse momentum, rapidity and centrality of the collisions and compare the results with previous ALICE measurements at $\sqrt{s_{\mathrm{NN}}}$ = 5.02. The experimental results will also be compared with different model calculations and other LHC measurements. This chapter is composed of two parts: in the first part, Υ analysis as a function of p_{T} and rapidity will be discussed and in the second part, Υ(1S) analysis as a function of centrality will be presented. The results of this chapter are published in reference [1].

6.1 Beam configuration

The rapidity in the center-of-mass frame of reference y_{CMS} in p–Pb collision is shifted with respect to the laboratory frame of reference by an amount of $\Delta y = \pm 0.46$ according

to the following formula

$$\Delta y = \frac{1}{2}[\ln(Z_1 A_2) - \ln(Z_2 A_1)] \tag{6.1}$$

where Z1 = 82, A1 = 208, Z2 = 1, A2 = 1.

p–Pb collision

When the proton beam going towards the Muon Spectrometer and the lead beam comes from the spectrometer side is called p–Pb collisions as shown in Fig 6.1 left panel. The center-of-mass rapidity coverage of this beam configuration is $2.03 < y < 3.53$ and called forward rapidity region.

Pb–b collision

When the proton beam comes from the spectrometer side and the lead beam going towards the Muon Spectrometer, is called Pb–p collisions as shown in Fig 6.1 right panel. The center-of-mass rapidity coverage of this beam configuration is $-4.46 < y < -2.96$ and called backward rapidity region.

6.2 Definition of the variables

Cross-section

It has been described in the previous chapter.

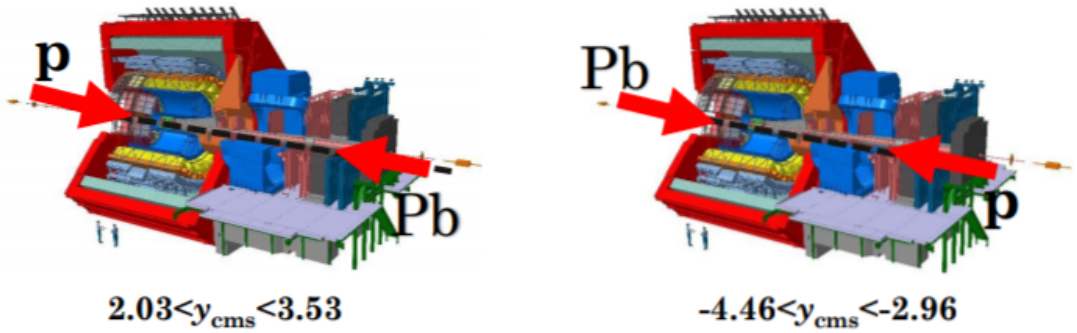

Figure 6.1: The p–Pb (left panel) and Pb–p (right panel) beam configurations in the ALICE.

Nuclear modification factor

$R_{\rm pA}$

The nuclear matter effects on the bottomonium production can be studied by comparing the p–Pb production cross section with the reference pp cross section obtained at the same kinematic domain and scaled by the Pb nucleus's atomic mass. This quantity called as nuclear modification factor, $R_{\rm pPb}$ and is defined as

$$R_{\rm pPb} = \frac{{\rm d}^2\sigma^{\Upsilon}_{\rm pPb}/{\rm d}y_{\rm cms}{\rm d}p_{\rm T}}{A_{\rm Pb} \times {\rm d}^2\sigma^{\Upsilon}_{\rm pp}/{\rm d}y_{\rm cms}{\rm d}p_{\rm T}}. \tag{6.2}$$

where:

- ${\rm d}^2\sigma^{\Upsilon}_{\rm pPb}/{\rm d}y_{\rm cms}{\rm d}p_{\rm T}$ is the cross section in p–Pb collision.
- ${\rm d}^2\sigma^{\Upsilon}_{\rm pp}/{\rm d}y_{\rm cms}{\rm d}p_{\rm T}$ is the cross section in pp collision.
- $A_{\rm Pb}$ is the atomic mass for Pb nucleus, A=208.

$Q_{\rm pA}$

The nuclear modification factor in centrality classes, is denoted as $Q_{\rm pPb}$ [2]. In general the $R_{\rm pPb}$ is not used due to the possible bias from the centrality selection and the determination of the nuclear thickness function $\langle T^{j}_{\rm pPb}\rangle$ in a particular centrality bin j. The $Q_{\rm pPb}$ is defined as:

$$Q^{j}_{\rm pPb} = \frac{N^{j}_{\Upsilon(1S)}}{\langle T^{j}_{\rm pPb}\rangle \;.\; N^{j}_{\rm MB} \;.\; (A\times\varepsilon) \;.\; {\rm B.R.}_{\Upsilon(1S)\to\mu^{+}\mu^{-}} \;.\; \sigma^{\rm pp}_{\Upsilon(1S)}} \tag{6.3}$$

where:

- $N^{j}_{\Upsilon(1S)}$ is the number of Υ(1S) signal obtained from the signal extraction for a centrality class j;
- $A\times\epsilon$ is the product of the detector acceptance times efficiency;
- ${\rm B.R.}_{\Upsilon(1S)\to\mu^{+}\mu^{-}}$ is the branching ratio of Υ(1S) in dimuonic decay channel = (2.48$\pm$0.05)%;
- $N^{j}_{\rm MB}$ is the number of minimum bias events for the centrality class j;
- $\langle T^{j}_{\rm pPb}\rangle$ is the average of the nuclear overlap function for the centrality class j;
- $\sigma^{\rm pp}_{\Upsilon(1S)}$ is the inclusive Υ(1S) reference cross section in pp collisions at the same energy and kinematic domain.

6.3 Monte Carlo production and $A\times\epsilon$ estimation

The Monte Carlo simulations have been carried out to estimate the correction factor for the acceptance and efficiency ($A\times\epsilon$) of the detector. The simulation data-sets are

produced run-by-run weighted by the corresponding number of CMUL7 triggers (the trigger class on which the data analyses are based) in a given run. The vertex position has been tested for both the estimated position and (0,0,0) options with no significant effect for mass resolution. The run-by-run detector conditions are taken into account using the ALICE OCDB. The official MC production can be found in LHC18k7a and LHC18k7b for p–Pb and Pb-p respectively.

6.3.1 Monte Carlo production

The $p_{\rm T}$ and y input shapes of Υ have been tuned directly on the p–Pb (Pb–p) at $\sqrt{s_{\rm NN}}$ = 8.16 TeV data, by an iterative procedure. The steps are briefly summarized here:

- step1: first set of MC simulations based on the $p_{\rm T}$ and y input shape obtained by using the existing AliGenMuonLib class of pp and p–Pb.
- step2: Next the number of Υ(1S) extracted as a function of $p_{\rm T}$ and y in p–Pb (Pb–p) data at $\sqrt{s_{\rm NN}}$ = 8.16 TeV and corrected by the acceptance $\times$ efficiency ($A \times \epsilon$) calculated in step 1. The resulting yields ($N_{\Upsilon(1S)}/A \times \epsilon$) are then fitted using the following functions:

$$f(p_{\rm T}) = a \times \frac{p_{\rm T}}{(b + {p_{\rm T}}^{c})^{d}}$$

$$f(y) = a + b \times y * y$$

- step3: The modified $f(p_{\rm T})$ and $f(y)$ are used as input shape of new Υ(1S) MC simulation.
- step4: This iteration process is continued, till the input shapes, are very close to the Υ(1S) yield distributions.

Due to the lower statistics of Υ(2S) in p–Pb (Pb–p) data at $\sqrt{s_{\rm NN}} = 8.16$ TeV, the MC input shapes are taken the same as Υ(1S).

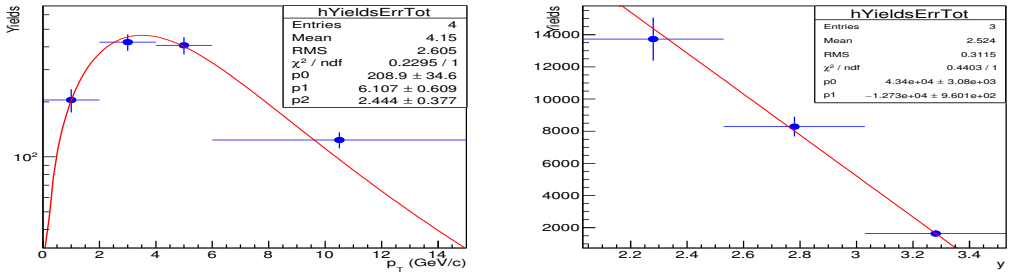

Figure 6.2: The MC input shapes of ALICE data tuned ($p_{\rm T}$ (left) and y (right) for p–Pb.

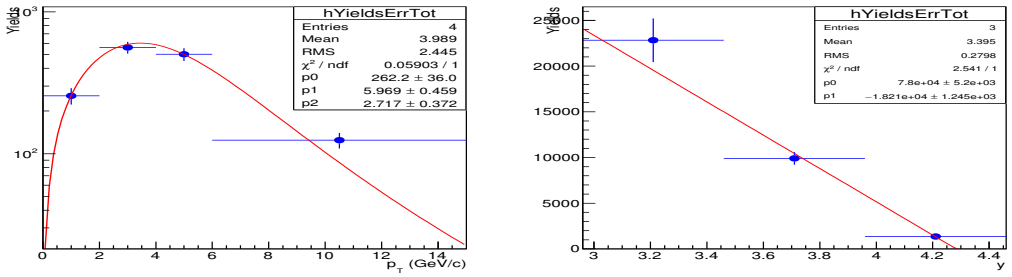

Figure 6.3: The MC input shapes of ALICE data tuned ($p_{\rm T}$ (left) and y (right) for Pb–p.

6.3.2 $A \times \epsilon$

The $A \times \epsilon$ is defined as the ratio of the number of reconstructed Υ(nS) to the number of generated Υ(nS).

$$\mathrm{A} \times \epsilon = \frac{N_{\rm reconstructed}}{N_{\rm generated}}$$

The statistical uncertainties associated with the $A \times \epsilon$ evaluated as:

$$\frac{1}{N_{\rm generated}} \times \sqrt{N_{\rm reconstructed} \times (1 - \frac{N_{\rm reconstructed}}{N_{\rm generated}})}$$

The selection cuts are the same as in data. The $A \times \epsilon$ factor is evaluated by averaging over all the runs. Each run is weighted by $\frac{N^{run}_{\rm CMUL7}}{N^{period}_{\rm CMUL7}}$.

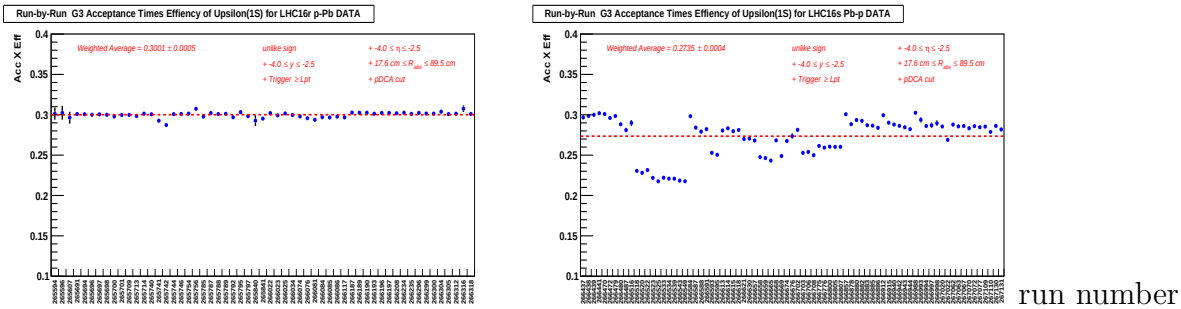

Figure 6.4: The $A \times \epsilon$ of Υ(1S) as a function of run number for p–Pb (left) and Pb–p (right).

The $A \times \epsilon$ of Υ(1S) as a function of run number is shown in Fig. 6.4. For p–Pb collisions, the distribution is stable for all the runs. In the Pb–p collisions, $A \times \epsilon$ distributions show significant fluctuations due to the HV trips in station 2 (chamber-03 and chamber-04). The value of $A \times \epsilon$ of the higher states are almost the same as of Υ(1S) and the average value of $A \times \epsilon$ are reported in Tab. 6.1.

Table 6.1: The $p_{\rm T}$ and rapidity integrated $A \times \epsilon$ values in p–Pb and Pb–p collisions of Υ(1S), Υ(2S) and Υ(3S).

Beam conditions	particle	$A \times \epsilon$ (%)
p–Pb	Υ(1S)	30.01 ± 0.05
	Υ(2S)	30.12 ± 0.08
	Υ(3S)	30.04 ± 0.06
Pb–p	Υ(1S)	27.35 ± 0.04
	Υ(2S)	27.41 ± 0.06
	Υ(3S)	27.47 ± 0.06

The $p_{\rm T}$ and y dependence of the $A \times \epsilon$ of Υ(1S) are plotted at Fig. 6.5 and the values are listed in Tab. 6.2 and Tab. 6.3 respectively. The acceptance efficiency as function of $p_{\rm T}$ is flat while as function of rapidity, the detector edge effects are observed.

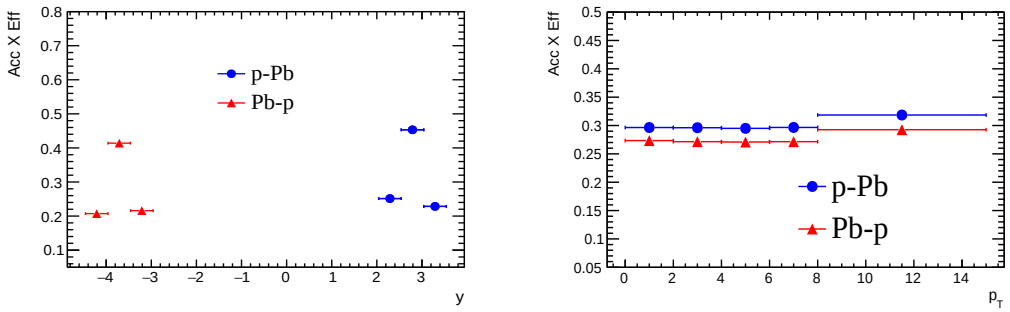

Figure 6.5: The $A \times \epsilon$ of Υ(1S) as a function of $p_{\rm T}$ (left) and $y_{\rm CMS}$ (right).

Table 6.2: The $A \times \epsilon$ values as a function of $y_{\rm CMS}$ in p–Pb and Pb–p.

Beam conditions	$y_{\rm CMS}$	$A \times \epsilon$ (%)
p-Pb	$[2.03, 2.53]$	22.49 ± 0.06
	$[2.53, 3.03]$	44.22 ± 0.04
	$[3.03, 3.53]$	23.18 ± 0.04
Pb-p	$[-4.46, -3.96]$	19.55 ± 0.05
	$[-3.96, -3.46]$	40.85 ± 0.04
	$[-3.46, -2.46]$	21.07 ± 0.06

Table 6.3: The $A \times \epsilon$ values as a function of $p_{\rm T}$ in p–Pb and Pb–p.

Beam conditions	p_T (GeV/c)	$A \times \epsilon$ (%)
p-Pb	$[0, 2]$	29.68 ± 0.06
	$[2, 4]$	29.65 ± 0.04
	$[4, 6]$	29.50 ± 0.04
	$[6, 8]$	29.60 ± 0.05
	$[8, 15]$	31.63 ± 0.07
Pb-p	$[0, 2]$	27.18 ± 0.06
	$[2, 4]$	26.94 ± 0.03
	$[4, 6]$	26.91 ± 0.06
	$[6, 8]$	27.05 ± 0.07
	$[8, 15]$	29.31 ± 0.08

6.4 Signal extraction

The Υ(nS) signals are extracted by combining the opposite sign muon tracks reconstructed in the Muon Spectrometer.

The dimuon invariant mass distribution has been fitted with a sum of three Extended

Crystal Ball functions for Υ(1S), Υ(2S), Υ(3S) and various functions for continuum background. The fitting functions have been discussed in the Appendix. The signal extraction procedure is described in the following sections:

6.4.1 Tail Parameter

Due to the small S/B ratio in data, some constraints are applied in the fitting method. To reproduce the signal shape, one need to fix the tail parameters of the signal function to the values obtained from MC simulations (see Fig. 6.6 (CB2) and Fig. 6.7 (NA60)). Since no variation is observed for the tail parameters of Υ(1S), Υ(2S) and Υ(3S), the parameters of Υ(1S) are used for three Υ(nS) signal functions to fit the invariant mass spectrum.

Tail for Extended Crystal Ball

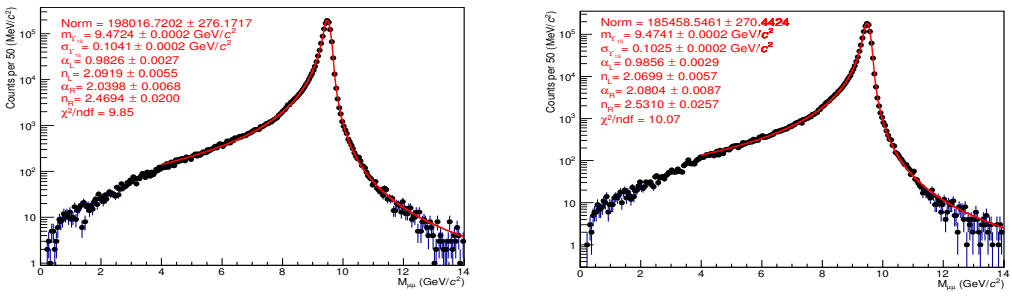

Figure 6.6: The mass fit to the simulated Υ(1S) signals for p–Pb (left) and Pb–p (right) to extract the tail parameters for CB2.

The tail parameter values, obtained from the MC are:

$\alpha_L = 0.982 \pm 0.002$, $n_L = 2.092 \pm 0.005$, $\alpha_R = 2.039 \pm 0.007$, $n_R = 2.469 \pm 0.020$ for p–Pb period.

$\alpha_L = 0.985 \pm 0.003$, $n_L = 2.069 \pm 0.006$, $\alpha_R = 2.081 \pm 0.009$, $n_R = 2.531 \pm 0.025$ for Pb–p period.

In each $p_{\rm T}$ and y bins, the same set of tail parameters have been used.

Tail for NA60

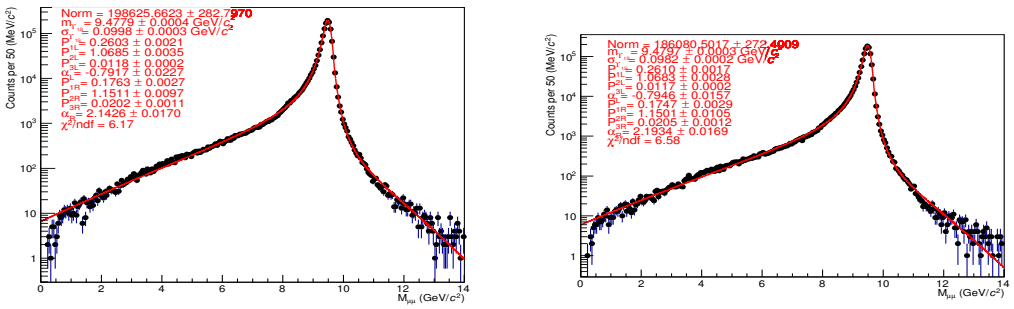

Figure 6.7: The mass fit to the simulated Υ(1S) signals for p–Pb (left) and Pb–p (right) to extract the tail parameters for NA60.

$P_{1L} = 0.260 \pm 0.002$, $P_{2L} = 1.068 \pm 0.003$, $P_{3L} = 0.012 \pm 0.001$, α_L = -0.791 $\pm$ 0.022

$P_{1R} = 0.176 \pm 0.003$, $P_{2R} = 1.152 \pm 0.009$, $P_{3R} = 0.020 \pm 0.001$, $\alpha_R = 2.143 \pm 0.017$ for p–Pb period.

$P_{1L} = 0.261 \pm 0.002$, $P_{2L} = 1.068 \pm 0.002$, $P_{3L} = 0.012 \pm 0.001$, α_L = -0.794 $\pm$ 0.002

$P_{1R} = 0.174 \pm 0.002$, $P_{2R} = 1.150 \pm 0.015$, $P_{3R} = 0.022 \pm 0.001$, $\alpha_R = 2.170 \pm 0.017$ for Pb–p period.

In each $p_{\rm T}$ and y bins, the same set of tail parameters have been used.

Different set of tails

We have assigned a systematic uncertainty for the tail parameter fixing. Different sets of tails have been tested for signal extraction. The choice of the tails provides the largest variation in the extraction of the $\Upsilon(1S)$ yields. The following sets of the tail are used for the CB2 function:

- p–Pb MC 8.16 TeV: Tail tuned on the invariant mass fit of p–Pb and Pb–p MC at $\sqrt{s_{\rm NN}} = 8.16$ TeV

- pp MC 8.00 TeV: Tail tuned on the invariant mass fit of pp MC at $\sqrt{s} = 8.00$ TeV

- pp DATA 13.00 TeV: Tails fixed to the values extracted directly from data in pp collisions at $\sqrt{s} = 13.00$ TeV

The graphical form of the different sets of the tails are shown in Fig. 6.8

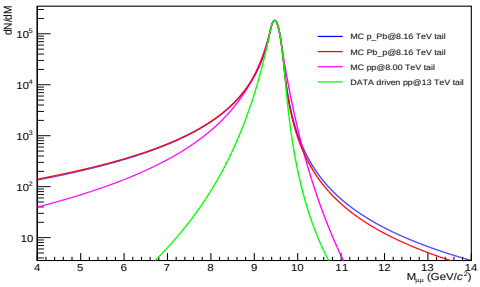

Figure 6.8: The visualization of the different tail parameters for the $\Upsilon(1S)$ signal.

The statistics in Υ mass range does not allow the determination of the data-driven tail at $\sqrt{s_{\rm NN}} = 8.16$ TeV.

No tail variation has been tested for the NA60 function, as the contribution in signal systematic due to the choice of the signal functions (CB2 or NA60) is negligible.

6.4.2 Mass and width of Υ(2S) and Υ(3S)

Due to the small significance of the higher mass states (Υ(2S), Υ(3S)), the mass position and width are scaled to Υ(1S) mass position and width value respectively in the following way.

$$\begin{aligned} M_{\Upsilon(2S)} &= M^{Fit}_{\Upsilon(1S)} + (M^{PDG}_{\Upsilon(2S)} - M^{PDG}_{\Upsilon(1S)}) \\ M_{\Upsilon(3S)} &= M^{Fit}_{\Upsilon(1S)} + (M^{PDG}_{\Upsilon(3S)} - M^{PDG}_{\Upsilon(1S)}) \\ \sigma_{\Upsilon(2S)} &= \sigma^{Fit}_{\Upsilon(1S)} \times \frac{\sigma^{MC}_{\Upsilon(2S)}}{\sigma^{MC}_{\Upsilon(1S)}} \\ \sigma_{\Upsilon(3S)} &= \sigma^{Fit}_{\Upsilon(1S)} \times \frac{\sigma^{MC}_{\Upsilon(3S)}}{\sigma^{MC}_{\Upsilon(1S)}} \end{aligned} \tag{6.4}$$

It is tested that no variation of Υ(1S) count has been observed for this scaling of higher states. However, a systematic uncertainty is assigned for this scaling in Υ(2S) and Υ(3S) signal extraction.

For Υ(2S) and Υ(3S), an additional systematic test has been added due to the width scaling. The method of this systematic is same as discussed in Pb–Pb analysis [3]. Here $\frac{\sigma^{MC}_{\Upsilon(2S)}}{\sigma^{MC}_{\Upsilon(1S)}}$ ($\frac{\sigma^{MC}_{\Upsilon(3S)}}{\sigma^{MC}_{\Upsilon(1S)}}$) has been varied between two extreme cases of the value obtained from official MC. Three set of $\frac{\sigma^{MC}_{\Upsilon(2S)}}{\sigma^{MC}_{\Upsilon(1S)}}$ ($\frac{\sigma^{MC}_{\Upsilon(3S)}}{\sigma^{MC}_{\Upsilon(1S)}}$) is used for this study :

- From official MC, 1.05 (1.07) in p–Pb and 1.05 (1.07) in Pb–p.

- Lowest possible value, which is 1 (1) for both p–Pb and Pb–p.

- Highest value of ratio among the different MC set which includes LHCb, AliGen input, etc. And the value is 1.07 (1.09) and 1.07(1.10) for p–Pb and Pb–p respectively.

6.4.3 Integrated invariant mass fit

The fits of the integrated spectra are shown in Fig. 6.9 by keeping Υ(1S) mass position and width free and the tail parameters are fixed to the values obtained from MC (following the discussion in 6.4.1) in the signal function CB2. The Υ(2S) and Υ(3S) mass position and widths are bound to Υ(1S) using equation 6.4.

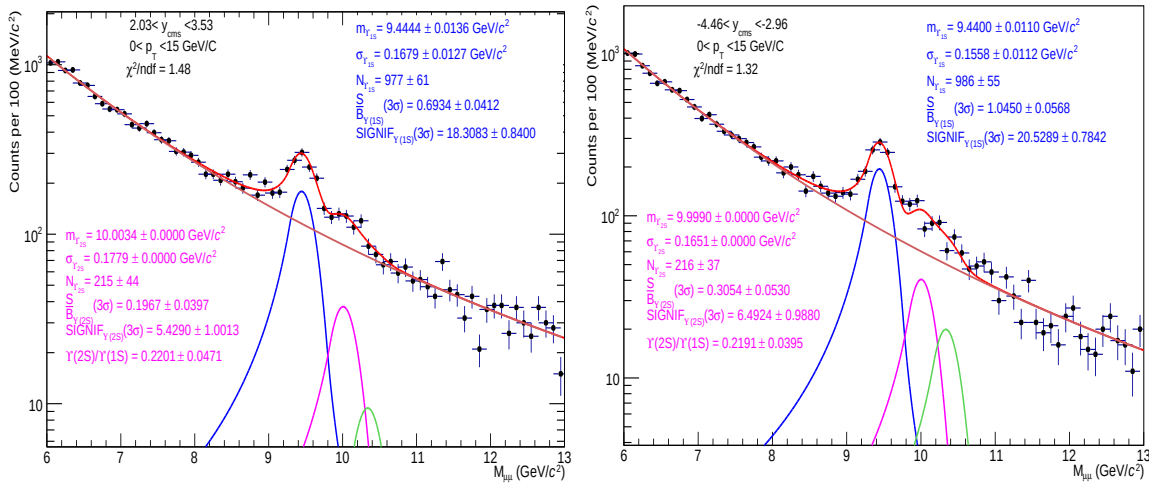

Figure 6.9: Typical fit to the invariant mass spectra for the signal extraction in p–Pb (left) and Pb–p (right) collisions using 3 CB2+VWG function. The shapes of the Υ(1S), Υ(2S) and Υ(3S) states are shown (blue, pink and green), together with the background function (brown) and the total fit (red).

A total of 977±61(6.2%) [986±55(5.5%)] Υ(1S) is found in p–Pb [Pb–p] collisions. The signal significance of Υ(1S) within 3σ range is 18 and 21 for forward and backward rapidity, respectively.

Signal systematics integrated over y and $p_{\rm T}$

The following tests are applied for the signal systematics evaluation:

- The signal is fitted with CB2 and NA60.
- The background is fitted with DE, DP, VWG, POL1, EXPO*POL1.
- The fitting is performed for $[6-13]$ GeV/c^2 and $[7-12]$ GeV/c^2 mass ranges.
- 3 sets of tail parameters (MC pPb@8.16, MC pp@8, DATA pp@13) are used for CB2 and 1 set of tail (MC pPb@8.16) is used for NA60

A total of 40 fitting methods are applied for the signal systematics evaluation of Υ(1S). A weightage factor is considered as the number of the tests using data-driven tail are not same as MC tail.

The fitting results that satisfy both, the convergence of the co-variance matrix and $\chi^2/\text{NDF} \leq 1.6$, are selected for the signal systematics evaluation.

The $p_{\rm T}$ and y integrated systematic plot of Υ(1S) shown in Fig. 6.10

For Υ(2S) and Υ(3S) additional systematic test has been added due to the width scaling described in 6.4.2. Total $40\times3 = 120$ test is applied for signal systematics evaluation (with weightage factor same as Υ(1S)). The $p_{\rm T}$ and y integrated systematic plot of Υ(2S) shown in Fig. 6.11.

The width scaling systematics for higher states have a negligible effect on Υ(1S) counts. The main contribution to the systematic uncertainty on the signal extraction is due to the choice of tail parameter. The summary of total number of Υ(1S), Υ(2S) and Υ(3S) signals are listed in Tab. 6.4.

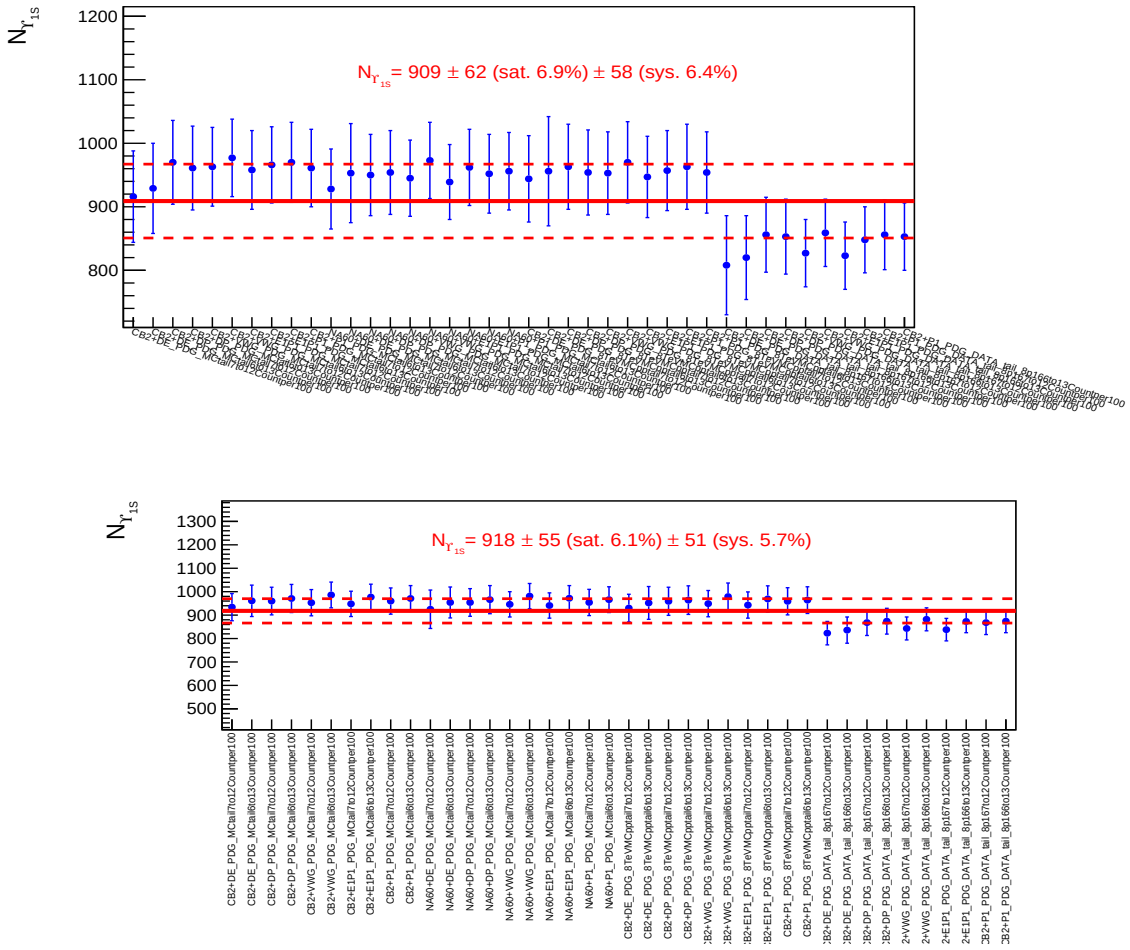

Figure 6.10: The signal systematic plot of Υ(1S) in p–Pb (top) and Pb–p (bottom). X-axis represents the different fitting methods and Y-axis represents the Υ(1S) signal count.

Table 6.4: The number of Υ(1S), Υ(2S) and Υ(2S) integrated over rapidity and $p_{\rm T}$ for both p–Pb and Pb–p periods.

Beam configuration	$N_{\Upsilon(1S)}$	$N_{\Upsilon(2S)}$	$N_{\Upsilon(3S)}$
p-Pb	909±62±58	192±39±14	48±36±8
Pb-p	918±55±51	194±34±13	95±30±11

6.4.4 Signal extraction in differential ($p_{\rm T}$ & $y_{\rm CMS}$) bins

In p–Pb and Pb–p collisions, the $p_{\rm T}$ and rapidity dependence have been estimated for the differential study using 5 intervals (0–2, 2–4, 4–6, 6–8, 8–15 GeV/c) and 3 intervals (2.5–3, 3–3.5, 3.5–4, lab frame), respectively. The same strategy which is discussed in

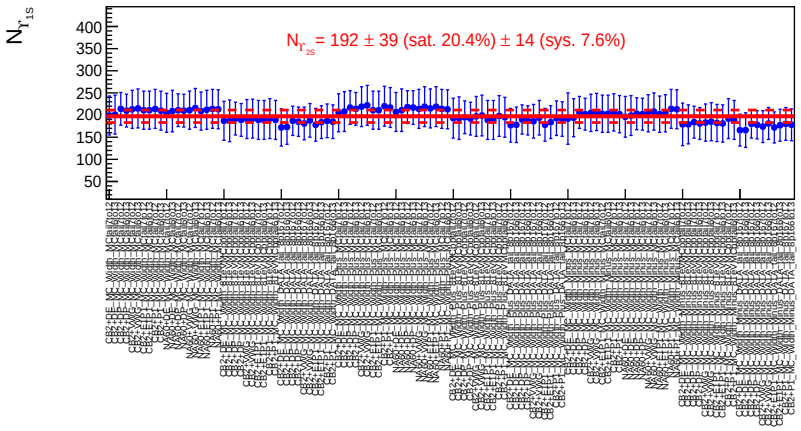

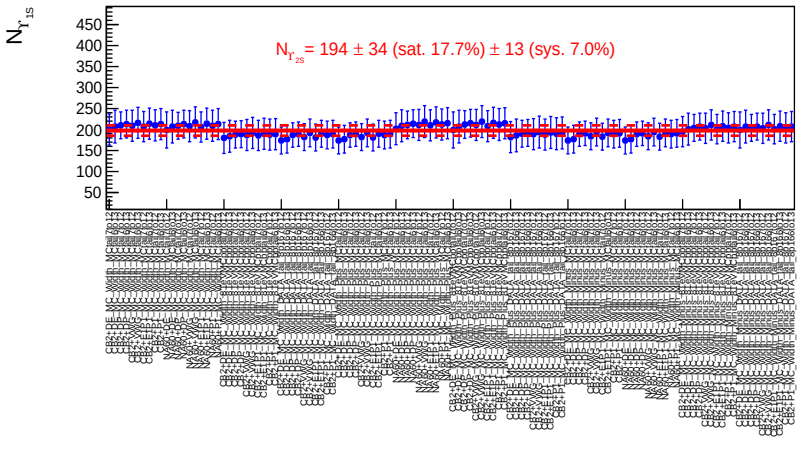

Figure 6.11: The signal systematic plot of Υ(2S) in p–Pb (top) and Pb–p (bottom). X-axis represents the different fitting methods and Y-axis represents the Υ(2S) signal count.

section 6.4.3 is applied for all rapidity and $p_{\rm T}$ bins to calculate the signal systematics. However, due to the limited statistics, the differential study of Υ(2S) and Υ(3S) could not be studied. The number of Υ(1S) signal as a function of $p_{\rm T}$ and $y_{\rm CMS}$ are presented in Tab. 6.5 and 6.6, respectively.

6.5 The proton-proton reference

To calculate the Υ nuclear modification factor, one has to evaluate the proton-proton reference cross section, at the same energy and same kinematic domain as of p–Pb and

Table 6.5: The number of Υ(1S) in $p_{\rm T}$ for both p–Pb and Pb–p periods.

$p_{\rm T}$ (GeV/c)	$N_{\Upsilon(1S)}$ in p-Pb	$N_{\Upsilon(1S)}$ in Pb-p
$[0, 2]$	126±23±7	133±21±8
$[2, 4]$	218±29 ±11	267±29±16
$[4, 6]$	237±28±14	237±27±13
$[6, 8]$	164±28±10	115±18±8
$[8, 15]$	206±36±32	159±28±9

Table 6.6: The number of Υ(1S) in $y_{\rm CMS}$ bin for both p–Pb and Pb–p periods.

p-Pb		Pb-p	
y	$N_{\Upsilon(1S)}$	y	$N_{\Upsilon(1S)}$
$[2.03, 2.53]$	258±31±18	$[-3.46, -2.96]$	287±27±15
$[2.53, 3.03]$	474±45±29	$[-3.96, -3.46]$	498±40±27
$[3.03, 3.53]$	179±26±13	$[-4.46, -3.96]$	149±28±9

Pb–p collisions. Both ALICE and LHCb have measured the Υ differential cross sections at $\sqrt{s}$ = 7 TeV and 8 TeV. The comparison of results between the two experiments can be found in [4] and [5].

A good agreement is observed between the two experiments for both energies within uncertainties. However, the pp results in the rapidity interval of p–Pb ($2.03 < y < 3.53$) and Pb–p ($-4.46 < y < -2.96$) are available from LHCb. Thus, the current energy extrapolation is entirely based on the LHCb results. The LHCb provides the Υ(1S), Υ(2S), and Υ(3S) differential cross section for $2.0 < y < 2.5$, $2.5 < y < 3.0$, $3.0 < y < 3.5$, $3.5 < y < 4.0$ and $4.0 < y < 4.5$ in pp collisions at 2.76 TeV [6], 7 TeV [7], 8 TeV [7], 13 TeV [8]. However, the LHCb pp 8 TeV result can not be directly used as a reference for the ALICE proton-nucleus results, since two corrections (energy and rapidity range) have to be applied.

The rapidity differential cross sections of LHCb results are added in order to obtain the rapidity ranges close to those used for the $R_{\rm pPb}$ measurement. The comparison of rapidity ranges in Tab. 6.7 shows good agreement of rapidity overlap between ALICE p–Pb/Pb–p and LHC pp measurements. We have neglected the remaining 0.03 shift

of rapidity between ALICE p–Pb/Pb–p and LHC pp measurements in the following analysis.

Table 6.7: The LHCb rapidity equivalence for ALICE in p–Pb and Pb–p measurements.

p–Pb		Pb–p	
ALICE p–Pb rapidity	LHCb pp range	ALICE Pb–p rapidity	LHCb pp range
$[2.03, 2.53]$	$[2.0, 2.5]$	$[-3.46, -2.96]$	$[3.0, 3.5]$
$[2.53, 3.03]$	$[2.5, 3.0]$	$[-3.96, -3.46]$	$[3.5, 4.0]$
$[3.03, 3.53]$	$[3.0, 3.5]$	$[-4.46, -3.96]$	$[4.0, 4.5]$
$[2.03, 3.53]$	$[2.5, 3.5]$	$[-4.46, -2.96]$	$[3.0, 4.5]$

Since the p–Pb data have been collected $\sqrt{s_{\rm NN}} = 8.16$ TeV, an energy correction factor has been applied in order to use the pp 8 TeV results. This factor ($\sigma_{8.16}/\sigma_{8.00}$) is evaluated by performing an energy extrapolation starting from LHCb data at $\sqrt{s} = 7$ TeV, 8 TeV and 13 TeV.

6.5.1 Extrapolation techniques

The extrapolation techniques (for calculating energy correction factor) are the same as discussed for interpolation methods in Pb–Pb collisions at $\sqrt{s_{\rm NN}} = 5.02$ TeV analysis [2]. The only difference is that no model shape functions have been considered. The interpolation is based on the fitting of experimental data points. The functions which are used for the interpolation is mentioned below.

- Linear function: $p_0 + p_1.\sqrt{s}$.
- Parabola: $p_0.\sqrt{s} + p_1.\sqrt{s^2}$.
- Positive exponential: $p_0.\sqrt{s}.e^{\frac{\sqrt{s}}{p_1}}$.
- Negative exponential: $p_0(1 - \sqrt{s}.e^{\frac{-\sqrt{s}}{p_1}})$.
- Power law $p_0.\sqrt{s^{p_1}}$.

For each rapidity and $p_{\rm T}$ range, the final result is obtained as the weighted average of the results obtained from all fitting functions. We have evaluated the cross section at 8.16 and 8 TeV from the fitting functions and the ratio of this cross section ($\sigma_{8.16}/\sigma_{8.00}$) is used as an energy correction factor. Multiplying this energy correction factor with the available LHCb pp 8 TeV result (ALICE p–Pb rapidity range), one can obtain the reference results for p–Pb collisions at $\sqrt{s_{\rm NN}}$ = 8.16 TeV.

Reference cross-section in rapidity bins of Υ(1S)

The Υ(1S) branching ratio times production cross sections of LHCb at $\sqrt{s}$ = 8 TeV [7] in ALICE $R_{\rm pPb}$ rapidity ranges are reported in Tab. 6.8. These results are obtained by adding the $p_{\rm T}$ differential cross section up to 15 GeV/c in the mentioned rapidity bin. The statistical and the uncorrelated component of the systematic uncertainties are added in quadrature while the correlated component of the systematic uncertainties is simply added.

Table 6.8: The values of ($BR_{\Upsilon(1S)\to\mu^+\mu^-} \times \sigma$) of LHCb in rapidity bins for pp collisions at $\sqrt{s}$ = 8.00 TeV.

Beam conditions	y	$BR_{\Upsilon(1S)\to\mu^+\mu^-} \times \sigma$ (pb) ± stat ± sys
p–Pb	$[2.03, 2.53]$	879.29±2.19±24.79 (2.94(uncorr) & 24.62(corr))
	$[2.53, 3.03]$	829.66±1.23±23.35 (2.33(uncorr) & 23.23(corr))
	$[3.03, 3.53]$	685.31±1.02±9.31 (2.12(uncorr) & 19.18(corr))
	$[2.03, 3.53]$	2394.26±2.71±67.18 (4.31(uncorr) & 67.04(corr))
Pb–p	$[-4.46, -3.96]$	292.76±1.22±8.28 (1.16(uncorr) & 8.20(corr))
	$[-3.96, -3.46]$	523.96±0.98±14.78 (1.74(uncorr) & 14.67(corr))
	$[-3.46, -2.46]$	685.31±1.02±19.31 (2.12(uncorr) & 19.18(corr))
	$[-4.46, -2.96]$	1502.03±1.87±42.16 (2.98(uncorr) & 42.06(corr))

The similar results as in Tab. 6.8 are also obtained for pp collisions at $\sqrt{s}$ = 7 TeV, 8 TeV and 13 TeV using LHCb measurements. These results are then fitted separately for each rapidity bins of p–Pb and Pb–p to find the extrapolated value for pp collisions at $\sqrt{s}$ = 8.16 and 8.00 TeV using the method as discussed in 6.5.1. The ratio of the cross section ($\sigma_{8.16}/\sigma_{8.00}$)) is used as energy correction factor.

The graphical representation of the fitting functions are shown in Fig. 6.12 and 6.13.

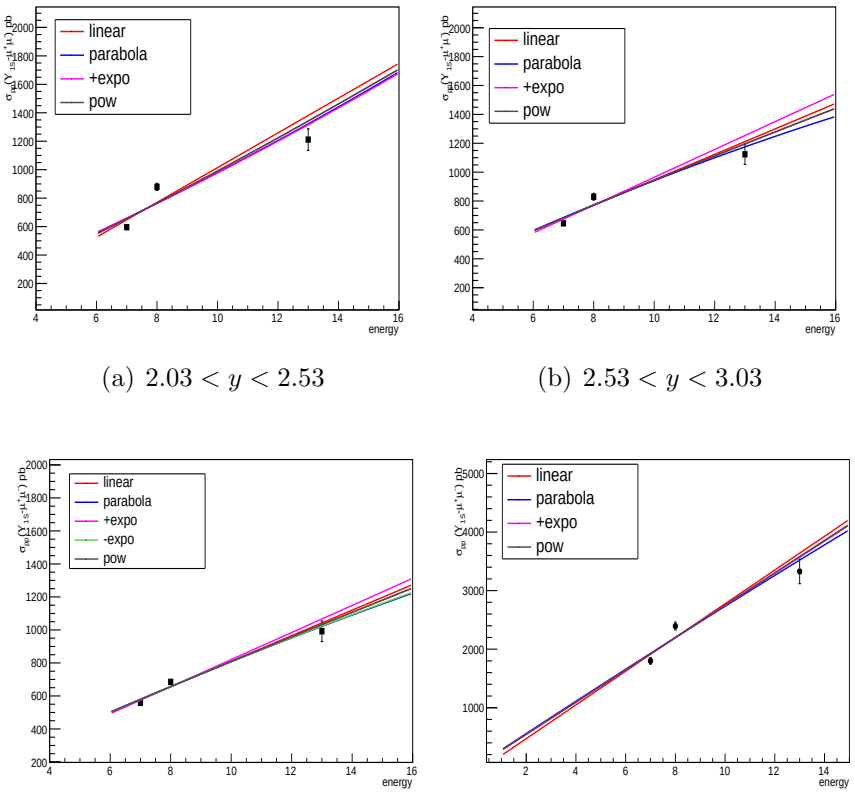

(a) $2.03 < y < 2.53$ (b) $2.53 < y < 3.03$

(c) $3.03 < y < 3.53$ (d) $2.03 < y < 3.53$

Figure 6.12: The energy extrapolation in y bins for the LHC16r (p–Pb) period.

All the functions do not fit the data. The fitting functions, that have $\tilde{\chi}^2$ values larger than three times the minimum value has been discarded. The $\sigma_{8.16}/\sigma_{8.00}$ is evaluated from each surviving function and the final result is obtained as the weighted average of these $\sigma_{8.16}/\sigma_{8.00}$ ratios. The weight is given by the uncertainties on the ratio of the cross sections.

In $\sigma_{8.16}/\sigma_{8.00}$, we have two uncertainties, one is associated with the fit (experimental uncertainty, propagating the fit parameter uncertainties to the extrapolated cross section) and the other is associated with the different interpolating functions, defined as the maximum spread among the various surviving functions and final weighted average. The former is correlated (fully) on 8 and 8.16 TeV cross sections and cancel out in the

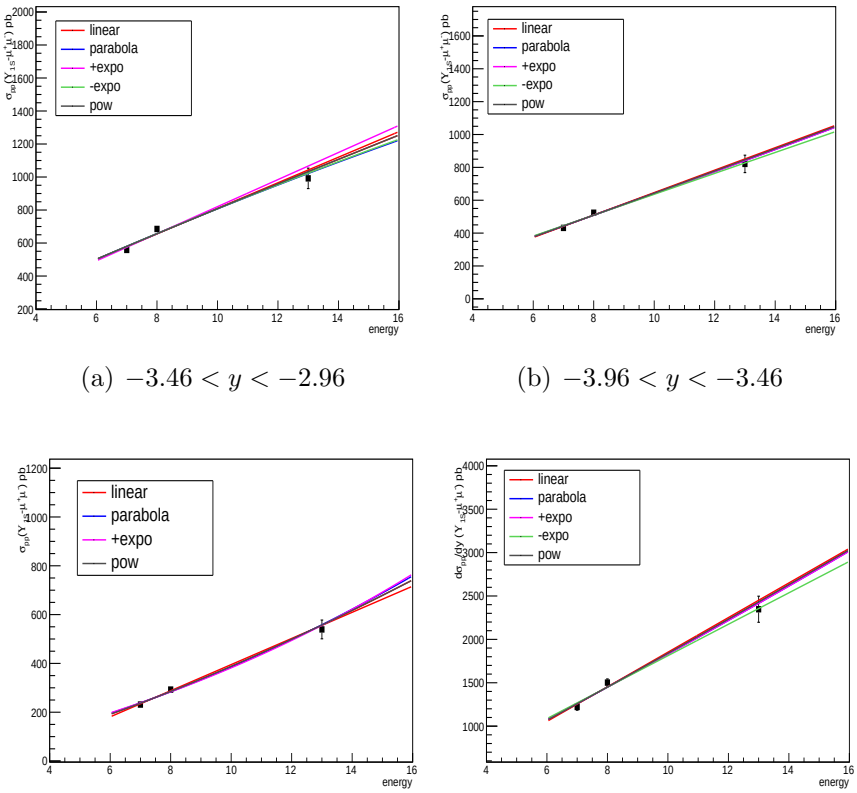

(a) $-3.46 < y < -2.96$ (b) $-3.96 < y < -3.46$

(c) $-4.46 < y < -3.96$ (d) $-4.46 < y < -2.96$

Figure 6.13: The energy extrapolation in y bins for the LHC16s (Pb–p) period.

ratio $\sigma_{8.16}/\sigma_{8.00}$, while the latter contributes to the uncertainty on $\sigma_{8.16}/\sigma_{8.00}$.

The $\sigma_{8.16}/\sigma_{8.00}$ in p–Pb and Pb–p collisions in different y bins are reported in Tab. 6.9.

Table 6.9: $\sigma_{8.16}/\sigma_{8.00}$ values in p–Pb and Pb–p rapidity bins.

Beam conditions	y	$\sigma_{8.16}/\sigma_{8.00}$
p–Pb	$[2.03, 2.53]$	1.020 ± 0.003
	$[2.53, 3.03]$	1.019 ± 0.001
	$[3.03, 3.53]$	1.021 ± 0.001
	$[2.03, 3.53]$	1.020 ± 0.002
Pb–p	$[-4.46, -3.96]$	1.026 ± 0.004
	$[-3.96, -3.46]$	1.021 ± 0.001
	$[-3.46, -2.96]$	1.021 ± 0.001
	$[-4.46, -2.96]$	1.022 ± 0.003

In order to get the pp cross section at 8.16 TeV, we have multiplied the energy factor

to the results in Tab. 6.8. These values are reported in Tab. 6.10.

Table 6.10: The values of ($BR_{\Upsilon(1S)\to\mu^+\mu^-} \times \sigma$) of LHCb in rapidity bins for pp collisions at $\sqrt{s}$ = 8.16 TeV.

Beam conditions	y	$BR_{\Upsilon(1S)\to\mu^+\mu^-} \times \sigma$ (pb) ± stat ± sys
p–Pb	$[2.03, 2.53]$	896.88±2.21±25.29 (3.00 (uncorr) & 25.11 (corr))
	$[2.53, 3.03]$	845.42±1.25±23.79 (2.37 (uncorr) & 23.67 (corr))
	$[3.03, 3.53]$	699.70±1.04±19.71 (1.18 (uncorr) & 19.59 (corr))
	$[2.03, 3.53]$	2442.14±2.78±68.52 (4.39 (uncorr) & 68.38 (corr))
Pb–p	$[-4.46, -3.96]$	300.37±1.25±8.49 (1.19 (uncorr) & 8.41 (corr))
	$[-3.96, -3.46]$	534.96±1.00±15.08 (1.13 (uncorr) & 14.98 (corr))
	$[-3.46, -2.46]$	699.70±1.04±19.71 (1.18 (uncorr) & 19.59 (corr))
	$[-4.46, -2.96]$	1535.08±1.91±43.09 (3.05 (uncorr) & 42.98 (corr))

Reference cross section in $p_{\rm T}$ bins of Υ(1S)

The Υ(1S) branching ratio times production cross sections of LHCb at $\sqrt{s}$ = 8 TeV [7] in p_T bins (ALICE $R_{\rm pPb}$ rapidity ranges) are reported in Tab. 6.11. Since the LHCb data at $\sqrt{s}$ = 8 TeV has been provided in 1 GeV/c wide $p_{\rm T}$ bins, some of them had merged for required $p_{\rm T}$ bin in ALICE $R_{\rm pPb}$ rapidity ranges. The statistical and systematic error are consider in same way as discussed in sec. 6.5.1.

Table 6.11: The values of ($BR_{\Upsilon(1S)\to\mu^+\mu^-} \times \sigma$) of LHCb in forward and backward $p_{\rm T}$ bins for pp collisions at $\sqrt{s}$ = 8.00 TeV.

Beam conditions	$p_{\rm T}$ (GeV/c)	$BR_{\Upsilon(1S)\to\mu^+\mu^-} \times \sigma$ (pb) ± stat ± sys
p–Pb	$[0, 2]$	382.62±1.11±10.84 (1.65(uncorr) & 10.71(corr))
	$[2, 4]$	702.20±1.48±19.86 (2.79(uncorr) & 19.66(corr))
	$[4, 6]$	565.47±1.33±15.97 (2.10(uncorr) & 15.83(corr))
	$[6, 8]$	351.25±1.02±9.96 (1.55(uncorr) & 9.84(corr))
	$[8, 15]$	392.71±1.05±11.05 (1.10(uncorr) & 11.00(corr))
Pb–p	$[0, 2]$	261.65±0.80±7.44 (1.31(uncorr) & 7.33(corr))
	$[2, 4]$	459.72±1.04±13.01 (1.90(uncorr) & 12.87(corr))
	$[4, 6]$	354.98±0.90±10.05 (1.52(uncorr) & 9.94(corr))
	$[6, 8]$	213.11±0.69±6.04 (0.93(uncorr) & 5.97(corr))
	$[8, 15]$	212.57±0.68±5.98 (0.61(uncorr) & 5.95(corr))

The energy correction factor is evaluated in the same way as in rapidity bins by fitting the experimental data points provided by LHCb at $\sqrt{s}$ = 7, 8 and 13 TeV. The graphical representation of the data fits are shown in Fig. 6.14 and 6.15.

$\sigma_{8.16}/\sigma_{8.00}$ obtained from the functional dependence (Fig. 6.14 and 6.15) in p–Pb and Pb–p collisions in different $p_{\rm T}$ bins are reported in Tab. 6.12.

Table 6.12: The values of $\sigma_{8.16}/\sigma_{8.00}$ in ALICE p–Pb and Pb–p $p_{\rm T}$ bins.

Beam conditions	$p_{\rm T}$ (GeV/c)	$\sigma_{8.16}/\sigma_{8.00}$
p–Pb	[0, 2]	1.017 ± 0.003
	[2, 4]	1.018 ± 0.002
	[4, 6]	1.020 ± 0.002
	[6, 8]	1.022 ± 0.001
	[8, 15]	1.026 ± 0.004
Pb–p	[0, 2]	1.017 ± 0.004
	[2, 4]	1.019 ± 0.002
	[4, 6]	1.022 ± 0.001
	[6, 8]	1.024 ± 0.004
	[8, 15]	1.030 ± 0.004

In order to get the pp cross section at 8.16 TeV, we have multiplied the energy factor to the results in Tab. 6.11. These value are reported in Tab. 6.13.

Table 6.13: The values of ($BR_{\Upsilon(1S)\to\mu^+\mu^-} \times \sigma$) of LHCb in forward and backward $p_{\rm T}$ bins for pp collisions at $\sqrt{s}$ = 8.16 TeV.

Beam conditions	$p_{\rm T}$ (GeV/c)	$BR_{\Upsilon(1S)\to\mu^+\mu^-} \times \sigma$ (pb) ± stat ± sys
p–Pb	[0, 2]	389.13±1.13±11.02 (1.68 (uncorr) & 10.90 (corr))
	[2, 4]	714.84±1.51±20.22 (2.84 (uncorr) & 20.02 (corr))
	[4, 6]	576.78±1.35±16.29 (2.15 (uncorr) & 16.15 (corr))
	[6, 8]	358.98±1.05±10.18 (1.59 (uncorr) & 10.05 (corr))
	[8, 15]	402.92±1.08±11.34 (1.13 (uncorr) & 11.28 (corr))
Pb–p	[0, 2]	266.10± 0.82± 7.57 (1.33 (uncorr) & 7.45 (corr))
	[2, 4]	468.46±1.06±13.26 (1.94 (uncorr) & 13.12 (corr))
	[4, 6]	362.79±0.92±10.28 (1.55 (uncorr) & 10.16 (corr))
	[6, 8]	218.23±0.71±6.18 (0.96 (uncorr) & 6.11 (corr))
	[8, 15]	218.94±0.70±6.16 (0.63 (uncorr) & 6.13 (corr))

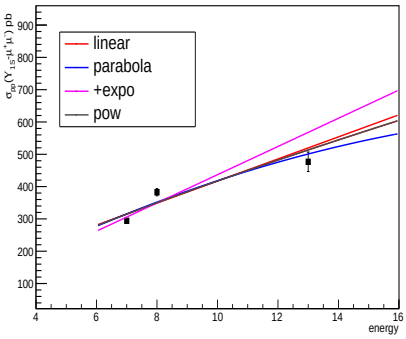

(a) $0 < p_T < 2$ GeV/c

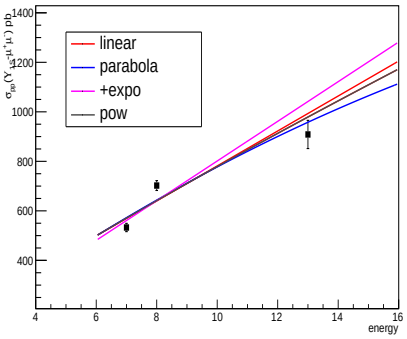

(b) $2 < y < 4$ GeV/c

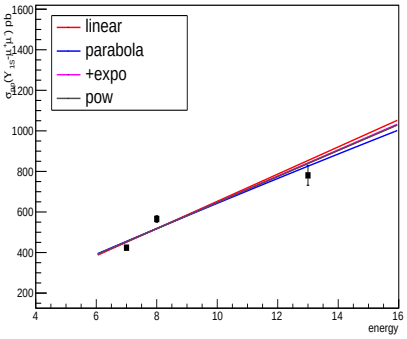

(c) $4 < p_T < 6$ GeV/c

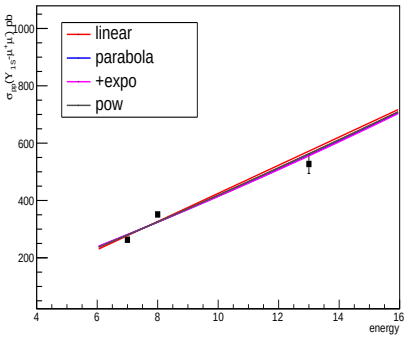

(d) $6 < p_T < 8$ GeV/c

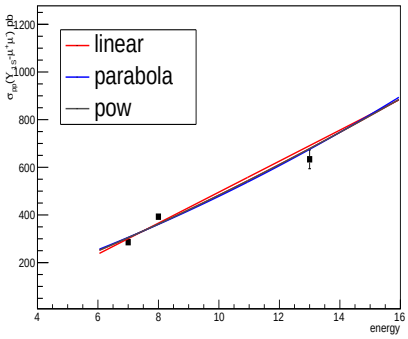

(e) $8 < p_T < 15$ GeV/c

Figure 6.14: The energy extrapolation in $p_{\rm T}$ bins for the LHC16r (p–Pb) period.

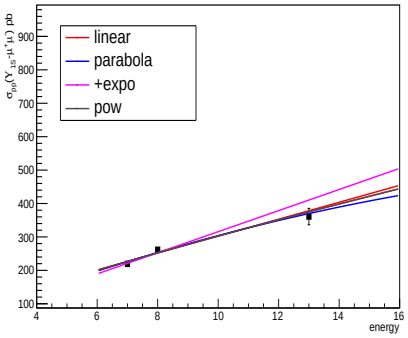

(a) $0 < p_T < 2$ GeV/c

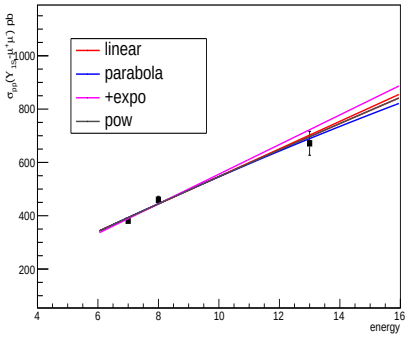

(b) $2 < y < 4$ GeV/c

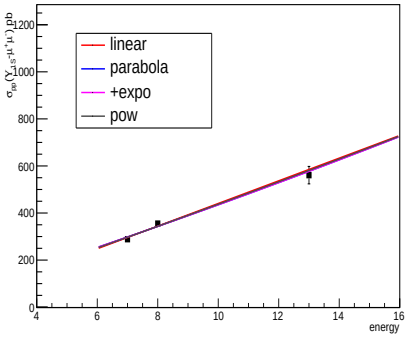

(c) $4 < p_T < 6$ GeV/c

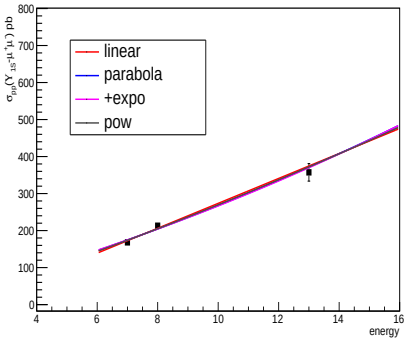

(d) $6 < p_T < 8$ GeV/c

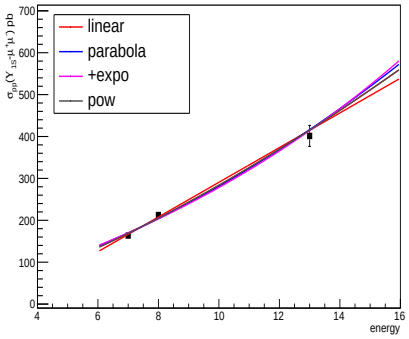

(e) $8 < p_T < 15$ GeV/c

Figure 6.15: The energy extrapolation in $p_{\rm T}$ bins for the LHC16s (Pb–p) period.

6.5.2 Integrated pp reference cross section of Υ(2S) and Υ(2S)

The Υ(2S) and Υ(3S) reference cross sections, integrated over rapidity and $p_{\rm T}$ are evaluated following the same procedure as of the Υ(1S). The values are reported in Tab. 6.14 and Tab. 6.15

Table 6.14: The values of $BR_{\Upsilon(2S)\to\mu^+\mu^-} \times \sigma$ of LHCb in rapidity bins for pp collisions at $\sqrt{s} = 8.16$ TeV.

Beam conditions	y	$BR_{\Upsilon(2S)\to\mu^+\mu^-} \times \sigma$ (pb) $\pm$ stat $\pm$ sys
p–Pb	$[2.03, 3.53]$	615.54±1.53±17.29 (1.41 (uncorr) & 17.24 (corr))
Pb–p	$[-4.46, -2.96]$	381.37±1.05±10.73 (1.03 (uncorr) & 10.68 (corr))

Table 6.15: The values of $BR_{\Upsilon(3S)\to\mu^+\mu^-} \times \sigma$ of LHCb in rapidity bins for pp collisions at $\sqrt{s} = 8.16$ TeV.

Beam conditions	y	$BR_{\Upsilon(3S)\to\mu^+\mu^-} \times \sigma$ (pb) $\pm$ stat $\pm$ sys
p–Pb	$[2.03, 3.53]$	281.91±1.11±7.91 (0.58 (uncorr) & 7.89 (corr))
Pb–p	$[-4.46, -2.96]$	180.03±0.77±5.06 (0.52 (uncorr) & 5.04 (corr))

6.6 Systematic uncertainties

The detector uncertainties (tracking efficiency, matching) which are supposed to be independent of the detected particle are taken the same as the J/ψ [9] analysis. The other systematic uncertainties are discussed in the following subsections.

6.6.1 Trigger efficiencies

The real trigger response in data is different from the trigger response in Monte Carlo (MC) simulation. This difference is counted as trigger response systematic uncertainty.

The steps are as follows:

- step1: Evaluate the response function (RF) in DATA and Embedding MC for Upsilon in Pb-Pb 5.02 TeV
- step2: The RF has fitted in DATA as well as MC with the fitting function

$$F(p_{\rm T}) = a + b \times \left(1 + erf(\frac{p_{\rm T} - p_{\rm T}^{\rm mean}}{2\sigma})\right) \tag{6.5}$$

- step3: Then evaluate the relative difference of fit parameters ($p_{\rm T}^{\rm mean}$, σ) between MC and data.
- step4: Evaluate RF in MC for Upsilon in p-Pb 8.16 TeV and fit with $F(p_{\rm T})$.
- step5: Modify the parameters ($p_{\rm T}^{\rm mean}$, σ) of the fit function obtained from the step 4 by the same relative difference estimated from step 3. This acts as RF for data in p–Pb (Pb–p) at 8.16 TeV.

The RF in Pb-Pb (data and MC) defined as:

$$RF = \frac{L_{pT}}{All_{pT}}$$

where:

L_{pT} : $GetMatchTrigger() >= 2$ (1.0 GeV/c single muon p_T cut)

All_{pT} : $GetMatchTrigger() >= 1$ (0.5 GeV/c single muon p_T cut)

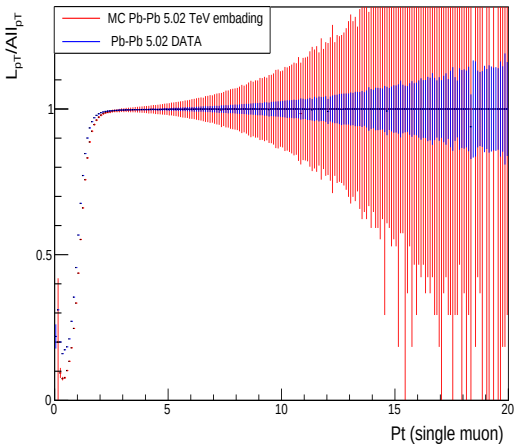

Figure 6.16: The trigger response function in Pb–Pb period.

The RF in data and embedding MC for Υ(1S) in Pb–Pb 5.02 TeV shown in Fig. 6.16

This RF are fitted with $F(p_{\rm T})$ and evaluate the relative difference of fit parameters ($p_{\rm T}^{\rm mean}$, σ) between MC and data of Pb–Pb.

Trigger Response function (RF) in p–Pb MC defined as:

$$RF = \frac{All_{pT}}{Total_{pT}}$$

Where:

All_{pT} : $GetMatchTrigger() >= 1$ (0.5 GeV/c single muon p_T cut)
$Total_{pT}$: No $GetMatchTrigger()$ cut

In order to get RF function in p–Pb data, we have fitted the RF MC p–Pb and modified $p_{\rm T}^{\rm mean}$ and σ by the relative difference obtained in Pb–Pb data and MC RF

fitting. The RF function for p–Pb is shown in Fig. 6.17.

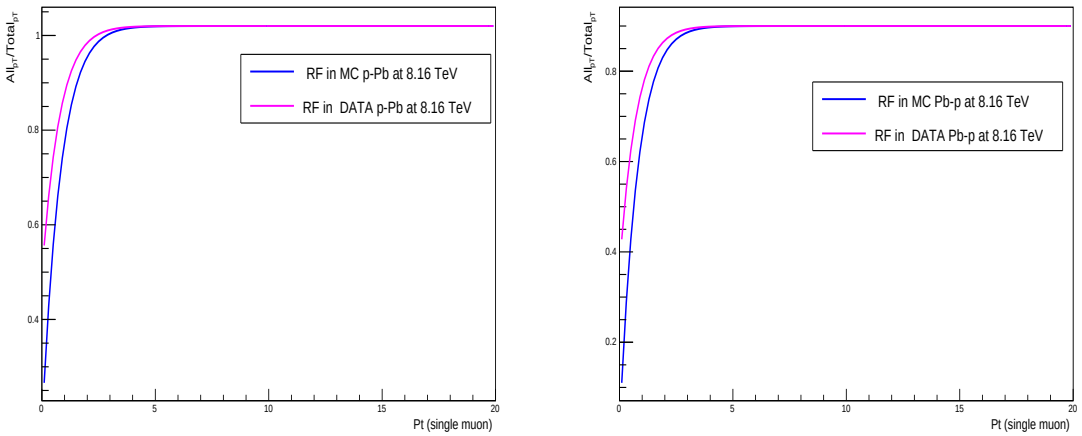

Figure 6.17: The trigger response function in p–Pb (left) and Pb-p(right) periods.

The trigger response systematic has been extracted as follows:

1. Select muons matching the All_{pT} trigger in Υ MC p–Pb 8.16 TeV simulation.

2. Fill the histogram with a weight of $RF_{MC_{pPb}}/RF_{DATA_{pPb}}$ and without weight.

3. Extract the number of Upsilon in the above two cases and take the relative difference as the systematic uncertainty.

The $p_{\rm T}$ and y integrated trigger response uncertainty amounts to 0.6% in p–Pb and 0.2% in Pb–p. As a function of $y_{\rm CMS}$ and $p_{\rm T}$, the uncertainties are reported in Tab. 6.16 and Tab. 6.17, respectively.

Another 1% trigger systematic error is added due to efficiency systematic error and A$\times\epsilon$ systematic error [9].

Table 6.16: The values of trigger RF uncertainty in p–Pb and Pb–p periods as a function of rapidity

Beam conditions	$y_{\rm CMS}$	uncertainty (%)
p–Pb	$[2.03, 2.53]$	0.50
	$[2.53, 3.03]$	0.55
	$[3.03, 3.53]$	0.87
Pb–p	$[-4.46, -3.96]$	0.11
	$[-3.96, -3.46]$	0.20
	$[-3.46, -2.46]$	0.24

Table 6.17: The values of trigger RF uncertainty in p–Pb and Pb–p periods as a function of $p_{\rm T}$.

Beam conditions	$p_{\rm T}$ (GeV/c)	uncertainty (%)
p–Pb	$[0, 2]$	0.33
	$[2, 4]$	0.65
	$[4, 6]$	0.83
	$[6, 8]$	0.85
	$[8, 15]$	0.89
Pb–p	$[0, 2]$	0.11
	$[2, 4]$	0.18
	$[4, 6]$	0.19
	$[6, 8]$	0.27
	$[8, 15]$	0.41

6.6.2 MC input systematic

Υ MC systematic are evaluated using the different input parameterizations. In order to calculate this, we have generated different MC data sets with varying $p_{\rm T}$ and y distributions. The input shapes are listed below:

- AliGenMuonLib: The $p_{\rm T}$ and y input shape were obtained by using the existing AliGenMuonLib class of pp. A shadowing parameterization for p–Pb at 8.8 TeV (PtUpsilonPPb8800ShFdummy) is multiplied to the input $p_{\rm T}$ and y distributions which are taken care of shadowing factor. We have added (subtracted) the rapidity shift for the asymmetric collision in p–Pb (Pb–p) with the y distributions.

- LHCb: This input parametrization was obtained by fitting the LHCb pp data at

$\sqrt{s_{\rm NN}}$ = 8 TeV in the ALICE rapidity range. The rapidity shift for p–Pb system and shadowing factor is also considered in the parameterization.

- ALICE: This input parameterization was obtained by fitting the ALICE p–Pb (Pb–p) data at $\sqrt{s_{\rm NN}}$ = 8.16 TeV

For the evaluation of systematic uncertainty, we have selected those MC sets which have the input shapes that are very close to the Υ yields distributions. The maximum relative difference between the various input parameterization has been assumed as MC systematic uncertainty. The $p_{\rm T}$ and y integrated systematic uncertainty of Υ(1S) (Υ(2S)) is $\approx$ 1% (1.3%) and 1% (1.6%) for p–Pb and Pb–p collisions, respectively. The MC systematic uncertainty for the rapidity and $p_{\rm T}$ bins are tabulated in Table 6.18 and Table 6.19, respectively.

Table 6.18: The MC systematic uncertainty values in p–Pb and Pb–p periods as a function of y.

Beam conditions	$y_{\rm CMS}$	uncertainty (%)
p–Pb	$[2.03, 2.53]$	4.0
	$[2.53, 3.03]$	0.5
	$[3.03, 3.53]$	1.5
Pb–p	$[-4.46, -3.96]$	4.0
	$[-3.96, -3.46]$	0.4
	$[-3.46, -2.46]$	1.3

6.6.3 List of systematic uncertainties

The systematic uncertainties in cross-section and nuclear modification factor measurements are summarized in Tab. 6.20.

Table 6.19: The MC systematic uncertainty values in p–Pb and Pb–p periods as a function of $p_{\rm T}$.

Beam conditions	$p_{\rm T}$ (GeV/c)	uncertainty (%)
p–Pb	$[0, 2]$	1.0
	$[2, 4]$	1.0
	$[4, 6]$	1.0
	$[6, 8]$	0.6
	$[8, 15]$	0.7
Pb–p	$[0, 2]$	1.0
	$[2, 4]$	1.4
	$[4, 6]$	1.1
	$[6, 8]$	1.2
	$[8, 15]$	0.6

Table 6.20: The systematic uncertainties, in percentage, on the three Υ state cross sections and $R_{\rm pPb}$ measurements for both p–Pb and Pb–p collisions. Ranges in parentheses stand for the maximum variation as a function of $y_{\rm CMS}$ or $p_{\rm T}$. When no ranges are mentioned, the quoted values are valid for both the integrated and the differential measurements. Error type I means that the uncertainties are correlated. If no error type is specified, the uncertainties are considered as uncorrelated.

Sources	Υ(1S)		Υ(2S)		Υ(3S)	
	p–Pb	Pb–p	p–Pb	Pb–p	p–Pb	Pb–p
Signal extraction	6.4 (5.1–15.9)	5.7 (5.5–8.5)	8.8	8.4	17.4	12.6
Trigger efficiency	1.2 (1.1–1.3)	1.0 (1.0–1.1)	1.2	1.0	1.2	1.0
Tracking efficiency	1.0	2.0	1.0	2.0	1.0	2.0
Matching efficiency	1.0	1.0	1.0	1.0	1.0	1.0
MC inputs	1.0 (0.5–4.0)	1.0 (0.4–4.0)	1.3	1.6	1.4	1.8
pp reference	0.2 (0.1–0.4)	0.2 (0.1–0.4)	0.2	0.3	0.2	0.2
pp reference (I)	2.8		2.8		2.8	
$\mathcal{L}_{\rm int}^{\rm pPb}$	2.1	2.2	2.1	2.2	2.1	2.2
$\mathcal{L}_{\rm int}^{\rm pPb}$ (I)	0.5	0.7	0.5	0.7	0.5	0.7
B.R. (I)	2.0		8.8		9.6	

6.7 Results

6.7.1 Production cross sections

The inclusive Υ(nS) production cross sections have been determined in the forward ($2.03 < y_{\rm cms} < 3.53$) and backward ($-4.46 < y_{\rm cms} < -2.96$) rapidities and their values are:

Forward:

- $\sigma^{\Upsilon(1S)}_{\rm pPb} = 14.50 \pm 0.99$ (stat.) ± 1.02 (uncor. syst.) ± 0.30 (cor. syst.) μb
- $\sigma^{\Upsilon(2S)}_{\rm pPb} = 3.92 \pm 0.80$ (stat.) ± 0.38 (uncor. syst.) ± 0.35 (cor. syst.) μb
- $\sigma^{\Upsilon(3S)}_{\rm pPb} = 0.87 \pm 0.66$ (stat.) ± 0.15 (uncor. syst.) ± 0.08 (cor. syst.) μb,

backward:

- $\sigma^{\Upsilon(1S)}_{\rm Pbp} = 10.470 \pm 0.63$ (stat.) ± 0.69 (uncor. syst.) ± 0.22 (cor. syst.) μb
- $\sigma^{\Upsilon(2S)}_{\rm Pbp} = 2.84 \pm 0.50$ (stat.) ± 0.26 (uncor. syst.) ± 0.25 (cor. syst.) μb
- $\sigma^{\Upsilon(3S)}_{\rm Pbp} = 0.87 \pm 0.66$ (stat.) ± 0.15 (uncor. syst.) ± 0.08 (cor. syst.) μb,

In the systematic uncertainties, the first term is correlated and the second term is uncorrelated in terms of rapidity.

The data collected during the p–Pb and Pb–p collisions at $\sqrt{s_{\rm NN}} = 8.16$ TeV allow for the measurement of the differential Υ(1S) production cross sections in $y_{\rm CMS}$ or $p_{\rm T}$ intervals, up to $p_{\rm T} < 15$ GeV/c. The differential cross sections are illustrated in Fig. 6.18

as a function of rapidity, integrated over transverse momentum, and in Fig. 6.19, as a function of $p_{\rm T}$, in the forward and backward rapidity regions. In both figures, the statistical uncertainties are shown as vertical error bars, while the systematic uncertainties are shown as boxes around the points. The horizontal error bars correspond to the $y_{\rm CMS}$ or $p_{\rm T}$ bin widths. The cross sections evaluated at forward and backward rapidities are also compared with the pp ones, obtained through the interpolation procedure described in sec. 6.5, scaled by the lead atomic mass number. The comparison plot shows that in

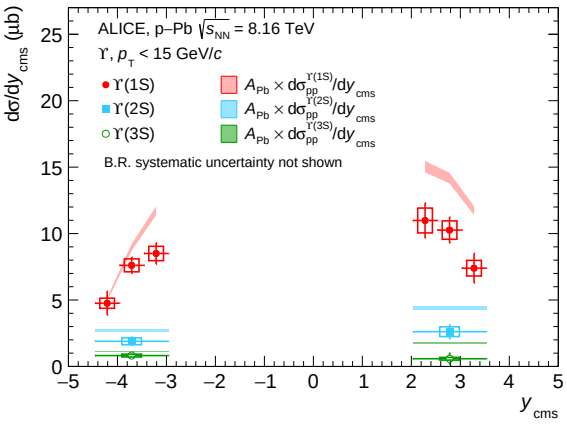

Figure 6.18: The differential production cross section of Υ(1S), Υ(2S) and Υ(3S) as a function of $y_{\rm CMS}$, at $\sqrt{s_{\rm NN}} = 8.16$ TeV. The reference cross section in pp collisions, obtained through the interpolation procedure described in Sec. 6.5 and scaled by $A_{\rm Pb} = 208$, is shown as a band [1]

the forward-rapidity the Υ(1S) production cross sections are smaller compared to the pp ones, especially at low $p_{\rm T}$, suggesting the role of CNM effects in p–Pb collisions. On the contrary, in the backward-rapidity range, the pp and the Pb–p cross sections are quite close and hence the nuclear effects seem to have a less prominent role.

The differential cross section times the branching ratio as function of $y_{\rm CMS}$ and $p_{\rm T}$ are reported in Tab. 6.21 and Tab. 6.22 respectively.

The limited statistics available in the data sample allows the evaluation of the overall Υ(2S) and Υ(3S) production cross sections in the forward and backward-rapidity regions as shown in Fig. 6.18. A suppression with respect to the corresponding pp reference,

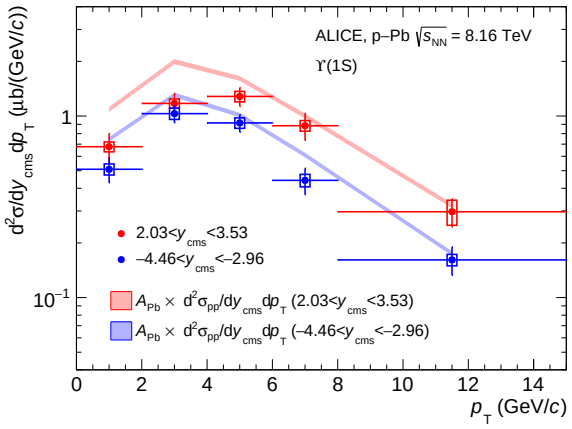

Figure 6.19: The differential production cross section of ϒ(1S) as a function of $p_{\rm T}$, at forward (closed symbols) and backward (open symbols) rapidity, at $\sqrt{s_{\rm NN}}$ = 8.16 TeV. The reference cross section in pp collisions, obtained through the interpolation procedure described in Sec. 6.5 and scaled by $A_{\rm Pb}$ = 208, is shown as a band [1].

Table 6.21: The value of BR . dσ/dy in $y_{\rm CMS}$ bin at $\sqrt{s_{\rm NN}}$ = 8.16 TeV in p–Pb and Pb–p collisions.

Beam conditions	$y_{\rm CMS}$	BR . dσ/dy (nb)
p–Pb	$[2.03, 2.53]$	272.409 ± 32.739 (stat) ± 23.208 (sys)
	$[2.53, 3.03]$	254.537 ± 24.166 (stat) ± 17.197 (sys)
	$[3.03, 3.53]$	183.371 ± 26.637 (stat) ± 14.602 (sys)
Pb–p	$[-4.46, -3.96]$	117.965 ± 22.170 (stat) ± 9.424 (sys)
	$[-3.96, -3.46]$	188.691 ± 15.157 (stat) ± 12.071 (sys)
	$[-3.46, -2.46]$	210.829 ± 19.843 (stat) ± 13.399 (sys)

Table 6.22: The value of BR . $d^2\sigma$/dyd$p_{\rm T}$ in $p_{\rm T}$ bin at $\sqrt{s_{\rm NN}}$ = 8.16 TeV in p–Pb and Pb–p collisions.

Beam conditions	$p_{\rm T}$ (GeV/c)	BR . $d^2\sigma$/dyd$p_{\rm T}$ (nb)
p–Pb	$[0, 2]$	16.801 ± 3.067 (stat) ± 1.058 (sys)
	$[2, 4]$	29.099 ± 3.871 (stat) ± 1.710 (sys)
	$[4, 6]$	31.796 ± 3.757 (stat) ± 2.115 (sys)
	$[6, 8]$	21.928 ± 3.744 (stat) ± 1.486 (sys)
	$[8, 15]$	7.364 ± 1.287 (stat) ± 1.165 (sys)
Pb–p	$[0, 2]$	12.623 ± 1.993 (stat) ± 0.879 (sys)
	$[2, 4]$	25.567 ± 2.777 (stat) ± 1.794 (sys)
	$[4, 6]$	22.719 ± 2.589 (stat) ± 1.484 (sys)
	$[6, 8]$	10.967 ± 1.171 (stat) ± 0.858 (sys)
	$[8, 15]$	3.998 ± 0.704 (stat) ± 0.265 (sys)

scaled by $A_{\rm Pb} = 208$, is observed.

6.7.2 Ratio of Υ(nS) $\to \mu^+\mu^-$ to Υ(1S) $\to \mu^+\mu^-$ cross section

The mass difference between the Υ states are very small, therefore most of the systematic uncertainties, apart from those on the signal extraction and MC input shape, cancel in the ratio of their yields. Thus it can be expressed as:

$$[\Upsilon({\rm nS})/\Upsilon({\rm 1S})]_{\rm pPb} = \frac{N_{\Upsilon({\rm nS})}/(A\times\epsilon)_{\Upsilon({\rm nS})}}{N_{\Upsilon({\rm 1S})}/(A\times\epsilon)_{\Upsilon({\rm 1S})}}.$$

The values of Υ(2S) over Υ(1S) ratio, evaluated at forward and backward rapidity, are similar:

$$[\Upsilon({\rm 2S})/\Upsilon({\rm 1S})]_{\rm pPb}(2.03 < y_{\rm cms} < 3.53) = 0.21 \pm 0.05\ ({\rm stat.}) \pm 0.02\ ({\rm syst.}),$$
$$[\Upsilon({\rm 2S})/\Upsilon({\rm 1S})]_{\rm pPb}(-4.46 < y_{\rm cms} < -2.96) = 0.21 \pm 0.04\ ({\rm stat.}) \pm 0.01\ ({\rm syst.}).$$

Fig. 6.20 shows the ratio $[\Upsilon({\rm 2S})/\Upsilon({\rm 1S})]_{\rm pPb}$ at $\sqrt{s_{\rm NN}} = 8.16$ TeV which also compared with the results obtained by the LHCb Collaboration in pp collisions at $\sqrt{s} = 8$ TeV [7]. The values have been found to be compatible, within experimental uncertainties.

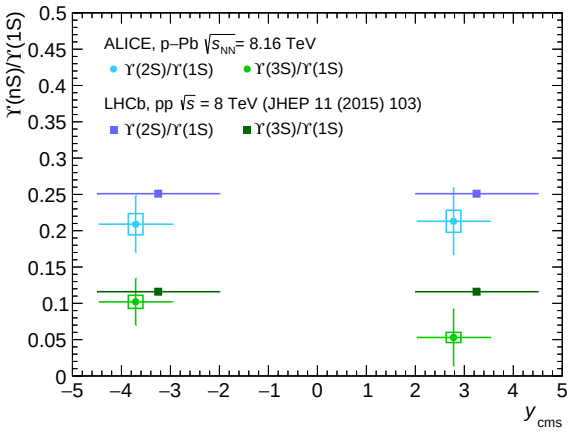

Figure 6.20: The ratio of Υ(nS) to Υ(1S) yields in p–Pb collisions at $\sqrt{s_{\rm NN}} = 8.16$ TeV and in pp collisions at $\sqrt{s} = 8$ TeV [7].

The comparison of the Υ(3S) to Υ(1S) ratio is shown in Fig. 6.20. The numerical values at forward and backward rapidity regions are:

$$[\Upsilon(3S)/\Upsilon(1S)]_{\rm pPb}(2.03 < y_{\rm cms} < 3.53) = 0.053 \pm 0.039\ (\text{stat.}) \pm 0.007\ (\text{syst.}),$$
$$[\Upsilon(3S)/\Upsilon(1S)]_{\rm pPb}(-4.46 < y_{\rm cms} < -2.96) = 0.102 \pm 0.032\ (\text{stat.}) \pm 0.009\ (\text{syst.}).$$

which are also in agreements with the LHCb pp results within the experimental uncertainties.

6.8 Nuclear Modification factor ($R_{\rm pPb}$)

The matter effects in p–Pb collisions can be better understood through the nuclear modification factor. The numerical values for the Υ states $R_{\rm pPb}$ in the forward- and in the backward-rapidity regions, integrated over $p_{\rm T}$, are:

$$R_{\rm pPb}^{\Upsilon(1S)}(2.03 < y_{\rm cms} < 3.53) = 0.71 \pm 0.05\ (\text{stat.}) \pm 0.05\ (\text{uncor. syst.}) \pm 0.02\ (\text{cor. syst.}),$$
$$R_{\rm pPb}^{\Upsilon(1S)}(-4.46 < y_{\rm cms} < -2.96) = 0.81 \pm 0.05\ (\text{stat.}) \pm 0.05\ (\text{uncor. syst.}) \pm 0.02\ (\text{cor. syst.}),$$
$$R_{\rm pPb}^{\Upsilon(2S)}(2.03 < y_{\rm cms} < 3.53) = 0.59 \pm 0.12\ (\text{stat.}) \pm 0.05\ (\text{uncor. syst.}) \pm 0.02\ (\text{cor. syst.})$$
$$R_{\rm pPb}^{\Upsilon(2S)}(-4.46 < y_{\rm cms} < -2.96) = 0.69 \pm 0.12\ (\text{stat.}) \pm 0.05\ (\text{uncor. syst.}) \pm 0.02\ (\text{cor. syst.}),$$
$$R_{\rm pPb}^{\Upsilon(3S)}(2.03 < y_{\rm cms} < 3.53) = 0.32 \pm 0.24\ (\text{stat.}) \pm 0.06\ (\text{uncor. syst.}) \pm 0.01\ (\text{cor. syst.})$$
$$R_{\rm pPb}^{\Upsilon(3S)}(-4.46 < y_{\rm cms} < -2.96) = 0.71 \pm 0.23\ (\text{stat.}) \pm 0.09\ (\text{uncor. syst.}) \pm 0.02\ (\text{cor. syst.})$$

The value of $R_{\rm pPb}$ as shown in Fig. 6.21, indicates a clear suppression of the Υ(1S) production in p–Pb collisions, with respect to pp collisions, both at forward and backward rapidity regions, with a hint of slightly higher suppression at forward $y_{\rm CMS}$. The measured $R_{\rm pPb}$ is found to be 4.0σ and 2.4σ below the unity line in p–Pb and Pb–p collisions,

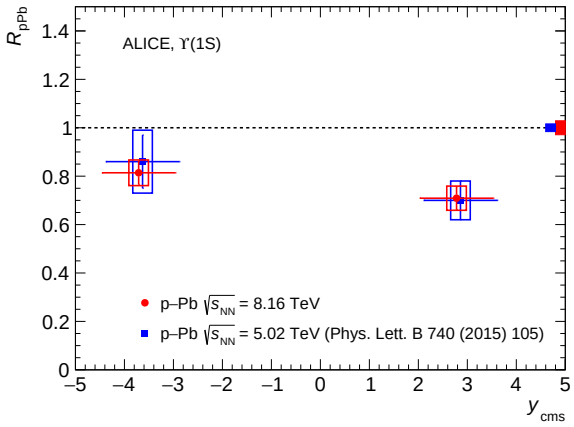

Figure 6.21: The $R_{\rm pPb}$ of Υ(1S) at $\sqrt{s_{\rm NN}} = 8.16$ TeV and 5.02 TeV obtained at same kinematic domain [10].

respectively. The results are also compatible with the values obtained in p–Pb collisions at $\sqrt{s_{\rm NN}} = 5.02$ TeV [10] measurements, as shown in Fig. 6.21. It may be noted that the global uncertainties at the two energies are different. In 5.02 TeV, only the correlated part of luminosity uncertainty is taken as global whereas, at 8.16 TeV, the uncertainties on the branching ratio, correlated pp reference and correlated luminosity uncertainty have been considered in the global systematic.

The value of $R_{\rm pPb}$ for Υ(2S) (Υ(3S)) is below unity with 3.1σ (2.7σ) at forward rapidity and 2.3σ (1.2σ) at backward rapidity. The $R_{\rm pPb}$ difference between Υ(2S) and Υ(1S) amount to $\approx 0.5\sigma$ at both the rapidity regions suggesting a similar effect on the production yields of the two Υ states in p–Pb collisions, with respect to pp. The large uncertainties on the Υ(3S) $R_{\rm pPb}$ do not allow any strong conclusions on the behavior of the most loosely bound bottomonium in p–Pb collisions.

6.8.1 $R_{\rm pPb}$ as a function of $y_{\rm CMS}$

The $R_{\rm Pbp}$ of Υ(1S) has been estimated in 3 rapidity bins and shown in Fig. 6.22 along with the results obtained at $\sqrt{s_{\rm NN}} = 5.02$ TeV. The values of $R_{\rm pPb}$ in the rapidity bins are reported in Tab. 6.23. At the backward rapidity, the study seems to indicate a slope

towards the mid rapidity. This is an unexpected result and might indicate the presence of a new effect. However, this result needs to be established with higher statistics and more finner rapidity bins.

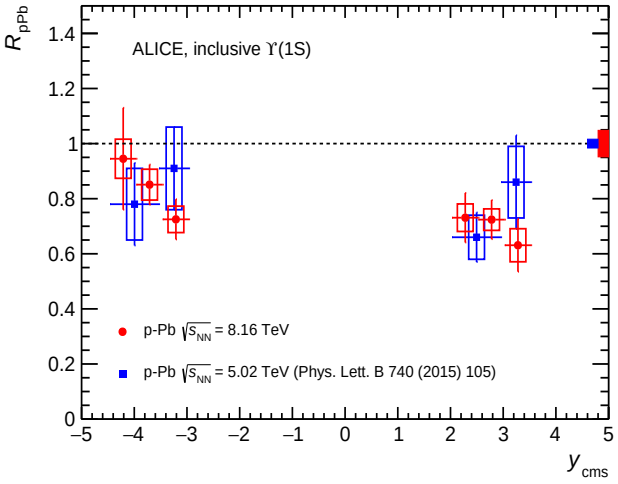

Figure 6.22: The nuclear modification factor for inclusive Υ(1S) production in p-Pb and Pb-p collisions at $\sqrt{s_{\rm NN}}$ = 8.16 TeV as function of rapidity. The vertical error bars represent the statistical uncertainties, the boxes around the points is the systematic and the box around unity represents the global uncertainties.

Table 6.23: The values of $R_{\rm pPb}$ vs $y_{\rm CMS}$ in p–Pb and Pb–p collisions at $\sqrt{s_{\rm NN}}$ = 8.16 TeV. The first uncertainty is the statistical, second one is the correlated systematic and third one is the uncorrelated systematic uncertainties.

p–Pb		Pb–p	
$y_{\rm CMS}$	$R_{\rm pPb}$ of Υ(1S)	$y_{\rm CMS}$	$R_{\rm Pbp}$ of Υ(1S)
$[2.03, 2.53]$	$0.731\pm0.088\pm0.062\pm2.844\%$	$[-3.46, -2.96]$	$0.725\pm0.068\pm0.046\pm2.886\%$
$[2.53, 3.03]$	$0.724\pm0.069\pm0.049\pm2.844\%$	$[-3.96, -3.46]$	$0.849\pm0.068\pm0.054\pm2.886\%$
$[3.03, 3.53]$	$0.631\pm0.092\pm0.050\pm2.844\%$	$[-4.46, -3.96]$	$0.945\pm0.178\pm0.075\pm2.886\%$

6.8.2 $R_{\rm pPb}$ as a function of $p_{\rm T}$

$R_{\rm pPb}$ has also been computed in 5 $p_{\rm T}$ bins. The results are shown in Fig. 6.23. The value of $R_{\rm pPb}$ in the $p_{\rm T}$ bins are reported in Table 6.24. Suppression of Υ(1S) is observed at the low $p_{\rm T}$ in the both forward and backward rapidities. However, more suppression is observed at low-$p_{\rm T}$ backward region.

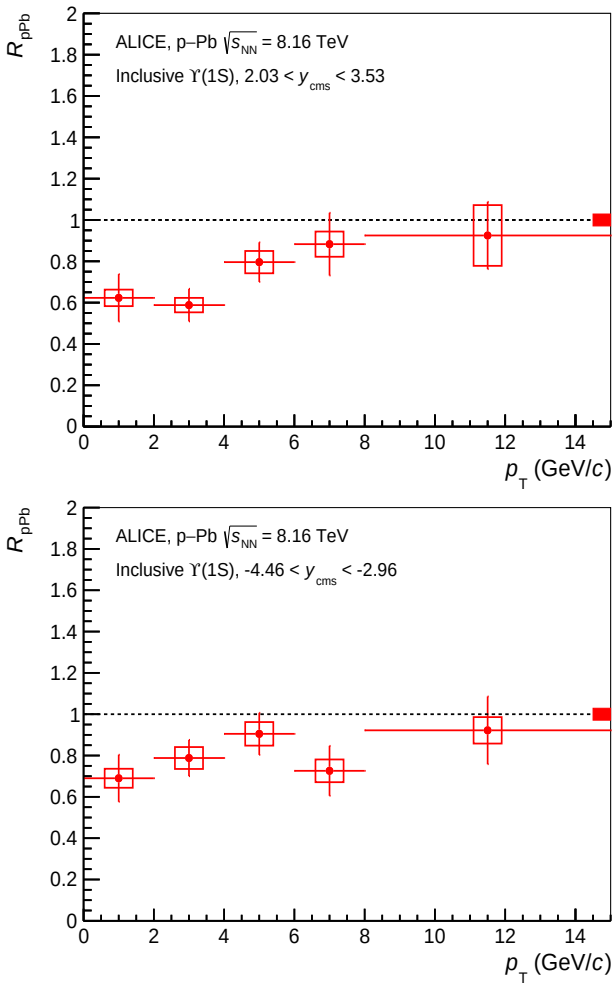

Figure 6.23: The nuclear modification factor for inclusive Υ(1S) production in p-Pb (left) and Pb-p (right) collisions at $\sqrt{s_{\rm NN}} = 8.16$ TeV as function of $p_{\rm T}$. The vertical error bars represent the statistical uncertainties, the boxes around the points the is systematic and the box around unity represents the global uncertainties.

Table 6.24: The values of $R_{\rm pPb}$ vs $y_{\rm CMS}$ in p–Pb and Pb–p collisions at $\sqrt{s_{\rm NN}} = 8.16$ TeV. The first uncertainty is the statistical, second one is the correlated systematic and third one is the uncorrelated systematic uncertainties.

$p_{\rm T}$ (GeV/c)	$R_{\rm pPb}$ of Υ(1S) in p–Pb	$R_{\rm Pbp}$ of Υ(1S) in Pb–p
$[0, 2]$	0.623±0.114±0.039±2.844%	0.684±0.108±0.048±2.886%
$[2, 4]$	0.588±0.078±0.035±2.844%	0.788±0.086±0.055±2.886%
$[4, 6]$	0.796±0.094±0.053±2.844%	0.905±0.103±0.059±2.886%
$[6, 8]$	0.883±0.151±0.060±2.844%	0.726±0.114±0.057±2.886%
$[8, 15]$	0.925±0.162±0.146±2.844%	0.922±0.162±0.061±2.886%

6.8.3 Comparison of $R_{\rm pPb}$ with model prediction and LHCb measurement

The $\Upsilon(1S)$ $R_{\rm pPb}$ are also compared with the LHCb measurement [11] at the same centre-of-mass energy. The $y_{\rm CMS}$ and $p_{\rm T}$ coverage of LHCb results are $-4.5 < y_{\rm cms} < -2.5$ and $2 < y_{\rm cms} < 4$, $p_{\rm T} < 25$ GeV/c. A fair agreement between the two experiment's results has been be observed.

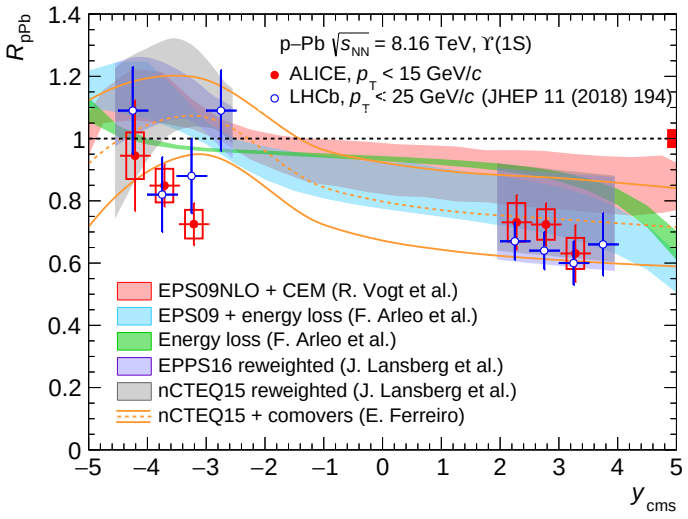

Figure 6.24: The $\Upsilon(1S)$ $R_{\rm pPb}$ are compared with the corresponding LHCb results [11] at $\sqrt{s_{\rm NN}} = 8.16$, as a function of $y_{\rm CMS}$. The $R_{\rm pPb}$ values are also compared to several model calculations based on implementations of nuclear shadowing (EPS09 NLO [12–14], nCTEQ15 & EPPS16 [15–20]) and on parton energy loss predictions, with or without the EPS09 shadowing contribution [13, 21]. A theoretical model including a shadowing contribution based on nCTEQ15 nPDFs plus the suppression induced by comover interactions [22, 23] is also shown. For the LHCb experimental results, the vertical error bars in data point represent the quadratic sum of the statistical and systematic uncertainties [1].

The differential $R_{\rm pPb}$ of $\Upsilon(1S)$ as function of $y_{\rm CMS}$ and $p_{\rm T}$ are plotted in Fig. 6.24 and Fig. 6.25 and have been compared with several theoretical models calculations based on EPS09 [14], nCTEQ15 [20] or EPPS16 [15] sets of nuclear PDFs. The EPS09 NLO parametrization is merged with a NLO CEM [12], which describes the Υ production. The corresponding uncertainty bands, shown in Fig. 6.24 and Fig. 6.25, mainly come from

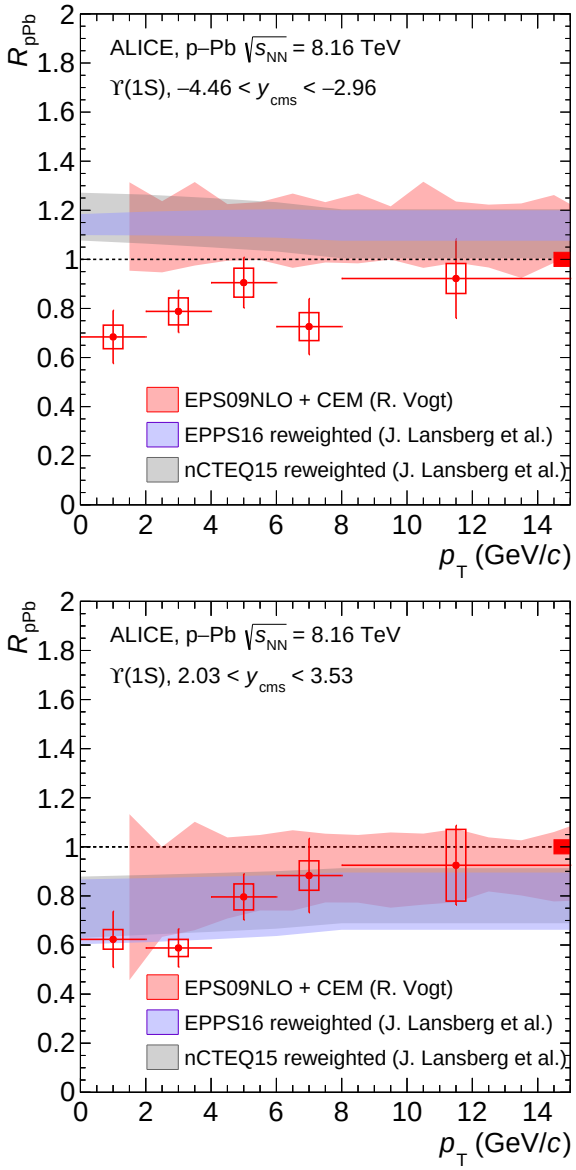

Figure 6.25: The Υ(1S) $R_{\rm pPb}$ as a function of $p_{\rm T}$ for Pb–p (left) and p–Pb collisions (right). The $R_{\rm pPb}$ values are also compared with theoretical model calculations based on EPS09 NLO [12, 13], nCTEQ15 and EPPS16 [15–20] shadowing implementations [1].

the uncertainties of the EPS09 parametrization. The details of the nCTEQ15 and the EPPS16 NLO nPDFs sets implementation following the Bayesian re-weighting technique have been described in [16–19]. In this scenario, the uncertainty bands constitute the convolution of the uncertainties in the nPDFs sets and those in the factorization scales. In the model by F. Arleo *et.al* [21] (green band in Fig. 6.24) the gluon PDFs are treated to be the same as in proton and lead nucleus. Thus the only uncertainty is due to that

on the energy loss parameters, which results in a narrow band of energy loss predictions.

It can be observed that the shadowing calculation describes the $y_{\rm CMS}$ and $p_{\rm T}$ dependence of the Υ(1S) $R_{\rm pPb}$ at forward rapidity within the uncertainties while they overestimate the data at backward rapidity. Moreover, while the $p_{\rm T}$ dependence of the ALICE results indicates a strong cold nuclear matter effect at low $p_{\rm T}$, the shadowing calculations do not have $p_{\rm T}$ dependence. The $y_{\rm CMS}$ dependence of nuclear modification factor is also compared with a model calculation that combines the effects of parton coherent energy loss with or without the contribution of the EPS09 nuclear shadowing [13, 21] parameterization. The energy loss in p–Pb collisions is implemented by a shift of the rapidity range relative to pp collisions. This calculation predicts a soft dependence of the energy loss mechanism on $y_{\rm CMS}$. The Υ(1S) $R_{\rm pPb}$ values are also compared with model calculations which include the shadowing contribution based on nCTEQ15 set of nPDFs plus the comover interaction [22, 23]. In this case also, the comparison with data shows a slight overestimation of ALICE results at backward rapidity while at forward region the data agree with the model calculations.

The model that includes the nuclear shadowing contribution with nCTEQ15 PDF and the comovers interactions [22, 23] hints at a difference between the $R_{\rm pPb}$ of the three Υ states. This difference is more pronounced in the backward-rapidity, while it becomes negligible at forward rapidity range. In the ratio of the Υ(nS) to Υ(1S) $R_{\rm pPb}$, the shadowing contribution (taken same for all states) and most of the theory uncertainties, as well as some part of the uncertainties on experimental data, cancel out. Therefore, the theoretical predictions are mainly driven by the comovers interaction which affects mostly the higher excited states of Υ in the backward region. The bottom panel of Fig. 6.26 shows that the ALICE results and the model prediction are in fair agreement, although the uncertainties on the data do not yet allow a definitive conclusion on the role of the comovers.

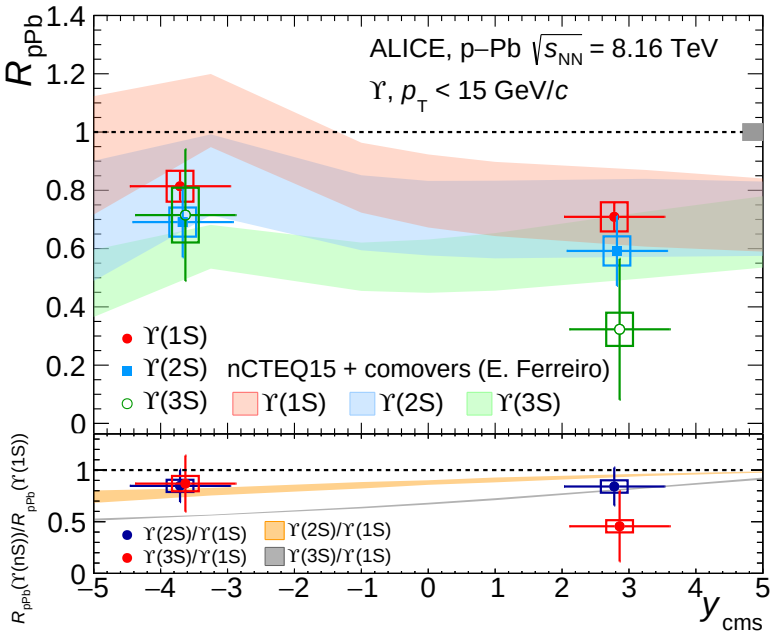

Figure 6.26: The Υ(1S), Υ(2S) and Υ(2S) $R_{\rm pPb}$ at $\sqrt{s_{\rm NN}} = 8.16$ as a function of $y_{\rm CMS}$. Theoretical model calculations including nCTEQ15 shadowing contribution and interactions with comoving particles [22, 23] are also shown for all the Υ states. In the bottom panel, the ratio of the Υ(2S) to Υ(1S) and Υ(3S) to Υ(1S) $R_{\rm pPb}$ is shown, together with a calculation based on the aforesaid model predictions [22, 23].

6.9 Centrality analysis

The data sample collected in p–Pb collisions during 2016 also allows the study of Υ(1S) production as a function centrality of the collisions. The centrality is determined based on a hybrid model approach, described in detail in [24]. In this model, the centrality of the collisions is determined by measuring the energy deposited in the ZDC detector in the Pb-going direction. In each ZDC-selected centrality class, the number of average collisions $\langle N_{\rm coll}\rangle$ is calculated as $\langle N_{\rm coll}\rangle = \langle N_{\rm part}\rangle$-1, assuming the charged particle multiplicity is proportional to the number of participant nucleons and $N_{\rm part}$ measured at mid-rapidity.

The data sample is split into four centrality classes correspond to 2–20%, 20–40%, 40–60% and 60–90% of the MB cross section. The most central collisions, 0–2% centrality are excluded from analysis because of pile-up events in this centrality window and residual contamination may be present even though the pile-up rejection cuts [2] are applied.

6.9.1 The number of MB events and nuclear thickness function

The normalization factor for centrality class j ($F^{j}_{\rm norm}$) is estimated using the normalization factor integrated over the all centrality ($F_{\rm norm}$) in following way:

$$F^{j}_{\rm norm} = F_{\rm norm} \times \frac{CINT7^{j}}{CINT7} \times \frac{CMUL7}{CMUL7^{j}} \tag{6.6}$$

The number of equivalent MB events is obtained from:

$$N^{eq,j}_{\rm MB} = F^{j}_{\rm norm} \times CMUL7^{j} \tag{6.7}$$

Table 6.25 lists the values of CMUL7 trigger and $F_{\rm norm}$ in ZN centrality classes.

The average number of nucleon collisions ($\langle N_{\rm coll}\rangle$) or the average nuclear overlap

Table 6.25: The values of CMUL7 trigger and $F_{\rm norm}$ in multiplicity bins for p-Pb and Pb-p collisions.

	p-Pb ($2.03 < y_{\rm cms} < 3.53$)			Pb-p ($-4.46 < y_{\rm cms} < -2.96$)		
ZN multiplicity percentile	CMUL7	CINT7	$F_{\rm norm}$	CMUL7	CINT7	$F_{\rm norm}$
2-20%	6.77336e+06	8.3301e+06	404.05	2.29937e+07	9.64434e+06	178.36
20-40%	6.10969e+06	9.25969e+06	497.93	1.72209e+07	1.07226e+07	264.77
40-60%	4.39644e+06	9.27712e+06	693.27	9.78955e+06	1.07449e+07	466.74
60-90%	3.5366e+06	1.40555e+07	1305.73	5.69048e+06	1.62358e+07	1213.29

function ($\langle T_{\rm pPb} \rangle$) in p–Pb collisions for a given centrality class, obtained by a selected range of energy deposited in the Pb-remnant side of ZN and is obtained using the hybrid method described in [2, 24]. The Tab. 6.26 shows the values of $\langle N_{\rm coll} \rangle$ and $\langle T_{\rm pPb} \rangle$ with their associated systematic uncertainties for ZN centrality estimator.

Table 6.26: The average numbers of nucleon-nucleon collisions $\langle N_{\rm coll} \rangle$ and average nuclear overlap function $\langle T_{\rm pPb} \rangle$ with their associated systematic uncertainty for ZN centrality estimator. Values are taken from [25].

ZN centrality classes	$\langle N_{\rm coll} \rangle$	Total syst. on $\langle N_{\rm coll} \rangle$ (%)	$\langle T_{\rm pPb} \rangle$	Total syst. on $\langle T_{\rm pPb} \rangle$ (%)
2-20%	12.03	5.7	0.166	5.8
20-40%	9.81	1.7	0.135	2.1
40-60%	7.09	4.1	0.0978	4.2
60-90%	3.70	4.9	0.0510	5.2

6.9.2 A×ϵ & pp reference for the centrality dependence

No significant centrality dependence is expected for the A×ϵ correction. Hence the centrality integrated values have been used for all the centrality bins.

The integrated values of Υ(1S) cross-sections for forward and backward rapidity are reported in Tab 6.27. This value is used in all centrality classes.

Table 6.27: The value of $BR_{\Upsilon(1S)\to\mu^+\mu^-} \times \sigma$ of LHCb in ALICE p-Pb and Pb-p rapidity ranges for pp at $\sqrt{s} = 8.16$ TeV.

Beam conditions	$y_{\rm CMS}$	$BR_{\Upsilon(1S)\to\mu^+\mu^-} \times \sigma$ (pb) $\pm$ stat $\pm$ sys
p-Pb	$[2.03, 3.53]$	2442.14±2.78±68.52 (4.39(uncorr) & 68.38(corr))
Pb-p	$[-4.46, -2.96]$	1535.08±1.91±43.09 (3.05(uncorr) & 42.98(corr))

6.9.3 Signal extraction

The signal extraction procedure is the same as described in Sec. 6.4 except the width of Υ(1S) keep fixed to that obtained from the fit to the integrated invariant mass spectra.

The systematic uncertainty on signal extraction has been determined extracting the Υ(1S) signal from the following fitting methods :

- Two different signal fitting functions: CB2 and NA60 functions
- Five different background functions: VWG, DE, DP, P1, E1P1 functions
- Two different fitting ranges: $[6-13]$ GeV/c^2 and $[7-12]$ GeV/c^2
- Three sets of tail parameters: p-Pb MC at 8.16 TeV (used for both CB2 and NA60), pp 8 TeV MC (used only for CB2) and pp 13 TeV tails from data (used only for CB2).

This process lead to 40 tests. As the width of Υ(1S) has been fixed in the fitting procedure, a systematic has been assigned. The width of Υ(1S) has been varied within the error limits of the fit to the integrated invariant mass spectra. Thus, 120 fitting methods have been considered. The final extracted signal is the average of these 120 values, while the RMS of the distribution gives the systematic uncertainty on the signal. Table 6.28 show the number of Υ(1S) with statistical and systematic uncertainties.

Table 6.28: The number of Υ(1S) as a function of different ZN centrality classes.

	$2.03 < y_{\rm cms} < 3.53$	$-4.46 < y_{\rm cms} < -2.96$
ZN multiplicity percentile	N_{Υ}(1S) (p-Pb)	N_{Υ}(1S) (Pb-p)
2-20%	236 ± 25 (stat) ± 15 (syst)	253 ± 23 (stat) ± 21 (syst)
20-40%	218 ± 25 (stat) ± 18 (syst)	215 ± 22 (stat) ± 14 (syst)
40-60%	150 ± 21 (stat) ± 13 (syst)	157 ± 18 (stat) ± 11 (syst)
60-90%	131 ± 18 (stat) ± 8 (syst)	120 ± 16 (stat) ± 8 (syst)

6.9.4 Summary of systematic uncertainties

Table 6.29 summarizes the sources of various systematic uncertainties for Υ(1S) in p–Pb and Pb–p collisions for the centrality analysis. Except for the signal extraction, $T_{\rm pPb}$ and $F_{\rm norm}$ all the other systematic uncertainties are the same as in the integrated spectrum which has been discussed in 6.6.

Table 6.29: The systematic uncertainties on the quantities associated to Υ(1S) $Q_{\rm pPb}$ measurement. Type I and II stands for uncertainties correlated with centrality of the collisions and collision system (within p-Pb and Pb-p) respectively.

Source	p-Pb (%)	Pb-p (%)
Signal extraction	6.6 - 8.9	6.6 - 8.5
Trigger efficiency	0.6+1 (I)	0.2+1 (I)
Tracking efficiency	1 (I)	2 (I)
Matching efficiency	1 (I)	1 I)
Input MC parametrization	1 (I)	1 (I)
$F_{\rm norm}$	1 (I)	1 (I)
$F_{\rm norm}$	0.42 - 0.81	0.34 - 0.66
$T_{\rm pPb}$	2.1 - 5.8 (II)	2.1 - 5.8(II)
pp reference	2.8+0.7 (I+II)	2.8+0.8 (I+II)
pile-up	2	2

6.9.5 Results

Fig. 6.27 show the $Q_{\rm pPb}$ of Υ(1S) as a function of the average number of collisions at $\sqrt{s_{\rm NN}}$ = 8.16 TeV for p-Pb (left) and Pb-p (right) collisions. It can be observed that there is almost no centrality dependence of Υ(1S) $Q_{\rm pPb}$ both at backward and

forward rapidities. The correlated systematics are the systematic on MC input, $F_{\rm norm}$, pp reference, trigger matching and tracking efficiencies while the uncorrelated systematics are systematic on signal extraction, $T_{\rm pPb}$, $F_{\rm norm}$ (uncorrelated part) and plie-up. The correlated systematic is represented in the figure by the red box around the unity.

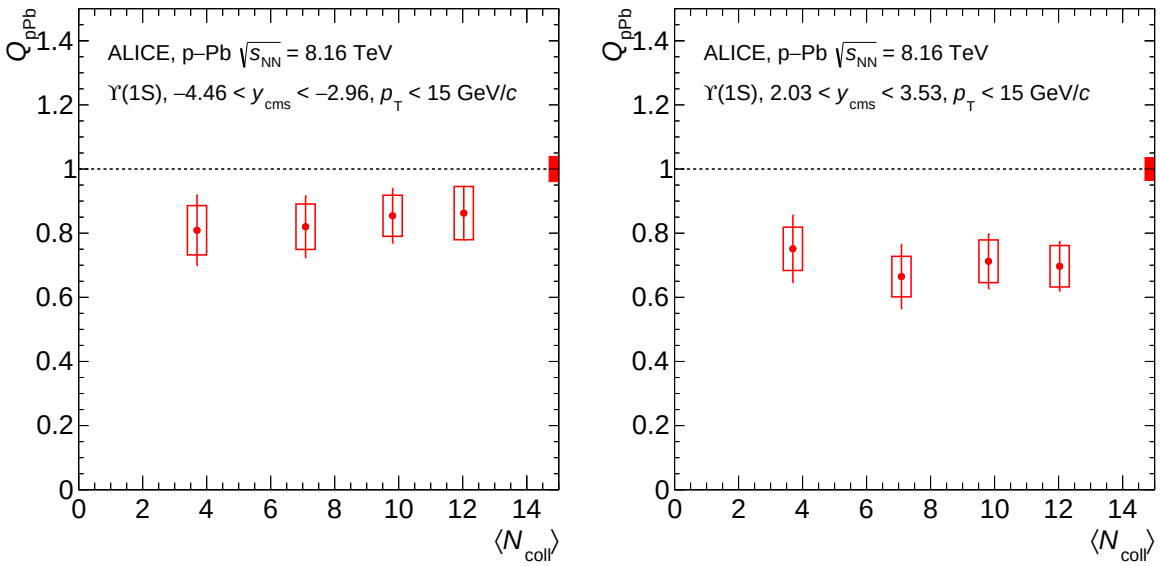

Figure 6.27: The Υ(1S) $Q_{\rm pPb}$ as a function of $\langle N_{\rm coll}\rangle$ at backward (left panel) and forward (right panel) rapidities at $\sqrt{s_{\rm NN}} = 8.16$ TeV [1].

The numerical values of $Q_{\rm pPb}$ of Υ(1S) are reported in Tab. 6.30.

Table 6.30: The Υ(1S) $Q_{\rm pPb}$ values as function of centrality of the collisions at backward and forward rapidity in p-Pb collisions at $\sqrt{s_{\rm NN}} = 8.16$ TeV.

centrality	$Q_{\rm pPb}$ $(-4.46 < y_{\rm cms} < -2.96)$ $\pm$ Global syst 3.9%	$Q_{\rm pPb}$ $(2.03 < y_{\rm cms} < 3.53)$ $\pm$ Global syst 3.6%
2-20%	0.885 $\pm$ 0.080 (stat) $\pm$ 0.095 (syst)	0.709 $\pm$ 0.075 (stat) $\pm$ 0.065 (syst)
20-40%	0.832 $\pm$ 0.089 (stat) $\pm$ 0.058 (syst)	0.724 $\pm$ 0.083 (stat) $\pm$ 0.062 (syst)
40-60%	0.837 $\pm$ 0.096 (stat) $\pm$ 0.071 (syst)	0.687 $\pm$ 0.096 (stat) $\pm$ 0.068 (syst)
60-90%	0.812 $\pm$ 0.108 (stat) $\pm$ 0.076 (syst)	0.759 $\pm$ 0.104 (stat) $\pm$ 0.068 (syst)

6.10 Summary

The Υ production has been studied in p–Pb collisions at $\sqrt{s_{\rm NN}}$ = 8.16 TeV in forward ($2.03 < y_{\rm CMS} < 3.53$) and backward ($-4.46 < y_{\rm CMS} < -2.96$) regions. The inclusive production cross-section and nuclear modification factor of Υ(1S) as a function of rapidity, transverse momentum and centrality of the collisions have been measured. The Υ(1S) production cross-section scaled by the Pb mass number in p–Pb collisions has been found to be suppressed with respect to the ones measured in pp collisions at the same centre-of-mass energy. The value of $R_{\rm pPb}$ are similar at both forward and backward rapidity interval with slight hints of stronger suppression at low $p_{\rm T}$. In both the rapidity regions, there is no evidence for a centrality dependence of the Υ(1S) $Q_{\rm pPb}$. The $R_{\rm pPb}$ results obtained at $\sqrt{s_{\rm NN}}$ = 8.16 TeV are similar within the experimental uncertainties to those measured by ALICE in p–Pb collisions at the lower energy of $\sqrt{s_{\rm NN}}$ = 5.02 TeV [10]. The rapidity dependence of ALICE $R_{\rm pPb}$ of Υ(1S) at $\sqrt{s_{\rm NN}}$ = 8.16 TeV has been compared with LHCb measurement [11], which show a good agreement within the uncertainties. The models based on nuclear shadowing and coherent parton energy loss or interactions with comoving particles give a fair description of the data at forward rapidity, while they tend to overestimate the $R_{\rm pPb}$ backward rapidity. One can however remark that the initial-state model calculations predict equal modification of all Υ states and the results are higher than the measured $R_{\rm pPb}$ values. A better agreement with data has been observed when the comover interactions have been considered.The Υ(2S) $R_{\rm pPb}$ has also been measured, showing a strong suppression, similar to the one measured for the Υ(1S), in the two rapidity intervals. Finally, a first measurement of the Υ(3S) production cross section and the $R_{\rm pPb}$ have also been reported, although the large uncertainties prevent a detailed comparison of its behavior in p–Pb collisions with respect to the other bottomonium states. The large uncertainty bands in different theoretical model predictions do not allow us to discriminate one over the other for the description of experimental results. This is due to the large uncertainties in the nPDF values at the

forward rapidity. However, one may expect more precise nPDF values from the p–Pb analysis of the high statistics data obtained from Run3 and Run4.

Bibliography

[1] ALICE collaboration, S. Acharya et al., Υ *production in p–Pb collisions at* $\sqrt{s_{NN}}$*=8.16 TeV*, *Phys. Lett. B* **806** (2020) 135486, [1910.14405].

[2] ALICE collaboration, J. Adam et al., *Centrality dependence of inclusive J/ψ production in p-Pb collisions at* $\sqrt{s_{\rm NN}} = 5.02$ *TeV*, *JHEP* **11** (2015) 127, [1506.08808].

[3] ALICE collaboration, S. Acharya et al., Υ *suppression at forward rapidity in Pb-Pb collisions at* $\sqrt{s_{\rm NN}}$ *= 5.02 TeV*, *Phys. Lett. B* **790** (2019) 89–101, [1805.04387].

[4] ALICE collaboration, B. B. Abelev et al., *Measurement of quarkonium production at forward rapidity in pp collisions at* $\sqrt{s} = 7$ *TeV*, *Eur. Phys. J. C* **74** (2014) 2974, [1403.3648].

[5] ALICE collaboration, J. Adam et al., *Inclusive quarkonium production at forward rapidity in pp collisions at* $\sqrt{s} = 8$ *TeV*, *Eur. Phys. J. C* **76** (2016) 184, [1509.08258].

[6] LHCb collaboration, R. Aaij et al., *Measurement of* Υ *production in pp collisions at* $\sqrt{s} = 2.76$ *TeV*, *Eur. Phys. J. C* **74** (2014) 2835, [1402.2539].

[7] LHCb collaboration, R. Aaij et al., *Forward production of* Υ *mesons in pp collisions at* $\sqrt{s} = 7$ *and 8TeV*, *JHEP* **11** (2015) 103, [1509.02372].

[8] LHCb collaboration, R. Aaij et al., *Measurement of* Υ *production in pp collisions at* $\sqrt{s}$*= 13 TeV*, *JHEP* **07** (2018) 134, [1804.09214].

[9] ALICE collaboration, S. Acharya et al., *Inclusive J/*ψ *production at forward and backward rapidity in p-Pb collisions at* $\sqrt{s_{\rm NN}}$ *= 8.16 TeV*, *JHEP* **07** (2018) 160, [1805.04381].

[10] ALICE collaboration, B. B. Abelev et al., *Production of inclusive* Υ*(1S) and* Υ*(2S) in p-Pb collisions at* $\sqrt{\mathbf{s}_{\rm NN}}$ **= 5.02** *TeV*, *Phys. Lett. B* **740** (2015) 105–117, [1410.2234].

[11] LHCb collaboration, R. Aaij et al., *Study of* Υ *production in pPb collisions at* $\sqrt{s_{NN}}$ = 8.16 *TeV*, *JHEP* **11** (2018) 194, [1810.07655].

[12] R. Vogt, *Shadowing effects on J/*ψ *and* Υ *production at energies available at the CERN Large Hadron Collider*, *Phys. Rev. C* **92** (2015) 034909, [1507.04418].

[13] J. L. Albacete et al., *Predictions for Cold Nuclear Matter Effects in p+Pb Collisions at* $\sqrt{s_{_{NN}}}$ = 8.16 *TeV*, *Nucl. Phys. A* **972** (2018) 18–85, [1707.09973].

[14] K. Eskola, H. Paukkunen and C. Salgado, *EPS09: A New Generation of NLO and LO Nuclear Parton Distribution Functions*, *JHEP* **04** (2009) 065, [0902.4154].

[15] K. J. Eskola, P. Paakkinen, H. Paukkunen and C. A. Salgado, *EPPS16: Nuclear parton distributions with LHC data*, *Eur. Phys. J. C* **77** (2017) 163, [1612.05741].

[16] J.-P. Lansberg and H.-S. Shao, *Towards an automated tool to evaluate the impact of the nuclear modification of the gluon density on quarkonium, D and B meson production in proton–nucleus collisions*, *Eur. Phys. J. C* **77** (2017) 1, [1610.05382].

[17] A. Kusina, J.-P. Lansberg, I. Schienbein and H.-S. Shao, *Gluon Shadowing in Heavy-Flavor Production at the LHC*, *Phys. Rev. Lett.* **121** (2018) 052004, [1712.07024].

[18] H.-S. Shao, *HELAC-Onia 2.0: an upgraded matrix-element and event generator for heavy quarkonium physics*, *Comput. Phys. Commun.* **198** (2016) 238–259, [1507.03435].

[19] H.-S. Shao, *HELAC-Onia: An automatic matrix element generator for heavy quarkonium physics*, *Comput. Phys. Commun.* **184** (2013) 2562–2570, [1212.5293].

[20] K. Kovarik et al., *nCTEQ15 - Global analysis of nuclear parton distributions with uncertainties in the CTEQ framework*, *Phys. Rev. D* **93** (2016) 085037, [1509.00792].

[21] F. Arleo and S. Peigne, *Heavy-quarkonium suppression in p-A collisions from parton energy loss in cold QCD matter*, *JHEP* **03** (2013) 122, [1212.0434].

[22] E. G. Ferreiro, *Global description of bottomonium suppression in proton-nucleus and nucleus-nucleus collisions at LHC energies*, *PoS* **DIS2018** (2018) 130, [1810.12874].

[23] E. G. Ferreiro and J.-P. Lansberg, *Is bottomonium suppression in proton-nucleus and nucleus-nucleus collisions at LHC energies due to the same effects?*, *JHEP* **10** (2018) 094, [1804.04474].

[24] ALICE collaboration, J. Adam et al., *Centrality dependence of particle production in p-Pb collisions at* $\sqrt{s_{\rm NN}}$ *= 5.02 TeV*, *Phys. Rev. C* **91** (2015) 064905, [1412.6828].

[25] "Ncoll." http://cds.cern.ch/record/2636623/files/centrality%20determination%20note.pdf.

CHAPTER 7

Υ production in Pb–Pb collisions at $\sqrt{s_{\rm NN}}$ = 5.02 TeV

ALICE has reported a strong suppression of Υ(2S) over Υ(1S) in Pb–Pb collisions at $\sqrt{s_{\rm NN}}$ = 5.02 TeV [1]. The results have been also compared with 2.76 TeV [2] and no significant energy dependence of $R_{\rm AA}$ is found. The $R_{\rm AA}$ of Υ(1S) as function of $p_{\rm T}$ is almost flat and no rapidity dependence in forward region is observed. The Υ(1S) $R_{\rm AA}$ decreases towards most central collisions. Different theoretical models prediction describe the results within the uncertainties.

In this chapter, the Υ production will be reported from the combined data sample collected during 2015 and 2018. Due to the higher statistics, the study of differential $R_{\rm AA}$ of Υ(2S) with the centrality of collisions and rapidity have become possible. The measurement is performed reconstructing bottomonium resonances via their dimuon decay channel.

7.1 Data Processing

The data set, trigger & physics selection, event and track selection have been described in detail in chapter 4.

7.2 Acceptance and efficiency corrections

The number of measured Υ has been corrected with the acceptance times efficiency ($(A\times\epsilon)$) of the spectrometer in order to get the yields. The $A\times\epsilon$ has been evaluated from the embedding MC simulation described in ref [1]. The $p_{\rm T}$ and rapidity input distributions extrapolated from collider data [3, 4]. A run-by-run weightage factor (proportional to the number of CMUL events) has been applied to account for the accumulated statistics in each run.

The $A\times\epsilon$ integrated over $p_{\rm T}$ ($p_{\rm T}$ <15 GeV/c), rapidity and centrality (0-90%) of combined data sample of 2015 and 2018 amount to 0.2569 and 0.2562 for Υ(1S) and Υ(2S), respectively. The $A\times\epsilon$ as a function of $p_{\rm T}$ is flat and no variation is observed as shown in Fig. 7.1 except the last bin. The centrality and rapidity dependence of $A\times\epsilon$ is shown in Fig. 7.2. A relative increase is observed from peripheral to central collision due to the increased occupancy in the muon chambers. The rapidity dependency reflects the geometry of the spectrometer.

7.3 Signal extraction

The signal extraction procedure is the same as discussed in the previous chapter. Additionally, the event-mixing technique has been applied to improve the signal-to-background

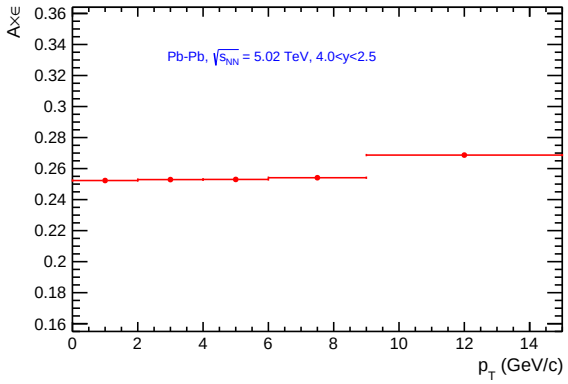

Figure 7.1: The $A \times \epsilon$ of Υ(1S) as function of $p_{\rm T}$ in Pb–Pb collisions at $\sqrt{s_{\rm NN}} = 5.02$ TeV.

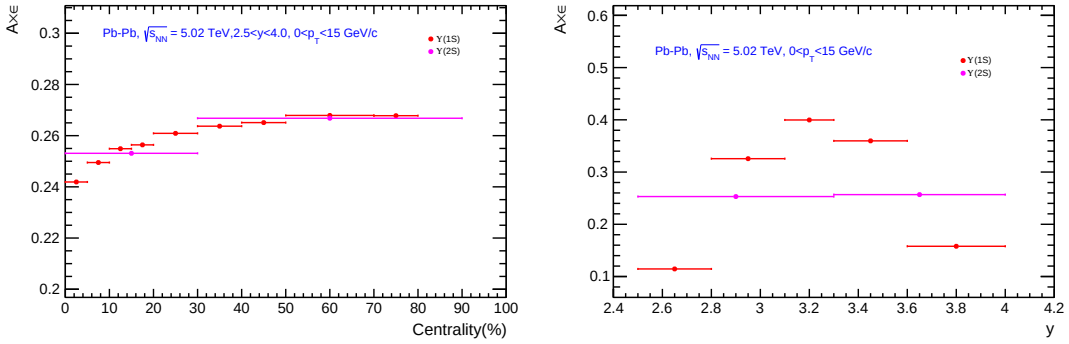

Figure 7.2: The $A \times \epsilon$ of Υ (1S) and Υ (2S) as function of collision centrality (left panel) and rapidity (right panel) in Pb–Pb collisions at $\sqrt{s_{\rm NN}} = 5.02$ TeV.

ratios in Pb–Pb analysis. The detail of the event-mixing technique is described in [5]. The fits to the integrated invariant mass spectra obtained from the raw and the background-subtracted data are shown in Fig. 7.3.

7.3.1 Systematic on signal extraction

The following variations in the fitting parameters have been considered to estimate signal systematic:

- 3 sets of tail parameters from embedding MC (GEANT3), pure MC (GEANT4) and pp MC at $\sqrt{s} = 5.02$ TeV.
- Width scaling systematic same as in chapter 4.

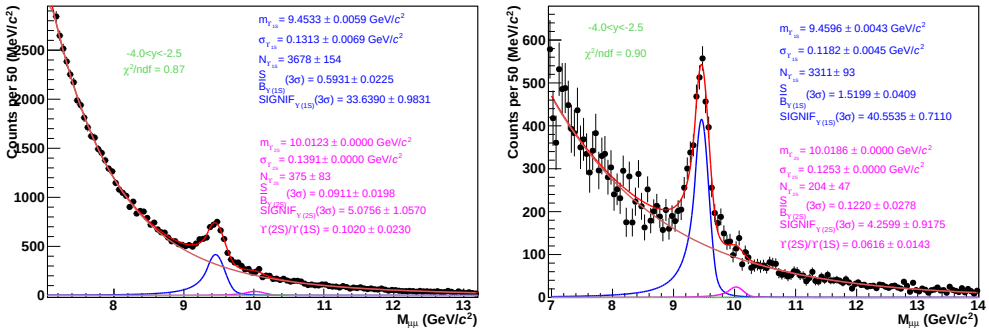

Figure 7.3: The typical fits to the invariant mass spectra obtained from full Run 2 (0–90% centrality) data sample with raw (left) and mixed-background subtracted (right) analysis in the bottomonium mass range.

- The sum of two exponentials and a variable width gaussian (VWG) function have been used raw data background. For the event mixing case, the residual background is fitted with the shape of a single exponential and a power law function.

- Two fitting range have been used ([6-13], [7-14] GeV/c^2).

The centrality-integrated signal extraction results for Υ(1S) and Υ(2S) are reported in Tab 7.1

Table 7.1: The number of Υ(nS) integrated over $p_{\rm T}$, y and centrality.

particle	N $\pm$ (stat.) $\pm$ (sys)
Υ(1S)	3506$\pm$ 117 (3.3%) $\pm$ 137 (3.9%)
Υ(2S)	289$\pm$ 61 (21.1%) $\pm$ 62 (20.3%)

Centrality dependence

The full Run2 data sample was further divided into 9 centrality bins for Υ(1S) differential study. First time at the forward rapidity, the centrality dependency of Υ(2S) production has been studied by splitting the data sample into 2 centrality bins. The signal extraction procedure and evaluation of signal systematic are identical to the integrated case. The results are reported in Tab. 7.2 and Tab. 7.3.

Table 7.2: The number of Υ(1S) in different centrality bins.

Centrality (%)	$N_{\Upsilon(1S)}$ ± (stat.) ± (syst.)
0–5	643 ± 73(11.4%)± 40(6.3%)
5–10	612 ± 50(8.2%) ± 34(5.6%)
10–15	471 ± 45(9.6%) ± 28(6.1%)
15–20	353 ± 35(9.9%) ± 22(6.5%)
20–30	644 ± 50(7.9%) ± 41(6.5%)
30–40	375 ± 43(11.5%) ± 14(3.9%)
40–50	230 ± 29(12.9%) ± 20(8.9%)
50–70	160 ± 22(14.1%) ± 14(9.1%)
70–90	59 ± 11(19.1%) ± 3(5.7%)

Table 7.3: The number of Υ(2S) in the two centrality bins.

Centrality (%)	$N_{\Upsilon(2S)}$ ± (stat.) ± (syst.)
0–30	173 ± 31(18.2%) ± 49(28.7%)
30–90	102 ± 31(30.8%) ± 12(11.9%)

$p_{\rm T}$ dependence

For $p_{\rm T}$ differential study of Υ(1S), the data have been divided in 5 bins. The signal extraction procedure in $p_{\rm T}$ bins is the same as in the integrated case. The numbers in $p_{\rm T}$ bins reported in Tab. 7.4.

Table 7.4: The number of Υ(1S) in different $p_{\rm T}$ bins.

$p_{\rm T}$ (GeV/c)	$N_{\Upsilon(1S)}$ ± (stat.) ± (syst.)
$0 < p_{\rm T} < 2$	623± 57 (9.2%) ± 61 (9.8%)
$2 < p_{\rm T} < 4$	1127± 62 (5.6%) ± 56 (5.0%)
$4 < p_{\rm T} < 6$	830 ± 51 (6.2%) ± 30 (3.6%)
$6 < p_{\rm T} < 9$	540 ± 55 (10.3%)± 54 (10.0%)
$9 < p_{\rm T} < 15$	383 ± 40 (10.7%)± 21 (5.7%)

Rapidity dependence

The data were split into 5 rapidity bins for Υ(1S) differential study and 2 bins for Υ(2S). In the rapidity bins, fluctuations in the mass position and width have been observed. To

account for these fluctuations, the mass and width have been fixed to their integrated value in following way:

$$m_i = m_{\rm int} \times \frac{m_i^{\rm MC}}{m_{\rm int}^{\rm MC}}, \qquad \sigma_i = \sigma_{\rm int} \times \frac{\sigma_i^{\rm MC}}{\sigma_{\rm int}^{\rm MC}}$$

The associated systematic study to this fixing method is evaluated by changing the integrated value within the statistical uncertainty limits of the integrated result. The number of Υ(1S) and Υ(2S) in different y bins reported in Tab. 7.5 and Tab. 7.6, respectively.

Table 7.5: The number of Υ(1S) in different rapidity bins.

Rapidity	$N_{\Upsilon(1S)} \pm$ (stat.) $\pm$ (syst.)
$2.5 < y < 2.8$	500 $\pm$ 55 (11.2%) $\pm$ 40 (8.0%)
$2.8 < y < 3.1$	1137 $\pm$ 69 (6.1%) $\pm$ 47 (4.2%)
$3.1 < y < 3.3$	811 $\pm$57 (7.1%) $\pm$ 33 (4.2%)
$3.3 < y < 3.6$	812 $\pm$ 59 (7.3%) $\pm$ 33 (4.1%)
$3.6 < y < 4.0$	308 $\pm$ 37 (12.1%) $\pm$ 23 (7.6%)

Table 7.6: The number of Υ(2S) in the two rapidity bins.

Rapidity	$N_{\Upsilon(2S)} \pm$ (stat.) $\pm$ (syst.)
$2.5 < y < 3.3$	136 $\pm$ 50 (36.9%) $\pm$ 21 (15.8%)
$3.3 < y < 4.0$	140 $\pm$ 36 (26.2%) $\pm$ 17 (12.4%)

7.4 pp reference cross section

The inclusive Υ(nS) production in pp collision at $\sqrt{s} = 5.02$ TeV, reported in chapter 5 has not been directly used as the reference of Pb–Pb measurements. The large statistical uncertainty on results and non-availability of the differential result as per Pb–Pb analysis requirement, are the two main reasons for not using the pp measurements as a reference.

Instead, interpolation procedure described in [6] has been applied to evaluate the pp reference using the available ALICE [7, 8] and LHCb [9–11] pp measurements. In interpolation the procedure, the ALICE results at $\sqrt{s} = 5.02$ TeV has also been used. The differential reference cross section are reported in Tab. 7.7, Tab. 7.8 and Tab 7.9. For centrality bins, the integrated reference cross-section has been used.

Table 7.7: The Υ(1S) $p_{\rm T}$-differential reference cross-sections.

$p_{\rm T}$ (GeV/c)	$\frac{d^2\sigma_{pp}^{\Upsilon(1S)\to\mu^+\mu^-}}{dydp_{\rm T}}$ (nb/(GeV/c))
$0 < p_{\rm T} < 2$	74±5
$2 < p_{\rm T} < 4$	122±8
$4 < p_{\rm T} < 6$	97±6
$6 < p_{\rm T} < 9$	49±4
$9 < p_{\rm T} < 15$	13±2

Table 7.8: The Υ(1S) y-differential reference cross-sections.

y	$\frac{d\sigma_{pp}^{\Upsilon(1S)\to\mu^+\mu^-}}{dy}$ (nb)
$2.5 < y < 2.8$	1033±51
$2.8 < y < 3.1$	909±60
$3.1 < y < 3.3$	796±67
$3.3 < y < 3.6$	679±71
$3.6 < y < 4.0$	513±73

Table 7.9: The Υ(2S) y -differential reference cross-sections.

y	$\frac{d\sigma_{pp}^{\Upsilon(2S)\to\mu^+\mu^-}}{dy}$ (nb)
$2.5 < y < 3.3$	241±19
$3.3 < y < 4.0$	147±21

7.5 Systematic uncertainties

The list of systematic uncertainties and the associated percentage contributions are reported in Table 7.10 and Table 7.11 for Υ(1S) and Υ(2S), respectively.

Table 7.10: The summary of all the systematic uncertainties (in %) of Υ(1S)

Source	Integrated	Centrality	y	$p_{\rm T}$
Signal extraction	4.4	3.9–7.4	3.6–10.2	3.6–9.1
MC input	0.4	0.4	0.2–0.4	0.1–0.6
Tracker	3	3+(0–1)	3+1	3+1
Trigger	3	3	1.4–3.7	1–2.6
Matching	1	1	1	1
$F_{\rm norm}$	0.5	0.5	0.5	0.5
$\langle T_{\rm AA} \rangle$	1	0.7–2.4	1	1
Centrality	–	0.1–5.5	–	–
$\sigma_{\Upsilon}^{\rm pp}$	5.3	5.3	4.9–14.3	5.7–15.8

Table 7.11: The summary of systematic uncertainties (in %) of Υ(2S).

Source	Integrated	Centrality	y
Signal extraction	18.4	14.0–23.4	9.7–39.0
MC input	0.3	0.3	0.7
Tracker	3	3+(0–1)	3+1
Trigger	3	3	1.4–3.7
Matching	1	1	1
$F_{\rm norm}$	0.5	0.5	0.5
$\langle T_{\rm AA} \rangle$	1	0.8-2.56	1
Centrality	–	0.1–0.3	–
$\sigma_{\Upsilon}^{\rm pp}$	7.5	7.5	8.1–14.4

7.6 Results

The inclusive Υ production yields normalized by the nuclear overlap function along with the CMS measurements at mid-rapidity, are shown in Fig. 7.4. The rapidity dependence shows the characteristic fall at ALICE forward region and $p_{\rm T}$ spectrum hints to a softer dependence at forward rapidity than the mid-rapidity [12].

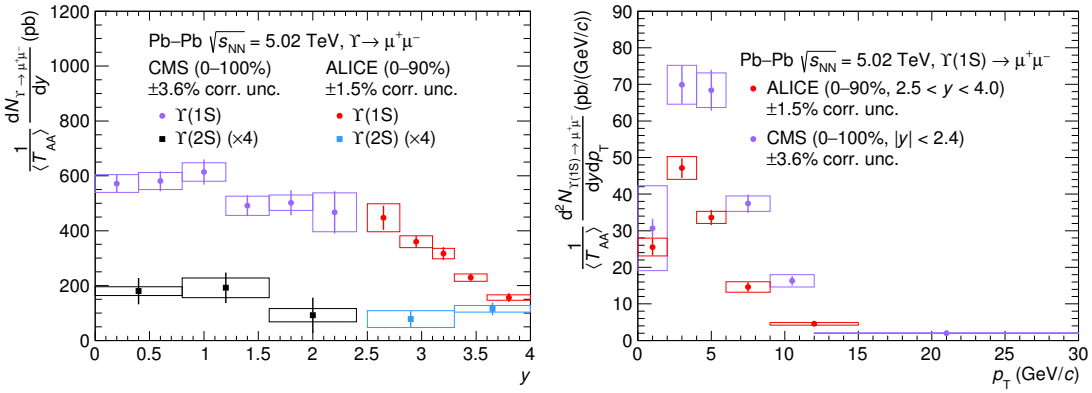

Figure 7.4: The inclusive ϒ(1S) production yields in Pb–Pb collision at $\sqrt{s_{\rm NN}}$ = 5.02 TeV as function of rapidity (left panel) and $p_{\rm T}$ (right panel) together with CMS results at mid-rapidity. The ϒ(2S) results are multiplied with a factor of 4 for clear visualization [12].

The integrated nuclear modification factor of ϒ(nS) in the kinematic range 0–90%, $0 < p_{\rm T} < 15$ GeV/c and $2.5 < y < 4.0$ are

- $R_{\rm PbPb}^{\Upsilon(1S)} = 0.353 \pm 0.012 \pm 0.029$
- $R_{\rm PbPb}^{\Upsilon(2S)} = 0.128 \pm 0.024 \pm 0.026$

The ratio of the two $R_{\rm PbPb}$ is

$$\frac{R_{\rm PbPb}^{\Upsilon(2S)}}{R_{\rm PbPb}^{\Upsilon(1S)}} = 0.360 \pm 0.069 \pm 0.055$$

In all the above cases, the first uncertainty is the statistical and the second one is systematic uncertainty. The results have been compared with the measured $R_{\rm AA}$ at $\sqrt{s_{\rm NN}}$ = 2.76 TeV [2](Table 7.12) and no significant energy dependence has been observed within the uncertainties.

The centrality dependence of $R_{\rm AA}$ is shown in Fig. 7.5. ϒ(1S) production shows a strong suppression towards the most central collisions whereas ϒ(2S) seems to have no

Table 7.12: The $\Upsilon(1S)$ $R_{\rm AA}$ at different energy measured by ALICE. The first uncertainty is statistical, while the second uncertainty the systematic one.

$\sqrt{s_{\rm NN}}$ (TeV)	$R_{\rm AA}$
2.76	0.300±0.050±0.040
5.02	0.353±0.012±0.029

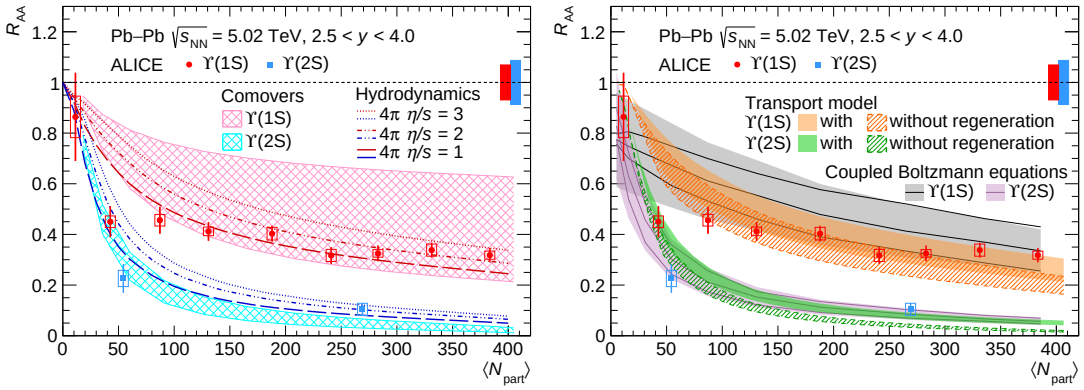

Figure 7.5: The $R_{\rm AA}$ of $\Upsilon(1S)$ and $\Upsilon(2S)$ as function of centrality (number of participants, $N_{\rm part}$). The vertical error bar represents statistical uncertainties, box around the data represents the uncorrelated systematic uncertainties and the filled box around the unity line corresponds to the correlated systematic uncertainties. All the following figures have the same convention. The results are also compared with several model predictions [12].

significant centrality dependence within the uncertainties. The experimental results are compared with theoretical model calculations based on the rate equations. In the comovers model [13], the modification of PDF in the nucleus is taken into account and the quarkonia are dissociated in the final state via the interaction with surrounding medium particles. In the transport model [14], the Upsilon yields are obtained by solving the rate equation in presence of binding energy modification in medium, regeneration and dissociation by the inelastic scatterings. The theoretical calculations based on the anisotropic hydrodynamics [15] have been derived by solving the thermally modified a complex heavy quark potential. In all the models, the major uncertainty comes from the nPDF and rate equation parameters. The various model predictions reproduce the trend of the ALICE data within the calculation uncertainties as shown in Fig. 7.5.

The $p_{\rm T}$ dependence of $R_{\rm AA}$ in 0–90% centrality is shown in Fig. 7.6. No significant variation with $p_{\rm T}$ up to 15 GeV/c has been observed. The Transport and Hydrodynamics model calculations describe the results within the uncertainties. However, one may note that the measurements are in better agreement with the hydrodynamics calculations for 4π . $\eta/s = 1$, which is also supported by the flow measurements of ALICE.

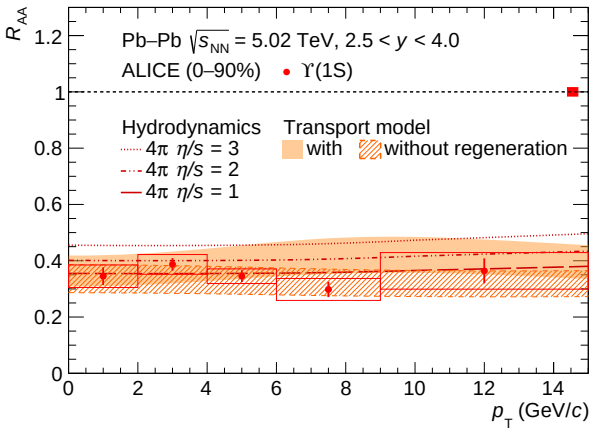

Figure 7.6: The $R_{\rm AA}$ of Υ(1S) as function of $p_{\rm T}$ [12]. The results are compared with Transport [14] and Hydrodynamics [15] model calculations.

The rapidity dependence of the nuclear modification factors is shown in Fig. 7.7. The ALICE results are compared with CMS measurements [16] at mid rapidity. The $R_{\rm AA}$ of Υ(1S) at mid-rapidity almost flat however its decreases if one goes towards the more forward regions. The $R_{\rm AA}$ is lower by $\sim 2\sigma$ in the most forward-y interval with respect to the central range of the ALICE measurement. However, the hydrodynamic calculations indicate the opposite behavior where the rapidity profile is estimated from the initial conditions of the simulated medium [15]. This rapidity dependence needs to be scrutinised in future analyses with high statistics data. The $R_{\rm AA}$ of Υ(2S) is flat at both mid and forward-rapidity within the uncertainties.

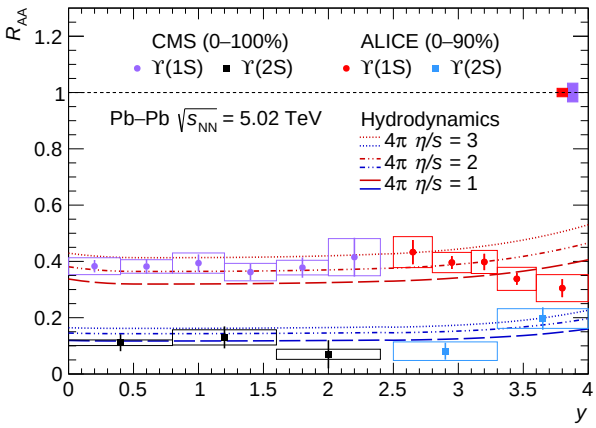

Figure 7.7: The $R_{\rm AA}$ of ϒ(1S) and ϒ(2S) as function of rapidity [12]. The results are compared with CMS [16] measurements at mid-rapidity and the Hydrodynamics [15] model calculations.

7.7 Summary

The detailed measurements of ϒ(1S) production, as well as the first differential measurement of ϒ(2S) at the forward rapidity combining the 2015 and 2018 data set, are reported in Pb–Pb collisions at $\sqrt{s_{\rm NN}}$ =5.02 TeV. The centrality (0-90%), transverse momentum ($p_{\rm T} < 15$ GeV/c) and rapidity ($2.5 < y < 4.0$) integrated nuclear modification factor for ϒ(1S) and ϒ(2S) are 0.353 ± 0.012 (stat.) ±0.029 (syst.) and 0.128 ± 0.024 (stat.) ± 0.026 (syst.), respectively. The suppression of ϒ(1S) gets stronger towards more central collisions. The rapidity dependence of ϒ(1S) $R_{\rm AA}$ hints a decrease in value at the most forward rapidity interval comparison to the central range of the ALICE measurement. Together with the CMS results [16], these measurements constrain the ϒ(1S) suppression as a function of rapidity with respect to pp collisions. No significant $p_{\rm T}$ dependence of $R_{\rm AA}$ is observed up to 15 GeV/c. It is worth noting that the nuclear modification factor in p–Pb collision shows a significant $p_{\rm T}$ dependence in both forward and backward rapidity interval measured by ALICE [6] and LHCb [17]. The difference in behaviour between p–Pb and Pb–Pb collisions may impose some constraints in theoretical models in near future.

The available theoretical model predictions, that describe the bottomonium produc-

tion in Pb–Pb collisions do not fully explain the rapidity dependence observed for the $R_{\rm AA}$ of Υ(1S) in the ALICE forward region.

The Υ(2S) state is found to have larger suppression than the ground state. The large uncertainties in Υ(2S) $R_{\rm AA}$ prevent any definitive conclusion on its centrality and rapidity dependence.

Bibliography

[1] ALICE collaboration, S. Acharya et al., Υ *suppression at forward rapidity in Pb-Pb collisions at* $\sqrt{s_{\rm NN}}$ *= 5.02 TeV*, *Phys. Lett. B* **790** (2019) 89–101, [1805.04387].

[2] ALICE collaboration, B. B. Abelev et al., *Suppression of* $\Upsilon(1S)$ *at forward rapidity in Pb-Pb collisions at* $\sqrt{s_{\rm NN}} = 2.76$ *TeV*, *Phys. Lett. B* **738** (2014) 361–372, [1405.4493].

[3] CDF Collaboration collaboration, D. Acosta, T. Affolder, H. Akimoto, M. G. Albrow, P. Amaral, D. Ambrose et al., *υ production and polarization in* $p\overline{p}$ *collisions at* $\sqrt{s}$ *= 1.8 tev*, *Phys. Rev. Lett.* **88** (Apr, 2002) 161802.

[4] LHCb collaboration, R. Aaij et al., *Measurement of Upsilon production in pp collisions at* $\sqrt{s}$ *= 7 TeV*, *Eur. Phys. J. C* **72** (2012) 2025, [1202.6579].

[5] ALICE collaboration, J. Adam et al., *Differential studies of inclusive J/ψ and ψ(2S) production at forward rapidity in Pb-Pb collisions at* $\sqrt{s_{\rm NN}} = 2.76$ *TeV*, *JHEP* **05** (2016) 179, [1506.08804].

[6] ALICE collaboration, S. Acharya et al., Υ *production in p–Pb collisions at* $\sqrt{s_{NN}}$*=8.16 TeV*, *Phys. Lett. B* **806** (2020) 135486, [1910.14405].

[7] ALICE collaboration, B. B. Abelev et al., *Measurement of quarkonium production at forward rapidity in pp collisions at* $\sqrt{s} = 7$ *TeV*, *Eur. Phys. J. C* **74** (2014) 2974, [1403.3648].

[8] ALICE collaboration, J. Adam et al., *Inclusive quarkonium production at forward rapidity in pp collisions at* $\sqrt{s} = 8$ *TeV*, *Eur. Phys. J. C* **76** (2016) 184, [1509.08258].

[9] LHCb collaboration, R. Aaij et al., *Measurement of* Υ *production in pp collisions at* $\sqrt{s} = 2.76$ *TeV*, *Eur. Phys. J. C* **74** (2014) 2835, [1402.2539].

[10] LHCb collaboration, R. Aaij et al., *Forward production of* Υ *mesons in pp collisions at* $\sqrt{s} = 7$ *and 8TeV*, *JHEP* **11** (2015) 103, [1509.02372].

[11] LHCb collaboration, R. Aaij et al., *Measurement of* Υ *production in pp collisions at* $\sqrt{s}$*= 13 TeV*, *JHEP* **07** (2018) 134, [1804.09214].

[12] ALICE collaboration, S. Acharya et al., Υ *production and nuclear modification at forward rapidity in Pb-Pb collisions at* $\sqrt{s_{NN}} = 5.02$ *TeV*, 2011.05758.

[13] E. G. Ferreiro and J.-P. Lansberg, *Is bottomonium suppression in proton-nucleus and nucleus-nucleus collisions at LHC energies due to the same effects?*, *JHEP* **10** (2018) 094, [1804.04474].

[14] X. Du, R. Rapp and M. He, *Color Screening and Regeneration of Bottomonia in High-Energy Heavy-Ion Collisions*, *Phys. Rev. C* **96** (2017) 054901, [1706.08670].

[15] B. Krouppa and M. Strickland, *Predictions for bottomonia suppression in 5.023 TeV Pb-Pb collisions*, *Universe* **2** (2016) 16, [1605.03561].

[16] CMS collaboration, A. M. Sirunyan et al., *Measurement of nuclear modification factors of* Υ*(1S),* Υ*(2S), and* Υ*(3S) mesons in PbPb collisions at* $\sqrt{s_{\mathrm{NN}}} = 5.02$ *TeV*, *Phys. Lett. B* **790** (2019) 270–293, [1805.09215].

[17] LHCb collaboration, R. Aaij et al., *Study of* Υ *production in pPb collisions at* $\sqrt{s_{NN}} = 8.16$ *TeV*, *JHEP* **11** (2018) 194, [1810.07655].

CHAPTER 8

Nuclear modification factor of average D meson in an anisotropic quark-gluon plasma at the LHC energies

This chapter presents the theoretical calculations carried out during the course of this thesis work, on the charm mesons p_{T} spectrum and nuclear modification factor (R_{AA}) of average D meson. After the introduction, the formalism to calculate the radiative energy loss in aQGP with infinite extent has been discussed. Next the hardonic p_{T} spectrum both in pp and A–A collisions along with the calculation of R_{AA} are presented. The main features of anisotropic hydrodynamics in (1+1)d have been briefly summarized in the next section. In the end, the numerical results have been discussed.

8.1 Introduction

In ultra-relativistic heavy-ion collisions, the hardonic matter undergoes a phase transition to a new state of matter which is characterized by high temperature and energy density. According to Quantum Chromodynamics (QCD), such extreme conditions lead to the formation of a deconfined medium of quarks and gluons, known as Quark–Gluon Plasma

(QGP) [1, 2]. Many experimental evidences support the production of the deconfined medium at Brookhaven National Laboratory in Relativistic Heavy Ion Collider (RHIC) experiments [3] and at CERN in Large Hadron Collider experiments [4]. One of the most striking signatures of the deconfined medium produced in nucleus-nucleus ($A-A$) collisions is the suppression of high transverse-momentum hadrons compared to the binary scaled proton-proton collisions, commonly known as jet quenching [5–13]. The jets are produced at the very early stages of the collision. In $A-A$ collisions, the initial hard partons lose energy via collisional and radiative processes inside the deconfined QCD medium, which leads to the suppression of jets compared to the proton-proton collisions. The energy loss experienced by the initial hard partons of both light and heavy flavors in the deconfined medium, is of considerable interest because it unravels the dynamical properties of the plasma medium.

The heavy quarks i.e. charm and bottom, are produced in the hard scattering processes at the initial stages of the heavy-ion collisions and while passing through the transient matter, they can interact with the medium and lose energy via both inelastic processes (radiative energy loss) and elastic scatterings (collisional energy loss). The description of the partonic energy loss mechanism in the deconfined QCD medium has been improved remarkably in recent years. Experimentally, it can be probed by measuring the high-p_T hadrons emanating from the ultra-relativistic heavy ion collisions.

The heavy quarks, after losing energy, fragment into open-charm (bottom) heavy mesons (D,B). The formation of the QGP can be established by measuring the energy loss vis-a-vis the nuclear modification factors ($R_{\rm AA}$) of various heavy mesons such as D, B, J/Ψ, Υ etc. The experimental data at various LHC energies exhibit considerable modifications of the transverse-momentum spectra of these mesons in A–A collisions compared pp collisions [14–20]. Different theoretical models have also been employed to explain the data. In this work, we concentrate on the charm mesons $p_{\rm T}$ spectrum and nuclear modification factors ($R_{\rm AA}$) within the ambit of anisotropic quark gluon plasma

(aQGP) [21] and extract the isotropization time, $\tau_{\rm iso}$ by comparing with the experimental data. In the following paragraph, we argue how an aQGP can be realised in relativistic heavy ion collisions.

It is to be noted that many properties of the QGP probes are still poorly understood. The most relevant question is whether the medium produced in the relativistic heavy-ion collisions is in thermal equilibrium or not. The experimental studies of the elliptic flow coefficient (v_2) and its theoretical explanations suggest that the medium quickly comes into thermal equilibrium (with $\tau_{\rm therm}$ <1 fm/c, where $\tau_{\rm therm}$ is the thermalization time) [22]. On the contrary, perturbative QCD assessments suggest a relatively slower thermalization of QGP [23]. The hydrodynamical calculations [24] have shown that there is a sizable amount of uncertainty in the estimation of thermalization or isotropization time, due to the insufficient knowledge of the initial conditions (energy density distribution). It is suggested that (momentum) anisotropy-driven plasma instabilities may speed up the process of isotropization [25–29], in which case one is allowed to use hydrodynamical evolution of the medium. However, instability-based isotropization is not yet proven at RHIC and LHC energies.

During the rapid expansion in the longitudinal direction at the initial moment, the plasma cools faster in the longitudinal direction than in the transverse direction leading to $\langle p_z^2\rangle << \langle p_T^2\rangle$. As a result, the system becomes anisotropic in the momentum space [21, 30–42]. Thus for the time interval $\tau_i < \tau < \tau_{\rm iso}$ the equilibrium hydrodynamics is not applicable. We use, for simplicity, the (1+1)d anisotropic hydrodynamics developed in [43]. In our work it is assumed that an isotropic QGP is formed at the time τ_i and at temperature T_i.

8.2 Formalism

8.2.1 Radiative energy loss

In this section, we briefly mention the basic formalism of the radiative energy loss at first order in opacity for a heavy quark in an infinitely extended anisotropic plasma. The assumption of infinite medium will have important consequences, as we shall see when we compare our results of R_{AA} in result section. Heavy quark radiative energy loss is caused by the gluon radiation which is produced by collisional interactions between the quarks and the parton in the medium. We consider on-shell heavy quark jets produced at remote past and propagating through the infinite QCD medium that consists of randomly distributed static scattering centers ("static QCD medium"). In the static interaction, the heavy-quark potential has been derived by using HTL resumed propagators for all gluons.

The retarded gluon self-energy in HTL approximation has the form [44]

$$\Pi^{\mu\nu}(q) = \mathrm{g}^2 \int \frac{d^3\mathbf{p}}{(2\pi)^3} v^\mu \frac{\partial f(\mathbf{p})}{\partial p^\beta} \Big(g^{\nu\beta} - \frac{v^\nu q^\beta}{q\cdot v + i\epsilon} \Big) \tag{8.1}$$

where $f(\mathbf{p})$ is the distribution function which is completely arbitrary.

Let us consider an anisotropic relativistic plasma which has a strong anisotropy in the momentum distribution. In this scenario, the phase space distribution can be obtained by rescaling an arbitrary isotropic distribution along one direction in momentum space and can be expressed as follows [21]:

$$f(\mathbf{p}) = f_{\mathrm{iso}}(\sqrt{\mathbf{p}^2 + \xi(\mathbf{p}\cdot\hat{\mathbf{n}})^2}, p_{\mathrm{hard}}) \tag{8.2}$$

where $\xi \geq -1$ is a parameter that reflects the strength of anisotropy and $\hat{\mathbf{n}}$ is the direction of anisotropy. p_{hard} is a hard momentum scale which is related to the average momentum

in the partonic distribution function. In the isotropic scenario, $p_{\rm hard}$ can be identified with the temperature (T) of the medium and $\xi = 0$ in this case. Because of anisotropy, the self-energy depends not only on the four momentum k^μ but also on the direction of the anisotropy vector $n^\mu = (0, \hat{\mathbf{n}})$. Using a suitable tensorial basis [21], the self-energy can now be written as

$$\Pi^{\mu\nu} = \alpha A^{\mu\nu} + \beta B^{\mu\nu} + \gamma\, C^{\mu\nu} + \delta D^{\mu\nu} \tag{8.3}$$

where

$$\begin{aligned}
A^{\mu\nu} &= -g^{\mu\nu} + \frac{q^\mu q^\nu}{q^2} + \frac{\tilde{u}^\mu \tilde{u}^\nu}{\tilde{u}^2} \\
B^{\mu\nu} &= -\frac{q^2}{(u\cdot q)^2}\frac{\tilde{u}^\mu \tilde{u}^\nu}{\tilde{u}^2} \\
C^{\mu\nu} &= \frac{\tilde{u}^2 q^2}{\tilde{u}^2 q^2 + (n\cdot q)^2}[\tilde{n}^\mu \tilde{n}^\nu - \frac{\tilde{u}\cdot\tilde{n}}{\tilde{u}^2}(\tilde{u}^\mu \tilde{n}^\nu + \tilde{n}^\mu \tilde{u}^\nu) + \frac{(\tilde{u}\cdot\tilde{n})^2}{\tilde{u}^4}\tilde{u}^\mu \tilde{u}^\nu] \\
D^{\mu\nu} &= \frac{q^2}{u\cdot q}[2\frac{\tilde{u}\cdot\tilde{n}}{\tilde{u}^2}\tilde{u}^\mu \tilde{u}^\nu - (\tilde{u}^\mu \tilde{n}^\nu + \tilde{n}^\mu \tilde{u}^\nu)]
\end{aligned} \tag{8.4}$$

Here, $u^\mu = (1,0,0,0)$ is the four velocity of the medium at rest and $\tilde{u}^\mu = u^\mu - \frac{u\cdot q}{q^2}q^\mu$. Using the anisotropic distribution function, the spatial component of the self-energy can be written as

$$\Pi^{ij} = \mu^2 \int \frac{d\Omega}{4\pi} v^i \frac{v^l + \xi(\mathbf{v}\cdot\mathbf{n})n^l}{1+\xi(\mathbf{v}\cdot\mathbf{n})^2}\Big(\delta^{jl} + \frac{v^j q^l}{q\cdot v + i\epsilon}\Big) \tag{8.5}$$

where μ is the isotropic Debye mass. Now the four structure functions can be determined by the following contractions:

$$\begin{aligned}
q^i \Pi^{ij} q^j &= \mathbf{q}^2\beta, \qquad A^{il}n^l\Pi^{ij}k^j = (\mathbf{q}^2 - (n\cdot q)^2)\delta, \\
A^{il}n^l\Pi^{ij}A^{jm}n^m &= \frac{\mathbf{q}^2 - (n\cdot q)^2}{\mathbf{q}^2}(\alpha+\gamma), \qquad \mathrm{Tr}\Pi^{ij} = 2\alpha + \beta + \gamma
\end{aligned} \tag{8.6}$$

In the isotropic limit, the structure functions α and β are directly related to the isotropic HTL self-energies and other structure functions vanish. With these structure functions,

one can construct the effective propagator in an anisotropic medium as

$$\Delta^{\mu\nu} = \frac{1}{q^2-\alpha}[A^{\mu\nu} - C^{\mu\nu}] + \Delta_G[(q^2-\alpha-\gamma)\frac{\omega^4}{q^4}B^{\mu\nu} + (\omega^2-\beta)C^{\mu\nu} + \delta\frac{\omega^2}{q^2}D^{\mu\nu}] - \frac{\lambda}{q^4}q^\mu q^\nu \quad (8.7)$$

where $\Delta_G^{-1} = (q^2-\alpha-\gamma)(\omega^2-\beta) - \delta^2[q^2-(n\cdot q)^2]$ The heavy quark potential in an anisotropic plasma can be determined from the static gluon propagator in the following way:

$$\begin{aligned} V(\mathbf{q},\xi) &= \mathrm{g}^2\Delta^{00}(\omega=0,\mathbf{q},\xi) \\ &= \mathrm{g}^2\frac{1}{(\mathbf{q}^2+m_\beta^2)-m_\delta^2}. \end{aligned} \quad (8.8)$$

Here

$$m_\beta^2 = \mu^2\frac{(\sqrt{\xi}+(1+\xi)\arctan\sqrt{\xi})(\mathbf{q}^2+\xi q_\perp^2) + \xi q_z(q_z\sqrt{\xi} + \frac{\mathbf{q}^2(1+\xi)}{\mathbf{q}^2+\xi q_\perp^2}\arctan\frac{\sqrt{\xi}q_z}{\sqrt{\mathbf{q}^2+\xi q_\perp^2}})}{2\sqrt{\xi}(1+\xi)(\mathbf{q}^2+\xi q_\perp^2)} \quad (8.9)$$

and

$$m_\delta^2 = -\mu^2\frac{\pi\xi q_z q_\perp|\mathbf{q}|}{4(\mathbf{q}^2+\xi q_\perp^2)^{\frac{3}{2}}} \quad (8.10)$$

where $q_z = \mathbf{q}\cdot\hat{\mathbf{n}}$ and $q_\perp = \mathbf{q} - \hat{\mathbf{n}}(\mathbf{q}\cdot\hat{\mathbf{n}})$ denote the particle momentum along and transverse to the direction $\hat{\mathbf{n}}$ of anisotropy, respectively. For the special case $q_z = 0$, the potential in an anisotropic medium reduces to

$$V(\mathbf{q},\xi) = \frac{\mathrm{g}^2}{\mathbf{q}^2+\mathcal{R}(\xi)\mu^2} \quad (8.11)$$

where $\mathcal{R}(\xi) = \frac{1}{2}(\frac{1}{1+\xi} + \frac{\arctan\sqrt{\xi}}{\sqrt{\xi}})$.

The heavy quark radiative energy loss per unit length [45, 46] is obtained by folding the gluon radiation rate $\Gamma(E)$ with the gluon energy $\omega + q_0$. The soft gluon and soft

rescattering approximations ($\omega >> |\mathbf{k}| \sim |\mathbf{q}|$), $\omega + q_0 \approx \omega$, leads to

$$\frac{dE}{dL} = \frac{1}{D_R}\int d\omega\, \omega \frac{d\Gamma(E)}{d\omega} \approx \frac{E}{D_R}\int dx\, x\frac{d\Gamma(E)}{dx} \tag{8.12}$$

where in anisotropic media we have [47]

$$x\frac{d\Gamma(E)}{dx} = D_R\frac{C_R\alpha_s}{\pi}\frac{1}{\lambda}\int \frac{d^2\mathbf{k}}{\pi}\frac{d^2\mathbf{q}}{\pi}|V(\mathbf{q},\xi)|^2\frac{\mu^2}{(4\pi\alpha_s)^2}\Big(\frac{\mathbf{k}}{\mathbf{k}^2+\chi} - \frac{\mathbf{k}+\mathbf{q}}{(\mathbf{k}+\mathbf{q})^2+\chi}\Big)^2 \tag{8.13}$$

Here, the quantity x is the longitudinal momentum fraction of the heavy quark carried away by the radiated gluon and $\chi = m_q^2x^2 + m_g^2$, $m_g^2 = \frac{\mu^2}{2}$ is the effect gluon mass and m_q is the mass of quark.

This finally leads to

$$\begin{aligned}
\frac{\Delta E}{E} &= \frac{C_R\alpha_s}{\pi}\frac{L}{\lambda}\int dx\,\frac{d^2\mathbf{k}}{\pi}\frac{d^2\mathbf{q}}{\pi}\frac{\mu^2}{(\mathbf{q}^2+\mathcal{R}(\xi)\mu^2)^2}\Big(\frac{\mathbf{k}}{\mathbf{k}^2+\chi} - \frac{\mathbf{k}+\mathbf{q}}{(\mathbf{k}+\mathbf{q})^2+\chi}\Big)^2 \\
&= \frac{C_R\alpha_s}{2\pi^2}\frac{L}{\lambda}\int dx\, d^2\mathbf{q}\frac{\mu^2}{(\mathbf{q}^2+\mathcal{R}(\xi)\mu^2)^2}\Bigg[-1 - \frac{2k_{\max}^2}{k_{\max}^2+\chi} + \frac{\mathbf{q}^2 - k_{\max}^2+\chi}{\sqrt{\mathbf{q}^4+2\mathbf{q}^2(\chi-k_{\max}^2)+(k_{\max}^2+\chi)^2}} \\
&+ \frac{2(\mathbf{q}^2+2\chi)}{\mathbf{q}^2\sqrt{1+\frac{4\chi}{\mathbf{q}^2}}}\ln\Big(\frac{k_{\max}^2+\chi}{\chi}\frac{(\mathbf{q}^2+3\chi)+\sqrt{1+\frac{4\chi}{\mathbf{q}^2}}(\mathbf{q}^2+\chi)}{(\mathbf{q}^2-k_{\max}^2+3\chi)+\sqrt{1+\frac{4\chi}{\mathbf{q}^2}}\sqrt{\mathbf{q}^4+2\mathbf{q}^2(\chi-k_{\max}^2)+(k_{\max}^2+\chi)^2}}\Big)\Bigg]
\end{aligned} \tag{8.14}$$

where $k_{\max} = 2E\sqrt{x(1-x)}$. Here we assume that α_s is not running.

In the above expression, λ is defined as the effective mean free path for a heavy quark scattering from quark-type and gluon-type static scattering centers [47]:

$$\frac{1}{\lambda} = \frac{1}{\lambda_q} + \frac{1}{\lambda_g} = 18\alpha_s\frac{1.202}{\pi^2}\frac{T}{\sqrt{1+\xi}\mathcal{R}(\xi)}\frac{1+\frac{N_f}{6}}{1+\frac{N_f}{4}} \tag{8.15}$$

where N_f is the number of flavour.

8.2.2 Hadronic p_{T} spectrum

The differential cross section of heavy meson in nucleon-nucleon collisions can be obtained by convoluting the bare heavy quark production cross section with the fragmentation function $D_Q^h(z)$ [48] as

$$\frac{d\sigma^h}{dp_{\mathrm{T}}} = \sum_f \int_0^1 dz \frac{D_Q^h(z)}{z^2} \frac{d\sigma}{dp_{\mathrm{T}}^f} \tag{8.16}$$

Here, f is the number of flavours , $z = p_T/p_T^f$ is the hadron momentum fraction. $\frac{d\sigma}{dp_{\mathrm{T}}}$ has been estimated using FONLL [49, 50]. To obtain the functional form of $\frac{d\sigma}{dp_{\mathrm{T}}}$, we fit it with the following empirical function were a, b, c, d are the fitting parameters.

$$f(p_{\mathrm{T}}) = a \frac{p_{\mathrm{T}}}{\left(1 + \left(\frac{p_{\mathrm{T}}}{b}\right)^c\right)^d} \tag{8.17}$$

In Fig. 8.1, the quark production cross sections as a function of p_{T} are shown at $\sqrt{s_{\mathrm{NN}}}$ = 2.76 TeV (left) and 5.02 TeV (right) together with the fitted function.

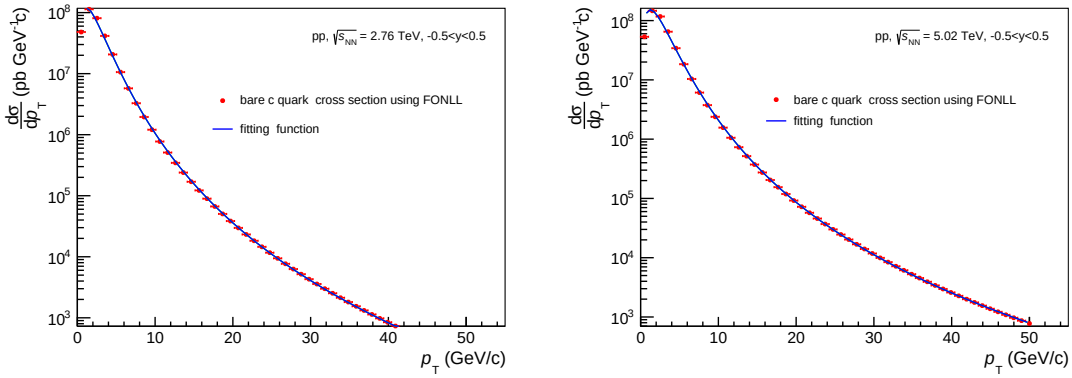

Figure 8.1: bare c quark cross section in proton proton collisions at $\sqrt{s_{\mathrm{NN}}}$ = 2.76 TeV (left panel) and 5.02 TeV (right panel)

Having obtained the differential cross-section of hadron in $p-p$ collision one can obtain the p_{T} differential cross section in $A-A$ collisions by multiplying the $p-p$ result with the nuclear overlap function for a given centrality class. Nevertheless, the consideration of jet-quenching as a final state effect in $A-A$ collisions can be implemented by modifying

the fragmentation function [51]. The modification of the fragmentation function includes the final state effect in the presence of anisotropy. Now the energy loss of high energy quarks and gluons traveling through the dense plasma can measure the integrated density of the colored particles. This non-Abelian energy loss is a function of parton opacity L/λ. We use the expression given by Eq.(8.14) which is derived to first order in opacity.

Now in order to get the hadronic $p_{\rm T}$ spectrum in $A-A$ collisions we modify the fragmentation function to obtain an effective fragmentation function as follows [52]:

$$D_{A-A}(z,Q) = \frac{z^*}{z} D_{pp}(z^*,Q), \tag{8.18}$$

where, $z^* = z/(1\text{-}\Delta E/E)$ is the modified hadron momentum fraction. In order to consider the jet production geometry it has been assumed that all the jets are not produced at the same point and the path lengths traversed in the QGP medium by these partons before fragmentation are not the same. It is also assumed that the jet initially produced at (r,ϕ), propagates at an angle ϕ with respect to $\hat{\mathbf{r}}$ in the transverse plane and leaves the plasma after a proper time ($t_{\rm L}$) or equivalently after traversing a distance L(r,ϕ) $= \sqrt{R_{\rm T}^2 - r^2 sin\phi^2}$ - $R_{\rm T}$cosϕ, where $R_{\rm T}$ is the transverse radius of the colliding system. Thus, the hadron $p_{\rm T}$ spectra depends on the path length of the initial parton and the temperature profile along that path. This is not the same for all jets as it depends on the location of jet production and the propagation direction. Consequently, it is necessary to convolute the resulting expression over all transverse positions and directions. Since the jet production at $\mathbf{r}$ is proportional to the number of binary collisions, the probability is proportional to the product of nuclear thickness functions:

$$P(\mathbf{r}) \propto T_{\rm A}(\mathbf{r}) T_{\rm B}(\mathbf{r}) \tag{8.19}$$

For hard sphere, this probability is given by

$$P(\mathbf{r}) = \frac{2}{\pi R_{\rm T}^2}\left(1 - \frac{r^2}{R_{\rm T}^2}\right)\theta(R_T - r) \tag{8.20}$$

in which $\int d^2rP(\mathbf{r})$=1

Using all the above mentioned conditions the hadron $p_{\rm T}$ spectra can be written as:

$$\frac{d^2N^h}{dp_{\rm T}dy} = \sum_f \int d^2rP(\mathbf{r}) \int_{t_{\rm i}}^{t_{\rm L}} \frac{dt}{t_{\rm L} - t_{\rm i}} \int \frac{dz}{z^2} \times D(z,Q)\frac{d^2N}{dp_{\rm T}^f dy} \tag{8.21}$$

where $\frac{d^2N^i}{dp_{\rm T}^f dy}$ is the distribution of initial momentum of jets and can be evaluated using FONLL formalism discussed in start of this section.The nuclear modification factor, $R_{\rm AA}$ is defined as

$$R_{\rm AA} = \frac{\frac{d^2N}{dp_{\rm T}dy}}{\left[\frac{d^2N}{dp_{\rm T}dy}\right]_0} \tag{8.22}$$

In the denominator, the suffix '0' indicates that energy loss has not been considered while evaluating the expression.

8.2.3 Space-time evaluation

For the calculation of the hadron p_T spectra, the evolution dynamics of the system needs to be incorporated. As the anisotropy is associated with of the early stage of heavy-ion collision, we are going to discuss the evolution of the anisotropy parameter ξ and the hard momentum scale $p_{\rm hard}$ which change with time. In the present work, the formalisam given in Ref. [39] has been closely followed to estimate the p_T distribution of hadrons over the initial few Fermi of the evolution of the plasma. The system evolves anisotropically from τ_i to $\tau_{\rm iso}$, where the study of the time dependence of $p_{\rm hard}(\tau)$ and $\xi(\tau)$ is essential. When the system approaches isotropization stage, a hydrodynamical evolution is applicable from $\tau_{\rm iso}$ onward. A transition width γ^{-1} is introduced owing to

a smooth transfer from the free streaming pre-equilibrium momentum space anisotropy to hydrodynamical behavior. The time dependence of different quantities are, therefore, obtained in respect to a smeared step function [53]:

$$\Lambda(\tau) = \frac{1}{2}\Big(\tanh[\gamma(\tau - \tau_{\rm iso})/\tau_{\rm iso}] + 1 \Big) \tag{8.23}$$

For $\tau \ll \tau_{\rm iso}$ ($\gg \tau_{\rm iso}$), we have $\Lambda(\tau) = 0$ (1) which corresponds to anisotropic (hydrodynamics) evolution. With this, the time dependence of relevant quantities are as follows:

$$\xi(\tau) = \left(\frac{\tau}{\tau_i}\right)^{\delta[1-\Lambda(\tau)]} - 1, \quad p_{\rm hard}(\tau) = T_i \bar{\mathcal{U}}^{c_s^2}(\tau) \tag{8.24}$$

where

$$\begin{aligned} \mathcal{U}(\tau) &\equiv \left[\mathcal{R}\Big((\frac{\tau_{\rm iso}}{\tau})^{\delta} - 1\Big)\right]^{\frac{3}{4}\Lambda(\tau)} \left(\frac{\tau_{\rm iso}}{\tau}\right)^{1-\delta[1-\Lambda(\tau)]/2}, \\ \bar{\mathcal{U}}(\tau) &\equiv \frac{\mathcal{U}(\tau)}{\mathcal{U}(\tau_i)} \end{aligned} \tag{8.25}$$

T_i is the initial temperature of the plasma and c_s^2 is the velocity of sound. The exponent $\delta = 2$ corresponds to free-streaming and $\delta = 0$ corresponds to thermal equilibrium. For the isotropic case, $p_{\rm hard} = T$ and $\tau_{\rm iso} = \tau_i$. It has been assumed that the longitudinal expansion of the plasma at the early stage is negligible because of the transverse expansion. The stronger strength of the momentum space anisotropy at the early stage justifies this assumption. Due to the transverse density profile of the colliding nuclei, the initial temperature profile may be assumed to be [43]

$$T_i(r) = T_i[2(1 - \frac{r^2}{R_T^2})]^{\frac{1}{4}} \tag{8.26}$$

Thus, the profile of the hard momentum scale is modified according to Eq. 8.26.

The formation of an isotropic QGP at an initial time τ_i and in its corresponding temperature T_i has been presumed in the present work. Subsequently, the rapid longitudinal expansion entails an anisotropic QGP which sustains till $\tau_{\rm iso}$. While calculating the initial temperature, in case of isentropic expansion the correlation between the experimentally measured hadron multiplicity and the initial temperature and the thermalization time can be established in the following way [54]:

$$T_i^3 \tau_i = \frac{2\pi^3}{45\zeta(3)\, R_T^2 4a_k} \left\langle \frac{dN}{d\eta} \right\rangle \tag{8.27}$$

where $\left\langle dN/d\eta \right\rangle$ is the total hadron multiplicity (mainly pions) for a given centrality class and can be obtained by experimentally measured charge particle multiplicity as $\left\langle dN/d\eta \right\rangle = 1.5 \times \left\langle dN_{ch}/d\eta \right\rangle$. τ_i is the initial thermalization time, $\zeta(3)$ is the Riemann zeta function and $a_k = (\pi^2/90)\, g_k$ is the degeneracy of the system created, where $g_k = (7/8 \cdot 2 \cdot 2 \cdot N_F \cdot N_c + 2 \cdot 8)$ and N_c being the number of colors. The initial temperatures for different centrality classes of ALICE measurement at $\sqrt{s_{\rm NN}} = 2.76$ TeV [55] and 5 TeV [56] in Pb–Pb collisions are presented in Table 8.1.

Table 8.1: Initial temperatures for different centrality class at LHC energies from ALICE measurements.

$\sqrt{s_{\rm NN}}$ (TeV)	Centrality	$< dN_{ch}/d\eta >$	τ_i (fm)	$T_i(MeV)$
2.76	0% - 10%	1447.5	0.1	650
	30% - 50%	343.5	0.2	319
5.02	0% - 10%	1764	0.1	690
	30% - 50%	415	0.2	340

8.3 Results

The momentum dependence of the fractional energy loss from the radiative process in an infinitely extended static anisotropic plasma has been calculated. For this numerical result, a plasma at a temperature $T = 450$ MeV, with effective light quark flavour

$N_F = 2.5$ and strong interaction coupling constant $\alpha_s = 0.3$ over an assume effective path length $L = 6.2$ fm have been consider. The charm quark mass is assumed to be $M = 1.3$ GeV and the Debye screening mass $\mu = gT\sqrt{1 + N_f/6}$ MeV.

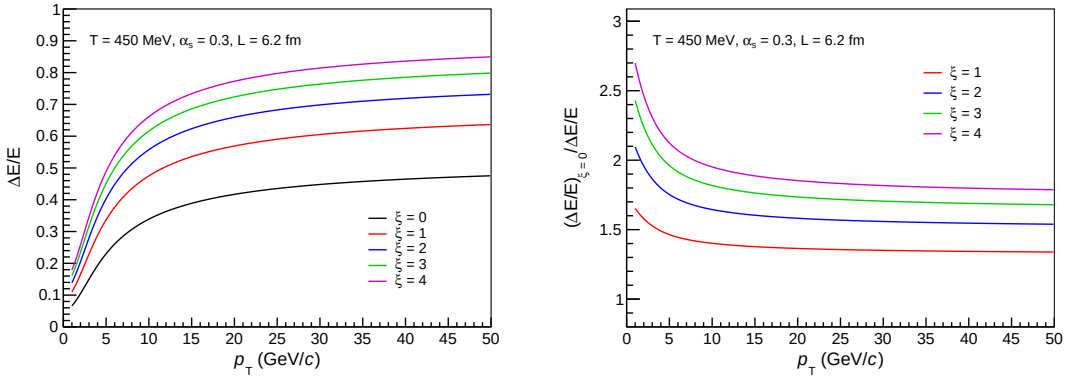

Figure 8.2: Fractional energy loss of a charm quark as a function of momentum at different anisotropy parameter (ξ) value inside the QGP medium (left panel). The ratio of the fractional energy loss in isotropic medium to that in anisotropic medium is also presented (right panel).

In the left panel of Fig. 8.2, the fractional energy loss is depicted for a charm quark at different strengths of the anisotropy parameter ($\xi = \{0, 1, 2, 3, 4\}$) when it propagates along the direction of anisotropy. It is observed that the rate of increment of the energy loss is higher in the lower momentum region, whereas it saturates in the higher momentum region for all values of ξ considered here. This typical nature, as we shall see later, is also observed in the nuclear modification factor. We also notice that the fractional energy loss is enhanced with the increasing values of ξ. This enhancement can be understood by plotting the ratio of the fractional energy loss in an anisotropic medium to that in the isotropic case. The right panel of Fig. 8.2 indicates that in anisotropic plasma, with the increase of ξ, the two-body potential increases which intensifies the energy loss of the quarks [57].

Now let us turn to the calculation of nuclear modification factor at LHC energies. The initial conditions are taken from Table 8.1. The results for $R_{\rm AA}$ as a function of $p_{\rm T}$ for average D meson in Pb-Pb collisions for various values of the isotropization time,

$\tau_{\rm iso}$ have been compared with the ALICE data [14] for the centrality 0%- 10% at $\sqrt{s_{\rm NN}}$ = 2.76 TeV in the left panel of Fig. 8.3 . It is observed that the value of R_{AA} decreases by increasing the $\tau_{\rm iso}$. At high p_T the data show a rising tendency of R_{AA}, whereas the theoretical results saturate beyond certain p_T. This, as mentioned previously, is may be due to the assumption of aQGP with infinite extent (in fact, in all the cases of R_{AA} for different external conditions same behaviour have been observed). In the right panel of Fig. 8.3 the $R_{\rm AA}$ for 30%- 50% at $\sqrt{s_{\rm NN}}$ = 2.76 TeV is shown and it decreases with increasing $\tau_{\rm iso}$.

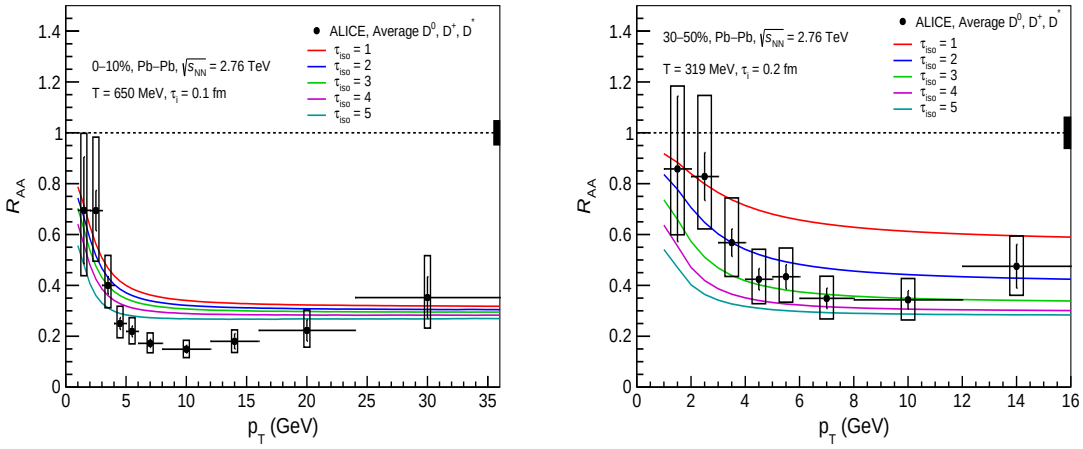

Figure 8.3: The nuclear modification factor $R_{\rm AA}$ of average D meson for (0-10)% (left panel) and (30-50)% (right panel) centrality in Pb-Pb collisions at $\sqrt{s_{\rm NN}}$ = 2.76 TeV. The initial conditions are taken as T_i = 650 (319) MeV and τ_i = 0.1 (0.2) fm/c form centrality 0-10 % (30-50 %). The different color line represent the $R_{\rm AA}$ values at different $T_{\rm iso}$. The experimental results are taken from ALICE measurement [14]

These numerical calculation have been compared our results with ALICE measurements at $\sqrt{s_{\rm NN}}$ = 5 TeV [15]. The Fig. 8.4 shows the $R_{\rm AA}$ as a function of $p_{\rm T}$ for centrality classes 0%- 10% and 30%- 50%. The dependency of $R_{\rm AA}$ with isotropization time is same as in $\sqrt{s_{\rm NN}}$ = 2.76 TeV case for both centrality classes. It is worth noting that the $p_{\rm T}$ spectra evaluated using our formalism reproduce the data reasonably well in the range $2 \leq \tau_{\rm iso} \leq 4$ fm/c at both energy and centrality classes.

The CMS Collaboration have also measured the D meson $R_{\rm AA}$ at $\sqrt{s_{\rm NN}}$ =2.76 TeV [16]. In Fig. 8.5, we have compared our results with the CMS measurement for centrality class

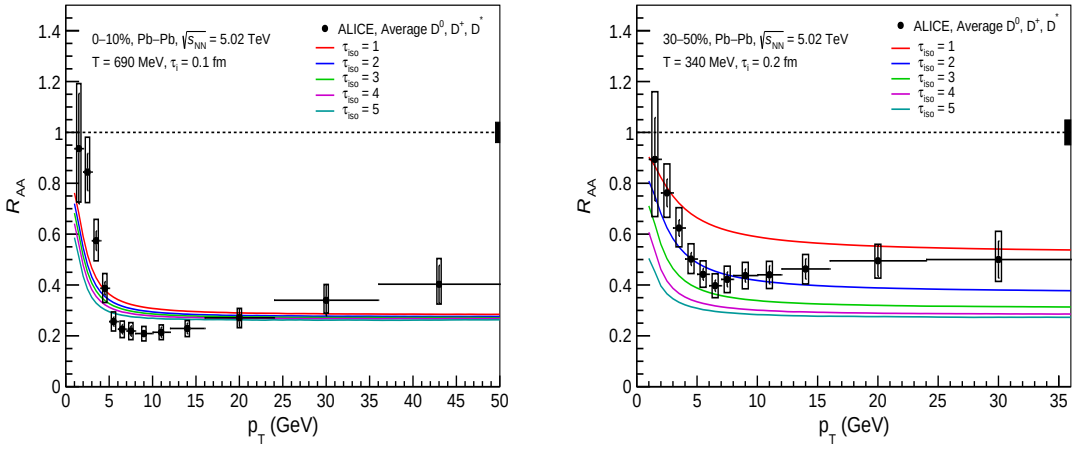

Figure 8.4: The nuclear modification factor $R_{\rm AA}$ of average D meson for (0-10)% (left panel) and (30-50)% (right panel) centrality in Pb-Pb collisions at $\sqrt{s_{\rm NN}} = 5.02$ TeV. The initial conditions are taken as $T_i = 690$ (340) MeV and $\tau_g = 0.1$ (0.2) fm/c form centrality 0-10 % (30-50 %). The different color line represent the $R_{\rm AA}$ values at different $T_{\rm iso}$. The experimental results are taken from ALICE measurement [15]

0-10 % at different $\tau_{\rm iso}$. Again our results are in fair agreement with CMS data with $\tau_{\rm iso}$ in the range $2 \leq \tau_{\rm iso} \leq 4$ fm/c. This agreement is better as CMS collaboration uses a higher $p_{\rm T}$ cut in $R_{\rm AA}$ measurement.

The ratio of the $R_{\rm AA}$ at $\sqrt{s_{\rm NN}} = 5$ to 2.76 TeV as a function of $p_{\rm T}$ for the centrality class 0%- 10% is shown in Fig. 8.6 at different value of $\tau_{\rm iso}$. The ratios are seen to decrease by about 6-8% depending upon the value of $\tau_{\rm iso}$ with a harder $p_{\rm T}$ distribution and are consistent with model prediction by Djordjevic [58].

8.4 Summary

we have briefly recapitulated the formalism of radiative fractional energy loss of a fast moving heavy quark where it radiates gluons due to the scattering from static scattering center in an infinitely extended anisotropic medium. It is shown that the fractional energy loss changes with the anisotropy parameter, ξ due to the modification of the heavy quark potential in the aQGP.

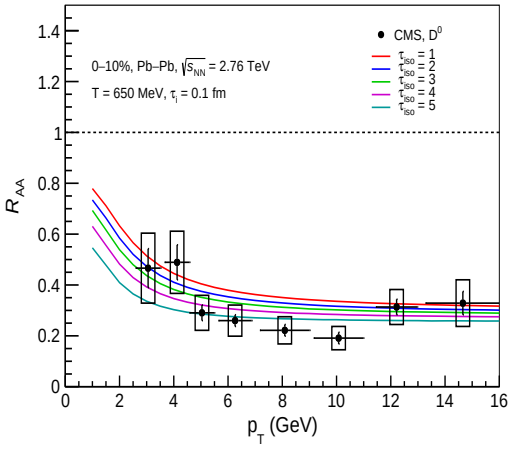

Figure 8.5: The nuclear modification factor $R_{\rm AA}$ of average D meson for (0-10)% at $\sqrt{s_{\rm NN}}$ = 2.76 TeV. The different color line represent the $R_{\rm AA}$ values at different $T_{\rm iso}$. The experimental results are taken from CMS measurement [16].

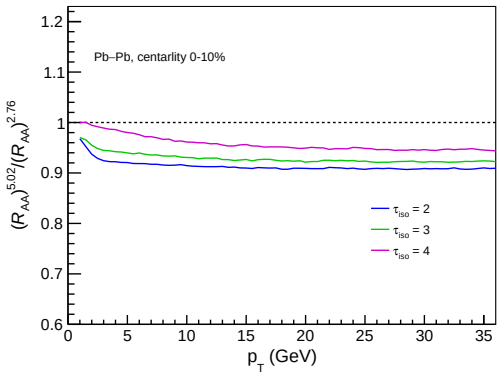

Figure 8.6: Ratio of $R_{\rm AA}$ at $\sqrt{s_{\rm NN}}$ = 5.02 TeV to $\sqrt{s_{\rm NN}}$ = 2.76 TeV at different τ_{iso} for centrality bin 0-10%.

We then used the fractional energy loss of heavy quarks to evaluate the D-meson p_T spectrum vis-a-vis its nuclear modification factor (R_{AA}) by incorporating this effect in the fragmentation function of the energy depleted heavy quarks. To take into account the time dependence of the anisotropic parameter (ξ) and the hard momentum scale ($p_{\rm hard}$), a simple (1+1)d space-time evolution model [43] has been invoked with the introduction of an intermediate time scale $\tau_{\rm iso}$, called the isotropization time. The results for nuclear modification factor (R_{AA}) of D-meson are then compared with the ALICE data at $\sqrt{s_{NN}}$ = 2.76 and 5.02 TeV in two centrality classes. It is found that the value of $\tau_{\rm iso}$, which describes the data reasonably, lies in the range $2 \leq \tau_{\rm iso} \leq 4$ fm/c for both

the energies and centrality classes considered here. By comparing with the CMS data at $\sqrt{s_{NN}} = 2.76$ in the 0-10% centrality class, we conclude that the data are described fairly well when $\tau_{\rm iso}$ lies in the same range as extracted from the ALICE data. Ratio of $R_{\rm AA}$ at $\sqrt{s_{NN}} = 5.02$ to 2.76 TeV have been calculated which we find to similar to that prediction in Djordjevic [58].

Bibliography

[1] E. V. Shuryak, *Theory of Hadronic Plasma*, *Sov. Phys. JETP* **47** (1978) 212–219.

[2] J. C. Collins and M. J. Perry, *Superdense matter: Neutrons or asymptotically free quarks?*, *Phys. Rev. Lett.* **34** (May, 1975) 1353–1356.

[3] BRAHMS collaboration, I. Arsene et al., *Quark gluon plasma and color glass condensate at RHIC? The Perspective from the BRAHMS experiment*, *Nucl. Phys.* **A757** (2005) 1–27, [nucl-ex/0410020].

[4] U. W. Heinz and M. Jacob, *Evidence for a new state of matter: An Assessment of the results from the CERN lead beam program*, nucl-th/0002042.

[5] M. H. Thoma and M. Gyulassy, *Quark Damping and Energy Loss in the High Temperature QCD*, *Nucl. Phys.* **B351** (1991) 491–506.

[6] E. Braaten and M. H. Thoma, *Energy loss of a heavy quark in the quark - gluon plasma*, *Phys. Rev.* **D44** (1991) R2625.

[7] M. G. Mustafa, D. Pal, D. K. Srivastava and M. Thoma, *Radiative energy loss of heavy quarks in a quark gluon plasma*, *Phys. Lett.* **B428** (1998) 234–240, [nucl-th/9711059].

[8] R. Baier, Y. L. Dokshitzer, A. H. Mueller and D. Schiff, *Quenching of hadron spectra in media*, *JHEP* **09** (2001) 033, [hep-ph/0106347].

[9] S. Jeon and G. D. Moore, *Energy loss of leading partons in a thermal QCD medium*, *Phys. Rev.* **C71** (2005) 034901, [hep-ph/0309332].

[10] A. K. Dutt-Mazumder, J.-e. Alam, P. Roy and B. Sinha, *Stopping power of hot QCD plasma*, *Phys. Rev.* **D71** (2005) 094016, [hep-ph/0411015].

[11] P. Roy, J.-e. Alam and A. K. Dutt-Mazumder, *Quenching of light hadrons at RHIC in a collisional energy loss scenario*, *J. Phys.* **G35** (2008) 104047, [0806.0446].

[12] M. Djordjevic and U. W. Heinz, *Radiative energy loss in a finite dynamical QCD medium*, *Phys. Rev. Lett.* **101** (2008) 022302, [0802.1230].

[13] R. Abir, C. Greiner, M. Martinez, M. G. Mustafa and J. Uphoff, *Soft gluon emission off a heavy quark revisited*, *Phys. Rev.* **D85** (2012) 054012, [1109.5539].

[14] ALICE collaboration, J. Adam et al., *Transverse momentum dependence of D-meson production in Pb-Pb collisions at* $\sqrt{s_{NN}} = 2.76$ *TeV*, *JHEP* **03** (2016) 081, [1509.06888].

[15] ALICE collaboration, S. Acharya et al., *Measurement of* D^0, D^+, D^{*+} *and* D_s^+ *production in Pb-Pb collisions at* $\sqrt{s_{NN}} = 5.02$ *TeV*, *JHEP* **10** (2018) 174, [1804.09083].

[16] CMS collaboration, V. Khachatryan et al., *Nuclear Modification Factor of prompt* D^0 *in PbPb Collisions at* $\sqrt{s_{NN}} = 2.76$ *TeV*, *CMS-PAS-HIN-15-005* .

[17] CMS collaboration, A. M. Sirunyan et al., *Measurement of the* $B^{\pm}$ *Meson Nuclear Modification Factor in Pb-Pb Collisions at* $\sqrt{s_{NN}} = 5.02$ TeV, *Phys. Rev. Lett.* **119** (2017) 152301, [1705.04727].

[18] ALICE collaboration, S. Acharya et al., Υ *suppression at forward rapidity in Pb-Pb collisions at* $\sqrt{s_{NN}} = 5.02$ *TeV*, *Phys. Lett.* **B790** (2019) 89–101, [1805.04387].

[19] ALICE collaboration, J. Adam et al., *J/ψ suppression at forward rapidity in Pb-Pb collisions at $\sqrt{s_{NN}} = 5.02$ TeV*, *Phys. Lett.* **B766** (2017) 212–224, [1606.08197].

[20] ALICE collaboration, W. Shaikh, *Quarkonium measurements at forward rapidity with ALICE at the LHC*, in *18th International Conference on Strangeness in Quark Matter (SQM 2019) Bari, Italy, June 10-15, 2019*, 2019. 1910.06695.

[21] P. Romatschke and M. Strickland, *Collective modes of an anisotropic quark-gluon plasma*, *Phys. Rev. D* **68** (Aug, 2003) 036004.

[22] U. W. Heinz, *'RHIC serves the perfect fluid': Hydrodynamic flow of the QGP*, in *Proceedings, Workshop on Extreme QCD, 2005*, pp. 3–12, 2005. nucl-th/0512051.

[23] R. Baier, A. H. Mueller, D. Schiff and D. T. Son, *'Bottom up' thermalization in heavy ion collisions*, *Phys. Lett.* **B502** (2001) 51–58, [hep-ph/0009237].

[24] M. Luzum and P. Romatschke, *Conformal Relativistic Viscous Hydrodynamics: Applications to RHIC results at s(NN)**(1/2) = 200-GeV*, *Phys. Rev.* **C78** (2008) 034915, [0804.4015].

[25] S. Mrowczynski, *Plasma instability at the initial stage of ultrarelativistic heavy ion collisions*, *Phys. Lett.* **B314** (1993) 118–121.

[26] S. Mrowczynski, *Instabilities driven equilibration of the quark-gluon plasma*, *Acta Phys. Polon.* **B37** (2006) 427–454, [hep-ph/0511052].

[27] P. Arnold, J. Lenaghan, G. D. Moore and L. G. Yaffe, *Apparent thermalization due to plasma instabilities in the quark-gluon plasma*, *Phys. Rev. Lett.* **94** (Feb, 2005) 072302.

[28] A. Rebhan, P. Romatschke and M. Strickland, *Hard-loop dynamics of non-abelian plasma instabilities*, *Phys. Rev. Lett.* **94** (Mar, 2005) 102303.

[29] P. Romatschke and R. Venugopalan, *Collective non-Abelian instabilities in a melting color glass condensate*, *Phys. Rev. Lett.* **96** (2006) 062302, [hep-ph/0510121].

[30] S. Mrowczynski, *Plasma instability at the initial stage of ultrarelativistic heavy ion collisions*, *Phys. Lett.* **B314** (1993) 118–121.

[31] S. Mrowczynski, *Color collective effects at the early stage of ultrarelativistic heavy ion collisions*, *Phys. Rev.* **C49** (1994) 2191–2197.

[32] J. Randrup and S. Mrowczynski, *Chromodynamic Weibel instabilities in relativistic nuclear collisions*, *Phys. Rev.* **C68** (2003) 034909, [nucl-th/0303021].

[33] P. B. Arnold, J. Lenaghan and G. D. Moore, *QCD plasma instabilities and bottom up thermalization*, *JHEP* **08** (2003) 002, [hep-ph/0307325].

[34] P. B. Arnold, J. Lenaghan, G. D. Moore and L. G. Yaffe, *Apparent thermalization due to plasma instabilities in quark-gluon plasma*, *Phys. Rev. Lett.* **94** (2005) 072302, [nucl-th/0409068].

[35] A. Rebhan, P. Romatschke and M. Strickland, *Hard-loop dynamics of non-Abelian plasma instabilities*, *Phys. Rev. Lett.* **94** (2005) 102303, [hep-ph/0412016].

[36] P. Romatschke and M. Strickland, *Collective modes of an anisotropic quark-gluon plasma II*, *Phys. Rev.* **D70** (2004) 116006, [hep-ph/0406188].

[37] P. B. Arnold, G. D. Moore and L. G. Yaffe, *The Fate of non-Abelian plasma instabilities in 3+1 dimensions*, *Phys. Rev.* **D72** (2005) 054003, [hep-ph/0505212].

[38] B. Schenke and M. Strickland, *Fermionic Collective Modes of an Anisotropic Quark-Gluon Plasma*, *Phys. Rev.* **D74** (2006) 065004, [hep-ph/0606160].

[39] M. Martinez and M. Strickland, *Pre-equilibrium dilepton production from an anisotropic quark-gluon plasma*, *Phys. Rev. C* **78** (Sep, 2008) 034917.

[40] L. Bhattacharya and P. Roy, *Photons from anisotropic Quark-Gluon-Plasma*, *Phys. Rev.* **C78** (2008) 064904, [0809.4596].

[41] L. Bhattacharya and P. Roy, *Measuring isotropization time of Quark-Gluon-Plasma from direct photon at RHIC*, *Phys. Rev.* **C79** (2009) 054910, [0812.1478].

[42] M. Mandal and P. Roy, *Some Aspects of Anisotropic Quark-Gluon Plasma*, *Adv. High Energy Phys.* **2013** (2013) 371908.

[43] R. J. Fries, B. Muller and D. K. Srivastava, *High-energy photons from passage of jets through quark gluon plasma*, *Phys. Rev. Lett.* **90** (2003) 132301, [nucl-th/0208001].

[44] S. Mrówczyński and M. H. Thoma, *Hard loop approach to anisotropic systems*, *Phys. Rev. D* **62** (Jul, 2000) 036011.

[45] M. Djordjevic and U. Heinz, *Radiative heavy quark energy loss in a dynamical QCD medium*, *Phys. Rev.* **C77** (2008) 024905, [0705.3439].

[46] M. Djordjevic, *Theoretical formalism of radiative jet energy loss in a finite size dynamical QCD medium*, *Phys. Rev.* **C80** (2009) 064909, [0903.4591].

[47] P. Roy and A. K. Dutt-Mazumder, *Radiative energy loss in an anisotropic quark-gluon plasma*, *Phys. Rev. C* **83** (Apr, 2011) 044904.

[48] C. Peterson, D. Schlatter, I. Schmitt and P. M. Zerwas, *Scaling Violations in Inclusive e+ e- Annihilation Spectra*, *Phys. Rev.* **D27** (1983) 105.

[49] M. Cacciari, M. Greco and P. Nason, *The P(T) spectrum in heavy flavor hadroproduction*, *JHEP* **05** (1998) 007, [hep-ph/9803400].

[50] M. Cacciari, S. Frixione and P. Nason, *The p(T) spectrum in heavy flavor photoproduction*, *JHEP* **03** (2001) 006, [hep-ph/0102134].

[51] P. Roy, A. K. Dutt-Mazumder and J.-e. Alam, *Energy loss and dynamical evolution of quark p_T spectra*, *Phys. Rev. C* **73** (Apr, 2006) 044911.

[52] X.-N. Wang, *Effects of jet quenching on high p_T hadron spectra in high-energy nuclear collisions*, *Phys. Rev. C* **58** (Oct, 1998) 2321–2330.

[53] M. Martinez and M. Strickland, *Measuring quark-gluon-plasma thermalization time with dileptons*, *Phys. Rev. Lett.* **100** (Mar, 2008) 102301.

[54] S. Turbide, C. Gale, S. Jeon and G. D. Moore, *Energy loss of leading hadrons and direct photon production in evolving quark-gluon plasma*, *Phys. Rev. C* **72** (Jul, 2005) 014906.

[55] ALICE collaboration, K. Aamodt et al., *Charged-particle multiplicity density at mid-rapidity in central Pb-Pb collisions at $\sqrt{s_{NN}} = 2.76$ TeV*, *Phys. Rev. Lett.* **105** (2010) 252301, [1011.3916].

[56] ALICE collaboration, J. Adam et al., *Centrality dependence of the charged-particle multiplicity density at midrapidity in Pb-Pb collisions at $\sqrt{s_{\rm NN}} = 5.02$ TeV*, *Phys. Rev. Lett.* **116** (2016) 222302, [1512.06104].

[57] M. Mandal, L. Bhattacharya and P. Roy, *Nuclear modification factor in an anisotropic quark-gluon plasma*, *Phys. Rev. C* **84** (Oct, 2011) 044910.

[58] M. Djordjevic and M. Djordjevic, *Predictions of heavy-flavor suppression at 5.1 TeV Pb + Pb collisions at the CERN Large Hadron Collider*, *Phys. Rev.* **C92** (2015) 024918, [1505.04316].

CHAPTER 9

Future Outlook

There has been a decade long ongoing effort by ALICE to investigate the signatures of Hot Nuclear Matter (related to QGP) and Cold Nuclear Matter effects present in the medium produced in the ultra-relativistic collisions at LHC. The Muon Spectrometer has made important contribution towards this study. In the present thesis, the measurements of Υ(1S), Υ(2S) and Υ(3S) in pp, p–Pb and Pb–Pb collisions provide the new inputs for the characterization of the bottomonium production at the LHC energies.

The current pp measurements have not been directly used as the reference of R_{PbPb} analysis due to its statistical limitations. Hence, the future Υ(nS) measurements in pp collisions during Run 3 and Run 4 [1] will lead to a more accurate reference for heavy-ions analysis and additionally provide the experimental constraints on quarkonium production models.

The suppression of Υ(1S) in Pb–Pb collisions at LHC energies can be explained by color-screening mechanism, whereas the J/ψ suppression can be explained by the interplay of color-screening and regeneration mechanisms. The elliptic flow coefficient v_2 of Υ(1S) has been found to be zero in Pb–Pb collisions measured by both ALICE [2]

and CMS [3] experiments. This observation is in contrast with the J/ψ $v2$ in Pb–Pb collisions, suggesting different medium effects for bottomonia and charmonia. Due to the limited statistics, Υ(3S) suppression could not be measured at the forward rapidity. The sequential suppression in bottomonium sector will lead to the estimation of the temperature of the fireball created in Pb–Pb collisions from the ratios of Υ(nS)/Υ(1S). The larger data samples in Run 3 and Run 4 periods, together with improved detector performance and measurement techniques, will allow us to significantly improve the $R_{\rm PbPb}$ and v_2 measurements, with extended kinematic coverage (in transverse momentum) and study the currently-unobserved quarkonium state Υ(3S), in Pb–Pb collisions [4]. It is worth noting that more accurate measurements in y, $p_{\rm T}$ and centrality bins at the forward rapidity may impose new constraints in theoretical models in near future, thereby, improving our understanding of the characteristics of the fireball.

During Run 1 and Run 2 periods, the bottomonium measurements in p–Pb collisions confirm the Υ(1S) suppression in forward and backward rapidity regions with a hint for a stronger suppression for Υ(2S). These measurements represent an important platform for the understanding the role of cold nuclear matter effects in p–Pb collisions and open up the way for future precision analyses with the upcoming LHC Run 3 and Run 4 data.

For the phenomenological calculations of D-meson, the $R_{\rm PbPb}$ evaluation does not include the collisional energy loss as its contribution will be marginal at LHC energies. It is worthwhile to mention that the chromo-electromagnetic field fluctuations in the QGP can lead to the energy gain of the heavy quark which is an opposite effect to the present observations. We have not included this effect in the present work. These two perspectives, namely, collisional energy loss and chromo-electromagnetic field fluctuation can be added to the radiative energy loss in the estimation of isotropization time to impose better constraint on the extracted value of $\tau_{\rm iso}$. Another improvement is to

be consider the finite size of the aQGP. It may alter the observed saturation behavior in R_{PbPb} possibly explaining the data better in the high p_T region.

These are few research directions connected to the present thesis work, which will be addressed in near future.

Bibliography

[1] J. Jowett, *Colliding Heavy Ions in the LHC*, in *Proc. 9th International Particle Accelerator Conference (IPAC'18), Vancouver, BC, Canada, April 29-May 4, 2018*, no. 9 in International Particle Accelerator Conference, (Geneva, Switzerland), pp. 584–589, JACoW Publishing, June, 2018. DOI.

[2] ALICE collaboration, S. Acharya et al., *Measurement of* Υ(1S) *elliptic flow at forward rapidity in Pb-Pb collisions at* $\sqrt{s_{\rm NN}} = 5.02$ *TeV*, *Phys. Rev. Lett.* **123** (2019) 192301, [1907.03169].

[3] CMS collaboration, *Measurement of the elliptic flow of* Υ*(1S) and* Υ*(2S) mesons in PbPb collisions at* $\sqrt{s_{NN}} = 5.02$ *TeV*, .

[4] Z. Citron et al., *Report from Working Group 5: Future physics opportunities for high-density QCD at the LHC with heavy-ion and proton beams*, *CERN Yellow Rep. Monogr.* **7** (2019) 1159–1410, [1812.06772].

Summary

The bottomonium (Υ), is a useful probe to investigate the properties of the deconfined medium, created in ultra-relativistic heavy-ion collisions. The modification of charmonium (J/ψ) production at LHC energies in heavy-ion collisions with respect to the binary-scaled yield in pp collisions has been explained as an interplay of the suppression and the regeneration mechanisms. In the Υ sector, the regeneration effects are expected to be negligible due to the small number of b quarks produced in relativistic heavy-ion collisions. However, the Cold Nuclear Matter (CNM) effects which include shadowing, parton energy loss, interaction with hadronic medium may also lead to a modification of bottomonium production. In order to disentangle the CNM effects from the hot nuclear matter effects, Υ production has been studied in p–Pb collisions in which the QGP is not expected to be formed. I have studied the bottomonium production via $\Upsilon \rightarrow \mu^+\mu^-$ decay channel in pp, p–Pb and Pb–Pb collisions using the ALICE Muon Spectrometer. Besides, a phenomenological study of the nuclear modification factor ($R_{\rm AA}$) of D meson in an anisotropic quark-gluon plasma at the LHC energies has been carried out by me.

The inclusive Υ(nS) production cross sections have been measured at forward rapidity ($2.5 < y < 4$) in pp collisions at $\sqrt{s} = 5.02$ TeV. The inclusive evaluated cross-sections, integrated over y and $p_{\rm T}$ ($p_{\rm T} < 15$ GeV/c) are: $\sigma_{\Upsilon(1S)} = 45.5 \pm 3.9({\rm stat.}) \pm 3.5({\rm syst.})$ nb, $\sigma_{\Upsilon(2S)} = 22.4 \pm 3.2({\rm stat.}) \pm 2.7({\rm syst.})$ nb and $\sigma_{\Upsilon(3S)} = 4.9 \pm 2.2({\rm stat.}) \pm 1.0({\rm syst.})$ nb, where the first uncertainty is statistical and the second is systematic. The energy de-

pendence of Υ(nS) states have been evaluated and a steady increase of the cross sections is observed with increasing center-of-mass energy for all the Υ states. The differential cross sections have been compared with ICEM calculations and CEM calculations with NLO corrections. A good agreement within the uncertainties has been observed between the experimental results and model calculations.

The Υ production in p–Pb collisions has been studied at $\sqrt{s_{\rm NN}}$ = 8.16 TeV in the forward ($2.03 < y_{\rm CMS} < 3.53$) and the backward ($-4.46 < y_{\rm CMS} < -2.96$) regions. The Υ(1S) production cross-section scaled by the Pb mass number in p–Pb has been found to be suppressed with respect to the ones measured in pp collisions at the same center-of-mass energy. The value of nuclear modification factor ($R_{\rm pPb}$) is similar at both forward and backward rapidity intervals with slight hints of stronger suppression at low $p_{\rm T}$. In both the rapidity regions, there is no evidence for a centrality dependence of the Υ(1S) $Q_{\rm pPb}$. The $R_{\rm pPb}$ results obtained at $\sqrt{s_{\rm NN}}$ = 8.16 TeV are similar within the experimental uncertainties to those measured by ALICE in p–Pb collisions at the lower energy of $\sqrt{s_{\rm NN}}$ = 5.02 TeV. The rapidity dependence of ALICE $R_{\rm pPb}$ of Υ(1S) at $\sqrt{s_{\rm NN}}$ = 8.16 TeV are found to be in good agreement with LHCb measurements. The models based on nuclear shadowing and coherent parton energy loss or interactions with comoving particles fairly describe the data at the forward rapidity, while they tend to overestimate the $R_{\rm pPb}$ at the backward rapidity. The Υ(2S) $R_{\rm pPb}$ has also been measured, showing a strong suppression, similar to the one measured for the Υ(1S), in the two investigated rapidity intervals. Finally, the first measurement of the Υ(3S) has also been reported, although the large uncertainties prevent a detailed comparison of its behavior in p–Pb collisions with respect to the other bottomonium states.

The measurements of Υ(1S) and Υ(2S) production at forward rapidity combining the 2015 and 2018 data sets are reported for Pb–Pb collisions at $\sqrt{s_{\rm NN}}$ =5.02 TeV. The centrality (0-90%), transverse momentum ($p_{\rm T} < 15$ GeV/c) and rapidity ($2.5 < y < 4.0$)

integrated $R_{\rm PbPb}$ for Υ(1S) and Υ(2S) are 0.353 $\pm$ 0.012 (stat.) $\pm$0.029 (syst.) and 0.128 $\pm$ 0.024 (stat.) $\pm$ 0.026 (syst.), respectively. The suppression of Υ(1S) gets stronger for the more central collisions. The rapidity dependence of Υ(1S) $R_{\rm PbPb}$ hints to a decrease in the value at the most forward rapidity interval comparison to the central range of the ALICE measurement. Together with the CMS results, these measurements report the Υ(1S) suppression as a function of full rapidity with respect to pp collisions. No significant $p_{\rm T}$ dependence of $R_{\rm PbPb}$ is observed up to 15 GeV/c. It is worth noting that the nuclear modification factor in p–Pb collision shows a significant $p_{\rm T}$ dependence in both forward and backward interval measured by ALICE and LHCb. The difference in behavior between p–Pb and Pb–Pb collisions may impose some constraints on theoretical models in near future. The available theoretical calculations fail to describe the bottomonium production fully the rapidity dependence observed for the $R_{\rm PbPb}$ of Υ(1S) in the ALICE forward region. The Υ(2S) state is found to have larger suppression than the Υ(1S). The large uncertainties in Υ(2S) $R_{\rm PbPb}$ prevent any conclusion on its centrality dependence.

The larger data samples expected in Run 3 and Run 4, together with improved detector performance and measurement techniques, will allow us to significantly improve over the $R_{\rm PbPb}$, $R_{\rm pPb}$ and v_2 measurements, with extended kinematic coverage (in transverse momentum) and allowing one to study the currently-unobserved Υ(3S) in Pb–Pb collisions.

I have studied the formalism of the radiative fractional energy loss of a fast moving heavy quark where it radiates gluons due to the scattering from the static scattering center in an infinitely extended anisotropic medium. It has been shown that the fractional energy loss changes with the anisotropy parameter, ξ due to the modification of the heavy quark potential in the aQGP. The fractional energy loss of heavy quarks has been used to evaluate the D-meson p_T spectrum vis-a-vis its nuclear modification factor (R_{AA})

by incorporating this effect in the fragmentation function of the energy depleted heavy quarks. The results for $R_{\rm PbPb}$ of D-meson are then compared with the ALICE and CMS data at $\sqrt{s_{NN}} = 2.76$ and 5.02 TeV in two centrality classes. It has been found that the value of $\tau_{\rm iso}$, which describes the data reasonably, lies in the range $2 \leq \tau_{\rm iso} \leq 4$ fm/c for both the energies and the centrality classes considered in the present work.

APPENDIX A

Fitting functions

A.1 Extended Crystal-Ball or Double Crystal-Ball (CB2)

The Extended Crystal Ball function (CB2) consists of a Gaussian core portion and power-law tails on the both side of the Gaussian core. It has a normalization constant N, two parameters (x and μ) for Gaussian core and four tail parameters ($\alpha_{\rm L}, n_{\rm L}, \alpha_{\rm R}, n_{\rm R}$). The CB2 is defined by the following equation:

$$f(x;\mu,\sigma,\alpha_{\rm L},n_{\rm L},\alpha_{\rm R},n_{\rm R}) = N.\begin{cases} exp(\frac{-(x-\mu)^2}{2\sigma^2}) & \text{for } \alpha_{\rm R} > \frac{x-\mu}{\sigma} > -\alpha_{\rm L} \\ A.(B-\frac{x-\mu}{\sigma})^{-n_{\rm L}} & \text{for } \frac{x-\mu}{\sigma} \leq -\alpha_{\rm L} \\ C.(D+\frac{x-\mu}{\sigma})^{-n_{\rm R}} & \text{for } \frac{x-\mu}{\sigma} \geq \alpha_{\rm R} \end{cases} \tag{A.1}$$

where,

$$A = \left(\frac{n_{\rm L}}{|\alpha_{\rm L}|}\right)^{n_{\rm L}} . \, exp\left(-\frac{|\alpha_{\rm L}|^2}{2}\right)$$

$$B = \frac{n_{\rm L}}{|\alpha_{\rm L}|} - |\alpha_{\rm L}|$$

$$C = \left(\frac{n_{\mathrm{R}}}{|\alpha_{\mathrm{R}}|}\right)^{n_{\mathrm{R}}} . \, exp\left(-\frac{|\alpha_{\mathrm{R}}|^2}{2}\right)$$

$$D = \frac{n_{\mathrm{R}}}{|\alpha_{\mathrm{R}}|} - |\alpha_{\mathrm{R}}|$$

A.2 NA60

NA60 is similar to CB2 function. It is a gaussian shape with variable sigma. This function has total eleven parameters: the normalization factor N , and the two Gaussian core parameters (x and μ) eight tail parameters ($\alpha_{\mathrm{L}}, p^1_{\mathrm{L}}, p^2_{\mathrm{L}}, p^3_{\mathrm{L}}, \alpha_{\mathrm{R}}, p^1_{\mathrm{R}}, p^2_{\mathrm{R}}, p^3_{\mathrm{R}}$). It is defined as:

$$f(x; \mu, \sigma, \alpha_{\mathrm{L}}, p^1_{\mathrm{L}}, p^2_{\mathrm{L}}, p^3_{\mathrm{L}}, \alpha_{\mathrm{R}}, p^1_{\mathrm{R}}, p^2_{\mathrm{R}}, p^3_{\mathrm{R}}) = N.exp\left(-0.5\left(\frac{t}{t_o}\right)^2\right) \tag{A.2}$$

with

$$t = \frac{x - \mu}{\sigma}$$

where:

$$\begin{cases} t_0 = 1 + p^1_{\mathrm{L}}\left(\alpha_{\mathrm{L}} - t\right)^{(p^2_{\mathrm{L}} - p^3_{\mathrm{L}}\sqrt{\alpha_{\mathrm{L}} - t})} & \text{for } t < \alpha_{\mathrm{L}} \\ t_0 = 1 & \text{for } \alpha_{\mathrm{L}} < 1 < \alpha_{\mathrm{R}} \\ t_0 = 1 + p^1_{\mathrm{R}}\left(\alpha_{\mathrm{R}} - t\right)^{(p^2_{\mathrm{R}} - p^3_{\mathrm{R}}\sqrt{\alpha_{\mathrm{R}} - t})} & \text{for } t > \alpha_{\mathrm{R}} \end{cases}$$

A.3 Double Exponential (DE)

The DE is the sum of two exponential function. This function has four parameters and is defined as:

$$f(x; a, b, c, d) = exp(a + b * x) + exp(c + d * x) \tag{A.3}$$

A.4 Double Power Law (DP)

The DP is the sum of two power law functions. This function has four parameters and It can be written as:

$$f(x; a, b, c, d) = a.x^b + c.x^d \tag{A.4}$$

A.5 Variable Width Gaussian (VWG)

The VWG has the following four parameters: normalization factor N and three parameters (μ, α, β). The function is defined as:

$$f(x; N, \mu, \alpha, \beta) = N.exp\left(-\frac{(x-\mu)^2}{2\sigma^2}\right) \tag{A.5}$$

with

$$\sigma = \alpha + \beta\left(\frac{x-\mu}{\mu}\right)$$

Thesis Highlight

Name of the Student: Wadut Shaikh

Name of the CI/OCC: Saha Institute of Nuclear Physics **Enrolment No.:** PHYS05201504011

Thesis Title: Bottomonium studies at LHC energy using ALICE Muon Spectrometer

Discipline: Physical Science **Sub-Area of Discipline:** High Energy Experimental Particle Physics

Date of viva voce: 03/02/2021

The bottomonium (ϒ), is a useful probe to investigate the properties of the deconfined medium, created in ultra-relativistic heavy-ion collisions. The medication of ϒ production at LHC energies in heavy-ion collisions with respect to the binary-scaled yield in pp collisions has been explained by color screening mechanisms. In the bottomonium sector, the regeneration effects are expected to be negligible due to the small number of b quarks produced in relativistic heavy-ion collisions. However, the Cold Nuclear Matter (CNM) effects which include shadowing, parton energy loss, interaction with hadronic medium may also lead to a modification of bottomonium production. In order to disentangle the CNM effects from the hot nuclear matter effects ϒ production has been studied in p-Pb collisions in which the QGP is not expected to be formed. I have studied the bottomonium production via di-muon decay channel in pp, p-Pb and Pb-Pb collisions using the ALICE Muon Spectrometer.

The inclusive ϒ (nS) production cross sections have been measured at forward rapidity ($2.5 < y < 4$) in pp collisions at $\sqrt{s} = 5.02$ TeV. The energy dependency of ϒ (nS) states have been evaluated and a steady increase of the cross sections is observed with increasing $\sqrt{s}$. The differential cross sections have been compared with ICEM and CEM model calculation. A good agreement within the uncertainties has been observed between the experimental results and model calculations.

The measurements of the rapidity, transverse momentum and centrality dependence of the ϒ(1S) nuclear modification factor in p-Pb collisions at $\sqrt{s_{\mathrm{NN}}} = 8.16$ TeV have been reported. The results show a suppression of the ϒ(1S) yields, with respect to the ones measured in pp collisions at the same centre-of-mass energy. The R_{pPb} values are similar at forward and backward rapidity with a slightly stronger suppression at low p_T, while in both rapidity intervals there is no evidence for a centrality dependence of the ϒ(1S) Q_{pPb}. Models based on nuclear shadowing, coherent parton energy loss or interactions with comoving particles fairly describe the data at forward rapidity, while they tend to overestimate the RpPb at backward y_{cms}. The ϒ(2S) R_{pPb} has also been measured, showing a strong suppression, similar to the one measured for the ϒ(1S), in the two investigated rapidity intervals. Finally, a first measurement of the ϒ(3S) has also been performed, even if the large uncertainties prevent a detailed comparison of its behaviour in p–Pb collisions with respect to the other bottomonium states.

The measurements of ϒ (1S) and ϒ (2S) production at forward rapidity combining the 2015 and 2018 data sets are reported for Pb-Pb ollisions at $\sqrt{s_{\mathrm{NN}}} = 5.02$ TeV. The suppression of ϒ (1S) gets stronger for the more central collisions. The rapidity dependence of ϒ (1S) R_{PbPb} hints to a decrease in the value at the most forward rapidity interval comparison to the central range of the ALICE measurement. No significant pT dependence of R_{PbPb} is observed up to 15 GeV/c. It is worth noting that the nuclear modification factor in p-Pb collision shows a significant p_T dependence in both forward and backward interval measured by ALICE and LHCb. The difference in behavior between p-Pb and Pb-Pb collisions may impose some constraints on theoretical models in near future. The available theoretical calculations fail to describe the bottomonium production fully the rapidity dependence observed for the R_{PbPb} of ϒ (1S) in the ALICE forward region. The ϒ (2S) state is found to have larger suppression (3 times) than the ϒ (1S).